JOURNAL
OF
APPLIED PHYSICS

LIBRARY

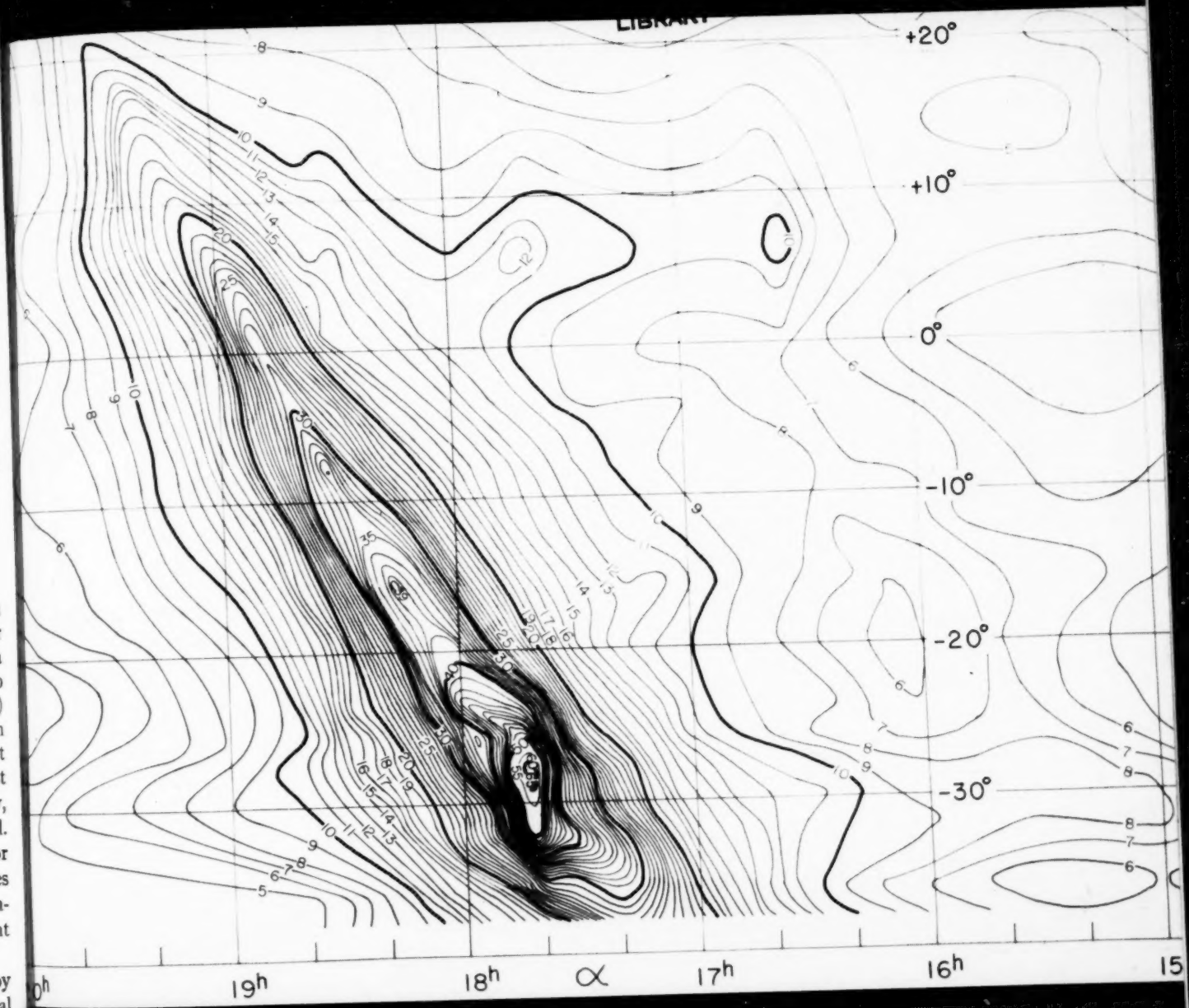

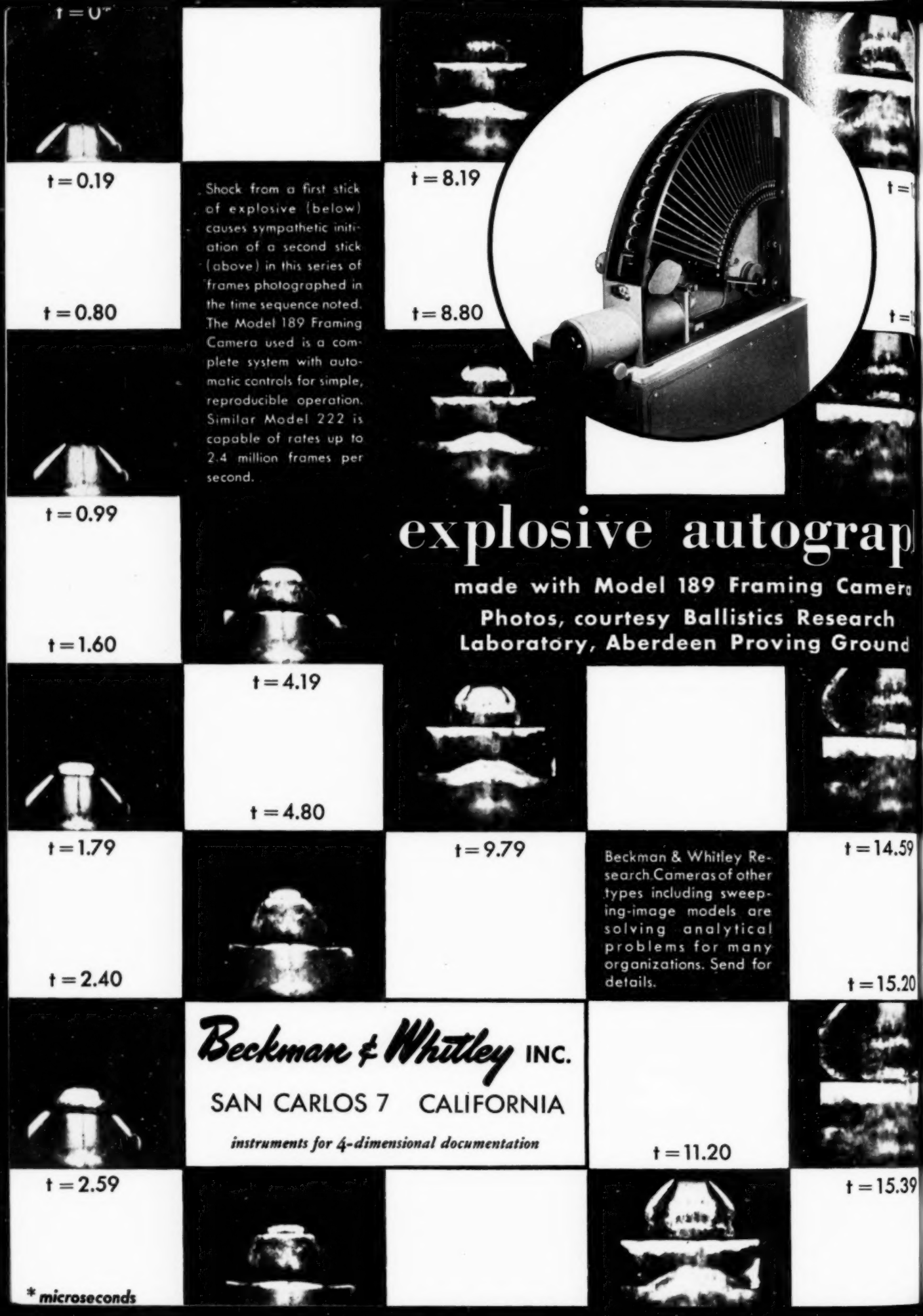
t = 0.19
t = 0.80
t = 0.99
t = 1.60
t = 1.79
t = 2.40
t = 2.59
t = 4.19
t = 4.80
t = 8.19
t = 8.80
t = 9.79
t = 11.20
t = 14.59
t = 15.20
t = 15.39
Shock from a first stick of explosive (below) causes sympathetic initiation of a second stick (above) in this series of frames photographed in the time sequence noted. The Model 189 Framing Camera used is a complete system with automatic controls for simple, reproducible operation. Similar Model 222 is capable of rates up to 2.4 million frames per second.
explosive autograp
made with Model 189 Framing Camera
Photos, courtesy Ballistics Research Laboratory, Aberdeen Proving Ground
Beckman & Whitley Research Cameras of other types including sweeping-image models are solving analytical problems for many organizations. Send for details.
Beckman & Whitley INC.
SAN CARLOS 7 CALIFORNIA
instruments for 4-dimensional documentation
* microseconds

JOURNAL OF APPLIED PHYSICS

Vol. 26, No. 4 APRIL, 1955

In This Issue

Page

Extension of the Rouse Theory of Viscoelastic Properties to Undiluted Linear Polymers . . . John D. Ferry, Robert F. Landel, and Malcolm L. Williams 359

Rate of Formation of Film on Metals and Alloys . . . G. P. Chatterjee 363

Creep of Aluminum under Cyclotron Irradiation . . . M. R. Jeppson, R. L. Mather, A. Andrew, and H. P. Yockey 365

Azimuthal Surface Waves on Circular Cylinders . . . Robert S. Elliott 368

Thermoelectric Power and Electrical Resistivity of Dilute Alloys of Silicon in Copper, Nickel, and Iron . . . C. A. Domenicali and F. A. Otter 377

Injected Current Carrier Transport in a Semi-Infinite Semiconductor and the Determination of Lifetimes and Surface Recombination Velocities . . . W. van Roosbroeck 380

Diffraction of Electromagnetic Waves by a Metallic Wedge of Acute Dihedral Angle . . . W. W. Grannemann and R. B. Watson 392

Moderation of Neutrons in SiO_2 and $CaCo_3$ . . . Jay Tittman 394

Re-Examination of the Nonsteady Theory of Jet Formation by Lined Cavity Charges . . R. J. Eichelberger 398

Relation to Diffusion Measurements of Some Beta-Ray Absorption Phenomena . . . A. E. Berkowitz 403

Measurement of the Elastic Constants of Single Crystal Cobalt . . . H. J. McSkimin 406

Theory of Frequency Modulation Noise in Tubes Employing Phase Focusing . . . John L. Stewart 409

Measurement of the Lifetime of Minority Carriers in Germanium . . . William G. Spitzer, Tomas E. Firle, Melvin Cutler, Robert G. Shulman, and Milton Becker 414

Electron Temperature in the Parallel Plane Diode . . . T. N. Chin 418

X-Ray Diffraction Study of Silver Iodide Aerosols . . . James E. Manson 423

Measurement of Detonation Velocity by Doppler Effect at Three-Centimeter Wavelength . . . Melvin A. Cook, Ray L. Doran, and Glen J. Morris 426

Reflection of Sound in the Ocean from a Continuous Stratum Containing a Velocity Extremum . . . E. O. Cook and H. S. Heaps 429

Dependence of the Electric Strengths of Liquids on Electrode Spacing . . . A. H. Sharbaugh, J. K. Bragg, and R. W. Crowe 434

Barium Getters in Carbon Monoxide . . . J. Morrison and R. B. Zetterstrom 437

Crystallization Kinetics in High Polymers. II. Polymer-Diluent Mixtures . . . Leo Mandelkern 443

Surface Matching of Dielectric Lenses . . . E. M. T. Jones and S. B. Cohn 452

Field Produced by an Arbitrary Slot on an Elliptic Cylinder . . . James R. Wait 458

Properties of Elastic and Plastic Waves Determined by Pin Contactors and Crystals . . Stanley Minshall 463

Orientation and Temperature Effects on the Electrical Resistivity of High-Purity Magnesium . . . James L. Nichols 470

Cubic to Orthorhombic Diffusionless Phase Change—Experimental and Theoretical Studies of AuCd . . . D. S. Lieberman, M. S. Wechsler, and T. A. Read 473

On a Nonlinear Transfer System . . . I. Flügge-Lotz and W. S. Wunch 484

Letters to the Editor:

Growth of Anodic Ta_2O_5 Films During Illumination with Ultraviolet Light . . D. A. Vermilyea 489

Laminar Flow in Channels with Porous Walls at High Suction Reynolds Numbers . . . John R. Sellars 489

Variation of Noise with Ambient in Germanium Filaments . . . T. G. Maple, L. Bess, and H. A. Gebbie 490

Note on Self-Diffusion of Nickel . . . H. Burgess and R. Smoluchowski 491

Information Required for Missile Guidance . . . Fred P. Adler 492

Books Reviewed . . . 492

Books Received . . . 494

Announcements . . . 494

Index to Advertisers . . . xxiv

JOURNAL OF APPLIED PHYSICS

A journal of applications of physics to other sciences and to industry

Published by the

American Institute of Physics

OFFICERS

FREDERICK SEITZ
Chairman

GEORGE B. PEGRAM
Treasurer

GOVERNING BOARD

ALLEN V. ASTIN
ROBERT F. BACHER
H. A. BETHE
J. W. BUCHTA
S. A. GOUDSMIT
DEANE B. JUDD
HUGH S. KNOWLES
W. H. MARKWOOD, JR.
WILLIAM F. MEGGERS
PHILIP M. MORSE
BRIAN O'BRIEN
HARRY F. OLSON
R. F. PATON
GEORGE B. PEGRAM
ERIC RODGERS
RALPH A. SAWYER
FREDERICK SEITZ
WILLIAM SHOCKLEY
H. D. SMYTH
J. H. VAN VLECK
MARK W. ZEMANSKY

Consultant on Printing

MELVIN LOOS

ADMINISTRATIVE STAFF

HENRY A. BARTON
Director

WALLACE WATERFALL
Executive Secretary

THEODORE VORBURGER
Advertising Manager

RUTH F. BRYANS
Publication Manager

EDITH I. NEFTEL
Circulation Manager

KATHRYN SETZE
Assistant Treasurer

Editor
Robert L. Sproull

Editorial Board

Maurice A. Biot	Elmer Hutchisson	W. R. Smythe
Walker Bleakney	D. O. North	Arthur V. Tobolsky
Wallace J. Eckert	Louis A. Pipes	A. M. Weinberg

THE JOURNAL OF APPLIED PHYSICS is devoted to the application of physics to other sciences, to engineering, and to industry. Previous to 1937, this journal was called PHYSICS.

The JOURNAL OF APPLIED PHYSICS welcomes articles of two distinct kinds: (1) Descriptions of new results in experimental or theoretical physics which are of general interest to applied physicists. The author should explain his contribution in such a way that a physicist or engineer in another field of specialization can appreciate its objectives and essential features. (2) Critical reviews of particular areas of applied physics. Authors contemplating writing such reviews should correspond with the Editor before they begin writing.

The JOURNAL OF APPLIED PHYSICS welcomes letters to the editor which describe in a few words the content of laboratory reports and theses and which tell readers how they may obtain copies of such reports.

Manuscripts should be submitted to the Editor, Rockefeller Hall, Cornell University, Ithaca, New York. Authors should read the "Information for Contributors," facing page 1 of the January issue, before writing articles or letters. The *Style Manual* of the American Institute of Physics is also helpful to writers preparing manuscripts for journals published by the American Institute of Physics. It can be obtained for $1.00 from the American Institute of Physics, 57 East 55th Street, New York 22, New York.

Corrected proofs and all correspondence concerning papers in the process of publication should be addressed to the Publication Manager, American Institute of Physics, 57 East 55 Street, New York 22, New York.

Subscriptions, renewals, and orders for back numbers should be addressed to the American Institute of Physics, 57 East 55 Street, New York 22, New York.

Subscription Price	U.S. and Canada	Elsewhere
To members of the American Institute of Physics and Affiliated Societies	$10.00	$11.00
To all others	12.00	14.00

Back Number Prices

Yearly back number rate when complete year is available: $15.00.
Single copies: $1.50 each.

Changes of address should be sent to the American Institute of Physics.

Advertising rates supplied on request. Orders, advertising copy, and cuts should be sent to the American Institute of Physics.

Entered as second class matter January 22, 1937, at the Post Office at Lancaster, Pennsylvania, under the Act of March 3, 1879. Accepted for mailing at the special rate of postage provided for in paragraph (d-2), section 34.40, P. L. & R. of 1948, authorized May 2, 1932.

Journal
of
Applied Physics

Volume 26, Number 4 April, 1955

Extensions of the Rouse Theory of Viscoelastic Properties to Undiluted Linear Polymers*

John D. Ferry, Robert F. Landel, and Malcolm L. Williams†
Department of Chemistry, University of Wisconsin, Madison, Wisconsin
(Received May 5, 1954)

The Rouse theory for viscoelastic properties of very dilute solutions is modified for application to undiluted linear polymers. With the effective segment mobility expressed in terms of steady-flow viscosity, the theory is applied to polymers of rather low molecular weight essentially without further change. In high molecular weight polymers, it is assumed that for modes of motion with relaxation times above a critical value the effective segment mobility drops abruptly, in accordance with the effect of entanglement coupling on steady-flow viscosity as described by Bueche. Properties in both the transition region between glasslike and rubberlike consistency and the rubberlike or plateau region are predicted semiquantitatively with no arbitrary parameters. In an alternative application to the transition region, the average effective friction coefficient per monomer unit can be calculated for both linear and lightly cross-linked systems.

INTRODUCTION

THE theory of Rouse[1] has been quite successful in molecular interpretation of the viscoelastic properties of very dilute polymer solutions and their dependence on temperature, concentration, molecular weight, and choice of solvent.[2] The only information needed for quantitative prediction of viscoelastic properties at a given temperature and concentration is the polymer molecular weight and the difference between steady-flow viscosities of solution and solvent. The result is obtained in the form of a discrete spectrum of relaxation mechanisms, corresponding to various modes of cooperative motion of a flexible polymer molecule.

In a recent application of the theory to concentrated solutions,[3] it was assumed that the interlacing of foreign polymer molecules through a given polymer coil prolonged all relaxation times to the same degree. This permitted moderately successful prediction of the viscoelastic behavior at very long times, near the termination of the relaxation distribution function. At shorter times the theory diverged from experiment, showing that shorter relaxation times are not in fact prolonged so much by intermolecular interlacing. The extreme prolongation of the longest relaxation times was attributed to the coupling effect postulated by Bueche[4] in connection with the dependence of steady-flow viscosity on molecular weight.

In the present paper, the theory of Rouse is applied to undiluted polymers. For polymers of very low molecular weight, it is essentially unmodified. At higher molecular weights, a very simple modification suggested by the viscosity concepts of Bueche[4] provides a semiquantitative prediction of the plateau region of the relaxation spectrum. Finally, when the theory is applied to the lower part of the region where the spectrum goes through the transition from rubberlike to glasslike consistency, it is possible to calculate the monomeric frictional coefficient for a number of undiluted polymers as well as diluted polymer systems.

POLYMERS OF LOW MOLECULAR WEIGHT

In an undiluted polymer of quite low molecular weight, above its glass-transition temperature, the intermolecular coupling effect described by Bueche[4] is absent, and it is reasonable to describe the mobilities of all segments of a polymer molecule by a single average value B just as done in dilute solution by

* Part XV of a series on Mechanical Properties of Substances of High Molecular Weight.
† Union Carbide and Carbon Fellow in Physical Chemistry, 1952–1954.
[1] P. E. Rouse, Jr., J. Chem. Phys. **21**, 1272 (1953).
[2] P. E. Rouse, Jr., and K. Sittel, J. Appl. Phys. **24**, 690 (1953).
[3] Ferry, Jordan, Evans, and Johnson, J. Polymer Sci. **14**, 261 (1954).
[4] F. Bueche, J. Chem. Phys. **20**, 1959 (1952).

Rouse.[1] The reciprocal of B is the friction coefficient f_0 introduced by Bueche,[4] and Bueche's Eq. (1) is identical with Rouse's Eq. (32) for the steady flow viscosity η if the now nonexistent contribution from the solvent is eliminated:

$$\eta = n\sigma^2 N^2/36B, \tag{1}$$

where n is the number of molecules per cc, σ^2 the mean square segment length, and N the number of segments in a molecule.

The unknown mobility B appearing in Rouse's viscoelastic equations can be eliminated in terms of η, following the procedure for dilute solutions, to provide for example the following expression for the real part of the complex shear modulus, G':

$$G' = (\rho RT/M) \sum_{p=1}^{N} \omega^2\tau_p^2/(1+\omega^2\tau_p^2), \tag{2}$$

$$\tau_p = 6\eta M/\pi^2 p^2 \rho RT, \tag{3}$$

where ρ is the density, M the molecular weight, and ω the circular frequency. The validity is limited to $p<N/5$. Thus the dynamic mechanical properties can be predicted if η, M, and ρ are known. A comparison is made in Fig. 1 for a polyisobutylene liquid studied by Harper, Markovitz, and DeWitt.[5] The values of η (850 poises) and M (weight-average, 10 900) used are those provided by another investigation of this same sample by Leaderman.[6] Because of the small value of N associated with such a low molecular weight, the theory should be applicable only within a narrow frequency range; however, the probably broad distribution of molecular weights in this sample extends the range of qualitative applicability, and in fact, the agreement is fairly good. The distribution of molecular weights naturally causes the dispersion to extend to lower frequencies than predicted by theory. The use of the weight-average molecular weight in the calculation is somewhat arbitrary. Nevertheless, Eqs. (2) and (3) should be useful for semiquantitative prediction of viscoelastic properties of low molecular weight polymers.

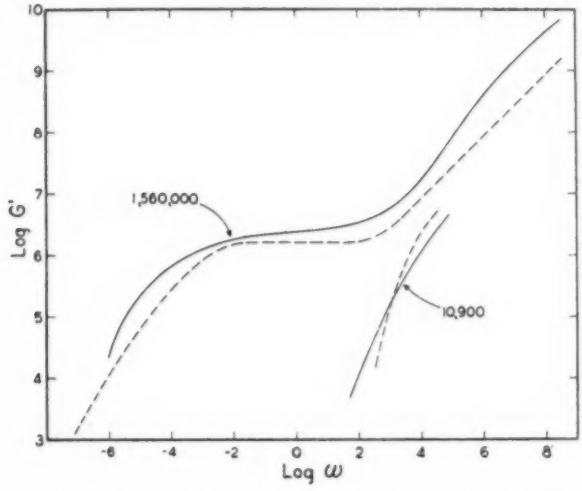

FIG. 1. Real part of complex dynamic shear modulus at 25°C, plotted logarithmically against frequency, for two samples of polyisobutylene identified by their weight-average molecular weights. Solid curves, measured (see references 5, 11–13) and reduced to 25°C; dashed curves, calculated from Eqs. (2) and (3) (low molecular weight), and from Eqs. (2), (4), and (5) (high molecular weight).

[5] Harper, Markovitz, and DeWitt, J. Polymer Sci. 8, 435 (1952).
[6] Leaderman, Smith, and Jones, J. Polymer Sci. 14, 47 (1954).

POLYMERS OF HIGH MOLECULAR WEIGHT

In a polymer of high molecular weight, there is a broad zone where the dynamic mechanical properties change with frequency much more gradually than predicted by Eqs. (2) and (3), corresponding to the box[7] or plateau[8] region of the relaxation distribution function. This zone, which appears in both undiluted polymers and concentrated solutions,[8] is attributed to the intermolecular coupling postulated by Bueche[4] to explain the enhanced dependence of steady-flow viscosity on molecular weight above a critical value. Entanglements with neighboring molecules cause the average segmental friction coefficient f_0 operative in translation of an entire molecule to be sharply increased to a new value f; the ratio f/f_0 depends on the degree of entanglement. In treating viscoelastic properties, we now suppose that for long-range cooperative motions with long-relaxation times the average effective friction coefficient is f, while for short-range cooperative motions with short relaxation times the average effective friction coefficient is f_0. Thus, if the entanglements are relatively far apart, as would be deduced from the value of M at which the viscosity molecular weight relation changes,[9] then motions involving short-range cooperation should remain unaffected by their presence.[10]

Properly, the effective coefficient should no doubt change gradually from f to f_0 for mechanisms with progressively decreasing relaxation times [increasing index p in Eq. (3)]. However, for simplicity we assume an abrupt transition at a critical value of the index, p_e. Then Eq. (3) is replaced by

$$\tau_p = 6\eta M/\pi^2 p^2 \rho RT, \quad p \le p_e, \tag{4}$$

$$\tau_p = 6\eta M/(f/f_0)\pi^2 p^2 \rho RT, \quad p > p_e. \tag{5}$$

A theoretical curve for G' can be constructed from Eqs. (2), (4), and (5) if f/f_0 and p_e can be determined.

[7] Andrews, Hofman-Bang, and Tobolsky, J. Polymer Sci. 3, 669 (1948).
[8] Ferry, Fitzgerald, Johnson, and Grandine, J. Appl. Phys. 22, 717 (1951).
[9] T. G. Fox, Jr., and P. J. Flory, J. Phys. Colloid Chem. 55, 221 (1951).
[10] A much more elaborate treatment of the plateau region by W. G. Hammerle (Ph.D. thesis, Princeton University, 1954) involves a frictional coefficient which varies from one monomer unit to the next along the length of the polymer molecule. It does not, however, provide absolute values for either the time scale or the magnitudes of mechanical properties.

For comparison with experiment, we choose the polyisobutylene distributed by the National Bureau of Standards, using values of G' compiled by Marvin,[11] especially from stress relaxation measurements of Tobolsky[12] and dynamic measurements from this laboratory.[13] The value of p_e is estimated from the quasi-equilibrium modulus of high molecular weight polyisobutylenes in the region where stress is independent of time and molecular weight over a considerable range of both variables[14]: $G_e=3.3\times10^6$ dyn/cm² at 25°C. If this behavior is attributed to entanglements acting effectively as cross links, the average molecular weight between entanglements, M_e, is 6700. The effect of entanglements in increasing the friction coefficient should appear when M is about twice this value,[15] which also corresponds roughly to the point ($M=17\,000$) where the slope of a log-log plot of viscosity *vs* molecular weight suddenly increases.[16] We expect cooperative motions to be at sufficiently short range to be oblivious of entanglements when $p>M/2\times6700$; i.e. $p_e\cong M/13\,400$. The value of f/f_0 is also based on this choice of a critical molecular weight, being taken as the ratio of the steady-flow viscosities at molecular weights 1 560 000 and 13 400 divided by the ratio which would be observed in the absence of entanglement. In the latter case,[4] η would be directly proportional to M_w; actually,[9] it is proportional to the 3.4 power. Thus

$$\log f/f_0=(3.4-1)\log M_w/2M_e \qquad (6)$$

which in the present case is 4.96.

The resulting theoretical curve for G' is also compared with the experimental curve in Fig. 1. It lies a little too far to the right, primarily because of the choice of weight-average molecular weight in Eqs. (4) and (5). A somewhat higher average would apparently be more successful.[17] The remaining discrepancies are probably largely due to the presence of a wide distribution of molecular weights, and the artificially abrupt change from f to f_0 in the application of the theory.[18] Deviations at high frequencies are to be expected because the theory does not include mechanisms with very short relaxation times (corresponding to $p>N/5$). The fit is of course much inferior to that achieved by the empirical wedge-box distribution function of Tobolsky,[12] which involves several arbitrary parameters. However, the method should be useful for semiquantitative predictions.

POLYMER SYSTEMS IN THE TRANSITION REGION

In the transition region between rubberlike and glasslike consistency, viscoelastic properties are practically independent of molecular weight,[14,19] showing that the effective average friction coefficient is unaffected by entanglements. The values of p are sufficiently high that the discrete spectrum implied in Eq. (2) can be replaced by a continuous spectrum $\Phi d\ln\tau=-(\rho RT/M)\times(dp/d\tau)d\tau$. Differentiation of the Rouse expression for τ, with the segmental mobility B replaced by $1/f_0$, gives[20]

$$\Phi=(n\sigma N/2\pi)(f_0kT/6)^{\frac{1}{2}}\tau^{-\frac{1}{2}}. \qquad (7)$$

The magnitudes of f_0, N, and σ are indefinite because they involve an arbitrary segment length which remains unspecified in the theory. This can be circumvented by defining the friction coefficient per monomer unit,[21] ζ_0 as f_0/q, where q is the number of monomer units in a segment. For a Gaussian coil, the root-mean-square distance between chain ends $(\langle r_0^2\rangle)^{\frac{1}{2}}$ (the subscript 0 denoting, in Flory's sense,[22] that in undiluted polymer or concentrated solution the configuration is not affected by long-range interactions) may be expressed either as $\sigma(N)^{\frac{1}{2}}$ or as $a(qN)^{\frac{1}{2}}$, where a is a length of the order of a chain bond (qN being the degree of polymerization, M/M_0). Then $\sigma=a(q)^{\frac{1}{2}}$, and Eq. (7) becomes

$$\Phi=(1/2\pi\sqrt{6})(a\rho N_0/M_0)(\zeta_0kT)^{\frac{1}{2}}\tau^{-\frac{1}{2}}, \qquad (8)$$

where N_0 is Avogadro's number and M_0 is the molecular weight of a monomer unit.[23]

Thus Φ in the transition region should be proportional to $\tau^{-\frac{1}{2}}$, and its magnitude involves only two microscopic properties of the monomer unit, a and ζ_0. Since a is obtainable from intrinsic viscosity measurements,[24] ζ_0

[11] R. S. Marvin, Proc. Second Internatl. Congress on Rheology, p. 156 (1954).

[12] R. D. Andrews and A. V. Tobolsky, J. Polymer Sci. **7**, 221 (1951) and unpublished; A. V. Tobolsky, J. Am. Chem. Soc. **74**, 3786 (1952).

[13] (a) Fitzgerald, Grandine, and Ferry, J. Appl. Phys. **24**, 650 (1953); (b) Ferry, Grandine, and Fitzgerald, J. Appl. Phys. **24**, 911 (1953).

[14] A. V. Tobolsky and J. R. McLoughlin, J. Polymer Sci. **8**, 543 (1952).

[15] F. Bueche, private communication.

[16] T. G. Fox, Jr., and P. J. Flory, J. Appl. Phys. **21**, 581 (1950).

[17] Application of the Rouse theory to stress relaxation, using the viscosity-average molecular weight, and comparison with experimental data of Andrews and Tobolsky (see reference 12) reveals a similar deviation which is exaggerated in unfractionated samples of very high molecular weight.

[18] Better agreement is afforded by specifying a gradual change of arbitrary form, e.g. by applying the exponent $p^2/(p^2+p_e^2)$ to f/f_0 in Eq. (5) for all values of p.

[19] J. R. McLoughlin and A. V. Tobolsky, J. Colloid Sci. **7**, 555 (1952).

[20] Exactly the same expression is obtained by replacing the sum in Eq. (2) with an integral, following Rouse (see reference 1), and subjecting the resulting equation for G' to the second approximation calculation of M. L. Williams and J. D. Ferry [J. Polymer Sci. **11**, 169 (1953)].

[21] J. G. Kirkwood, J. Chem. Phys. **14**, 51 (1946).

[22] P. J. Flory, J. Chem. Phys. **17**, 303 (1949).

[23] The retardation distribution function $Ld\ln\tau$ (contribution to steady-state or equilibrium compliance associated with retardation times in the range $d\ln\tau$) can be obtained from Φ through an exact relation derived by B. Gross and H. Pelzer [J. Appl. Phys. **22**, 1035 (1951)]. Under the conditions to which Eq. (8) is restricted, $L=1/\pi^2\Phi$. The identical relation is obtained by taking the complex reciprocal of the shear modulus $G'+iG''$, and applying second approximation calculations (see reference 20) to the resulting complex compliance $J'-iJ''$. The relation $L=1/\pi^2\Phi$ is found to hold fairly well experimentally in the transition region even when $d\log\Phi/d\log\tau$ is not exactly $-\frac{1}{2}$; see Table III, reference 13(b).

[24] T. G. Fox, Jr., and P. J. Flory, J. Am. Chem. Soc. **73**, 1909 (1951).

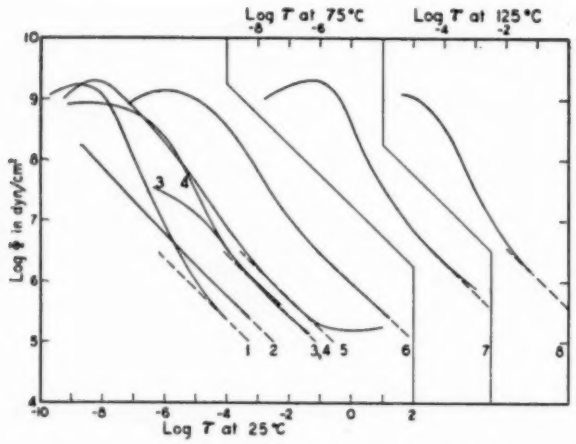

FIG. 2. Experimental relaxation distribution functions in the transition region; dashed lines are drawn with the theoretical slope of $-\frac{1}{2}$ (Eq. 8). 1, 10 percent polyvinyl chloride in dimethyl thianthrene (see reference 25); 2, 20 percent cellulose tributyrate in dimethyl phthalate (see reference 26); 3, 62 percent polystyrene in Decalin (see reference 28); 4, 50 percent polyvinyl acetate in tricresyl phosphate (see reference 27); 5, polyisobutylene (see reference 13); 6, 40 percent polyvinyl chloride in dimethyl thianthrene (see reference 25); 7, polyvinyl acetate (see reference 27); 8, polystyrene (see reference 28). Temperature 25° except for 7 (75°) and 8 (125°).

can be calculated from experimental data, thus determining a parameter which is fundamental in all considerations of polymer Brownian movement.

The function Φ is plotted with a double logarithmic scale in Fig. 2 for three undiluted polymers as well as five concentrated polymer solutions, whose dynamic mechanical properties have been studied through the transition region in this laboratory.[13,25–28] In each case the theoretical slope of $-\frac{1}{2}$ is approached near the bottom of the transition. For the solutions, this slope is followed for 1 to 2 decades of logarithmic time; for the undiluted polymers, about half a decade. At shorter times, most of the experimental curves first become steeper and then flatten into maxima. These deviations reflect short-range cooperations influenced by local steric effects and motions within the segments, which are not included in the theory.

[25] E. R. Fitzgerald and J. D. Ferry, J. Colloid Sci. 8, 1, 224 (1953).
[26] R. F. Landel, Ph.D. thesis (University of Wisconsin, 1954).
[27] M. L. Williams, Ph.D. thesis (University of Wisconsin, 1954).
[28] L. D. Grandine, Jr., and J. D. Ferry, J. Appl. Phys. 24, 679 (1953).

Values of ζ_0 may be calculated from the portions of the Φ curves which follow the theoretical slope as indicated by the dashed lines in Fig. 2. At 25°, log ζ_0 (in dyn sec/cm) ranges from -5.36 for 10 percent polyvinyl chloride in dimethyl thianthrene to -1.26 for the same system with 40 percent polymer. Probably ζ_0 is the most important parameter characterizing the differences in mechanical behavior of polymer systems in the transition region. The shapes of Φ are roughly similar for all the systems in Fig. 2 (except the cellulose tributyrate gel), but the position of each on the time scale at a given temperature is determined by ζ_0. The changes in viscoelastic properties with temperature are primarily determined by the temperature dependence of ζ_0, which is practically identical with that of the reduction factor a_T used empirically to characterize temperature effects and to calculate apparent activation energies of the relaxation processes.[13,25,28]

Figure 2 includes several lightly cross-linked systems. It would not be expected that the friction coefficient involved in short-range cooperative motions would be much affected by the presence of a few cross links. Nevertheless, the temperature dependence of the average effective coefficient ζ_0 may well be enhanced by the presence of cross links or branch points because they diminish the free volume, as pointed out by Fox,[29] so that the glass transition temperature is elevated. With decreasing temperature, therefore, there may be an increasing tendency for cross links to diminish segmental mobility and augment the value of ζ_0.

ACKNOWLEDGMENTS

This work was part of a program of research on the physical structure and properties of cellulose derivatives and other polymers supported by the Allegany Ballistics Laboratory, Cumberland, Maryland, an establishment owned by the United States Navy and operated by the Hercules Powder Company under Contract NOrd 10431. It was also supported in part by a grant from Research Corporation and by the Research Committee of the Graduate School of the University of Wisconsin from funds supplied by the Wisconsin Alumni Research Foundation. The Fellowship in Physical Chemistry given by Union Carbide and Carbon Corporation is gratefully acknowledged. We are indebted to David B. Ludlum for helpful discussions.

[29] T. G. Fox and S. Loshaek, J. Polymer Sci. 15, 371 (1955).

JOURNAL OF APPLIED PHYSICS VOLUME 26, NUMBER 4 APRIL, 1955

Rate of Formation of Film on Metals and Alloys

G. P. CHATTERJEE
Bengal Engineering College, University of Calcutta, India
(Received December 9, 1953)

The rate of atmospheric corrosion of Cu−Zn and Cu−Mg alloys are retarded by Al or Mn, and the law of the growth of film in the case of Cu−Zn alloys changes over from the parabolic to the logarithmic law on the addition of Al or Mn. For Cu−Mg alloys under a given set of conditions the law of the growth of film is governed by

$$x^{\frac{1}{2}} = k_1 \log t + k_2,$$

where x is the film thickness, t is time, and k_1 and k_2 are constants. It has been indicated that some experimental data on the corrosion of metals and alloys may be quantitatively represented if two or more functions, representing different mechanisms of the growth of film, are taken into consideration simultaneously.

INTRODUCTION

AN attempt has been made in this paper to study the laws of the growth of films on some copper-zinc and copper-magnesium alloys with or without the addition of aluminum or manganese under different humidity conditions at atmospheric temperature and to show that the experimental data may not only be qualitatively explained but represented quantitatively, if two or more functions, representing different mechanisms of the growth of the film, are taken into consideration simultaneously.

EXPERIMENTAL PROCEDURE

The alloys were carefully prepared in an electrical resistance furnace and cast into small ingots. Test pieces in the form of cylinders (25 to 30 mm long and 5 to 10 mm in diameter) were annealed under vacuum at 200°C for 8 hours. The samples were exposed to air in a vessel for different periods of time at known temperature, pressure, and humidity conditions. The film thickness was measured accurately before and after atmospheric corrosion at known magnifications (100× to 450×).

EXPERIMENTAL RESULTS AND DISCUSSIONS

The experimental results are given in Tables I, II, and III and plotted in Figs. 1, 2, and 3. It may be noted from Fig. 1 that with 65 percent humidity at 22°C and 755 mm Hg pressure:

A. (a) for the Cu−Zn alloy, the film thickness x as function of $t^{\frac{1}{2}}$ is linear, and hence it obeys the parabolic law of growth of film;
   (b) for the Cu−Zn−Mn alloy, however, x as function of $t^{\frac{1}{2}}$ is not linear, but x as function of $\log t$ is linear (curve *I*, Fig. 1). Thus the growth of the film obeys the logarithmic law;
   (c) the film on the Cu−Zn−Al alloy also obeys the logarithmic law (curve II, Fig. 1);

B. (a) for the Cu−Mg alloy, x is neither a parabolic nor a logarithmic function of t (it will be explained later that $\sqrt{x}$ is a linear function of $\log t$ for this alloy);
   (b) for the Cu−Mg−Mn alloy, x is a logarithmic function of t;
   (c) for the Cu−Mg−Al alloy also x is a logarithmic function of t.

Thus the effects of Mn and Al tend to change the rate of growth of films on Cu−Zn alloys from the parabolic to the logarithmic law. It is not unlikely that the lower conductivities of oxides of manganese and the comparatively higher strength of Al_2O_3 are primarily responsible for such changes.

TABLE I. The composition of the alloys.

Alloys	Cu	Zn	Mg	Mn	Al
Cu−Zn	60.28	39.70	···	···	···
Cu−Zn−Mn	58.70	39.12	···	2.10	···
Cu−Zn−Al	59.10	39.83	···	···	1.00
Cu−Mg	77.0	···	23.0	···	···
Cu−Mg−Mn	70.0	···	28.0	1.96	···
Cu−Mg−Al	73.0	···	25.3	···	1.78

TABLE II. The film thicknesses as function of time t, for the different alloys at 220°C, 755 mm Hg pressure of air with 65 percent average humidity. Data plotted in Fig. 1.

Time t in hours	Film thickness ×10⁴ mm			Film thickness ×10³ mm		
	Cu−Zn	Cu−Zn −Mn	Cu−Zn −Al	Cu−Mg	Cu−Mg −Mg	Cu−Mg −Al
25 hours	84	52	60	391	191	176
50 hours	91	71	66	404	208	192
110 hours	113	90	76	428	229	206
206 hours	132	100	83	445	242	218
350 hours	156	112	88	464	253	226

TABLE III. The film thickness x as function of time t for the different alloys at 34°C, 752 mm of air saturated with moisture. Data plotted in Figs. 2 and 3.

Time t in hours	Film thickness ×10³ mm	
	Cu−Mg	Cu−Mg−Mn
25 hours	400	120
50 hours	412	140
110 hours	452	182
206 hours	580	280
350 hours	960	462

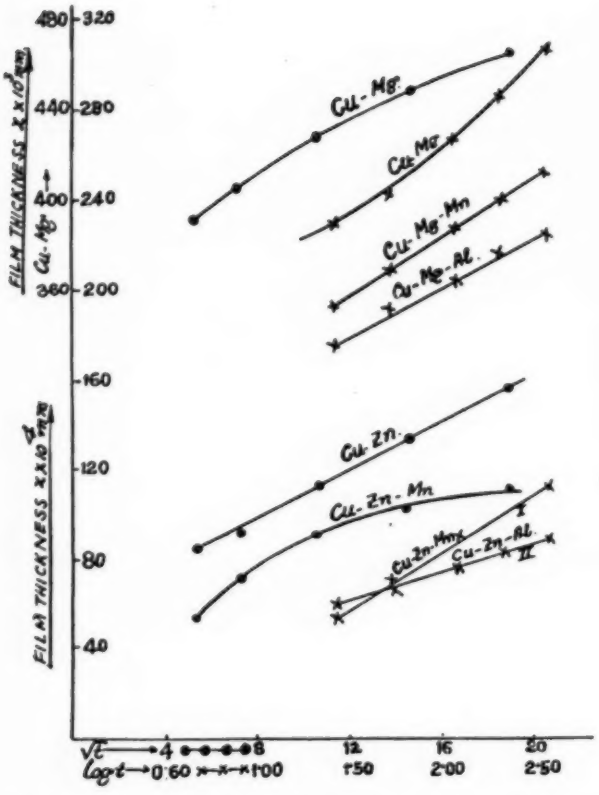

FIG. 1. Film thickness x as function of $t^{\frac{1}{3}}$ (●—●—●) and as function of log$t$ (×—×—×) for different alloys at 22°C, 755 mm Hg pressure and 65 percent humidity.

The data in Table III plotted in Fig. 2 show that the film thickness x on Cu−Mg alloys tends to increase progressively with time when the atmosphere is saturated with moisture. It is not unlikely that in the case of Cu−Mg alloys with 100 percent humidity the growth of film tends to follow an exponential law. In connection with the atmospheric corrosion of iron, Evans[1] has pointed out that Vernon obtained similar results in an atmosphere of fairly high humidity intermittently reaching the saturation value.

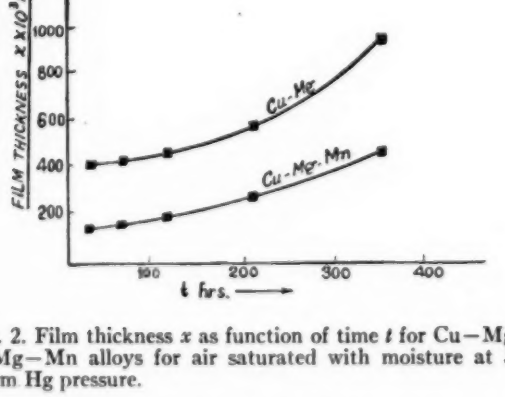

FIG. 2. Film thickness x as function of time t for Cu−Mg and Cu−Mg−Mn alloys for air saturated with moisture at 34°C, 752 mm Hg pressure.

[1] U. R. Evans, *Corrosion of Metals* (Edward Arnold and Company, London, 1926), p. 164.

In another paper[2] an equation has been derived by a combination of the parabolic and logarithmic law and the rates of formation of films on some metals and alloys have been explained on the basis of simultaneous actions of different factors. In connection with iodide films on silver, Evans and Bannister[3] have shown that x is first a linear and then a parabolic function of t. Bircumshaw and Everdell[4] obtained similar results with iodide films on copper. It is not unlikely that in one case a factor which tends to produce a linear function and another which tends to produce a parabolic function may be operative simultaneously. For example, it may be easily shown that if dx/dt be proportional to x and also proportional to $e^{-cx^{\frac{1}{2}}}$ one gets on integration

$$x^{\frac{1}{2}} = k_1 \log t + k_2.$$

In other words, $x^{\frac{1}{2}}$ is a linear function of log$t$. How far this is true may be seen from Fig. 3 where the value of

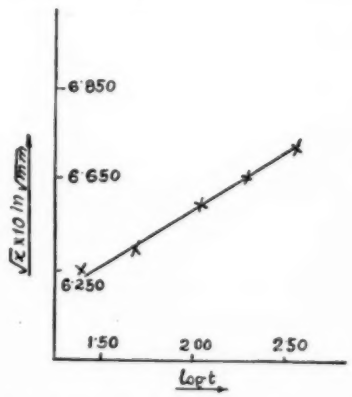

FIG. 3. $\sqrt{x}$ as function of log$t$ for Cu−Mg alloys at 22°C, 755 mm Hg pressure and 65 percent humidity.

$x^{\frac{1}{2}}$ for Cu−Mg alloys has been plotted as function of log$t$. It is evident, therefore, that many experimental data on the rate of formation of films on metals and alloys may be quantitatively explained when different factors and equations are taken into consideration simultaneously.

CONCLUSIONS

1. The rate of atmospheric corrosion of Cu−Zn and Cu−Mg alloys is retarded by the addition of Al and Mn.

2. The law of growth of film in the case of Cu−Zn alloys changes over from the parabolic to the logarithmic law on the addition of Mn or Al.

3. The rate of growth of films on Cu−Mg−Mn or Cu−Mg−Al obeys the logarithmic law of the growth of film.

[2] G. P. Chatterjee, Proc. Indian Sci. Congr. **III**, 247 (1952).

[3] U. R. Evans and L. C. Bannister, Proc. Roy. Soc. (London) **A125**, 125, 375 (1929).

[4] L. L. Bircumshaw and M. H. Everdell, Proc. Roy. Soc. (London) **A183**, 598 (1942).

4. Cu–Mg alloys at 22°C, 755 mm pressure and 65 percent humidity tends to obey a law of growth of films given by

$$x^{\frac{1}{3}} = k_1 \log t + k_2,$$

where x = film thickness and t = time.

5. When the humidity approaches 100 percent, the rate of growth of films on Cu–Mg alloys progressively increases with time and within certain limits tends to obey an exponential law.

6. Many experimental data on the corrosion of metals and alloys may be explained on the basis of simultaneous actions of different factors, i.e., when two or more equations, representing different mechanisms of the growth of film, are taken into consideration simultaneously.

ACKNOWLEDGMENT

The author wishes to acknowledge the help of research scholars K. C. Shome and P. K. Sen in drawing the figures.

JOURNAL OF APPLIED PHYSICS VOLUME 26, NUMBER 4 APRIL, 1955

Creep of Aluminum under Cyclotron Irradiation*

M. R. Jeppson,† R. L. Mather,‡ A. Andrew, and H. P. Yockey§
Atomic Energy Research Department, North American Aviation, Incorporated, Downey, California

(Received June 14, 1954)

The effect of cyclotron irradiation by 38-Mev alpha particles on the steady-state creep rate (*ca* 10^{-6} per second) of aluminum has been measured at beam densities up to 1.2×10^{13} particles per cm² per second. The data, which were taken on a 0.016-inch thick aluminum specimen for a stress range of 600 to 2500 psi and over a temperature range of 160° to 330°C, showed a slight decrease in rate (up to 19 percent) during irradiation. Since the effect is small, apparently independent of beam density, and is comparable to the usual deviations in the absence of radiation, it can be considered a null result.

I. INTRODUCTION

THE effect of radiation on creep of materials has been discussed by Nabarro,[1] Slater,[2] and Dienes.[3] In a preliminary report of the present work by Yockey, Jeppson, and Keen[4] a decrease in creep rate of aluminum of from 30 percent to 60 percent was given when beam densities as high as 2.4×10^{13} alpha particles/cm²/sec were used. The results quoted in the present paper are to be regarded as replacing those in the preliminary report. Witzig[5] has studied the effect of deuteron bombardment of OFHC copper at fluxes of about 10^{12} deuterons per cm² per second. He found no effect within about twenty percent. It should be noted that for a given velocity, an alpha particle is four times as effective as a deuteron or proton in producing radiation damage.

II. PROCEDURE

The creep tests were made on specimens milled from 0.016-inch aluminum sheet. This thickness diminishes the nonuniformity due to the Bragg Effect as 38-Mev alphas have a range of 0.023 inch in aluminum. The gauge length was 0.5 inch; the cross section 0.040 by 0.016 inch. Spectrographic analysis of a typical specimen gave the following impurities:

1. Copper, less than 0.1 percent.
2. Silicon, less than 0.1 percent.
3. Iron, less than 0.01 percent.

After the specimen was machined, it was electrolytically polished. No other heat treatment was used.

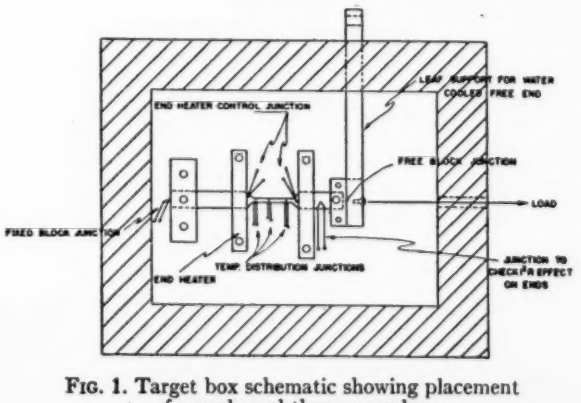

FIG. 1. Target box schematic showing placement of sample and thermocouples.

---

* This paper is based on work done for the U. S. Atomic Energy Commission under Contract AT-11-1-GEN-8. The report number is NAA-SR-206 (1952).

† Now at Applied Radiation Corporation, Walnut Creek, California.

‡ Now at Naval Research Development Laboratories, San Francisco, California.

§ Now at Oak Ridge National Laboratory, Oak Ridge, Tennessee.

[1] Nabarro, *Report of a Conference on Strength of Solids* (Physical Society, London, July, 1947), p. 85.

[2] J. C. Slater, J. Appl. Phys. 22, 237 (1951).

[3] G. J. Dienes, *Annual Reviews of Nuclear Science* (Annual Review, Inc., Stanford, 1953), Vol. 2, p. 187.

[4] Yockey, Jeppson, and Keen, "Effect of cyclotron irradiation on creep of aluminum," NAA-SR-121 (1951) (unpublished).

[5] W. F. Witzig, J. Appl. Phys. 23, 1263 (1952).

The specimen was mounted in a water-cooled target box (see Fig. 1) which was attached to the standard mount used for cyclotron irradiations.[6] One end of the specimen was clamped to an aluminum "fixed" block which was in turn fastened to the water-cooled aluminum box. The free end of the specimen, to which an invar pull wire was attached, was clamped to a copper block which was suspended on a flexible leaf or spring bronze. A differential transformer detected the motion of the specimen. Iron-Constantan thermocouple wires (0.003 inch in diameter), spark welded to the specimen, monitored temperatures at three points along the gauge length and in addition were used as voltage probes to measure the electrical resistance of the specimen.

The ends of the specimen outside the gauge length were heated by convection heaters which maintained the end temperatures constant. The gauge length was heated by helium gas which had been passed through a single thickness of 100-mesh stainless steel gauze heated by a controlled electrical current.

The beam density was estimated by measuring the beam current reaching the target box through a primary collimating slot and assuming an average distribution. A final collimating slot 0.5 inch long insured that the beam struck only the gauge length.

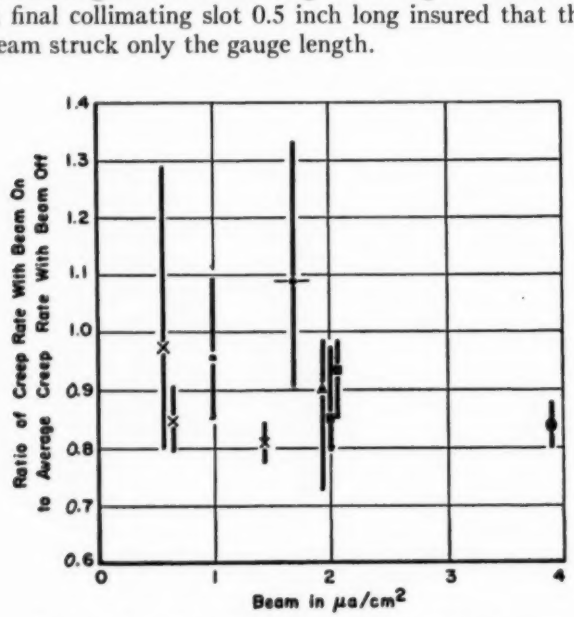

FIG. 2. Effect of irradiation on creep rate of aluminum.

	Date	Position	Temp.	Stress	Particles
×	6 Feb. 1952	outside magnetic field	335°C	1720 psi	protons
--•--	28 Mar. 1952	outside magnetic field	273°C	853 psi	protons
•	28 Mar. 1952	outside magnetic field	231°C	1550 psi	protons
▲	3 Jul. 1952	inside magnetic field	249°C	1335 psi	alphas
■	3 Jul. 1952	inside magnetic field	169°C	2543 psi	alphas
●	3 Jul. 1952	inside magnetic field	332°C	636 psi	alphas

The data of February 6 are on 17s aluminum; all other data are on aluminum. The vertical bars show the spread in creep rate between the beam-off conditions before and after irradiation.

[6] Yockey, Andrew, Fillmore, Glasgow, d'A Hunt, and Pepper, Rev. Sci. Instr. 25, 1011 (1954).

The data during a creep run on the cyclotron were recorded on a 16-point Leeds & Northrup Speedomax and four Foxboro Dynalogs, which also served as part of the temperature control circuits.

Some of the difficulties with reproducibility usually encountered in creep data were eliminated by cycling the radiation on and off using the same specimen. A constant creep rate was established for a period of 30 to 40 minutes with the beam shutter closed. The sample was irradiated for a similar period by opening the shutter. Another interval was then recorded with the beam off.

Two techniques were used to evaluate the thermal loading error caused by the heat drain of the thermocouple wires. The first was to note the change in resistance of the gauge length when the indicated temperature was maintained from beam-off to beam-on. This change was compared with the change in resistance when the temperature was increased a known amount. Knowing the temperature dependence of the creep rate, one could correct the beam-on value of the creep rate to the same temperature as with beam-off. This method of correction was justified because the effect of the beam was certainly small. The second technique was to maintain the resistance of the gauge length by manually reducing the controller set point when the beam was turned on. In this manner the true gauge length temperature was maintained from beam-off to beam-on.

III. EXPERIMENTAL RESULTS

The ratio of creep rate with radiation to the average of the preceding and succeeding rates without radiation is plotted as a function of beam density in Fig. 2. Detailed data for one of the tests are tabulated in Table I. In the first and second irradiations of this run, the thermocouple indications were kept constant from beam-on to beam-off conditions. In the third and fourth irradiations, the specimen resistance was kept constant by changing the control point of all thermocouple controllers but keeping the reading of the three gauge length thermocouples identical.

Data from two tests made outside the magnetic field are also included. Heating of the gauge length in this case was accomplished by the passage of an electric current through the specimen.

IV. DISCUSSION

One uncertainty that was evaluated in order to interpret the creep data obtained on the cyclotron was the effect of small temperature variations. These variations of about 0.3°C with beam-off increased to 1°C or more when the beam was applied. A specimen was set up in the laboratory and the damping in the gauge length temperature controller adjusted to give a temperature oscillation of ±2.5°C at the center and ±1°C at the ends at a frequency of 0.7 cycles per second. No change in creep rate was noticed when the thermal

TABLE I.

1	2	3	4	5	6	7	8	9	10	11	12	13
					Ind. temp. dist. °C. diff. from center T. C.		Indicated transition temperature changes °C					
Stress psi	Av. indicated specimen temperature °C	Beam density 38-Mev alpha part. μa/cm²	Observed creep rate $sec^{-1} \times 10^6$ (%)	Duration of test min.	Inside	Outside	Thermocouple	Resistance	Creep	Extension	True average specimen temperature °C	Corrected ratio of creep rates $\frac{\text{beam on}}{\text{beam off}}$
1335	249.6±0.2	···	0.92±5	32	0.5	0.2					249.6±0.2	
							−0.4	5.5	8.0	0.9		
	249.1±0.5	2.00±0.06	1.25±3	30	2.7	−3.6					254.1±1.0	0.83
							0.0	−4.6	0.0	−1.2		
	249.4±0.7	···	1.25±5	27	0.2	−0.2					249.4±0.7	
2543	168.9±0.8	···	1.41±3	30	−0.5	−0.5					168.9±0.8	
							0.0	3.9	−0.3	4.3		
	169.3±0.6	2.00±0.08	1.37±3	28	−0.2	−0.1					172.8±0.9	0.85
							−0.5	−3.0	−2.9	−3.4		
	168.9±0.7	···	1.09±5	20	−0.5	−0.5					168.9±0.7	
							−3.4	0.0	−2.1	0.2		
	165.8±0.7	2.02±0.10	0.94±5	15	−0.5	−1.0					168.9±0.9	0.92
							3.0	0.0	0.1	0.0		
	169.2±0.5	···	0.95±3	15	−0.7	−0.9					169.2±0.5	
636	332.0±0.5	···	1.68±5	26	−0.1	−0.1					332.0±0.5	
							−4.2	0.0	−4.0	−3.6		
	327.4±1.0	3.9 ±0.6	1.48±5	18	−0.5	−1.4					332.0±1.4	0.84
							5.0	0.0	7.0	3.6		
	332.0±0.5	···	1.84±6	10	−0.2	0.2					332.0±0.5	

oscillation was started or stopped, the average temperature being the same. Data were taken at 222°C and 329°C. The accuracy in measuring the creep rate was ±2 percent.

The length of the vertical lines in Fig. 2 indicates the difference of the preceding and succeeding creep rates without radiation. Were all tests strictly reproducible, these lines should have been of zero length. That they are not indicates a lack of control of some variable associated with the transients occasioned by turning the beam off and on. These lines do not strictly represent probable errors in that one point on Fig. 2 is better than another; but, taken all together, they indicate the degree of reproducibility of the test results. In general, the creep rate was slightly less with radiation, but not importantly so. A temperature change of 3 degrees would produce as much change.

Because of the large temperature dependence of the creep rate and the importance of separating any radiation effect from the temperature dependence, we were careful to record the three thermometric properties mentioned previously. We searched carefully for temperature mimetic radiation effects which might confuse the interpretation. It has been found that radiation affects the thermoelectric power[7] and electrical resistivity of metals, but the effects anneal out under the conditions of the present experiment. We looked carefully for a change in specimen length but none was found. Our apparatus was sensitive enough to detect a fractional change in length of about one part in ten thousand. Since the three thermometric phenomena agree in indicating that the specimen temperature was within the limits given in Table I, it is unlikely that a temperature mimetic radiation effect influenced the results.

[7] A. Andrew, and C. R. Davidson, Phys. Rev. **89**, 876 (1953).

In regard to a radiation expansion of the specimen it should be noted that McDonnell and Kierstad[8] report finding such an effect in copper at −196°C and at 25°C. The effect is not reported by Witzig and appears to be below the sensitivity of his extensometer at the intensity levels used by him. This is true even if we disregard annealing. If the effect were present in our specimens at even 10 percent of the value reported for copper we would have detected it.

The subjects of radiation damage and creep are far too great to discuss in detail in this paper. We do feel it pertinent to mention that our experiment was designed to study the effect of radiation on the "third stage" of creep under radiation intensities and annealing rates such that damage did not accumulate. The conclusion to be drawn is that creep in this material is not affected to a large degree under the conditions studied in this experiment. Since creep and radiation damage are complicated phenomena, the results of this paper should not be extended beyond the present conditions. In particular it should be noted that our creep rates are very much faster than those found in technological applications. Since the mode of deformation may be quite different, direct comparison should be discouraged.

ACKNOWLEDGMENT

It is a pleasure to acknowledge the interest and cooperation of many members of the staff of the University of California Radiation Laboratory, and especially J. G. Hamilton and the staff of Crocker Laboratory. Credit is also due R. C. Carter, J. H. Pepper, and F. R. Weber for designing and constructing much of the equipment.

[8] W. R. McDonnel, and H. A. Kierstad, Phys. Rev. **93**, 247 (1954).

Azimuthal Surface Waves on Circular Cylinders*

ROBERT S. ELLIOTT
Hughes Research and Development Laboratories, Culver City, California
(Received April 15, 1954)

Solutions of Maxwell's equations are presented which satisfy the boundary conditions for corrugated and dielectric-clad circular conducting cylinders. These solutions have the physical interpretation of leaky azimuthal surface waves. Values of the complex propagation constant are given as functions of the geometry. For large cylinders the leakage is small and the transmission properties are approximately those of a trapped wave on a flat surface. A coarse experiment gives reasonable agreement with the theory. Some possible applications to transmission lines and antennas are indicated.

I. INTRODUCTION

IN recent years, the subject of surface waves, initiated by Sommerfeld,[1] has received renewed attention. Cutler, in 1944, demonstrated the feasibility of trapped waves on flat corrugated surfaces[2] and also considered axial surface waves on corrugated circular cylinders. This work was enlarged by the Stanford group.[3] Goubau, extending the work of Sommerfeld, showed that axial surface waves could exist, with practical properties, on dielectric-coated cylindrical conductors.[4] Attwood applied this analysis to flat conductors coated with a dielectric film.[5]

The case of azimuthal surface waves on cylinders does not appear to have been treated extensively in the literature.[6] In view of its potential importance in the fields of transmission lines and antennas, it seemed desirable to develop this case in some detail. The present paper is concerned with the nature of azimuthal waves trapped over (a) corrugated conducting cylinders and (b) dielectric-clad conducting cylinders. It is found that leaky trapped waves of essentially the same nature can be obtained as solutions of Maxwell's equations for both structures. The propagation properties are derivable in a simple manner from the field solutions and are found to approach the properties for a flat surface smoothly with increasing radius.

Throughout the discussion mks rationalized units will be used.

II. THE CORRUGATED CYLINDER

Referring to the structure of Fig. 1, it is desired to obtain a field solution in Region 1 of the form,

$$f(\rho)e^{i(\gamma a\theta-\omega t)}, \tag{1}$$

which involves little if any radial power flow. Region 3 is a perfect conductor of base radius "b" but containing teeth, or corrugations, which extend out to a radius "a." The teeth are uniform in size and spacing and run parallel to the cylinder axis. Region 2 is the space between the teeth and is composed of pure dielectric (which may be air). Region 1 is air. The structure is assumed infinitely long, thus accounting for the absence of a z dependence in Eq. (1).

Since Region 3 is a periodic structure, Floquet's theorem applies[7,8] and the field components in Region 1 must have the θ dependence

$$F(\theta)=e^{i\gamma a\theta}\sum_{n=-\infty}^{\infty}A_n\exp\left[i2\pi n\frac{a\theta}{a(\theta_G+\theta_T)}\right] \tag{2}$$

$$=\sum_{n=-\infty}^{\infty}A_ne^{i\gamma_n a\theta}, \tag{3}$$

where

$$\gamma_n=\gamma+\frac{2\pi n}{a(\theta_G+\theta_T)}. \tag{4}$$

$\theta_G+\theta_T$ is the angular spacing from one corrugation to the next, θ_G being the angular gap width, and θ_T the angular tooth width. The constant γ is to be determined from the boundary conditions[9] as are the complex coefficients A_n.

The appropriate field solutions in Region 1 for *TM*

* The work reported in this article was performed at the Hughes Aircraft Company and was sponsored by the Air Force Cambridge Research Laboratory, Cambridge, Massachusetts, under contract.

[1] For an excellent review of Sommerfeld's work on this problem, see J. A. Stratton, *Electromagnetic Theory* (McGraw-Hill Book Company, Inc., New York, 1941), pp. 516–537.

[2] C. C. Cutler, "Electromagnetic waves guided by corrugated conducting surfaces," Bell Laboratories Report No. MM-44-160-218, October 25, 1944.

[3] Stanford Research Institute, "Ridge and corrugated antenna studies," Quarterly Progress Reports 1–6, covering period July 1, 1949 to January 1, 1951.

[4] G. Goubau, J. Appl. Phys. **21**, 1119 (1950).

[5] S. A. Attwood, J. Appl. Phys. **22**, 504 (1951).

[6] For an approximate analysis of *TE* azimuthal surface waves on dielectric-clad cylinders, see K. Horiuchi, J. Appl. Phys. **24**, 961 (1953).

[7] J. C. Slater, *Microwave Electronics* (D. Van Nostrand Company, Inc., New York, 1950), pp. 169–177.

[8] R. S. Elliott, Trans. Professional Group on Antennas and Propagation, Inst. Radio Engrs., **AP-2**, No. 2, 71–81 (April, 1954).

[9] It is recognized that unless $e^{i\gamma 2\pi a}=1$, we are dealing with a partial cylinder, bounded by the half-planes $\theta=\theta_1$ and $\theta=\theta_2$. For this case, the half planes are assumed to contain all the sources necessary to properly terminate the azimuthal waves.

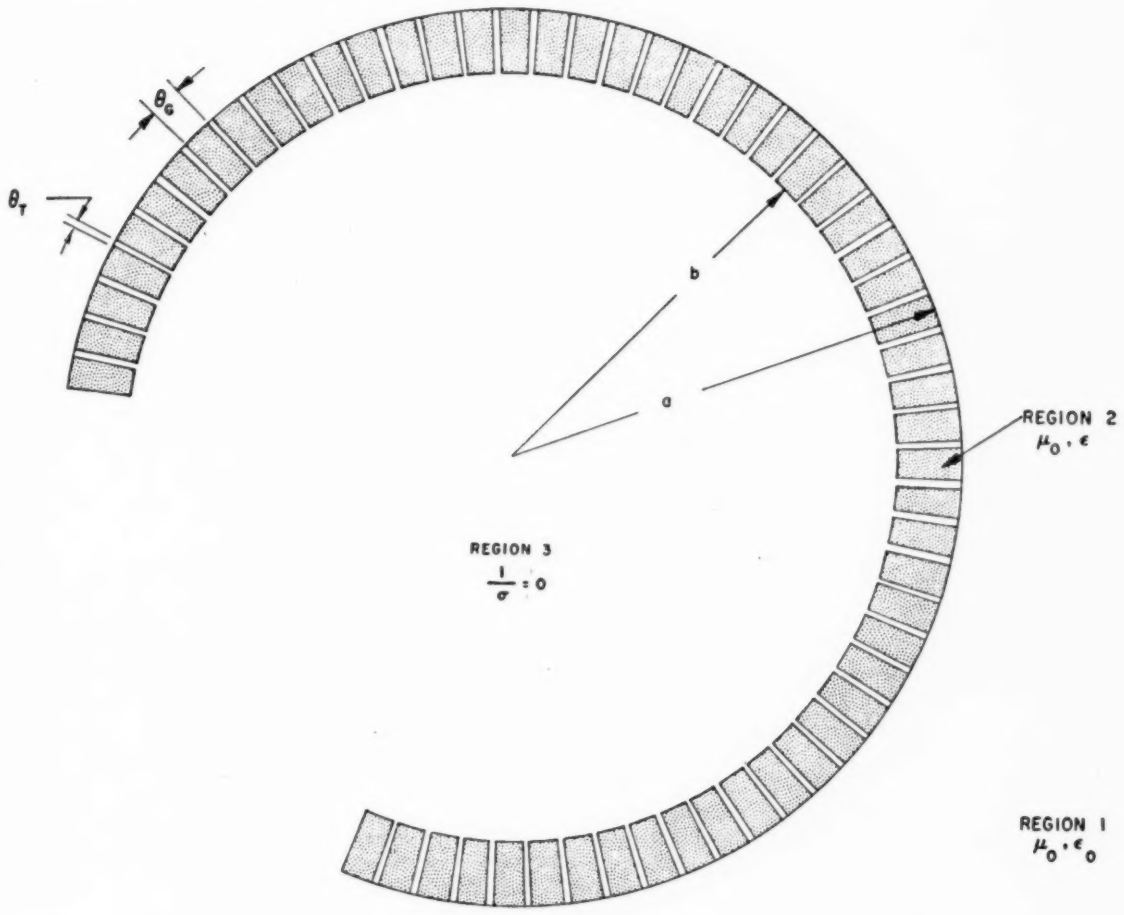

FIG. 1. The corrugated cylinder.

excitation[10] are therefore

$$E_\rho^e = -\frac{e^{-i\omega t}}{i\omega\epsilon_0\rho}\sum_{n=-\infty}^{\infty} i\gamma_n a A_n e^{i\gamma_n a\theta} H_{\gamma_n a}^{(1)}(k_0\rho),$$

$$E_\theta^e = \frac{k_0 e^{-i\omega t}}{i\omega\epsilon_0}\sum_{n=-\infty}^{\infty} A_n e^{i\gamma_n a\theta} H_{\gamma_n a}^{(1)\prime}(k_0\rho), \qquad (5)$$

$$H_z^e = e^{-i\omega t}\sum_{n=-\infty}^{\infty} A_n e^{i\gamma_n a\theta} H_{\gamma_n a}^{(1)}(k_0\rho),$$

$$k_0 = \omega(\mu_0\epsilon_0)^{\frac{1}{2}}.$$

The radial dependence is taken to be a Hankel function of the first kind because it represents only outgoing power at infinity even if γ_n is complex.[11] Neither the Bessel nor the Neumann function satisfies this condition.

Let the space between two adjacent teeth be thought of as a wedge transmission line. The TM solutions are then

$$E_\rho^i = \frac{e^{-i\omega t}}{i\omega\epsilon\rho}\sum_{m=1}^{\infty}\frac{m\pi}{\theta_G}\cdot B_m\cdot\sin\frac{m\pi\theta}{\theta_G}\cdot H_{m\pi/\theta_G}^{(2)}(k\rho),$$

$$E_\theta^i = -\frac{ke^{-i\omega t}B_0}{i\omega\epsilon\sqrt{\rho}}\cdot\sin k(\rho-b) + \frac{ke^{-i\omega t}}{i\omega\epsilon}\sum_{m=1}^{\infty} B_m\cos\frac{m\pi\theta}{\theta_G}\cdot H_{m\pi/\theta_G}^{(2)\prime}(k\rho). \qquad (6)$$

$$H_z^i = \frac{e^{-i\omega t}B_0}{\sqrt{\rho}}\cos k(\rho-b) + e^{-i\omega t}\sum_{m=1}^{\infty} B_m\cos\frac{m\pi\theta}{\theta_G}\cdot H_{m\pi/\theta_G}^{(2)}(k\rho)$$

$$k = \omega(\mu_0\epsilon)^{\frac{1}{2}}, \quad 0\leqslant\theta\leqslant\theta_G.$$

Implicit in Eq. (6) are the assumptions that the θ origin is taken at the boundary between a tooth and a gap; that kb is large enough to permit the use of asymptotic expressions for $H_0^{(1)}(k\rho)$ and $H_0^{(2)}(k\rho)$; but that θ_G is

[10] TM in this connection means $H_\theta \equiv 0$. For the steps leading to Eqs. (5), see reference 1, p. 525.

[11] It is apparent from (5) that for $k_0 a$ finite γ_n must indeed be complex. If γ_n were pure real, the factor $e^{i\gamma_n a\theta}$ would indicate no leakage whereas the factor $H_{\gamma_n a}^{(1)}(k_0\rho)$ *would* indicate a radial flow of power, a contradiction.

small enough to cause $m\pi/\theta_G$ to be much greater than ka for all $m>0$. Hence all higher order modes are cut off and assumed to be attenuated to a negligible amplitude before reaching the bottom of the gap. Practically, this means our attention is confined to cylinders at least several wavelengths in radius and whose surfaces contain many corrugations per wavelength.

In the manner of Lucke,[3,8] the solutions (5) and (6) may be matched across the boundary $\rho=a$ by equating the two expressions for complex power. Thus,

$$\int_0^{a(\theta_G+\theta_T)} ad\theta \int_0^l E_\theta^e(a,\theta,t)H_z^{e*}(a,\theta,t)dz = \int_0^{a\theta_G} ad\theta \int_0^l E_\theta^i(a,\theta,t)H_z^{i*}(a,\theta,t)dz, \quad (7)$$

and because all field components are independent of z, this reduces to

$$\int_0^{a(\theta_G+\theta_T)} E_\theta^e(a,\theta,t)H_z^{e*}(a,\theta,t)d(a\theta) = \int_0^{a\theta_G} E_\theta^i(a,\theta,t)H_z^{i*}(a,\theta,t)d(a\theta). \quad (8)$$

Since

$$A_n=\frac{i\omega\epsilon_0}{e^{-i\omega t}k_0a(\theta_G+\theta_T)H_{\gamma_n a}^{(1)\prime}(k_0a)}\int_0^{a(\theta_G+\theta_T)} E_\theta^e e^{-i\gamma_n a\theta}d(a\theta),$$

$$B_0=-\frac{i\omega\epsilon\cdot\sqrt{a}}{e^{-i\omega t}ka\theta_G\sin k(a-b)}\int_0^{a\theta_G} E_\theta^i d(a\theta), \quad (9)$$

$$B_m=\frac{2i\omega\epsilon}{e^{-i\omega t}ka\theta_G H_{m\pi/\theta_G}^{(2)\prime}(ka)}\int_0^{a\theta_G} E_\theta^i\cos\frac{m\pi\theta}{\theta_G}d(a\theta),$$

(8) can be expressed in terms of the unknown tangential electric field, $E(a,\theta,t)$, in the form

$$\cot k(a-b)=\frac{\left(\frac{\epsilon_0}{\epsilon}\right)^{\frac{1}{2}}\frac{\theta_G}{\theta_G+\theta_T}\sum_{n=-\infty}^{\infty}\left[-\frac{H_{\gamma_n a}^{(2)}(k_0a)}{H_{\gamma_n a}^{(2)\prime}(k_0a)}\right]\int_0^{a(\theta_G+\theta_T)} Ee^{-i\gamma_n a\theta}d(a\theta)\int_0^{a(\theta_G+\theta_T)} E^*e^{i\gamma_n a\theta}d(a\theta) + 2\sum_{m=1}^{\infty}\frac{H_{m\pi/\theta_G}^{(1)}(ka)}{H_{m\pi/\theta_G}^{(1)\prime}(ka)}\int_0^{a\theta_G} E\cos\frac{m\pi\theta}{\theta_G}d(a\theta)\int_0^{a\theta_G} E^*\cos\frac{m\pi\theta}{\theta_G}d(a\theta)}{\int_0^{a\theta_G} Ed(a\theta)\int_0^{a\theta_G} E^*d(a\theta)}. \quad (10)$$

In a similar manner, one obtains an alternative formulation in terms of the unknown tangential magnetic field $H(a,\theta,t)$:

$$\frac{1}{\cot k(a-b)}=\frac{\left(\frac{\epsilon_0}{\epsilon}\right)^{\frac{1}{2}}\frac{\theta_G}{\theta_G+\theta_T}\sum_{n=-\infty}^{\infty}\left[-\frac{H_{\gamma_n a}^{(1)\prime}(k_0a)}{H_{\gamma_n a}^{(1)}(k_0a)}\right]\int_0^{a(\theta_G+\theta_T)} He^{-i\gamma_n a\theta}d(a\theta)\int_0^{a(\theta_G+\theta_T)} H^*e^{i\gamma_n a\theta}d(a\theta) + 2\sum_{m=1}^{\infty}\frac{H_{m\pi/\theta_G}^{(2)\prime}(ka)}{H_{m\pi/\theta_G}^{(2)}(ka)}\int_0^{a\theta_G} H\cos\frac{m\pi\theta}{\theta_G}d(a\theta)\int_0^{a\theta_G} H^*\cos\frac{m\pi\theta}{\theta_G}d(a\theta)}{\int_0^{a\theta_G} Hd(a\theta)\int_0^{a\theta_G} H^*d(a\theta)}. \quad (11)$$

Investigation discloses that neither Eq. (10) nor (11) is stationary with respect to the true field. (The proof follows the lines already presented for a similar problem[8] and hence will not be given.) However, for k_0a large, (11) is almost stationary, and if $\theta_G\gg\theta_T$, so, too, is (10).

Since the *true* field must satisfy both formulations, we may substitute the fundamental mode in each as a trial function to find if there are any conditions under which the fundamental mode is the true field. Thus, inserting $E=$ const in (10) we find

$$\cot k(a-b)\cong\left(\frac{\epsilon_0}{\epsilon}\right)^{\frac{1}{2}}\frac{\theta_G+\theta_T}{\theta_G}\left[-\frac{H_{\gamma^* a}^{(2)}(k_0a)}{H_{\gamma^* a}^{(2)\prime}(k_0a)}\right], \quad (12)$$

whereas insertion of $H=$ const in (11) yields

$$\cot k(a-b)\cong\left(\frac{\epsilon_0}{\epsilon}\right)^{\frac{1}{2}}\frac{\theta_G}{\theta_G+\theta_T}\left[-\frac{H_{\gamma a}^{(1)}(k_0a)}{H_{\gamma a}^{(1)\prime}(k_0a)}\right]. \quad (13)$$

These formulas are precise only for an infinite number of corrugations per wavelength, but they are excellent approximations if the number is 10 or more.[3] If $\theta_G\gg\theta_T$, formulas (12) and (13) approach being conjugates of each other (and hence approach equivalence), and the fundamental mode comprises the substance of the true field. We shall confine our attention to this case.

Letting $\gamma=\beta+i\alpha$, the interest is in trapped waves,

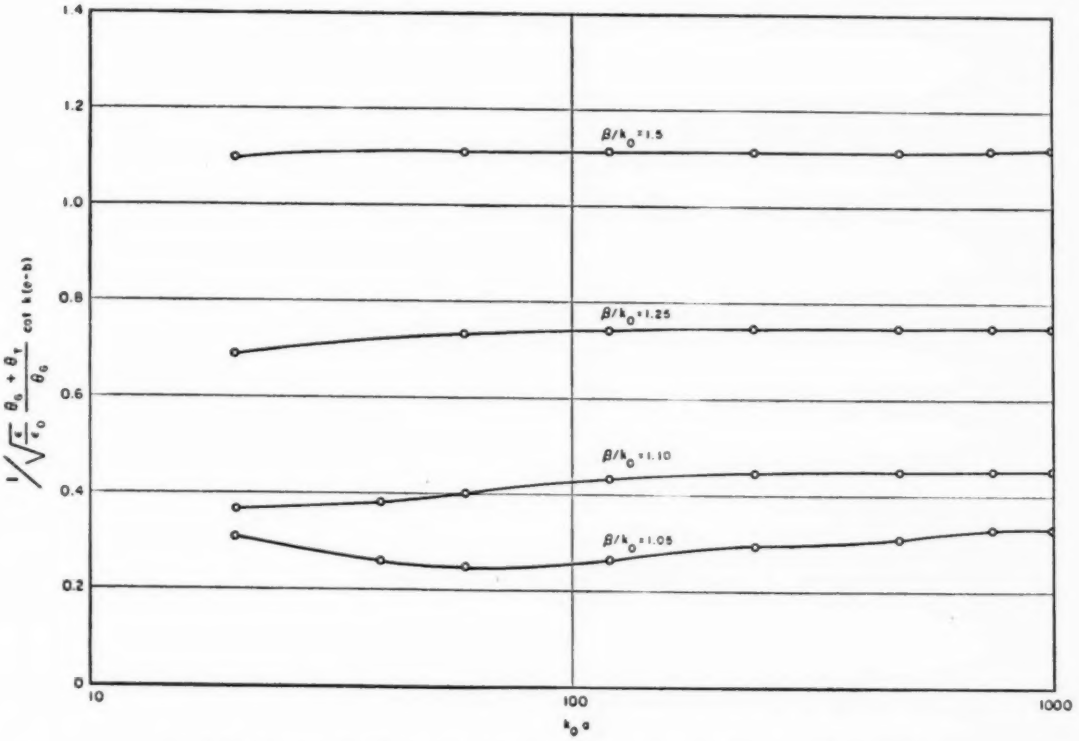

FIG. 2. First approximation to the propagation constant as a function of corrugation geometry and cylinder radius for *TM* azimuthal surface waves.

i.e., waves for which $\beta > k_0$ and $\beta \gg \alpha$. When, in addition, k_0a is large, we are dealing with Bessel functions of large argument but even larger order. Then,

$$H_{\gamma a}^{(1)}(k_0a) \cong iY_{\beta a}(k_0a) \cong -H_{\gamma^* a}^{(2)}(k_0a). \qquad (14)$$

A first approximation to Eq. (13) (the more nearly stationary of the two) is therefore

$$\cot k(a-b) = \left(\frac{\epsilon_0}{\epsilon}\right)^{\frac{1}{2}} \cdot \frac{\theta_G}{\theta_G+\theta_T}\left[\frac{-Y_{\beta a}(k_0a)}{Y'_{\beta a}(k_0a)}\right] \qquad (15)$$

under the assumptions:

(1) $\dfrac{\lambda_0}{a(\theta_G+\theta_T)} \gtrsim 10,$

(2) $\theta_G \gg \theta_T,$

(3) $\beta > k_0,$

(4) $\beta \gg \alpha,$

(5) k_0a large.

Equation (15) may be solved for βa in terms of the geometry to give a first approximation to the complex root γa. When this is done, the curves of Fig. 2 result. If $\cot k(a-b)$ is positive, $\beta > k_0$ and the waves are trapped. As can be seen from Fig. 2, for cylinder radii exceeding several wavelengths, the value of β/k_0 is almost independent of radius, depending chiefly on the corrugation geometry. As $k_0a \to \infty$, β/k_0 smoothly approaches its value for the plane case.

If now we let $\gamma a = (\beta a + \delta_1) + i\delta_2$ and explore Eq. (13) for a root by assuming a succession of values for δ_1 and δ_2, solutions can be found with moderate difficulty. For the range of interest, expansions of the complex order Hankel functions in the form proposed by Olver[12]

TABLE I. First and second approximations to propagation constants for azimuthal surface waves over corrugated cylinders.

k_0a	$\left(\frac{\epsilon}{\epsilon_0}\right)^{\frac{1}{2}}\cdot\frac{\theta_G+\theta_T}{\theta_G}$ $\times\cot k(a-b)$	First approximation βa	Second approximation γa
60	0.250	63	$64 + 0.9i$
	0.401	66	$66.1 + 0.3i$
	0.738	75	$75 + 10^{-4}i$
	1.098	90	$90 + 10^{-14}i$
120	0.269	126	$126.4 + 0.8i$
	0.439	132	$132 + 0.03i$
	0.739	150	$150 + 10^{-11}i$
	1.115	180	$180 + 10^{-31}i$
480	0.322	504	$504 + 0.002i$
	0.471	528	$528 + 10^{-10}i$
	0.747	600	$600 + 10^{-46}i$
	1.117	720	$720 + 10^{-122}i$
960	0.327	1008	$1008 + 2\times10^{-7}i$
	0.473	1056	$1056 + 10^{-22}i$
	0.753	1200	$1200 + 10^{-94}i$
	1.120	1440	$1440 + 10^{-268}i$

[12] F. W. J. Olver, Proc. Cambridge Phil. Soc. 48, Part I, 414–427 (1952).

are recommended. Table I lists some representative values of γa. α(which measures the leakage) is seen to decrease as either k_0a or βa is increased. The rate at which α decreases is significant. Even for moderate corrugation depth and cylinder radius, the leakage is small enough to make such structures attractive for use as transmission lines.

Without repeating the analysis, we may conclude that, for $G<\lambda_0/2$, the corrugated cylinder cannot admit surface propagation of *TE* waves. The reason for this is that the wedge transmission lines between the teeth cannot support a *TEM* mode of axial polarization. This is a disadvantage not shared by the dielectric-clad cylinder to which we now turn our attention.

III. THE DIELECTRIC-CLAD CYLINDER

The geometry is suggested by Fig. 3. Region 2 is a dielectric tube of inner radius "b," outer radius "a," and relative permittivity $\epsilon/\epsilon_0>1$. It is bounded on the inside by a perfect conductor and on the outside by air.

Assuming that k_0a is large, and hence that propagation is principally unimodal, the appropriate solutions for Region 2 may be constructed from the cylindrical wave functions[1]

$$\psi=e^{i\gamma a\theta}\frac{J_{\gamma a}(k\rho)}{Y_{\gamma a}(k\rho)}e^{-i\omega t} \tag{16}$$

and those for Region 1 from

$$\phi=e^{i\gamma a\theta}H_{\gamma a}^{(1)}(k_0\rho)e^{-i\omega t}. \tag{17}$$

γ is common to ψ and ϕ by virtue of the boundary conditions at $\rho=a$.

For *TM* waves, we derive from (16) and (17)

$$\begin{aligned}
E_\rho{}^i&=-\frac{\omega\mu_0\gamma a}{k^2\rho}[AJ_{\gamma a}(k\rho)+BY_{\gamma a}(k\rho)]e^{i(\gamma a\theta-\omega t)}\\
E_\theta{}^i&=-\frac{i\omega\mu_0}{k}[AJ_{\gamma a}'(k\rho)+BY_{\gamma a}'(k\rho)]e^{i(\gamma a\theta-\omega t)},\\
H_z{}^i&=[AJ_{\gamma a}(k\rho)+BY_{\gamma a}(k\rho)]e^{i(\gamma a\theta-\omega t)},
\end{aligned} \tag{18}$$

for all points such that $b\leqslant\rho\leqslant a$; and

$$\begin{aligned}
E_\rho{}^e&=-\frac{\omega\mu_0\gamma a}{k_0{}^2\rho}CH_{\gamma a}^{(1)}(k_0\rho)e^{i(\gamma a\theta-\omega t)},\\
E_\theta{}^e&=-\frac{i\omega\mu_0}{k_0}CH_{\gamma a}^{(1)\prime}(k_0\rho)e^{i(\gamma a\theta-\omega t)},\\
H_z{}^e&=CH_{\gamma a}^{(1)}(k_0\rho)e^{i(\gamma a\theta-\omega t)},
\end{aligned} \tag{19}$$

for all points such that $a\leqslant\rho<\infty$.

Since $E_\theta{}^i$ must vanish at $\rho=b$ we find

$$B=-A\frac{J_{\gamma a}'(kb)}{Y_{\gamma a}'(kb)}, \tag{20}$$

and from the continuity of the tangential field components at $\rho=a$,

$$\begin{aligned}
\frac{A}{k}\left[J_{\gamma a}'(ka)-\frac{J_{\gamma a}'(kb)}{Y_{\gamma a}'(kb)}\cdot Y_{\gamma a}'(ka)\right]&=\frac{C}{k_0}H_{\gamma a}^{(1)\prime}(k_0a),\\
A\left[J_{\gamma a}(ka)-\frac{J_{\gamma a}'(kb)}{Y_{\gamma a}'(kb)}\cdot Y_{\gamma a}(ka)\right]&=CH_{\gamma a}^{(1)}(k_0a)
\end{aligned} \tag{21}$$

which yields the ratio

$$\frac{J_{\gamma a}'(kb)}{Y_{\gamma a}'(kb)}=\frac{\dfrac{k}{k_0}\cdot\dfrac{J_{\gamma a}(ka)}{J_{\gamma a}'(ka)}\cdot\dfrac{H_{\gamma a}^{(1)\prime}(k_0a)}{H_{\gamma a}^{(1)}(k_0a)}-1}{\dfrac{k}{k_0}\cdot\dfrac{Y_{\gamma a}(ka)}{Y_{\gamma a}'(ka)}\cdot\dfrac{H_{\gamma a}^{(1)\prime}(k_0a)}{H_{\gamma a}^{(1)}(k_0a)}-1}\cdot\frac{J_{\gamma a}'(ka)}{Y_{\gamma a}'(ka)}. \tag{22}$$

Equation (22) may be solved for the propagation constant γ in terms of the parameters a, b, and ϵ/ϵ_0. As in the case of the corrugated cylinder, if k_0a is large, and $\beta>k_0$, $\gamma=\beta+i\alpha$ is principally real and a first approximation to the root can be obtained from

$$\frac{J_{\beta a}'(kb)}{Y_{\beta a}'(kb)}=\frac{\dfrac{k}{k_0}\cdot\dfrac{J_{\beta a}(ka)}{J_{\beta a}'(ka)}\cdot\dfrac{Y_{\beta a}'(k_0a)}{Y_{\beta a}(k_0a)}-1}{\dfrac{k}{k_0}\cdot\dfrac{Y_{\beta a}(ka)}{Y_{\beta a}'(ka)}\cdot\dfrac{Y_{\beta a}'(k_0a)}{Y_{\beta a}(k_0a)}-1}\cdot\frac{J_{\beta a}'(ka)}{Y_{\beta a}'(ka)}. \tag{23}$$

A plot of (23) for $\epsilon/\epsilon_0=4$ is shown in Fig. 4. It is observed that as the cylinder radius is decreased, a thicker dielectric film is required to maintain the same degree of trapping. However, for cylinder radii greater than a few wavelengths, the required film thickness is a slowly changing function of radius which smoothly approaches the plane value.

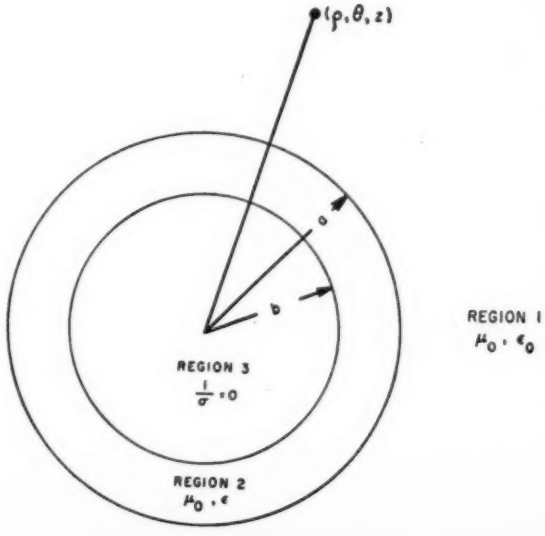

FIG. 3. The dielectric-clad cylinder.

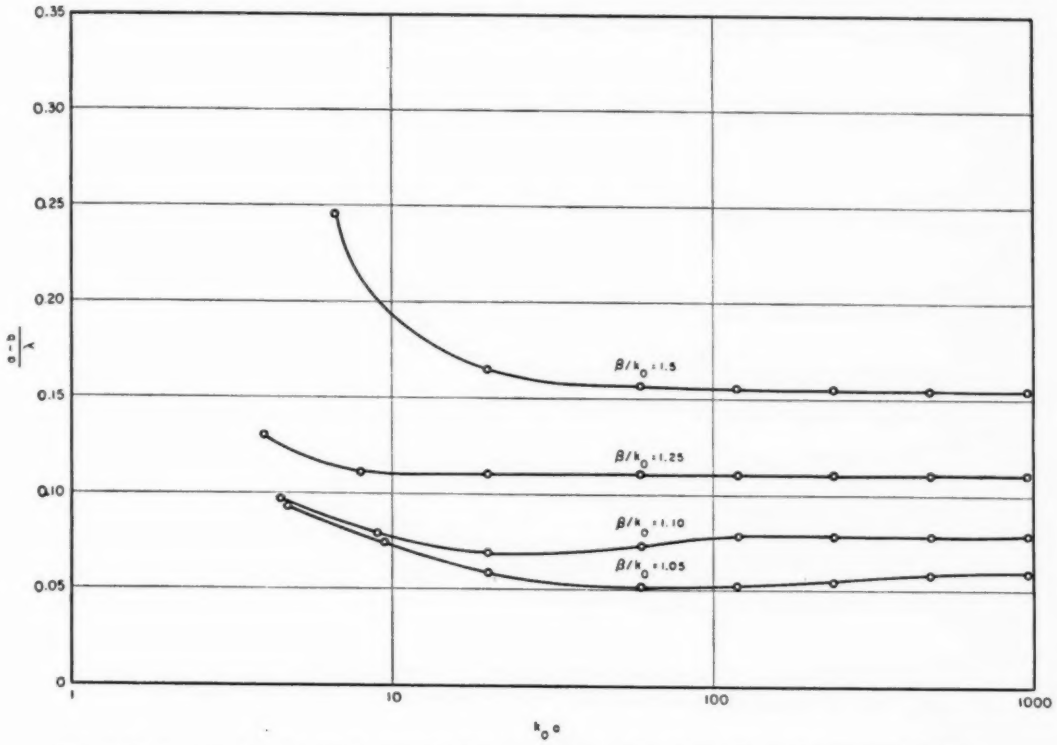

FIG. 4. First approximation to the propagation constant as a function of film thickness and cylinder circumference for *TM* azimuthal surface waves.

It seems reasonable to suppose that for a given k_0a and β/k_0, the value of γ which satisfies (22) should be close to the corresponding value of γ already found for the corrugated cylinder. This has been checked for the case $k_0a=120$, $\beta/k_0=1.05$ and the agreement was excellent.

Similarly, for *TE* waves, we derive from (16) and (17)

$$E_z^i=[A'J_{\gamma a}(k\rho)+B'Y_{\gamma a}(k\rho)]e^{i(\gamma a\theta-\omega t)}$$

$$H_\rho^i=\frac{\gamma a}{\omega\mu_0\rho}[A'J_{\gamma a}(k\rho)+B'Y_{\gamma a}(k\rho)]e^{i(\gamma a\theta-\omega t)}, \quad (24)$$

$$H_\theta^i=\frac{ik}{\omega\mu_0}[A'J_{\gamma a}'(k\rho)+B'Y_{\gamma a}'(k\rho)]e^{i(\gamma a\theta-\omega t)}$$

for $b\leqslant\rho\leqslant a$, and

$$E_z^e=C'H_{\gamma a}^{(1)}(k_0\rho)e^{i(\gamma a\theta-\omega t)},$$

$$H_\rho^e=\frac{\gamma a}{\omega\mu_0\rho}C'H_{\gamma a}^{(1)}(k_0\rho)e^{i(\gamma a\theta-\omega t)}, \quad (25)$$

$$H_\theta^e=\frac{ik_0}{\omega\mu_0}C'H_{\gamma a}^{(1)\prime}(k_0\rho)e^{i(\gamma a\theta-\omega t)},$$

for $\rho\geqslant a$. Since E_z^i must vanish at $\rho=b$,

$$B'=-A'\frac{J_{\gamma a}(kb)}{Y_{\gamma a}(kb)}, \quad (26)$$

and, from the continuity of the tangential field components at $\rho=a$,

$$A'\left[J_{\gamma a}(ka)-\frac{J_{\gamma a}(kb)}{Y_{\gamma a}(kb)}\cdot Y_{\gamma a}(ka)\right]=C'H_{\gamma a}^{(1)}(k_0a),$$

$$kA'\left[J_{\gamma a}'(ka)-\frac{J_{\gamma a}(kb)}{Y_{\gamma a}(kb)}Y_{\gamma a}'(ka)\right]=k_0C'H_{\gamma a}^{(1)\prime}(k_0a), \quad (27)$$

which yields the ratio

$$\frac{J_{\gamma a}(kb)}{Y_{\gamma a}(kb)}=\frac{\dfrac{k_0}{k}\dfrac{J_{\gamma a}(ka)}{J_{\gamma a}'(ka)}\dfrac{H_{\gamma a}^{(1)\prime}(k_0a)}{H_{\gamma a}^{(1)}(k_0a)}-1}{\dfrac{k_0}{k}\dfrac{Y_{\gamma a}(ka)}{Y_{\gamma a}'(ka)}\dfrac{H_{\gamma a}^{(1)\prime}(k_0a)}{H_{\gamma a}^{(1)}(k_0a)}-1}\cdot\frac{J_{\gamma a}'(ka)}{Y_{\gamma a}'(ka)}. \quad (28)$$

Equation (28) may be solved for the propagation constant γ in terms of the parameters a, b, and ϵ/ϵ_0. Proceeding as before, if k_0a is large, and $\beta>k_0$, $\gamma=\beta+i\alpha$ is principally real and a first approximation to the root can be obtained from

$$\frac{J_{\beta a}(kb)}{Y_{\beta a}(kb)}=\frac{\dfrac{k_0}{k}\dfrac{J_{\beta a}(ka)}{J_{\beta a}'(ka)}\dfrac{Y_{\beta a}'(k_0a)}{Y_{\beta a}(k_0a)}-1}{\dfrac{k_0}{k}\dfrac{Y_{\beta a}(ka)}{Y_{\beta a}'(ka)}\dfrac{Y_{\beta a}'(k_0a)}{Y_{\beta a}(k_0a)}-1}\cdot\frac{J_{\beta a}'(ka)}{Y_{\beta a}'(ka)}. \quad (29)$$

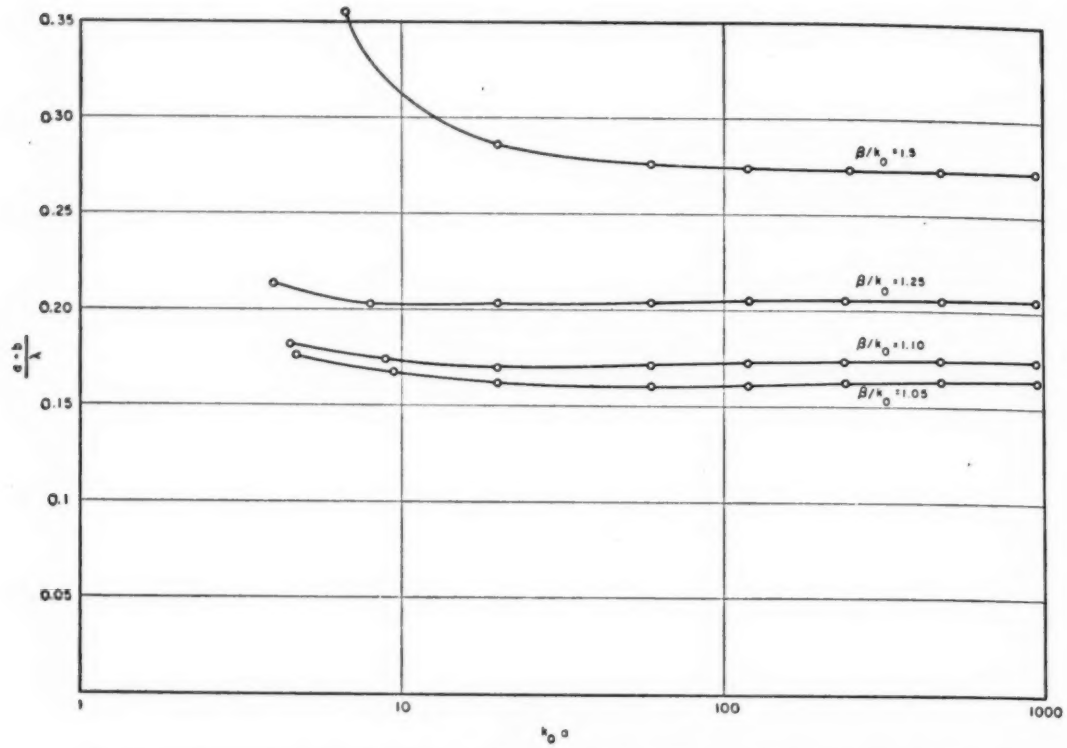

FIG. 5. First approximation to the propagation constant as a function of film thickness and cylinder circumference for *TE* azimuthal surface waves.

A plot of (29) for $\epsilon/\epsilon_0 = 4$ is shown in Fig. 5. Once again we observe that as the cylinder radius is decreased, a thicker dielectric film is required to maintain the same degree of trapping. However, for cylinder radii exceeding several wavelengths, the required film thickness is a slowly changing function of radius which smoothly approaches the plane value.

Although (29) refers to *TE* modes whereas the values of γ found for the corrugated cylinder apply to *TM* modes, a check was made of (28) using $k_0 a = 120$, $\beta/k_0 = 1.05$, and $\gamma a = 126.4 + 0.8i$. The agreement was remarkably good. This strongly suggests that for a given cylinder, the leakage is a function of the degree of trapping but not of the method of trapping nor the polarization.

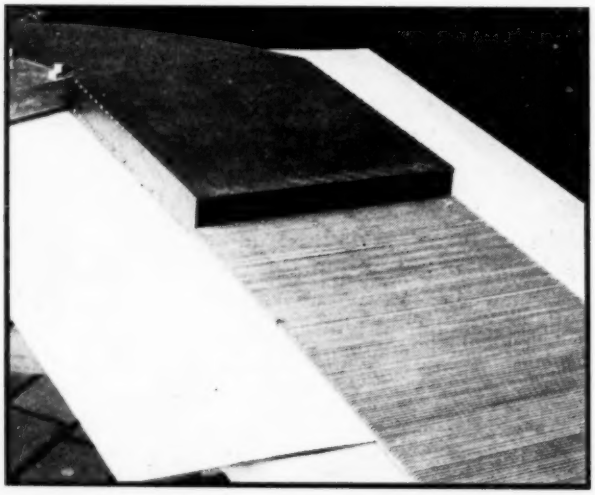

FIG. 6. S-band corrugated hog horn and flexible corrugated surface.

IV. EXPERIMENTAL RESULTS

A crude check of the data of Table I has been attempted using the apparatus shown in Fig. 6. An *S*-band corrugated hog-horn was used to feed a flexible *S*-band corrugated surface. The teeth had a depth which gave an experimental value[13] of $\beta/k_0 = 1.07$. The surface was $3\frac{1}{2}\,\lambda_0$ wide and $10\,\lambda_0$ long. A vertical reflecting plate was erected $7\,\lambda_0$ from the horn mouth as shown in Fig. 7. The corrugated surface was fitted with vertical side plates and flexed to different radii of curvature as the VSWR was recorded. Assuming that the changes in VSWR were caused entirely by leakage, the calculation of α was a simple matter. Table II summarizes the results at 3000 Mc. The experiment was too coarse to expect close agreement, but the measured values all lie within the theoretical curves for $\beta/k_0 = 1.05$ and 1.10.

The fact that surface waves can be made to leak merely by bending them around a curved surface can be put to good advantage in the design of a surface wave

[13] R. S. Elliott and E. N. Rodda, "Parasitic arrays excited by surface waves," Technical Memorandum No. 344, Research and Development Laboratories, Hughes Aircraft Company, March 1954.

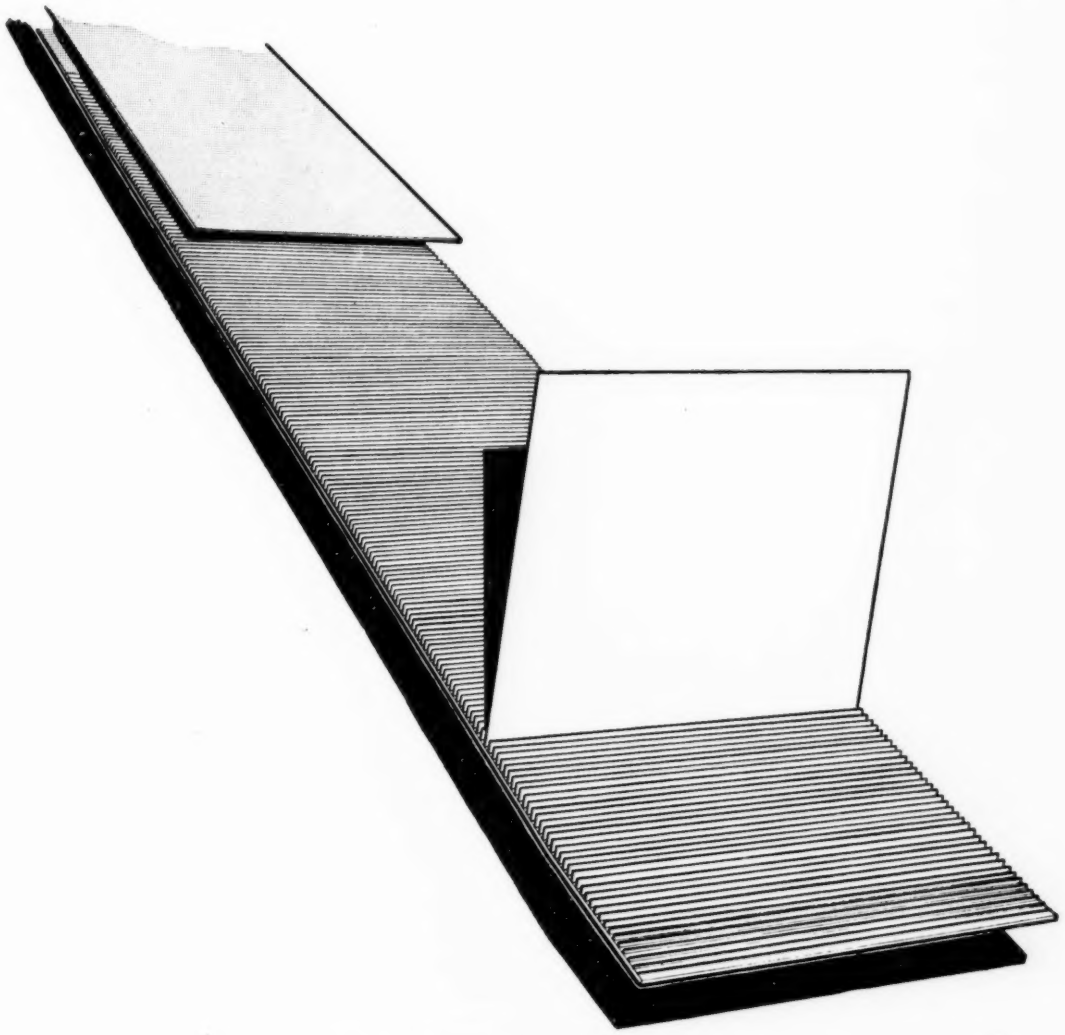

FIG. 7. Simulated corrugated transmission line.

antenna. It is well known that the basic pattern of a flat corrugated surface antenna is endfire and of the form

$$\frac{\sin\frac{\pi l}{\lambda}\left[\frac{\beta}{k_0}-\cos\theta\right]}{\frac{\pi l}{\lambda}\left[\frac{\beta}{k_0}-\cos\theta\right]}, \tag{30}$$

in which l is the length of the antenna and θ is measured from the endfire position. Such a pattern is characterized by recurrent nulls. A simple way to fill in these nulls is to curve the surface slightly. Fig. 8 shows the results for a $3\frac{1}{2}\,\lambda_0$ wide, $10\,\lambda_0$ long corrugated surface (experimental $\beta/k_0=1.07$). By merely flexing the surface to a curvature giving $k_0a=300$, the first null was raised 16 db, with more moderate improvement of the subsequent nulls. The trapping effect is graphically illustrated by the shift in position of the main beam, indicating a simple means of getting on-the-horizon coverage together with null-filling.

Further flexure of the surface caused negligible improvement in null-filling and resulted chiefly in widening of the main beam with a consequent loss in grain.

TABLE II. Leakage *versus* curvature as determined experimentally with a flexible corrugated surface.

k_0a	VSWR	$\frac{\alpha}{k_0}$ (Theoretical for $\beta/k_0=1.05$)	$\frac{\alpha}{k_0}$ (Experimental for $\beta/k_0=1.07$)	$\frac{\alpha}{k_0}$ (Theoretical for $\beta/k_0=1.10$)
∞	3.65	0	~ 0	0
480	3.65	4×10^{-6}	~ 0	2×10^{-13}
240	3.65	0.00083	~ 0	2×10^{-7}
120	2.60	0.0067	0.0028	0.00025
60	1.41	0.015	0.014	0.005

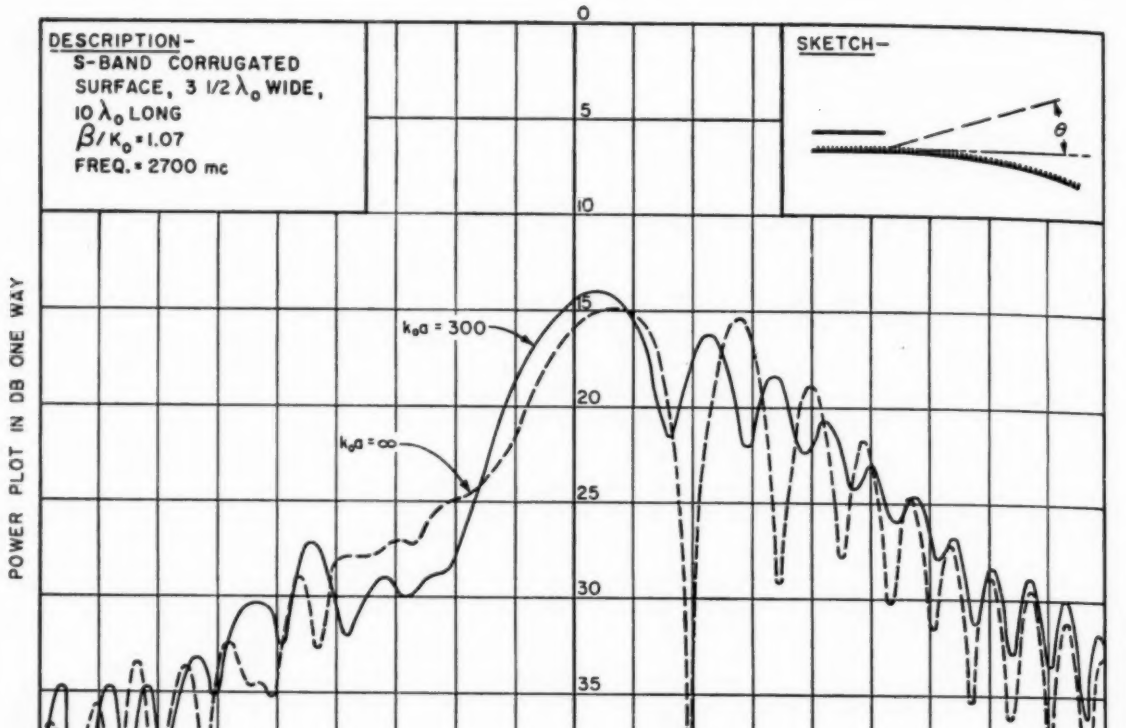

FIG. 8. Elevation patterns for an *S*-band corrugated surface antenna.

V. CONCLUSIONS

The foregoing analyses serve to show that trapped azimuthal surface waves can exist on properly modified circular cylinders. If the radius and/or degree of trapping is large, the leakage is small and essentially unimodal propagation can be achieved with a properly designed feed. The leakage can be kept within tolerable limits from the transmission line point of view. Curving a surface wave antenna can have desirable effects on the radiation pattern.

The analysis can be extended readily to trapped waves traveling azimuthally between properly modified concentric cylinders. For this case γ is pure real and the solutions are given in terms of Neumann functions and/or Bessel functions.

Additional considerations arise when a single cylinder of *variable* radius of curvature is contemplated for use as a trapping structure. If the radius is always large, the previous analysis indicates that γ is a slowly varying function and no difficulty should arise from merely extending the present data.

VI. ACKNOWLEDGMENTS

The author is indebted to A. Oliner, S. Sensiper, and C. Wilcox for their comments. The Mathematical Analysis Group of the Hughes Research and Development Laboratories performed the computations. E. Rodda assisted in the experimental work. Their efforts are gratefully acknowledged.

Thermoelectric Power and Electrical Resistivity of Dilute Alloys of Silicon in Copper, Nickel, and Iron*

C. A. DOMENICALI† AND F. A. OTTER
The Franklin Institute Laboratories for Research and Development, Philadelphia 3, Pennsylvania
(Received May 17, 1954)

Data are given on the thermoelectric power and on the resistivity of the dilute alloys, Cu–Si, Ni–Si, and Fe–Si, from −195° to +500°C (and higher for some of the alloys). The Cu–Si thermopower at first decreases with increasing Si content and then again increases, the minimum being at about 2 or 3 atomic percent Si, depending on the temperature. The Cu–Si resistivity is typical of Cu-base alloys, the resistivity increases per atomic percent Si changing from 7.2 $\mu\Omega$ cm at −190°C to 8.7 $\mu\Omega$ cm at 840°C. The thermopower and resistivity curves for Ni–Si show a characteristic knick at the Curie temperature of each alloy. The Fe–Si thermopowers are positive at lower temperatures and become negative at a temperature T_0 which decreases with increasing Si content. Furthermore, T_0 changes from about 300°C for pure iron to about +70°C for 2 atomic percent Si. The resistivity of Fe–Si alloys increases faster than linearly with temperature, and this is also the case for the Ni–Si alloys below the Curie temperature. Above the Curie temperature, the Ni–Si resistivities vary linearly with temperature. The increase in resistivity per atomic percent Si in Fe is 10.5 $\mu\Omega$ cm at all temperatures within the measured range.

INTRODUCTION

THERE are very few known rules describing the thermoelectric properties of metals and alloys. One such rule, which we may call the Borelius-Kohler rule,[1,2] describes what happens to the absolute thermoelectric power (or absolute "thermopower") of the nobel metals (Cu, Ag, Au) or of the alkali metals when one dissolves in them small amounts of some foreign atom. According to this rule the absolute thermopower is always reduced in magnitude by the addition of foreign atoms to the solvent. The only certain exception to this rule seems to be Mn dissolved in copper[3]; however, Ti and Cr in copper may also be exceptions.

A second rule, found by Norbury,[4] states that the initial slopes of curves showing thermopower *vs* percent impurity increase in magnitude as the valency of the added element dissolved in copper is increased.

A third rule, discovered by Crussard,[5] describes the effect of foreign atoms dissolved in aluminum. The absolute thermopower of Al is negative at ordinary temperatures. According to Crussard, when small amounts of a metal preceding Al in the column-of-eight periodic table are dissolved in Al, the absolute thermopower is algebraically increased (becomes less negative); when the dissolved metal follows Al in this table the thermopower is algebraically decreased (becomes more negative). Galt[6] has given a qualitative explanation of Crussard's rule, and the present authors have attempted to devise a more quantitative theory[7] including both Crussard's rule and that of Norbury, Borelius, and Kohler. There are of course exceptions to all of these rules.

It would be very useful for both practical and theoretical reasons to have more empirical rules pertaining to the thermoelectric behavior of alloys; while such rules can ordinarily be deduced only after very extensive studies of large numbers of alloy systems, we considered it advisable to investigate the effects on the thermopower of the neighboring elements,[8] Fe, Ni, and Cu when one dissolves in them varying amounts of the same foreign atom. The solute Si was chosen mainly on metallurgical grounds. Since both the thermoelectric power S and electrical resistivity ρ of a metal depend on the nature of the scattering of electrons in the metal, we have measured both of these parameters S and ρ on the same specimens.

PREPARATION AND DESCRIPTION OF SPECIMENS

The purity of the solvent metals used in our alloys was as follows: Cu, 99.99+percent (American Smelting Company) and 99.99+percent (Cupro-vac, Vacuum Metals Corporation); Fe, 99.95+percent (Ferrovac-R, Vacuum Metals Corporation); Ni, 99.98+percent (International Nickel Company); Si, 99.95+percent (du Pont de Nemours Company, Inc.). Since relatively small concentrations of Si were used in the alloys, there was obviously no need to employ such high-purity Si; we used it, nevertheless, because we had it on hand in reasonably large quantities.

The Cu–Si alloys were made in two separate batches. The first batch consisted of approximately 150 g ingots, made with Cupro-vac and melted in Vycor crucibles; the second batch consisted of approximately

* This work was supported by the Signal Corps Engineering Laboratories, Fort Monmouth, New Jersey.
† Now at Honeywell Research Center, Hopkins, Minnesota.
[1] G. Borelius, *Handbuch d. Metallphysik* (Leipzig, Akademische Verlagsgesellschaft m.b.h., 1935), Vol. 1, pt. 1, p. 404.
[2] M. Kohler, Z. Physik **126**, 481 (1949).
[3] J. L. Thomas, J. Research Natl. Bur. Standards **16**, 149 (1936).
[4] A. L. Norbury, Phil. Mag. **2**, 1188 (1928).
[5] C. Crussard, *Report of Conference on Strength of Solids* (H. H. Wills Laboratory, Bristol, July 1947), p. 119; Compt. rend. **226**, 1003 (1948).
[6] J. K. Galt, Phil. Mag. **40**, 309 (1949).
[7] C. A. Domenicali and F. A. Otter, Phys. Rev. **95**, 1134 (1954).
[8] We might perhaps have chosen Co rather than Fe; however, the metallurgy of Fe–Si alloys is so well known that we chose to use Fe rather than Co.

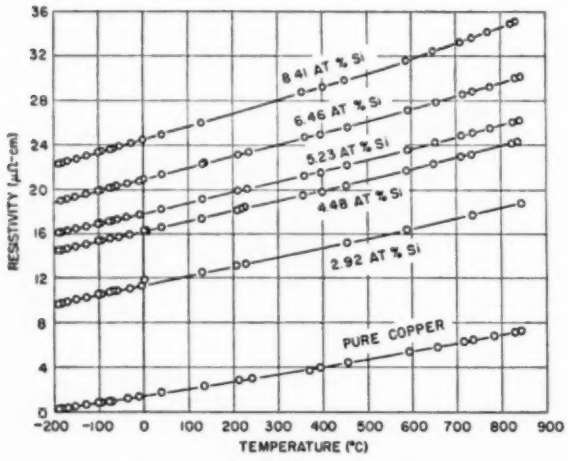

FIG. 1. Resistivity of Cu—Si alloys.

15 g ingots, made with American Smelting Company copper and melted in graphite crucibles. The Fe—Si and Ni—Si alloys were made in approximately 100 g ingots melted in alundum and zirconium oxide crucibles respectively. All the alloys were melted *in vacuo* (approximately 3–5 microns) in an induction furnace, except the Vycor-melted Cu—Si ingots which were made in a resistance furnace. All ignots were homogenized *in vacuo* for 6–10 hours at temperatures just below the solidus lines. The ingots were cold-rolled and swaged to wires 0.040 inch in diameter and were then annealed *in vacuo* at about 600°C for an hour or so before being placed in the measuring apparatus. Throughout this paper we express composition of the specimens in atomic percent.

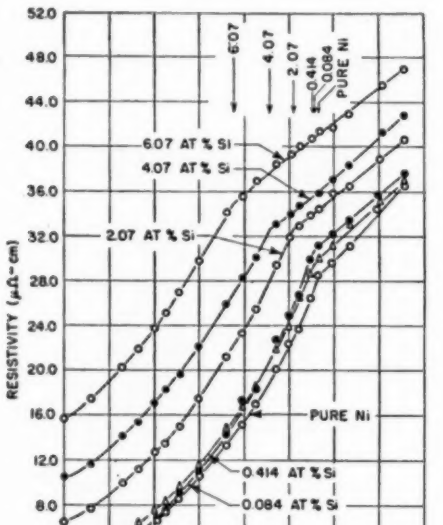

FIG. 2. Resistivity of Ni—Si alloys. The arrows at the top of the figure indicate the Curie temperatures.

EXPERIMENTAL PROCEDURE

The resistivities of the alloys were measured by comparing the voltage drop across a known length of each sample with the voltage drop across a standard resistor, by means of a Leeds and Northrup K-2 potentiometer. The samples were enclosed in a copper shield to help provide an isothermal region, and the high-temperature measurements were of course made *in vacuo*. Low temperatures were measured with copper-constantan thermocouples and high temperatures with platinum—platinum+10 percent rhodium couples.

The thermoelectric power was measured by making thermocouples with the alloys in one leg and pure copper in the reference leg. We measured the thermoelectric potential difference E of each thermocouple as a function of temperature (one junction in ice and high-temperature junction *in vacuo*) with a K-2 potentiometer, using copper-constantan or platinum—platinum +10 percent rhodium couples to indicate temperature. We then plotted E *vs* T and graphically measured the

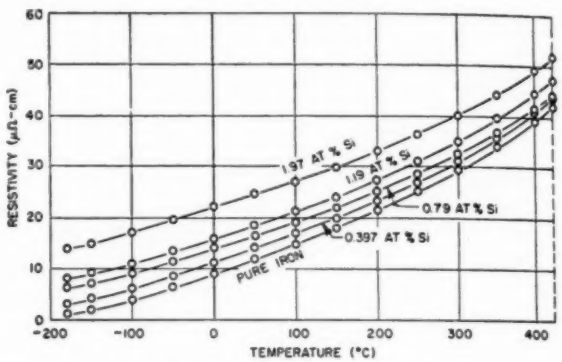

FIG. 3. Resistivity of Fe—Si alloys.

slopes to determine the thermopower relative to copper at various temperatures. In order to determine the absolute thermopower, we had merely to add algebraically the absolute thermopower of copper as reported by Borelius, Keesom, and Johansson[9] and by Nyström.[10]

RESULTS

The data are shown in the following figures: Figs. 1–3 show the resistivities; Figs. 4–6 show the thermopowers of the Cu—Si, Ni—Si, and Fe—Si alloys, respectively; Fig. 7 compares our data on thermopower with those of Hammer[11] for pure Ni in the region of the Curie temperature.

DISCUSSION OF RESULTS

The resistivity of Cu—Si (Fig. 1) is seen to obey the Matthiessen rule fairly well. The increase in resistivity per atomic percent silicon is 7.2 $\mu\Omega$ cm at -190°C

[9] Borelius, Keesom, and Johansson, Proc. Acad. Sci. Amsterdam **31**, 1046 (1928).
[10] J. Nyström, Arkiv astron. och Fysik. **34A**, No. 27 (1948).
[11] A. Hammer, Ann. Physik **30**, 728 (1937).

and 8.7 $\mu\Omega$ cm at 840°C. The Cu–Si thermopower (Fig. 4) against composition has the same shape at all temperatures and remains positive in sign, the behavior being similar to that of Sn in Cu.[12]

The resistivities of the Ni–Si alloys (Fig. 2) vary faster than linearly with temperature below the Curie temperature Tc and approximately linearly above Tc; each curve shows a knick at the Curie temperature. The resistivity curve for the sample containing 0.084

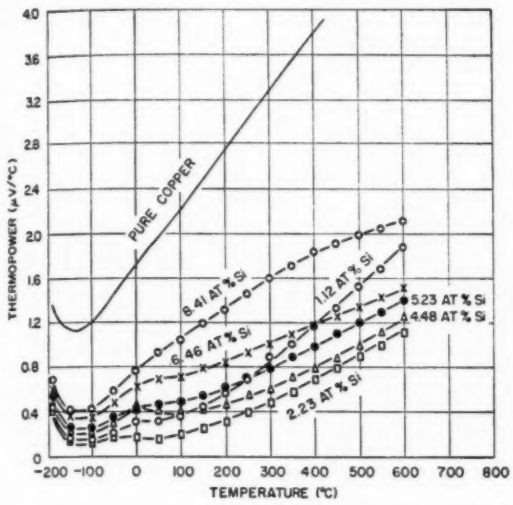

FIG. 4. Absolute thermopower of Cu–Si alloys. The solid curve (pure copper) show the data of Borelius *et al.* and of Nyström. See references 9 and 10.

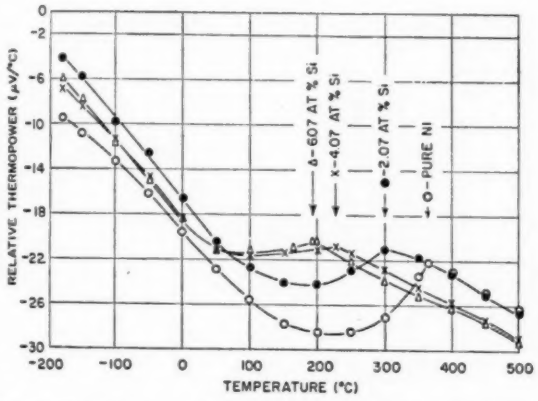

FIG. 5. Thermopower of Ni–Si alloys relative to copper. The vertical arrows indicate the positions of the "thermoelectric Curie temperatures," and the symbols at the tails of these arrows designate the various compositions.

percent Si crosses the curve for the 0.41 percent Si sample at about 200°C, although the Curie temperatures for the two specimens are in the correct order. We thought that perhaps the compositions of these two specimens had been changed slightly during the high-temperature measurements, so that upon cooling the 0.084 percent Si specimen would have higher room-temperature resistivity than the 0.41 percent Si wire.

[12] G. G. Andrewartha and E. J. Evans, Phil. Mag. **31**, 265 (1941).

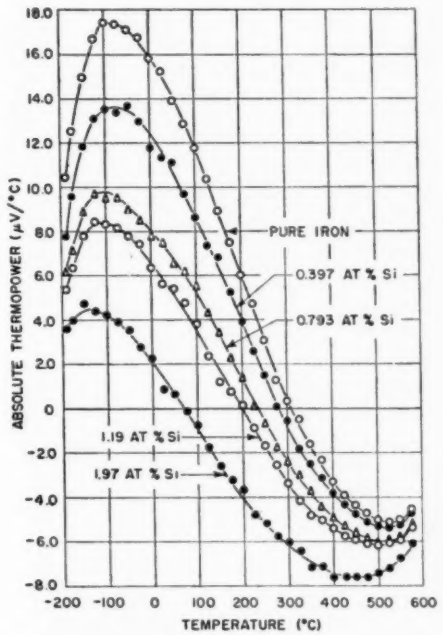

FIG. 6. Absolute thermopower of Fe–Si alloys.

This supposition turned out to be false and the resistivity curves for both wires were retraced. We have no good explanation of this reversal of resistivity at high temperatures. The Ni–Si thermopowers (Fig. 5) remain negative and also show a knick at the Curie temperature. It can be seen from both the resistivities and the thermopowers that the Curie temperature decreases rapidly with increasing amounts of Si.

The resistivities of the Fe–Si alloys (Fig. 3) also vary faster than linearly with temperature and seem to obey the Matthiessen rule reasonably well in the range in which we measured them. The resistivity increase per atomic percent is 10.5 $\mu\Omega$ cm at −180°C and 10.6 $\mu\Omega$ cm at 390°C. The thermopowers of the Fe–Si alloys (Fig. 6) change sign at temperatures that decrease with increasing amounts of Si.

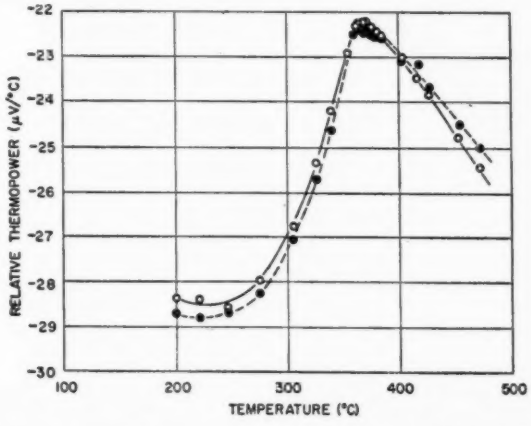

FIG. 7. Comparison of our data with those of Hammer (see reference 11) on the relative thermopower of pure Ni in the region of the Curie temperature. The open circles are our data, and the solid dots are those of Hammer.

The details of how the thermopower varies in the vicinity of the Curie temperature are seen in Fig. 7, which shows how the thermopower reflects changes in the magnetic structure of the metal.

We have given elsewhere[7] a discussion of the thermoelectric behavior of Cu–Si alloys, on the basis of Mott's[13] theory of thermoelectricity. The behavior of Ni–Si and Fe–Si is more difficult to explain because of complications arising from the ferromagnetic properties of these alloys. A tentative explanation may be given in terms of an effective "magnetic cross section," at least at very low temperatures and also in the region just below the Curie temperature; the added silicon then changes the "density" of these "magnetic scattering centers" and also introduces its own scattering effects.

The authors wish to acknowledge the continued interest of Dr. Foster C. Nix in this work; they also extend their thanks to the Squire Signal Laboratory for financial support.

[13] N. F. Mott and H. Jones, *Theory of Metals and Alloys* (Oxford University Press, New York, 1936).

JOURNAL OF APPLIED PHYSICS VOLUME 26, NUMBER 4 APRIL, 1955

Injected Current Carrier Transport in a Semi-Infinite Semiconductor and the Determination of Lifetimes and Surface Recombination Velocities

W. VAN ROOSBROECK
Bell Telephone Laboratories, Murray Hill, New Jersey

(Received May 10, 1954)

With both surface and volume recombination taken into account, time-dependent and steady-state Green's functions are obtained for a point source of added carriers in a semi-infinite semiconductor, and for infinite line and plane sources parallel to the surface. Small-signal theory is employed, and a compact Stieltjes-integral derivation is given. The Green's functions are specialized to provide: the time dependence of surface concentration following the instantaneous injection of carriers at a point on the surface; that following instantaneous injection which is uniform over the surface; and the distance dependences for steady point, infinite-line, semi-infinite plane, and semi-infinite line surface sources. Steady flows of minority carriers from these sources into a $p-n$ junction perpendicular to the surface are also calculated. Analytical approximations are found for the steady-source cases. Theoretical and experimental aspects of the determination of lifetimes and surface recombination velocities from data by means of these results are discussed.

1. INTRODUCTION

IN studies of semiconductor properties as well as in the evaluation of semiconductor material for technical applications the volume lifetime and surface recombination velocity which characterize the recombination of injected current carriers are of particular interest. These may be found from a theoretical analysis of experiments in which carriers are injected at one location and the resulting added carrier concentration or flow density determined at another. Light provides a convenient means for the injection; Goucher has shown that electron-hole pairs are produced in germanium with unit quantum efficiency in the absorption range from about 1 to 2 microns in wavelength.[1] With light, the added carriers may be produced either on the surface or in depth, and the injection location and geometry are readily controllable. In addition, the simplifying feature of a total current density which is zero or small is easily realized. The local added carrier concentration in the volume cannot be determined directly; but changes in the reverse current, zero-bias conductance, or floating potential of a fixed point contact on the surface provide a measure of the added concentration near the contact. Both experiment[2] and theory[3] have shown that simple proportionalities apply over a fairly wide range in experimental conditions. The point-contact detector is, indeed, basic to the technique of the experiments on the transport of pulses of injected carriers in semiconductor filaments. Effective lifetimes associated with recombination on filament surfaces have been found from such experiments.[2,4] Volume lifetimes in germanium filaments or rods have been found from steady-state measurements of the photovoltage of a point contact,[5] or the photocurrent through a $p-n$ junction,[6] as a function of distance from a light-spot emitter. To find lifetimes in massive samples, this steady-state technique has been employed, with the point-contact detector and a surface line source, for cases of negligible surface recombination.[7]

[1] F. S. Goucher, Phys. Rev. **78**, 816 (1950).

[2] Shockley, Pearson, and Haynes, Bell System Tech. J. **28**, 344 (1949); W. Shockley, *Electrons and Holes in Semiconductors* (D. Van Nostrand Company, Inc., New York, 1950), p. 65.

[3] J. Bardeen, Bell System Tech. J. **29**, 469 (1950). Floating potentials have been discussed in connection with $p-n$ junctions by W. Shockley, Bell System Tech. J. **28**, 435 (1949).

[4] J. R. Haynes and W. Shockley, Phys. Rev. **81**, 835 (1951).

[5] F. S. Goucher, Phys. Rev. **81**, 475 (1951).

[6] Goucher, Pearson, Sparks, Teal, and Shockley, Phys. Rev. **81**, 637 (1951).

[7] L. B. Valdes, Proc. Inst. Radio Engrs. **40**, 1420 (1952). See also Teal, Sparks, and Buehler, Proc. Inst. Radio Engrs. **40**, 906 (1952).

In this paper, general Green's functions derived for the semi-infinite semiconductor, from which solutions of a great variety of problems may, of course, be obtained, are specialized to cases of surface injection which appear especially suited for finding lifetimes and surface recombination velocities from measurements on massive samples. From the experimental viewpoint, the results are applicable to single crystals with a plane surface and with dimensions large compared with a diffusion length. Transient methods, such as the ones based on the elapsed time between a brief[8] point-source pulse of carriers and the concentration peak at another point on the surface at given distance, and on the decay of surface concentration following a brief pulse of carriers introduced uniformly over the entire surface,[9] presumably minimize errors introduced by finite sample size. Steady-state solutions apply, if an intermittent source is employed, for convenience in instrumentation, in general provided both the time on and the time off are large compared with π times the volume lifetime τ and with the larger of $x_s^2/4D_0$ and $x_s/(D_0/\tau)^{\frac{1}{2}}$, where x_s is distance between detector and source and D_0 is the diffusivity for added carriers. In this connection, the point source on the surface entails less error from edge effects than does the line source. The latter, however, gives comparatively better signal strength at the detector, but with the limitation of the error introduced by line width. As Brattain has pointed out, the semi-infinite plane source on the surface is therefore of particular advantage, as is the semi-infinite line with the detector on the line extended.

Surface recombination may be neglected if its velocity is small compared with the diffusion velocity $(D_0/\tau)^{\frac{1}{2}}$ associated with volume recombination. Provided the lifetime is not too large, it appears that this condition may be realized through suitable surface treatments.[4] On the other hand, if the product of surface recombination velocity and nearest distance between source and detector is large compared with D_0, the exact solutions may be replaced by approximations in which the dependence on surface recombination velocity is contained in a multiplying factor. The requisite condition is easily realized, and relative response data then provide lifetimes without reference to surface recombination.[10]

Both surface recombination velocity and volume lifetime may be found with good precision from the steady-state distance dependence of the quantum efficiency for flow into a $p-n$ junction, since the junction provides a calibration of the strength of the light source.[6,11] A transient method which also furnishes the surface recombination velocity is that of the decay of surface concentration following uniform illumination by a pulse of nonpenetrating light. For the surface recombination velocity, this method with relative response data is potentially much more precise than the steady-state methods which also employ the point-contact detector.[12]

The lifetime determined by experiment and theory is the limiting small-signal value of the lifetime function for added carrier concentration; it equals the mean lifetime of minority carriers only in strongly extrinsic material.[13] If trapping occurs under conditions such that carriers are immobilized for times not small compared with their mean lifetime before their recombination or release, then lifetime or surface recombination velocity may represent an oversimplification.[14] Experiment has shown, however, that in germanium a time-independent limiting small-signal value for the lifetime function generally obtains under conditions of technical interest, so that the decay with time of a relatively small uniform initial concentration of added carriers is exponential.[15]

2. DERIVATION OF THE GREEN'S FUNCTIONS

The small-signal differential equation in added carrier concentration Δp for zero total current density is[16] in a familiar notation

$$\partial \Delta p/\partial t = D_0 \operatorname{div} \operatorname{grad} \Delta p - \Delta p/\tau, \tag{1}$$

where

$$D_0 \equiv kT\mu_n\mu_p(n_0+p_0)/\sigma_0 = (n_0+p_0)/(n_0/D_p+p_0/D_n) \tag{2}$$

is the ambipolar diffusivity. The electron and hole flow densities are, for this case,

$$\mathbf{J}_p = \mathbf{J}_n \equiv \Delta\mathbf{J} = -D_0 \operatorname{grad} \Delta p. \tag{3}$$

In accordance with Eq. (3), recombination on the sur-

[8] The pulse duration should, of course, be small compared with the lifetime. The time constant associated with the resistance and capacitance of the detector point contact is in general negligible.

[9] The detector contact region should be shielded from light; but the radius of the shielded region should not be so large that the corresponding diffusion time becomes comparable with the duration of the pulse.

[10] This method has been employed with sandblasted surfaces by Brattain as well as by Goucher, who found it to furnish the same lifetime in a particular sample as did the zero-surface-recombination method of reference 7.

[11] F. S. Goucher and M. B. Prince, Phys. Rev. **89**, 651 (1953). Analysis of unpublished measurements of Goucher has furnished lifetimes and surface recombination velocities to both sides of $p-n$ junctions produced by the crystallization technique.

[12] In a small filament, in order that the decay of concentration or conductance with time or with distance provide a measure of surface recombination alone, the volume lifetime in the original crystal must be sufficiently large and must not have been unduly decreased during preparation of the filament. W. Shockley, *Electrons and Holes in Semiconductors* (D. Van Nostrand Company, Inc., New York, 1950), pp. 60–65; S. M. Ryvkin, J. Exptl. Theoret. Phys. (U.S.S.R.) **20**, 139 (1950); Navon, Bray, and Fan, Proc. Inst. Radio Engrs. **40**, 1342 (1952). Magnetic-field methods may also be employed to investigate surface recombination: W. Shockley, *op. cit.*, pp. 71–75; reference 3; Moss, Pincherle, and Woodward, Proc. Phys. Soc. (London) **66B**, 743 (1953); H. K. Henisch, private communication.

[13] W. van Roosbroeck, Phys. Rev. **91**, 282 (1953).

[14] Traps which can apparently be filled by carriers injected by nonpenetrating radiation have been observed in germanium at low temperatures: R. Lawrance, Phys. Rev. **89**, 1295 (1953); J. R. Haynes and J. A. Hornbeck, Phys. Rev. **90**, 152 (1953); D. Navon and H. Y. Fan, Phys. Rev. **91**, 491 (1953); **93**, 911 (1954).

[15] J. R. Haynes and W. Shockley, Phys. Rev. **75**, 691 (1949)

[16] See reference 13. The condition for linearity is given by (34) or (35) of this reference.

face of the semi-infinite solid $z \geq 0$ is specified by

$$D_0 \partial \Delta p / \partial z = s \Delta p, \quad z = 0, \tag{4}$$

where s is the surface recombination velocity. By introducing as dimensionless variables,

$$\Delta P \equiv \Delta p / n_s, \quad n_s \equiv n_0 - p_0; \quad U \equiv t/\tau; \quad X \equiv x/L,$$
$$Y \equiv y/L, \quad Z \equiv z/L; \quad L \equiv (D_0 \tau)^{\frac{1}{2}}, \tag{5}$$

Eqs. (1) and (4) may be written as

$$\partial \Delta P / \partial U = \text{div grad} \Delta P - \Delta P \tag{6}$$

and

$$\partial \Delta P / \partial Z = S \Delta P, \quad Z = 0, \tag{7}$$

where S is s measured in units of the diffusion velocity v_D:

$$S \equiv s/v_D, \quad v_D \equiv L/\tau = (D_0/\tau)^{\frac{1}{2}}. \tag{8}$$

Solutions of Eq. (6) are of the form of a product of $\exp(-U)$ and a solution of the heat flow equation. For the infinite semiconductor, solutions for instantaneous added-carrier sources of strength unity may accordingly be written as

$$\Delta P = \begin{pmatrix} \chi_1 \\ \chi_2 \\ \chi_3 \end{pmatrix} \exp[-(Z - Z_s)^2/4U], \tag{9}$$

where

$\chi_1 \equiv (4\pi U)^{-\frac{1}{2}} e^{-U}$ for a plane source of $n_s L$ carrier pairs per unit area at $Z = Z_s$;

$\chi_2 \equiv (4\pi U)^{-1} \exp[-U - (X - X_s)^2/4U]$ for a line source of $n_s L^2$ carrier pairs per unit length at $X = X_s$, $Z = Z_s$;

$\chi_3 \equiv (4\pi U)^{-\frac{1}{2}} \exp\{-U - [(X - X_s)^2 + (Y - Y_s)^2]/4U\}$ for a point source of $n_s L^3$ carrier pairs at $X = X_s$, $Y = Y_s$, $Z = Z_s$. (10)

The source strengths are normalized for the dimensionless quantities and correspond to $n_s L^3$ carrier pairs per area L^2, per length L, and at the point, respectively. These equations for ΔP give (time-dependent) Green's functions for the infinite semiconductor.

The corresponding Green's functions for the semi-infinite semiconductor with surface recombination according to Eq. (7) differ from those for the infinite case only in their dependence on Z. While they may be derived by methods of contour integration and of the Laplace transform,[17] a compact method of greater conceptual directness will be presented here, whose entire formalism has immediate interpretation in terms of sources and source distributions. It consists essentially in replacing the semi-infinite solid by the infinite one and determining an initial distribution of ΔP in the added semi-infinite portion such that the boundary condition [Eq. (7)] is satisfied for the known initial distribution in the original solid. Since instantaneous sources are involved, the condition that the initial distributions be bounded, sufficient for the validity[18] as solution of the well-known infinite integral of Laplace, does not hold. An appropriate generalization of Laplace's solution appears to consist in writing it in the form of a Stieltjes integral. Heuristic use will be made of this procedure.[19]

The Riemann-Stieltjes integral representation

$$\Delta P = \begin{pmatrix} \chi_1 \\ \chi_2 \\ \chi_3 \end{pmatrix} \int_{-\infty}^{\infty} \exp[-(Z - \zeta)^2/4U] d\mathfrak{F}(\zeta) \tag{11}$$

is employed, with the integrator function $\mathfrak{F}(\zeta)$ assumed to be real and of bounded variation.[20] The Green's function for the infinite semiconductor of Eqs. (9) and (10) result from this representation if $\mathfrak{F}(\zeta)$ is a step function with a single step of value unity at $\zeta = Z_s$ and elsewhere constant. For the problem under consideration, $\mathfrak{F}(\zeta)$ is evidently of this form for $\zeta \geq 0$, corresponding to the original semi-infinite semiconductor,[21] so that, from Eq. (11), writing $\mathfrak{F}(-\zeta) \equiv \mathfrak{F}^*(\zeta)$,

$$\Delta P = \begin{pmatrix} \chi_1 \\ \chi_2 \\ \chi_3 \end{pmatrix} \left\{ \int_0^{\infty} \exp[-(Z + \zeta)^2/4U] d\mathfrak{F}^*(\zeta) + \exp[-(Z - Z_s)^2/4U] \right\}. \tag{12}$$

It remains to find an $\mathfrak{F}^*(\zeta)$ such that the boundary condition Eq. (7) is satisfied, whence ΔP can then be found from Eq. (12). Making use of Eq. (12) and

$$\frac{\partial \Delta P}{\partial Z} = \begin{pmatrix} \chi_1 \\ \chi_2 \\ \chi_3 \end{pmatrix} \left\{ -\int_0^{\infty} \frac{Z + \zeta}{2U} \exp[-(Z + \zeta)^2/4U] d\mathfrak{F}^*(\zeta) - \frac{Z - Z_s}{2U} \exp[-(Z - Z_s)^2/4U] \right\}, \tag{13}$$

the condition [Eq. (7)] is found to be

$$-\int_0^{\infty} \frac{\zeta}{2U} \exp(-\zeta^2/4U) d\mathfrak{F}^*(\zeta) + \frac{Z_s}{2U} \exp(-Z_s^2/4U) = S\left[\int_0^{\infty} \exp(-\zeta^2/4U) d\mathfrak{F}^*(\zeta) + \exp(-Z_s^2/4U) \right]. \tag{14}$$

[17] H. S. Carslaw, *Introduction to the Mathematical Theory of the Conduction of Heat in Solids* (Dover Publications, New York, 1945), Chap. X; H. S. Carslaw and J. C. Jaeger, *Conduction of Heat in Solids* (Oxford University Press, London, 1947), Chap. XIII.

[18] H. S. Carslaw and J. C. Jaeger, *Conduction of Heat in Solids* (Oxford University Press, London, 1947), p. 18.

[19] Conditions for this generalization are given by: P. Hartman and A. Wintner, Am. J. Math. **72**, 367 (1950); S. F. Lidyaev, Uchenie Zapiski Moskov. Gosudarst. Univ. No. 135, Matematika, **II**, 86 (1948). See also Math. Rev. **11**, 440 (1950).

[20] For a discussion of the Stieltjes integral and its properties see D. V. Widder, *Advanced Calculus* (Prentice-Hall, Inc., New York, 1947), Chap. V; *The Laplace Transform* (Princeton University Press, Princeton, 1941), Chap. I.

[21] Note that $\mathfrak{F}(Z) - \mathfrak{F}(0)$ represents the total instantaneous source strength in the semi-infinite semiconductor up to the plane specified by Z.

Now, for $S=0$, this equation is clearly satisfied if $\mathfrak{F}^*(\zeta)$ is a step function with a single step of value unity at $\zeta=Z_s$, which corresponds, as may be expected, to an image source at $Z=-Z_s$. Denoting this step function by $\mathfrak{F}_0^*(\zeta)$ and writing

$$\mathfrak{F}^*(\zeta)=\mathfrak{F}_0^*(\zeta)+\mathfrak{F}_1^*(\zeta), \tag{15}$$

Eq. (14) becomes

$$\int_0^\infty \frac{\zeta}{2U}\exp(-\zeta^2/4U)d\mathfrak{F}_1^*(\zeta) +S\int_0^\infty \exp(-\zeta^2/4U)d\mathfrak{F}_1^*(\zeta) =-2S\exp(-Z_s^2/4U) \tag{16}$$

for the determination of $\mathfrak{F}_1^*(\zeta)$. Without further hypothesis concerning this integrator function, it is permissible to evaluate the second integral by parts,[22] so that

$$\int_0^\infty \frac{\zeta}{2U}\exp(-\zeta^2/4U)d\mathfrak{F}_1^*(\zeta) +S\exp(-\zeta^2/4U)\mathfrak{F}_1^*(\zeta)\Big|_0^\infty +S\int_0^\infty \frac{\zeta}{2U}\exp(-\zeta^2/4U)\mathfrak{F}_1^*(\zeta)d\zeta =-2S\exp(-Z_s^2/4U). \tag{17}$$

If

$$\mathfrak{F}_1^*(\zeta)=2, \quad 0\leq\zeta\leq Z_s, \tag{18}$$

the second term on the left cancels the one on the right, as is most directly verified simply by noting that there is no contribution to the integrals from a range in ζ over which the integrator function is constant, and accordingly replacing the lower limits in Eq. (17) by Z_s. Thus, for an $\mathfrak{F}_1^*(\zeta)$ which possesses a continuous derivative in the interval $Z_s<\zeta<\infty$, Eqs. (17) and (18) result in

$$\int_{Z_s}^\infty \frac{\zeta}{2U}\exp(-\zeta^2/4U)\left[\frac{d\mathfrak{F}_1^*(\zeta)}{d\zeta}+S\mathfrak{F}_1^*(\zeta)\right]d\zeta=0, \tag{19}$$

and $\mathfrak{F}_1^*(\zeta)$ may be sought as the solution of the differential equation obtained by equating to zero the expression in brackets, since S is arbitrary. In conjunction with Eq. (18), this differential equation gives

$$\mathfrak{F}_1^*(\zeta)=2\exp(-S(\zeta-Z_s), \quad Z_s\leq\zeta<\infty. \tag{20}$$

Introducing the notation $\mathbf{1}(Z_s)$ for the function which is the unit step in ζ at Z_s and which is normalized so as to equal zero for $\zeta\leq Z_s$, Eqs. (15), (18), and (20) give

$$\mathfrak{F}^*(\zeta)=\mathbf{1}(Z_s)+2\exp[-S(\zeta-Z_s)\mathbf{1}(Z_s)]. \tag{21}$$

Substituting for $\mathfrak{F}^*(\zeta)$ in Eq. (12), the solutions for the plane, line, and point sources are found to be

$$\begin{pmatrix} G_1(Z,U;Z_s) \\ G_2(X,Z,U;X_s,Z_s) \\ G_3(X,Y,Z,U;X_s,Y_s,Z_s)\end{pmatrix}=\begin{pmatrix}\chi_1\\ \chi_2\\ \chi_3\end{pmatrix}\left\{\exp[-(Z-Z_s)^2/4U]+\exp[-(Z+Z_s)^2/4U] -2S\int_0^\infty \exp[-S\zeta-(Z+Z_s+\zeta)^2/4U]d\zeta\right\}$$

$$=\begin{pmatrix}\chi_1\\ \chi_2\\ \chi_3\end{pmatrix}\left\{\exp[-(Z-Z_s)^2/4U]+\exp[-(Z+Z_s)^2/4U]-2\pi^{\frac{1}{2}}SU^{\frac{1}{2}}\exp[S(Z+Z_s)+S^2U] \times\operatorname{erfc}\left(\frac{Z+Z_s}{2U^{\frac{1}{2}}}+SU^{\frac{1}{2}}\right)\right\}, \tag{22}$$

where

$$\operatorname{erfc}u\equiv 1-2\pi^{-\frac{1}{2}}\int_0^u \exp(-\beta^2)d\beta, \tag{23}$$

and in which ΔP has been written as the corresponding Green's function G_1, G_2, or G_3. It is easily verified that Eq. (22) provides the correct solutions; and it is clear from the first expression for them that the image distribution corresponding to the instantaneous source at $Z=Z_s$ is a source of equal strength at $Z=-Z_s$ together with a sink distributed from $-Z_s$ to $-\infty$ whose strength varies with Z as $\exp S(Z+Z_s)$ and whose total strength is twice that of the source. The total strength of the actual source and its image distribution is thus zero. For S infinite, the image distribution reduces to a sink localized at $-Z_s$ such that the added hole concentration is zero at the surface.

The Green's functions for the steady state may be found by integrating Eq. (22) from zero to infinity with respect to U, since this variable is, in reduced form, the elapsed time after application of an instantaneous source. The integrals are conveniently found from tables[23] as Laplace transforms evaluated for the trans-

[22] The method of the Stieltjes integral generalizes one, treated in P. Frank and R. von Mises, *Die Differential- und Integralgleichungen der Mechanik und Physik* (Mary S. Rosenberg, New York, 1943), pp. 579 ff., which deals with Reimann integrals containing (bounded) distribution functions, which are derivatives of (continuous) integrator functions. With this less general method, the first integral in (16) would be integrated by parts in the manner which introduces the derivative of the distribution function. While it leads to an equivalent result, this procedure requires further assumption concerning continuity. Use of the integrator function thus appears in principle to constitute a better method than that based on the distribution function.

[23] G. A. Campbell and R. M. Foster, *Fourier Integrals for Practical Applications*, Bell System Monograph B-584; (D. Van

form variable equal to zero.[24] Or, with the particular forms which the Green's functions in Eq. (22) possess, use may be made of an integral representation for the modified Bessel functions of the second kind, $K_\nu(u)$: Provided the real part of u^2 is positive,[25]

$$K_\nu(u)=\tfrac{1}{2}(\tfrac{1}{2}u)^\nu\int_0^\infty U^{-(\nu+1)}\exp(-U-u^2/4U)dU. \quad (24)$$

Thus, from the tables, or from Eq. (24) with $\nu=-\frac{1}{2}$ and using[26]

$$K_{-\frac{1}{2}}(u)=K_{\frac{1}{2}}(u)=(\pi/2u)^{\frac{1}{2}}e^{-u}, \quad (25)$$

the Green's function corresponding to the steady plane source at $Z=Z_s$ is

$$\bar{G}_1(Z;Z_s)=\tfrac{1}{2}\left\{\exp[-|Z-Z_s|]-\frac{S-1}{S+1}\exp[-(Z+Z_s)]\right\}$$
$$=\begin{cases}\tfrac{1}{2}e^{-Z_s}\left[e^{Z}-\dfrac{S-1}{S+1}e^{-Z}\right], & Z\le Z_s\\ \tfrac{1}{2}\left[e^{Z_s}-\dfrac{S-1}{S+1}e^{-Z_s}\right]e^{-Z}, & Z\ge Z_s.\end{cases} \quad (26)$$

It might be noted that, for this one-dimensional case, if S equals unity so that the diffusion and surface recombination velocities are equal, the solution Eq. (26) is as if there were no surface present and the semiconductor were infinite in extent.

The Green's function corresponding to the steady line source at $X=X_s$, $Z=Z_s$, from the tables or from Eq. (24) with $\nu=0$, is

$$\bar{G}_2(X,Z;X_s,Z_s)$$
$$=(2\pi)^{-1}\Big(K_0\{[(X-X_s)^2+(Z-Z_s)^2]^{\frac{1}{2}}\}$$
$$+K_0\{[(X-X_s)^2+(Z+Z_s)^2]^{\frac{1}{2}}\}-2S\int_0^\infty e^{-S\zeta}$$
$$\times K_0\{[(X-X_s)^2+(Z+Z_s+\zeta)^2]^{\frac{1}{2}}\}d\zeta\Big). \quad (27)$$

Finally, the Green's function corresponding to the steady point source at $X=X_s$, $Y=Y_s$, $Z=Z_s$, from the tables or from Eqs. (24) and (25) with $\nu=\frac{1}{2}$, is

$$\bar{G}_3(X,Y,Z;X_s,Y_s,Z_s)=\frac{1}{4\pi}\Big(\frac{\exp\{-[(X-X_s)^2+(Y-Y_s)^2+(Z-Z_s)^2]^{\frac{1}{2}}\}}{[(X-X_s)^2+(Y-Y_s)^2+(Z-Z_s)^2]^{\frac{1}{2}}}$$
$$+\frac{\exp\{-[(X-X_s)^2+(Y-Y_s)^2+(Z+Z_s)^2]^{\frac{1}{2}}\}}{[(X-X_s)^2+(Y-Y_s)^2+(Z+Z_s)^2]^{\frac{1}{2}}}$$
$$-2S\int_0^\infty\frac{\exp\{-S\zeta-[(X-X_s)^2+(Y-Y_s)^2+(Z+Z_s+\zeta)^2]^{\frac{1}{2}}\}}{[(X-X_s)^2+(Y-Y_s)^2+(Z+Z_s+\zeta)^2]^{\frac{1}{2}}}d\zeta\Big). \quad (28)$$

3. SOLUTIONS FOR PARTICULAR CASES

(a) Time-Dependent Solutions

(1) The concentration of added carriers at a point on the surface at a given distance from an instantaneous surface point source will exhibit a maximum with time. For the point at the origin and the source at X_s on the X-axis, this concentration is given by

$$\Delta p/(\mathfrak{N}/L^3)=G_3(0,0,0,U;X_s,0,0)=\tfrac{1}{4}\pi^{-\frac{1}{2}}U^{-\frac{1}{2}}$$
$$\times\exp(-U-X_s^2/4U)[1-\pi^{\frac{1}{2}}SU^{\frac{1}{2}}$$
$$\times\exp(S^2U)\,\mathrm{erfc}SU^{\frac{1}{2}}], \quad (29)$$

from Eqs. (10) and (22), where $\mathfrak{N}$ is the number of carrier pairs injected. For a surface recombination velocity small so that $\pi^{\frac{1}{2}}SU_m^{\frac{1}{2}}\ll 1$, where U_m is t_m/τ, with t_m the elapsed time corresponding to the maximum, Eq. (29) gives

$$4U_m^2+6U_m-X_s^2=0. \quad (30)$$

Introducing dimensional quantities, it is found that

$$t_m/\tau=x_s^2/4D_0t_m-\tfrac{3}{2} \quad (31)$$

for $s\ll(D_0/\pi t_m)^{\frac{1}{2}}$. For a surface recombination velocity sufficiently large so that $\frac{2}{3}S^2U_m\gg 1$, the expression in parentheses on the right of Eq. (29) is approximately $(2S^2U)^{-1}$ for U of order U_m, whence

$$t_m/\tau=x_s^2/4D_0t_m-\tfrac{5}{2} \quad (32)$$

for $s\gg(3D_0/2t_m)^{\frac{1}{2}}$.

According to these results, measurements of elapsed times t_m for various distances of separation x_s will furnish τ, which may be found from the slope of $x_s^2/4D_0t_m$ plotted against t_m. The value of the intercept will indicate which assumption concerning surface recombination is the better approximation. Solving the

Nostrand and Company, Inc., New York, 1942), pairs 823, 920.1, 817. See also E. Labin, *Calcul Opérationnel* (Masson et Cie., Paris, 1949).

[24] This is evident from the general form of the integrals, or from the observation that the steady-state solutions satisfy the Laplace transforms with respect to U of the differential and boundary-condition equations with the transform variable set equal to zero.

[25] G. N. Watson, *A Treatise on the Theory of Bessel Functions* (Cambridge University Press, Cambridge, 1944), p. 183.

[26] G. N. Watson, reference 25, Sec. 3.71.

quadratic equation in U_m, it may be seen that for $x_s \gg L$ the relationship between τ and t_m is approximately that obtained by discarding the constant term in Eq. (31) or (32). According to it, t_m equals x_s divided by the diffusion velocity $2(D_0/\tau)^{\frac{1}{2}}$, independently of surface recombination. For $x_s \ll L$, the value of t_m is substantially that obtained by equating the expression on the right of Eq. (31) or (32) to zero. It is then a geometrical diffusion time, a measure of D_0, which does not depend on τ. To determine τ, distances of order L or larger are, of course, necessary in general. More formally expressed for the cases considered, errors $\delta\tau$ in τ resulting from errors δx_s in x_s alone, or δt_m in t_m alone, being given, respectively, by

$$\begin{aligned}\delta\tau/\tau)_{t_m} &= -(2+3\tau/t_m)\delta x_s/x_s \\ \delta\tau/\tau)_{x_s} &= (2+\tfrac{3}{2}\tau/t_m)\delta t_m/t_m,\end{aligned} \tag{33}$$

tend to be quite large if t_m/τ is small.

It is easily shown, from Eqs. (10) and (22), that Eqs. (30), (31), and (33) also apply, for no surface recombination, to the maximum in current of minority carriers for flow from an instantaneous point source or parallel line or plane source into a $p-n$ junction perpendicular to the surface (or for planar flow, say, into a junction at the surface of the semi-infinite semiconductor), considering the time constant of the junction to be negligible. It may be shown that the relative total charge which has flowed into the junction in elapsed time t is $\frac{1}{2}[\exp(X_s)\cdot\operatorname{erfc}(x_s/2D_0^{\frac{1}{2}}t^{\frac{1}{2}}+U^{\frac{1}{2}})+\exp(-X_s)\cdot\operatorname{erfc}(x_s/2D_0^{\frac{1}{2}}t^{\frac{1}{2}}-U^{\frac{1}{2}})]$, which reduces to $\exp(-X_s)$ for $t=\infty$ and to $\operatorname{erfc}(x_s/2D_0^{\frac{1}{2}}t^{\frac{1}{2}})$ for no volume recombination.

(2) The time dependence of the surface concentration following a pulse of carriers, $\mathfrak{N}_2$ per unit area, introduced uniformly over the surface is, from Eqs. (10) and (22), given by

$$\Delta p/(\mathfrak{N}_2/L) = G_1(0,U;0) = \pi^{-\frac{1}{2}}U^{-\frac{1}{2}}e^{-U}[1-\pi^{\frac{1}{2}}SU^{\frac{1}{2}} \times\exp(S^2U)\operatorname{erfc}SU^{\frac{1}{2}}]. \tag{34}$$

In Fig. 1, the quantity $\pi^{\frac{1}{2}}U^{\frac{1}{2}}G_1(0,U;0)$ is plotted logarithmically against U for a number of values of S as parameter. By means of this figure, an experimentally determined curve of the product of the square root of elapsed time and the detector response *versus* elapsed time may be fitted theoretically, since the scale factors which relate these experimental quantities to the corresponding theoretical ones do not affect the shape of the curve in the logarithmic plot. Both τ and s can be found in this way, for, as the figure shows, the curve shape depends on S quite appreciably.

(b) Steady-State Solutions

(1) The surface concentration of added carriers (along the Y-axis) resulting from a steady line source (of coordinate X_s) on the surface which supplies carrier pairs at the rate $\mathfrak{R}_1$ per unit length is given by

$$\Delta p = (\mathfrak{R}_1/D_0)\bar{G}_2(0,0;X_s,0), \tag{35}$$

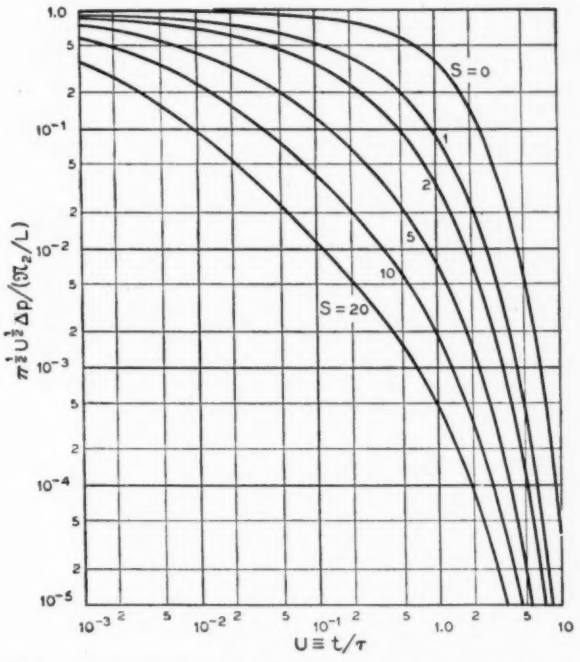

FIG. 1. The dependence of $\pi^{\frac{1}{2}}U^{\frac{1}{2}}\Delta p/(\mathfrak{N}_2/L)$ on reduced time U, where Δp is the surface concentration following a uniform instantaneous source over the surface of $\mathfrak{N}_2$ carrier pairs per unit area.

where, from Eq. (27),

$$\bar{G}_2(0,0;X_s,0) = \pi^{-1}\left\{K_0(X_s) - S\int_0^\infty e^{-S\zeta}K_0[(X_s^2+\zeta^2)^{\frac{1}{2}}]d\zeta\right\}. \tag{36}$$

By means of an integration by parts, Eq. (36) may be written in the form

$$\bar{G}_2(0,0;X_s,0) = \pi^{-1}\int_0^\infty e^{-S\zeta}K_1(R)\cos\Theta d\zeta, \tag{37}$$

or with R as variable of integration, where

$$R \equiv (X_s^2+\zeta^2)^{\frac{1}{2}}, \quad \cos\Theta \equiv \zeta/R. \tag{38}$$

This form furnishes a useful analytical approximation. For given X_s, if S is sufficiently large, the principal contributions to the integral will, because of the exponential, be associated with values of ζ in the neighborhood of $S^{-1} \ll X_s$. Thus, for $SX_s \gg 1$, or

$$sx_s \gg D_0, \tag{39}$$

it follows that $R \sim X_s$ and $\cos\Theta \sim \zeta/X_s$, so that

$$\bar{G}_2(0,0;X_s,0) \sim (K_1(X_s)/\pi X_s)\int_0^\infty \zeta\exp(-S\zeta)d\zeta = K_1(X_s)/\pi S^2X_s, \tag{40}$$

in which S occurs only in a multiplying factor.

In Fig. 2, $\bar{G}_2(0,0;X_s,0)$ is plotted against X_s for

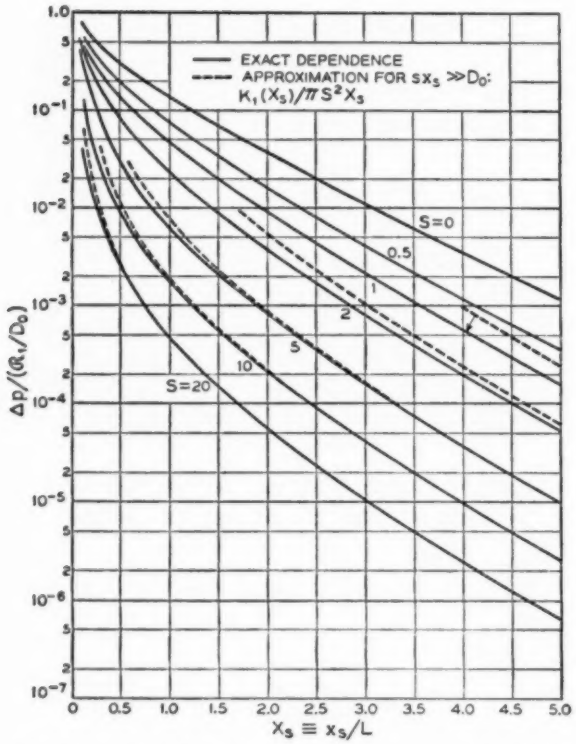

FIG. 2. Steady surface line source supplying carrier pairs at rate $\mathfrak{R}_1$ per unit length: the dependence of reduced surface concentration $\Delta p/(\mathfrak{R}_1/D_0)$ on reduced distance X_s.

values of S as parameter. The dashed curves in the figure give the approximation Eq. (40), which appears to be quite good, provided S is not too small, over most of the range in X_s shown.

(2) The surface concentration (at the origin) resulting from a steady point source on the surface (at X_s on the X-axis) which supplies carrier pairs at the rate $\mathfrak{R}$ is given by

$$\Delta p = (\mathfrak{R}/D_0 L)\bar{G}_3(0,0,0; X_s,0,0), \tag{41}$$

where, from Eq. (28),

$$\bar{G}_3(0,0,0; X_s,0,0) = (2\pi)^{-1}\left\{\exp(-X_s)/X_s - S\int_0^\infty (X_s^2+\zeta^2)^{-\frac{1}{2}} \exp[-S\zeta-(X_s^2+\zeta^2)^{\frac{1}{2}}]d\zeta\right\}$$

$$= (2\pi)^{-1}\int_0^\infty R^{-2}(R+1)\exp(-S\zeta-R)\cos\Theta d\zeta. \tag{42}$$

The approximation for $sx_s \gg D_0$ is

$$\bar{G}_3(0,0,0; X_s,0,0) \sim (X_s+1)e^{-X_s}/2\pi S^2 X_s^3. \tag{43}$$

Figure 3, in which are plotted $\bar{G}_3(0,0,0; X_s,0,0)$ and the approximation, is rather similar to Fig. 2; these figures show that the point source gives somewhat sharper variation with distance than the line source.

(3) The surface concentration (along the Y-axis) resulting from a steady semi-infinite plane source (from coordinate X_s to ∞) on the surface which supplies carrier pairs at the rate $\mathfrak{R}_2$ per unit area is

$$\Delta p = (\mathfrak{R}_2 L/D_0)\int_{X_s}^\infty \bar{G}_2(0,0; \xi_s,0)d\xi_s, \tag{44}$$

where $X_s > 0$ is the reduced distance to the edge of the source region. For $sx_s \gg D_0$,

$$\int_{X_s}^\infty \bar{G}_2(0,0; \xi_s,0)d\xi_s \sim (\pi S^2)^{-1}\left[K_1(X_s) - \int_{X_s}^\infty K_0(\xi_s)d\xi_s\right]. \tag{45}$$

In Fig. 4, the integral and the approximation[26] are plotted logarithmically against X_s, with S as parameter. The validity of the approximation is essentially the same as for the case of the infinite line source, or, as may be expected, slightly better. The logarithmic plot employed is the type best suited for the analysis of data.

(4) A steady semi-infinite line source on the surface (along the Y-axis from coordinate X_s to ∞) will produce a surface concentration at the point on the line extended at reduced distance $X_s > 0$ from its end (or at the origin)

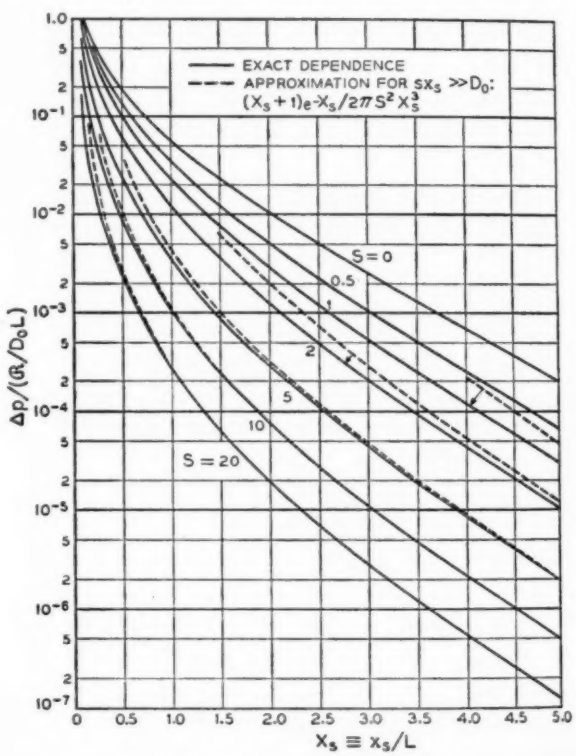

FIG. 3. Steady surface point source supplying carrier pairs at rate $\mathfrak{R}$: the dependence of reduced surface concentration $\Delta p/(\mathfrak{R}/D_0 L)$ on X_s.

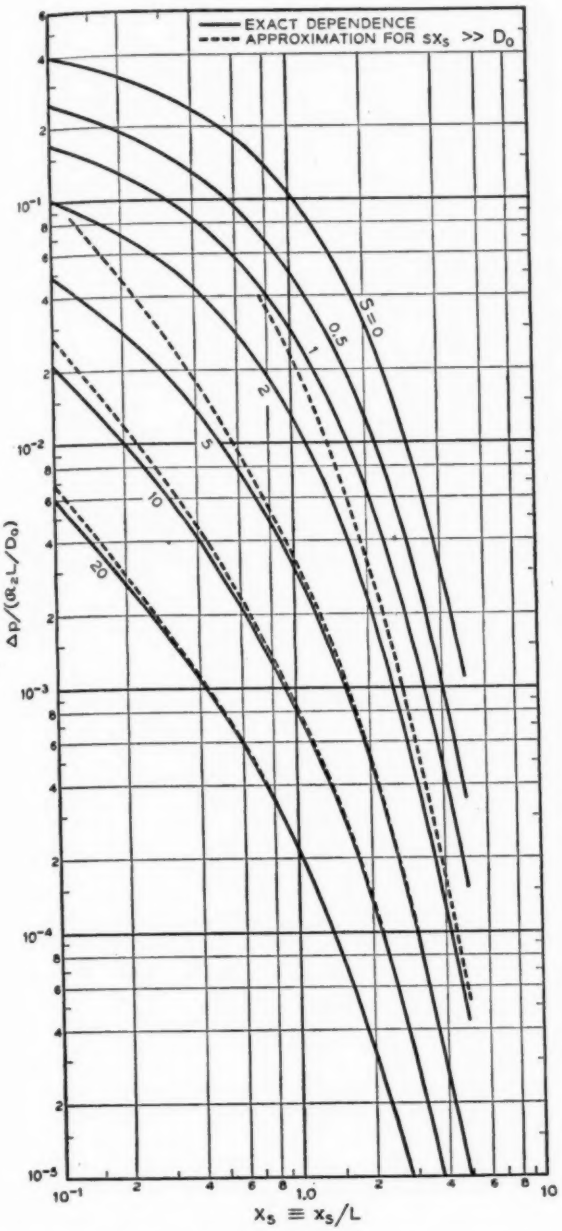

FIG. 4. Steady semi-infinite plane surface source supplying carrier pairs at rate $\mathcal{R}_2$ per unit area: the dependence of reduced surface concentration $\Delta p/(\mathcal{R}_2 L/D_0)$ on X_s.

equal to

$$\Delta p=(\mathcal{R}_1/D_0)\int_{X_s}^{\infty}\bar{G}_3(0,0,0;\xi_s,0,0)d\xi_s$$

$$\sim\tfrac{1}{2}(\mathcal{R}_1/D_0)(2\pi S^2)^{-1}\left[X_s^{-1}(1+X_s^{-1})\exp(-X_s)\right.$$

$$\left.-\int_{X_s}^{\infty}\xi_s^{-1}\exp(-\xi_s)d\xi_s\right]. \quad (46)$$

The integral for this case and the approximation to it, which applies for $sx_s \gg D_0$, are plotted logarithmically in Fig. 5.

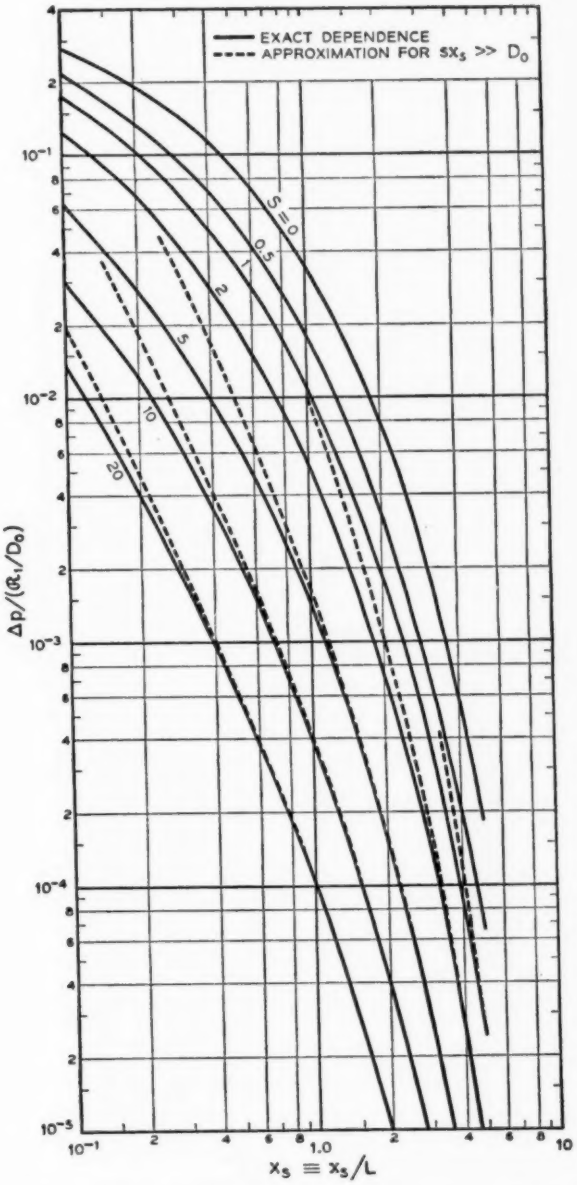

FIG. 5. Steady semi-infinite line surface source supplying carrier pairs at rate $\mathcal{R}_1$ per unit length: the dependence of reduced surface concentration $\Delta p/(\mathcal{R}_1/D_0)$ on X_s.

(5) The fraction of injected minority carriers which flows into a plane $p-n$ junction perpendicular to the surface from a parallel line source on the surface at a given distance may be evaluated by considering the flow in an infinite semiconductor between a line source and a parallel line sink on the surface at twice the distance; over the plane midway between, the added carrier concentration is evidently zero. From Eq. (3), the total flow rate is proportional to the integral over this plane of the concentration gradient.[27] With the plane

[27] The zero-total-current-density formulation employed is generally a good approximation for this case. In linear flow, if Δp_s is the added carrier concentration at a source, then the ratio at a junction of drift velocity $|v_0|$ to diffusion velocity $v_D \equiv (D_0/\tau)^{\frac{1}{2}}$ is, for n-type, approximately $\mu_0^* \Delta p_s/\mu_n n_0 \sinh X_s$. For given

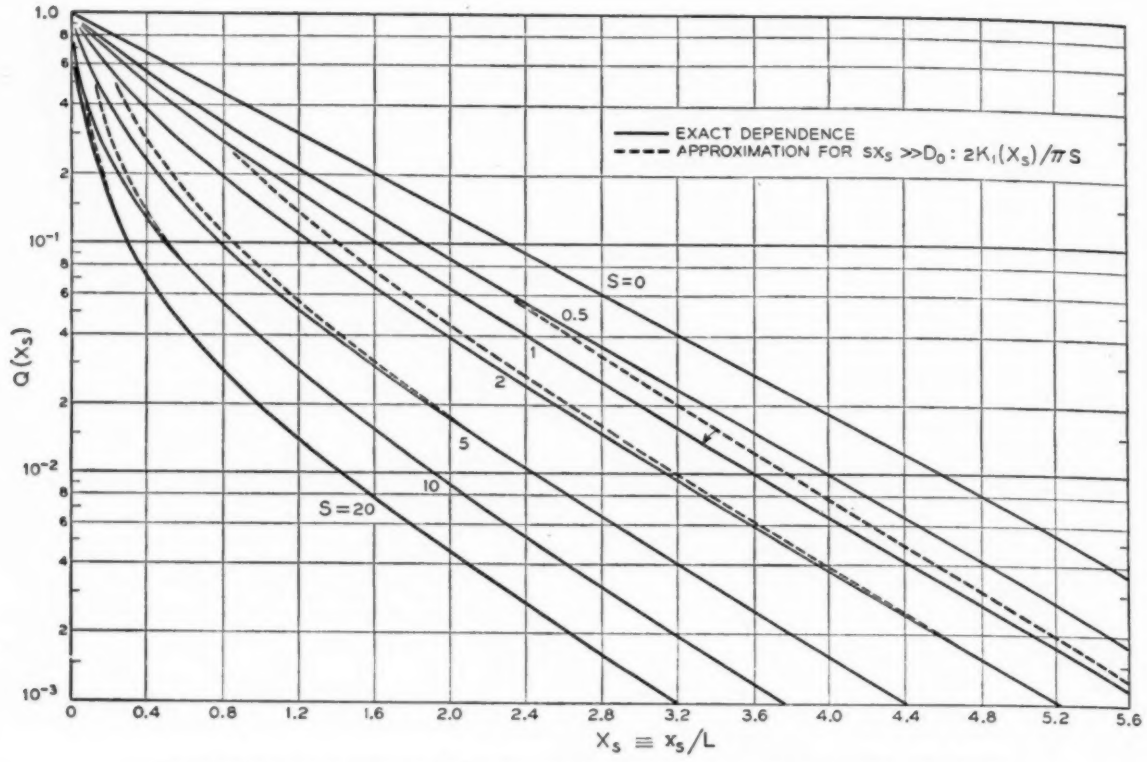

FIG. 6. The dependence on X_s of the fraction $Q(X_s)$ of injected carriers from a surface point or infinite line source that flows into a $p-n$ junction.

at $X=0$ and a steady line source on the surface at $X=X_s>0$, the solution for the concentration is, from Eq. (27),

$$\begin{aligned}\Delta p&=(\mathfrak{R}_1/D_0)[\bar{G}_2(X,Z;X_s,0)-\bar{G}_2(X,Z;-X_s,0)]\\&=(\mathfrak{R}_1/\pi D_0)\Big[K_0\{[(X-X_s)^2+Z^2]^{\frac{1}{2}}\}\\&\quad-K_0\{[(X+X_s)^2+Z^2]^{\frac{1}{2}}\}\\&\quad-S\int_0^\infty \exp(-S\zeta)(K_0\{[(X-X_s)^2+(Z+\zeta)^2]^{\frac{1}{2}}\}\\&\qquad-K_0\{[(X+X_s)^2+(Z+\zeta)^2]^{\frac{1}{2}}\})d\zeta\Big],\end{aligned}\tag{47}$$

whence

$$\begin{aligned}&(D_0/\mathfrak{R}_1)\int_0^\infty \left.\frac{\partial\Delta p}{\partial X}\right|_{X=0} dZ\\&=(2/\pi)X_s\Big\{\int_0^\infty (X_s^2+Z^2)^{-\frac{1}{2}}K_1[(X_s^2+Z^2)^{\frac{1}{2}}]dZ\\&\quad-S\int_0^\infty\int_0^\infty (X_s^2+(Z+\zeta)^2)^{-\frac{1}{2}}\\&\qquad\times\exp(-S\zeta)K_1[(X_s^2+(Z+\zeta)^2)^{\frac{1}{2}}]d\zeta dZ\Big\},\end{aligned}\tag{48}$$

since $dK_0(u)/du=-K_1(u)$. Writing $Q(X_s)$ for the expression on the left and evaluating the first integral on the right by use of the appropriate special case of the Sonine formula,[28]

$$\begin{aligned}&\int_0^\infty \frac{K_\nu[a(u^2+\beta^2)^{\frac{1}{2}}]}{(u^2+\beta^2)^{\nu/2}}\beta^{2m+1}d\beta\\&\qquad=\frac{2^m\Gamma(m+1)}{a^{m+1}}\,\frac{K_{\nu-m-1}(au)}{u^{\nu-m-1}},\end{aligned}\tag{49}$$

and by use of Eq. (25), it is found that

$$\begin{aligned}Q(X_s)&=\exp(-X_s)\\&\quad-(2/\pi)SX_s\int_0^\infty\int_0^\infty [X_s^2+(Z+\zeta)^2]^{-\frac{1}{2}}\\&\quad\times\exp(-S\xi)K_1\{[X_s^2+(Z+\zeta)^2]^{\frac{1}{2}}\}d\zeta dZ\\&=(2/\pi)X_s\int_0^\infty (X_s^2+\zeta^2)^{-\frac{1}{2}}\\&\qquad\times\exp(-S\zeta)K_1[(X_s^2+\zeta^2)^{\frac{1}{2}}]d\zeta.\end{aligned}\tag{50}$$

The function $Q(X_s)$, which equals unity for X_s zero, is clearly the fraction of injected minority carriers that flows into the junction. The simplified second form is obtained through suitable integration by parts and

$X_s>0$, this ratio may be made arbitrarily small by choice of Δp_s; for $\Delta p_s \ll (\sigma_0/\sigma_i)n_i$, as assumed here, it is small compared with $(1-p_0/n_0)/(b+1)\sinh X_s$, hence compared with unity, except for extreme cases of $x_s \ll L$ (see reference 13).

[28] G. N. Watson, reference 25, p. 417; a and the real part of $(m+1)$ must be positive.

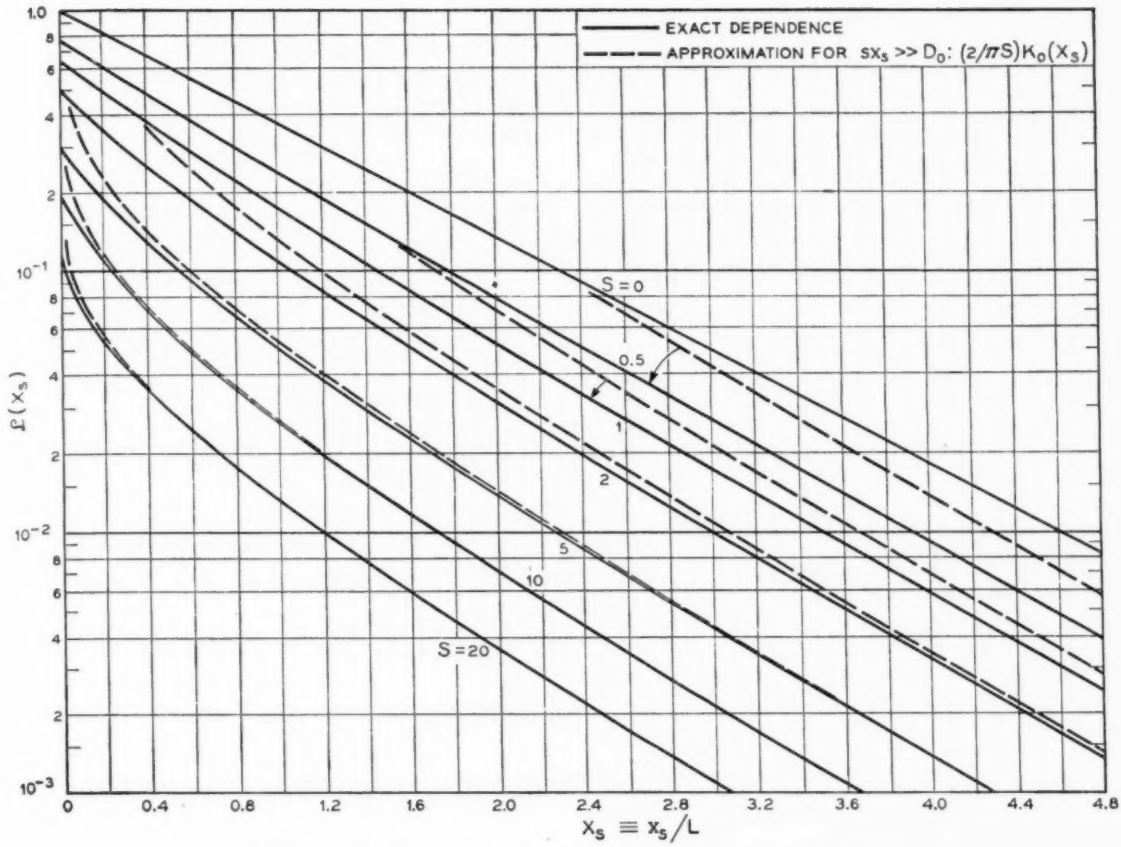

FIG. 7. The dependence on X_s of the reduced equivalent length $\mathfrak{L}(X_s)$ for flow into a $p-n$ junction from a semi-infinite line or plane surface source.

further application of Eq. (49). The approximation which applies for $sx_s \gg D_0$ is

$$Q(X_s) \sim (2/\pi S)K_1(X_s). \tag{51}$$

In Fig. 6, $Q(X_s)$ and this approximation are plotted against X_s for values of S as parameter.

The result Eq. (50) applies as well to the flow from a surface point source, since the flow from any element of the line source does not depend on the location of this element in the line, or as may be verified by direct calculation. For the surface recombination velocity zero, for which the flow is as if the semiconductor were infinite, the exponential term alone obtains and applies as well to the flow from a parallel plane source or from any element therein.[29] As is indicated by the curves of Fig. 6, the "peaking" in a semilogarithmic plot of an experimental quantum efficiency response curve as the source approaches the junction may be ascribed solely to recombination on the surface.[30]

(6) The total flow rate into the junction [over the (Y,Z)-plane] from a semi-infinite plane surface source (from coordinate X_s to ∞) whose edge is parallel to the junction, or from a perpendicular line element of this source, will equal the total rate at which carriers are injected over a certain length of the source. It may be specified in terms of this equivalent length expressed in units of L, which, from Eq. (50), is

$$\begin{aligned}\mathfrak{L}(X_s) &= \int_{X_s}^{\infty} Q(\xi_s)d\xi_s \\ &= (2/\pi)\int_0^{\infty} \exp(-S\zeta)K_0[(X_s^2+\zeta^2)^{\frac{1}{2}}]d\zeta \\ &= (2/S)[\pi^{-1}K_0(X_s) - \bar{G}_2(0,0;X_s,0)],\end{aligned} \tag{52}$$

with X_s the reduced distance from the junction to the edge of the source. The total flow rate is, of course, proportional to $\mathfrak{L}(X_s)$, which is plotted in Fig. 7 against X_s for values of S as parameter, together with

[29] This exponential dependence may also be derived from the Green's function given in Eq. (26) for the plane source, considering the junction equivalent to a surface for which S is infinite.

[30] If $X_s > 0$, then $Q(X_s)$ as well as the surface concentrations calculated for steady sources may be made arbitrarily small by choosing S sufficiently large. In practice, however, $Q(X_s)$ would approach a small nonzero minimum with increasing S because of the response associated with the doublet strength of slightly penetrating radiation. Solutions $\pi^{-1}K_\nu(R)\cos\nu\Theta$ may be obtained from the differential equation for the steady state by separating the variables in cylindrical coordinates. Selecting $\nu=0$ evidently gives the Green's function for the surface line source for $S=0$; and $\nu=1$, that for $S=\infty$, for which the surface concentration is zero and the line source replaced by a line doublet.

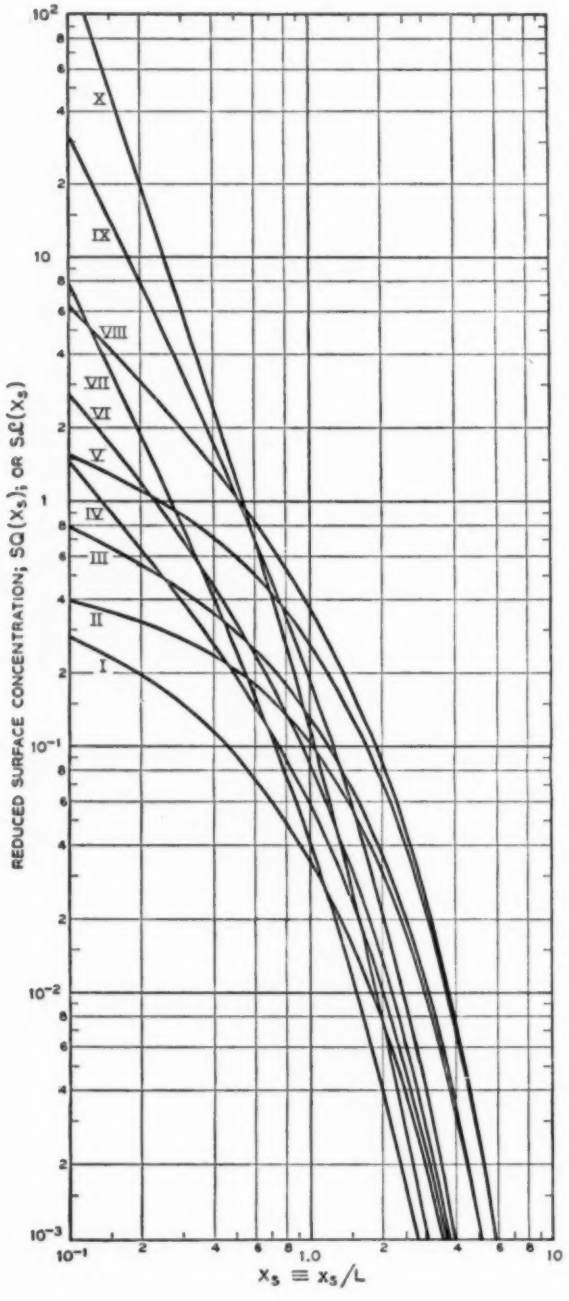

FIG. 8. The dependence on X_s of reduced surface concentrations, $SQ(X_s)$, and $S\mathfrak{L}(X_s)$ for $sx_s \gg D_0$, and reduced surface concentrations for $s \ll (D_0/\tau)^{\frac{1}{2}}$: I—$\Delta p$, semi-infinite line source, for $s \ll (D_0/\tau)^{\frac{1}{2}}$, times $D_0/\mathfrak{R}_1$: $(2\pi)^{-1} \int x_s^{\infty} \xi_s^{-1} \exp(-\xi_s) d\xi_s$; II—$\Delta p$, semi-infinite plane source, for $s \ll (D_0/\tau)^{\frac{1}{2}}$, times $D_0/\mathfrak{R}_2 L$: $\pi^{-1} \int x_s^{\infty} K_0(\xi_s) d\xi_s$; III—$\Delta p$, infinite line source, for $s \ll (D_0/\tau)^{\frac{1}{2}}$, times $D_0/\mathfrak{R}_1$: $K_0(X_s)/\pi$; IV—Δp, point source, for $s \ll (D_0/\tau)^{\frac{1}{2}}$, times $D_0 L/\mathfrak{R}$: $\exp(-X_s)/2\pi X_s$; V—$\mathfrak{L}(X_s)$ for $sx_s \gg D_0$, times S: $(2/\pi) K_0(X_s)$; VI—Δp, semi-infinite plane source, for $sx_s \gg D_0$, times $(D_0/\mathfrak{R}_2 L) S^2$: $\pi^{-1}[K_1(X_s) - \int x_s^{\infty} K_0(\xi_s) d\xi_s]$; VII—$\Delta p$, semi-infinite line source, for $sx_s \gg D_0$, times $(D_0/\mathfrak{R}_1) S^2$: $(4\pi)^{-1} \times [X_s^{-1}(1+X_s^{-1}) \exp(-X_s) - \int x_s^{\infty} \xi_s^{-1} \exp(-\xi_s) d\xi_s]$; VIII—$Q(X_s)$ for $sx_s \gg D_0$, times S: $(2/\pi) K_1(X_s)$; IX—Δp, infinite line source, for $sx_s \gg D_0$, times $(D_0/\mathfrak{R}_1) S^2$: $K_1(X_s)/\pi X_s$; X—Δp, point source, for $sx_s \gg D_0$, times $(D_0 L/\mathfrak{R}) S^2$: $(X_s+1) \exp(-X_s)/2\pi X_s^3$.

the approximation

$$\mathfrak{L}(X_s) \sim (2/\pi S) K_0(X_s) \tag{53}$$

for $sx_s \gg D_0$. If $S=0$, then $\mathfrak{L}(X_s)$, like $Q(X_s)$, equals $\exp(-X_s)$. For $X_s=0$, or injection up to the junction, Eq. (52) gives[31]

$$\mathfrak{L}(0) = (2/\pi)(\sinh^{-1}(S^2-1)^{\frac{1}{2}})/(S^2-1)^{\frac{1}{2}} = (2/\pi)(\cos^{-1}S)/(1-S^2)^{\frac{1}{2}}. \tag{54}$$

If, in addition, $S=0$, then $\mathfrak{L}(0)=1$, or the flow of minority carriers into the junction is as if all those injected within a diffusion length L reached it.

4. DISCUSSION

In the application of the methods based on surface concentration, the analysis of relative response data can furnish the surface recombination velocity with some precision only if the theoretical curves for different values of S differ appreciably in shape over the distance or time range of the measurements. The transient method associated with Fig. 1 has this property to a considerably greater extent than do the steady-state methods of Fig. 2 to Fig. 5, as comparison of the logarithmic plots shows quite clearly. This behavior results from the circumstance that where $sx_s \gg D_0$ applies in the steady state a change in S changes a curve substantially only through translation along the concentration axis.

Single universal curves for this approximation which do not depend on surface recombination velocity are accordingly convenient for determining volume lifetimes. These curves are plotted logarithmically in Fig. 8. Also included in this figure are the approximate curves for flow into a $p-n$ junction, and the steady-state surface concentrations for zero surface recombination velocity. As the figure shows, the latter curves, numbers I to IV, which apply if $s \ll (D_0/\tau)^{\frac{1}{2}}$, exhibit more variation in slope than do those for $sx_s \gg D_0$, numbers VII, VI, IX, and X, respectively. Their use, therefore, makes for greater precision in the determination of lifetimes. However, the condition for large sx_s may, particularly for the larger lifetimes, be more readily and unequivocally realized in practice than that for negligible s. Aside from this consideration, it might be noted that lifetimes may be found from data for the point source with negligible surface recombination simply by plotting the product of distance and detector response semilogarithmically against distance, since, from Eq. (42), this product is proportional to $\exp(-X_s)$. A method employing the semi-infinite plane or line source is probably best, however, because of the larger response it can furnish without departure from an ideal geometry. No consideration has been given to approximations[32] based on $x_s \gg L$ because accurate data for the larger values of x_s are not so easily obtained.

[31] Reference 25, p. 388.

[32] These approximations make use of: $K_\nu(u) \sim K_{\frac{1}{2}}(u) = (\pi/2)^{\frac{1}{2}} \times u^{-\frac{1}{2}} e^{-u}$ for $u>0$ large, independently of ν.

We are indebted to a number of our colleagues for their stimulating interest and advice, in particular to W. H. Brattain and F. S. Goucher, and to W. Shockley, J. A. Hornbeck, and L. B. Valdes as well for suggestions concerning the manuscript; to Miss R. A. Weiss and Miss D. J. Oxman, to whom most of the numerical computations for the figures are due; and to Miss M. C. Gray for her most helpful assistance in connection with these computations.

5. APPENDIX

Index of Solutions

The Green's Functions

(a) Time-dependent: Eq. (22).
(b) Steady-state: Eqs. (26), (27), (28).

Solutions for Particular Cases

(a) Time-independent solutions.—(1) Surface concentration, instantaneous surface point source: Eq. (29); elapsed time for maximum at given distance: Eqs. (31) and (32). (2) Flow into a $p-n$ junction; elapsed time for current maximum, and relative total charge in given elapsed time: Section 3(a). (3) Surface concentration, instantaneous source uniform over the surface: Eq. (34); Fig. 1.

(b) Steady-state solutions for various surface sources. —(1) Surface concentration, infinite line source: Eqs. (35), (36), (39), and (40); Fig. 2, Fig. 8. (2) Surface concentration, point source: Eqs. (41), (42), and (43); Fig. 3, Fig. 8. (3) Surface concentration, semi-infinite plane source: Eqs. (44) and (45); Fig. 4, Fig. 8. (4) Surface concentration, semi-infinite line source: Eq. (46); Fig. 5, Fig. 8. (5) Fraction $Q(X_s)$ of carriers that flows into a $p-n$ junction, point or parallel infinite line source: Eqs. (50) and (51); Fig. 6, Fig. 8. (6) Reduced equivalent length $\mathfrak{L}(X_s)$ for carrier flow into a $p-n$ junction, semi-infinite line or plane source: Eqs. (52), (53), and (54); Fig. 7, Fig. 8.

Symbols

$\chi_1, \chi_2, \chi_3 \equiv$ functions defined in Eqs. (10).
$D_n, D_p \equiv$ diffusion constants for electrons and holes.
$D_0 \equiv kT\mu_n\mu_p(n_0+p_0)/\sigma_0 = (n_0+p_0)/(n_0/D_p+p_0/D_n)$, diffusivity for (relatively small) added carrier concentration.
$G_1(Z,U;Z_s), G_2(X,Z,U;X_s,Z_s), G_3(X,Y,Z,U;X_s,Y_s,Z_s) \equiv$ Green's functions giving added carrier concentration in units of n_s resulting from instantaneous plane, line, and point sources normalized as for Eqs. (10).
$\bar{G}_1(Z,Z_s), \quad \bar{G}_2(X,Z;X_s,Z_s), \quad \bar{G}_3(X,Y,Z;X_s,Y_s,Z_s) \equiv$ Green's functions for steady plane, line, and point sources.
$k \equiv$ Boltzmann's constant.
$K_0(X_s), \ K_1(X_s) \equiv$ modified Bessel functions of the second kind of orders zero and one.
$L \equiv (D_0\tau)^{\frac{1}{2}}$, diffusion length.
$\mathfrak{L}(X_s) \equiv$ number of diffusion lengths of a semi-infinite surface source equivalent to the flow into a perpendicular $p-n$ junction.
$\mu_n, \mu_p \equiv$ mobilities for electrons and holes.
$n_0 \equiv$ electron concentration at thermal equilibrium.
$n_s \equiv n_0 - p_0$, electron concentration excess.
$\mathfrak{N}, \mathfrak{N}_2 \equiv$ numbers of carrier pairs injected at a point source, and per unit area at a plane source.
$p_0 \equiv$ hole concentration at thermal equilibrium.
$\Delta p \equiv$ added carrier concentration.
$Q(X_s) \equiv$ fraction of injected carriers that flows into a $p-n$ junction.
$\mathfrak{R}, \ \mathfrak{R}_1, \ \mathfrak{R}_2 \equiv$ rates of generation of carrier pairs at a point source, per unit length at a line source, and per unit area at a plane source.
$s \equiv$ surface recombination velocity.
$S \equiv s/(D_0/\tau)^{\frac{1}{2}} = sL/D_0$, reduced surface recombination velocity.
$t \equiv$ time variable.
$t_m \equiv$ elapsed time for concentration maximum.
$T \equiv$ temperature in degrees absolute.
$\tau \equiv$ lifetime of (relatively small) added carrier concentration.
$U \equiv t/\tau$, reduced time variable.
$x, y, z \equiv$ cartesian coordinates.
$X, Y, Z \equiv x/L, y/L, z/L$, reduced cartesian coordinates.
$x_s \equiv x$-coordinate of a source point; distance to (nearest boundary of) a source.
$X_s \equiv x_s/L$.
$Y_s, Z_s \equiv y_s/L, z_s/L$, reduced y- and z- coordinates of a source point.

Diffraction of Electromagnetic Waves by a Metallic Wedge of Acute Dihedral Angle*†

W. W. GRANNEMANN‡ AND R. B. WATSON
Department of Physics, University of Texas, Austin, Texas
(Received April 30, 1954)

In the rigorous theory of diffraction by a conducting wedge as developed by Sommerfeld and extended by Pauli, the total field is represented by the terms given by geometrical optics plus a contour integral which represents the diffracted waves. If the faces of the wedge form a dihedral angle of π/m, $m=1, 2, 3 \ldots$ the contour integral vanishes identically and the solution given by geometrical optics is exact. This prediction has been tested and checked by measurements and calculations of the diffraction patterns of wedges whose dihedral angles were 90° and 30°. The measurements were made at a wavelength of 1.25 cm.

THE problem of the diffraction of electromagnetic waves by a perfectly conducting wedge was solved by Sommerfeld.[1] An extension of the solution by Pauli[2] was used earlier to compute the diffraction from a narrow wedge,[3] leading to successful comparison between experiment and theory. The natural extension of the relations developed by Pauli leads to the following forms for the evaluation of the field for a wedge of acute dihedral angle:

$$v^*=\sum_N \exp[i\rho\cos(\varnothing+2\pi nN)]$$
$$\text{if } -\pi<-\varnothing+2\pi nN<+\pi$$
$$N=0, \pm1, \pm2, \cdots, \quad (1)$$

$$v_B=(1/2\pi n)\int_{D_1+D_2}\frac{\exp(i\rho\cos\beta)}{1-\exp[-i(\beta+\varnothing)/n]}d\beta. \quad (2)$$

To obtain a specific solution for the field for a particular wedge, these relations are substituted in the general form

$$u=v(\rho,\psi-\psi_0)\pm v(\rho,\psi+\psi_0), \quad (3)$$

where $v=v^*+v_B$ and the angles ψ, ψ_0 are illustrated in Fig. 1. The plus sign in Eq. (3) corresponds to the experimental H-plane patterns with the electric vector parallel to the line forming the wedge vertex, and the negative sign corresponds to the experimental E-plane patterns with the electric vector perpendicular to the wedge vertex line. In these equations $\rho=kr$ where $k=2\pi/\lambda$ and r is the radius vector measured in a plane normal to the wedge vertex; and $\pi n=2\pi-\theta$ where θ is the wedge angle as illustrated in Fig. 1. When the dihedral angle $(2\pi-\theta)$ of the wedge is an integral fraction of 180°, then $n=1/m$, where $m=1, 2, 3 \ldots$ and the integral in Eq. (2) vanishes identically. Thus the integrand of Eq. (2) becomes

$$\frac{\exp(i\rho\cos\beta)}{1-\exp[-i(\beta+\varnothing)m]}, \quad (4)$$

which is periodic in β with period 2π since m is an integer. The path of integration (D_1+D_2) is made up of two parallel parts, separated by a distance 2π; hence the value of the integrand is the same along the two parts, making the total integral vanish identically. Under these circumstances the only terms remaining in the expression for the field are the terms arising from Eq. (1); but these are the contributions which correspond to the terms based on geometrical optics.

For example, consider a wedge for which the diffracted wave vanishes, with $n=\frac{1}{2}$ or with a dihedral angle of 90°, as shown in Fig. 1. The space is divided into two regions by the direction of arrival of the incident wave; the several waves reaching region I are the incident wave, two waves each suffering a single reflection, and one wave suffering a double reflection. The theoretical analysis shows four terms arising from Eq. (3), since in accordance with Eq. (1) the allowed values of N are 0 and -1 for $n=\frac{1}{2}$, $\psi<\psi_0$, and $\varnothing=\psi-\psi_0$; and are

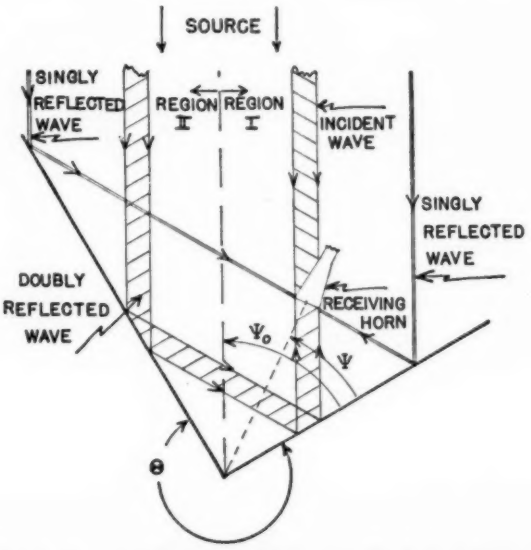

FIG. 1. Geometry for a wedge of acute dihedral angle.

* Much of the work presented herein is described in the doctoral dissertation by W. W. Grannemann, "Microwave diffraction by metal objects at 1.25 centimeters," University of Texas, June, 1953.

† This work was supported largely by the Defense Research Laboratory at the University of Texas.

‡ Now at the California Research Corporation, La Habra, California.

[1] A. Sommerfeld, Math. Ann. **45**, 263 (1894), and **47**, 317 (1896).
[2] W. Pauli, Phys. Rev. **54**, 924 (1938).
[3] R. B. Watson and C. W. Horton, J. Appl. Phys. **21**, 802 (1950).

0 and $+1$ for $\psi<\psi_0$ when $\varnothing=\psi+\psi_0$. These four terms are identified exactly with the incident and reflected waves in region I. By virtue of symmetry, a similar group of waves reaches region II, and the same theoretical expressions serve to describe these four terms.

It is clear that in general, as n is allowed to decrease smoothly from unity towards zero, a series of critical values given by $n=1/m$ will appear; at each critical value, the diffracted wave disappears and a new pair of reflected waves appears, corresponding to a new residue in the analysis. Counting the incident wave as well, the total number of waves for the dihedral angle of 90° has been shown to be four; this number increases (for example) to twelve when the angle is 30°.

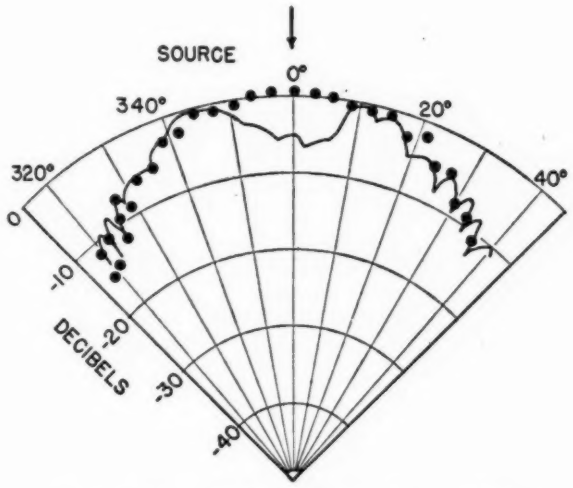

FIG. 2. Diffraction pattern for a 90° wedge: $\psi_0=45°$. H-plane. Solid curve, experiment; circles, theory.

Experimental diffraction patterns were obtained by rotating a detecting horn in a horizontal plane about the wedge vertex line as an axis, at the same time illuminating the wedge by an essentially plane progressive electromagnetic wave radiated from a pyramidal horn placed five meters from the wedge vertex. The receiving horn was kept at a distance of 15.5 cm from the wedge vertex. All data were taken at a wavelength of 1.25 cm, and all experiments were made on the roof of the physics building at the University of Texas. The receiving horn had a rectangular opening of 1.90 by 2.34 cm, or about 1.5 by 1.9 wavelengths. It subtended an angle at the center of rotation of 8.2° in the E-plane and 9.6° in the H-plane. The wedges used were hollow, and were constructed from two large copper sheets, each 30 in. by 60 in. by $\frac{1}{16}$ in. These sheets were supported on a wooden framework and were

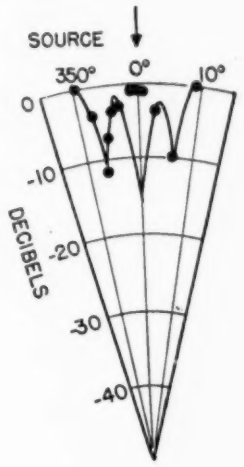

FIG. 3. Diffraction pattern for a 30° wedge: $\psi_0=15°$. H-plane. Solid curve, experiment; circles, theory.

stiffened to prevent bending and vibration with wind by means of dural stiffeners, in such a way as to bring the two edges of the sheets together to form a single line for the wedge vertex.

Typical diffraction patterns are shown in Figs. 2 and 3. Figure 2 shows both experimental and theoretical results for a 90° wedge, and Fig. 3 illustrates results for a 30° wedge. In both figures good agreement is obtained between theory and experiment except near 0°. For the 90° wedge, the receiving horn is sufficiently large that it shades the wedge vertex near 0° and reduces the intensity of the wave arriving by way of a double reflection. Because of the discrimination of the horn on account of its directional pattern against both the incident and the singly reflected waves, these doubly reflected waves control the magnitude of the received signal near 0°; it therefore should be expected that the experimental values lie below the computed values. Approximate calculations using reduced values of amplitude for the doubly reflected wave produced somewhat better agreement between theory and experiment. A similar argument applies to the data for the 30° wedge in Fig. 3.

It is concluded that the diffraction pattern from a wedge of dihedral angle equal to an integral fraction of 180° can be computed from terms corresponding to geometrical optics only. Experimental data are presented which confirm computations made on this basis.

ACKNOWLEDGMENT

The authors wish to acknowledge the invaluable advice and aid furnished by C. W. Horton in confirmation of the theoretical work, and in discussions on the entire problem.

Moderation of Neutrons in SiO_2 and $CaCO_3$*

JAY TITTMAN
Research Laboratory, Schlumberger Well Surveying Corporation, Ridgefield, Connecticut
(Received June 23, 1954)

The spatial distributions of indium resonance neutrons about a "point" Ra-Be source have been measured in pure $CaCO_3$ (limestone) and SiO_2 (sand) out to $r^2 \approx 9\tau$. Both media show nearly Gaussian distributions corresponding to Fermi ages $\tau(SiO_2) = 1906 \pm 90$ cm² and $\tau(CaCO_3) = 461 \pm 23$ cm² over most of the range observed. Excess resonance flux near the source, more pronounced in $CaCO_3$ than in SiO_2, appears to be due to inelastic scattering although such interpretation is not unambiguous. Space integrals indicate ~10 percent more absorption in $CaCO_3$ than in SiO_2 during moderation. Data were corrected for 4.5-hr activity, 54-min activation by high energy neutrons, and edge effects; consideration was given to the 3.9- and 9-ev In levels in defining the mean detection energy and to the nonmonoenergetic nature of the Ra-Be source in affecting the shape of the indium resonance spatial distribution.

I. INTRODUCTION

THE moderation of fast neutrons has been studied experimentally primarily in the media of interest in pile design[1] and shielding,[2] and for the purpose of examining source spectra and slow neutron resonance phenomena.[3] The present paper investigates how well age theory describes the moderation of Ra-Be neutrons to In resonance energy in two media of geologic interest, limestone ($CaCO_3$) and silica (SiO_2), and measures the effective ages, τ.[4]

The Boltzmann transport equation as applied to neutron moderation,[5] is usually written to imply (a) spherical symmetry (in the center-of-mass system) of the elastic scattering, (b) a lack of inelastic scattering, and (c) the neglect of chemical binding. Reduction to the Fermi age equation involves the further assumptions: (a) nearly isotropic collision density, (b) small fractional energy loss per collision, (c) slow variation of scattering mean-free-path, λ_s, with neutron energy, and (d) energy independence of ξ, the mean logarithmic energy loss per collision. For a point monoenergetic source in an infinite medium the well-known age solution for the isotropic component of the neutron flux per unit energy interval is

$$f = S\frac{\lambda_s}{\xi E}\frac{\exp(-r^2/4\tau)}{(4\pi\tau)^{\frac{3}{2}}}. \tag{1}$$

The second-order approximation in anisotropy and in energy dependence of the collision density[5] then corrects Eq. (1) by the factor

$$G = 1 + (4u)^{-2}F(r^2/\tau) \tag{2}$$

where

$$F(r^2/\tau) = a_1 - a_2(r^2/\tau) + a_3(r^2/\tau)^2, \tag{3}$$

and where $u = \ln(E_0/E)$ is the lethargy, and the a's are positive constants depending on the mass of the nuclei in the medium.

Age theory should fit $CaCO_3$ and SiO_2 quite well because of their relatively large average nuclear masses. Furthermore, chemical binding effects are negligible for In resonance detectors. However, strict comparison, even with second-order theory, is hampered by the broad energy spectrum of Ra-Be neutrons and by the perturbing effects of inelastic scattering.

II. EXPERIMENTAL APPARATUS AND TECHNIQUES

A 1.03 g Ra-Be source was used throughout these experiments. Earlier measurements using the same type of source in other media[6] indicate that a single age, corresponding to an average source energy of roughly 5 Mev, dominates the moderation process. From the work of Roberts, Hill, and McCammon[7] it is to be expected that the finite extension of the source ($\frac{3}{4}$ inch diameter by 1 inch high) does not perturb the In resonance neutron distributions in the present measurements.

One-inch diameter In foils, 99.97 percent pure and 104 mg/cm² thick, were exposed in Cd cassettes of 20-mil thickness. These were attached to the ends of long aluminum "swords" which were placed in $\frac{1}{16}$-inch wall aluminum "sheaths" in the silica or in slots milled in the limestone so that the foil centers were in the horizontal plane of the source. Experiments established that no significant 54-min activity was induced by the Ra γ-rays. Subsequent to subtraction of background,

* For preliminary reports see J. Tittman and F. F. Johnson, Phys. Rev. **91**, 452 (1953); J. Tittman, Phys. Rev. **95**, 660 (1954).

[1] D. J. Hughes, *Pile Neutron Research* (Addison-Wesley Press, Cambridge, Massachusetts, 1953); S. Bernstein, Phys. Rev. **73**, 956 (1948).

[2] A. M. Munn and B. Pontecorvo, Can. J. Research **A25**, 157 (1947); P. C. Gugelot and M. G. White, Phys. Rev. **74**, 1215 (1948). See also reference 6.

[3] E. Amaldi and E. Fermi, Phys. Rev. **50**, 899 (1936); Amaldi, Hafstad, and Tuve, Phys. Rev. **51**, 896 (1937); R. D. O'Neal, Phys. Rev. **70**, 1 (1946); J. H. Rush, Phys. Rev. **73**, 271 (1948).

[4] Throughout this paper experimental τ's refer to the parameters in the best fitting Gaussians; calculated τ's are evaluated from $\tau = \frac{1}{6}\int_0^u [\lambda_s^2 du/\xi(1-\langle\cos\theta\rangle_{Av})]$.

[5] R. E. Marshak, Revs. Modern Phys. **19**, 185 (1947); Marshak, Brooks, and Hurwitz, Nucleonics, **4**, No. 5, 19; **4**, No. 6, 43; **5**, No. 1, 53; **5**, No. 2, 59 (1949).

[6] Dacey, Paine, and Goodman, Technical Report No. 23 (Laboratory for Nuclear Science and Engineering, Massachusetts Institute of Technology, 1949); C. W. Tittle, Ph.D. thesis, Massachusetts Institute of Technology, 1948; B. T. Feld, MDDC-1437; E. Fermi, *Nuclear Physics* (University of Chicago Press, Chicago, 1950), revised edition, p. 191.

[7] Roberts, Hill and McCammon, Phys. Rev. **80**, 6 (1950).

TABLE I. Properties of the moderating media.

Composition	Density (g/cm³)	Size	Purity	Principal impurities
$CaCO_3$	2.72±.01	5-ft cube	>98%	Al—0.1% Mg—0.6% Fe—0.05% Organic—0.06% Si—0.1% H_2O—<0.008%
SiO_2	1.61±.02	8-ft cube	99.89%	Fe—0.0X% H_2O—<0.007%

which was <10 percent of the total counting rate for all foil positions except those farthest from the source, the measured activities were corrected to zero time and front-and-back counting rates were averaged to give A_{54}, one-half the 54-min saturation activity. Since the two media were studied one year apart, a 2.8 percent adjustment was made to one of the sets of data to compensate for decay of a Sr^{90} source used as a reference.

The limestone moderator consisted of ground Vermont marble blocks (see Table I), most of which were eon-foot cubes, the remainder being 1 ft by 1 ft by 3 in. A $\frac{3}{4}$-inch hole was drilled vertically through the central column for insertion of the source. During all exposures, this hole was filled with a thin-walled aluminum tube packed with limestone powder to reduce the effect of this inhomogeneity in the medium. Density and spectrographic analyses showed a high degree of homogeneity as well as the absence of any impurities which might affect the slowing-down properties.

The silica moderator consisted of an 8-foot cubical pit filled with silica sand (see Table I). Thin-walled aluminum tubes were shaped to provide $\frac{3}{16}$-inch thick sheaths running vertically through the medium. In agreement with Kolbuszewski,[8] there exists continuous variation in density of the poured sand from bottom to top, ranging from 1.63 to 1.59 g/cm³, with a median plane value of 1.61 g/cm³. Extensive examination of the sand indicated negligible adsorbed moisture. All exposures were made with a thin-walled tube of sand resting on the source to minimize inhomogeneity of the medium.

III. CORRECTIONS

The counting rate data were normalized to the Sr^{90} reference source and experimentally corrected for the 4.5-hr activity induced by γ-rays[9] and high-energy neutrons.[10] In both media this correction was found to be negligible for $r^2 > \tau/2$.

The 54-min activation cross section extends into the Mev region[11] so that activation by high-energy neutrons can affect "resonance" distributions, particularly in the vicinity of the source. Roberts, *et al.*[7] have corrected for this effect, using data taken with Cd and with Cd+In

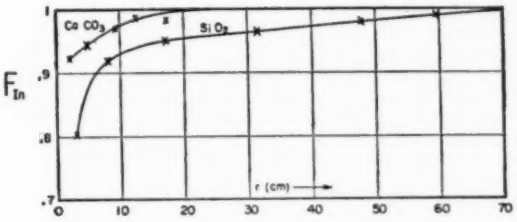

FIG. 1. The experimental correction factor, F_{In}, for high energy neutron 54-min activation. See Eq. (4).

absorbers surrounding the detector, by means of the relation

$$A_{54}(r,u) = A_{Cd}(r)\left\{\frac{1-\left(\frac{A_{Cd+In}}{A_{Cd}}\right)_r}{1-\left(\frac{A_{Cd+In}}{A_{Cd}}\right)_{r'}}\right\} \equiv A_{Cd}(r)F_{In}, \quad (4)$$

where r is the position of the foil, r' is some distance from the source sufficiently large to insure negligible contribution to the 54-min activity from high energy neutrons, and u is the lethargy corresponding to In resonance. Equation (4) assumes that the only effective resonance is at 1.46 ev. It is now known that the 3.9 ev and 9.2 ev resonances are also due to In^{115} and lead to this activity.[12] However, estimates of the effect of these other levels on the present measurements indicate that it is quite small. (See Appendix.) We have thus ignored the presence of these levels in making the correction.

Figure 1 shows the experimental values of F_{In} as a function of position for the two media. In neither moderator does the value of the dominant τ depend critically upon the points thus corrected. However, appreciably better fit of Eq. (1) to the data at small distances is brought about by taking this effect into account.

The first-order correction to age theory, expressed by Eq. (2), was calculated for a range of mass values and is shown in Fig. 2. We assumed $E_0 = 5$ Mev and $E = 1.5$ ev in evaluating u; appropriate averages over nuclei and energy were taken in determining the effective masses $M(CaCO_3) = 18.9$ and $M(SiO_2) = 18.7$.

The $CaCO_3$ pile was assembled on the floor of a large room, far from all walls. Since the source and detectors were in the median plane, the concrete floor had no effect on the data. However, the two foils farthest from the source on either side were sufficiently close to the surface to be affected by the loss of neutrons into the room. The two circled experimental points of Fig. 3 were thus moved upward by 4.6 and 2.7 percent for the smaller and larger r, respectively. The corrections were

[8] J. Kolbuszewski, Research (London) **3**, 478 (1950).
[9] Collins, Waldman, Stubblefield, and Goldhaber, Phys. Rev. **55**, 507, 1129 (1939).
[10] S. G. Cohen, Nature **161**, 475 (1948); A. A. Ebel and C. Goodman, Phys. Rev. **93**, 197 (1954); Martin, Diven and Taschek, Phys. Rev. **93**, 199 (1954).
[11] *Neutron Cross Sections*, AECU-2040, (Office of Technical Services, Department of Commerce, Washington, D. C., 1952); Hughes, Garth, and Levin, Phys. Rev. **91**, 1423 (1953).
[12] V. L. Sailor, Phys. Rev. **87**, 222 (1952); V. L. Sailor and L. B. Borst, Phys. Rev. **87**, 161 (1952).

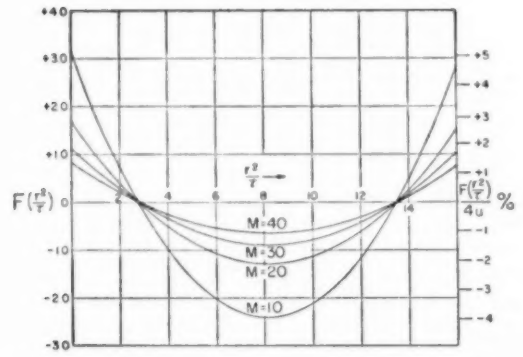

FIG. 2. First-order correction to age theory for several nuclear masses. Left-hand scale is the function of Eq. (3) which depends only on r^2/τ for given M; right-hand scale is percent correction for present measurements, using $u=15.1$.

calculated from the ratio of the age theory predictions of the slow neutron fluxes in infinite and finite media.[13]

The silica moderator was in a cubical pit, surrounded on five sides by cement walls backed by earth. The source and detectors were located in the median plane, about 4 feet from the cement bottom and an equal distance from the open surface. Experiments revealed no measurable edge effects in this medium.

IV. RESULTS

Indium resonance neutron distributions, extending to $r^2 \approx 9\tau$, are shown in Fig. 3. In each medium a single τ is adequate to describe the distribution, within the experimental error, except in the immediate vicinity of the source. The excess of resonance neutrons at small r in $CaCO_3$ can be ascribed to a component ($\tau \lesssim 100\ cm^2$) of $\lesssim 1$ percent strength in the source spectrum.[14] In SiO_2, the fit at $r^2 < 300\ cm^2$ can be improved somewhat by assuming a low energy component of $\tau \lesssim 100\ cm^2$ and strength $\lesssim 0.1$ percent. The presence of a low energy component in the source spectrum is consistent with the results of other investigators.[6,15] However, their reported strengths or upper limits on strengths are considerably larger. Some of the earlier work did not include the correction of Eq. (4) which may account for at least part of this difference. In the present measurements, however, this component must be considered purely empirical since it is not known whether the smaller τ's in the two media correspond to the same source energy. Furthermore, the fact that the low-energy source strengths required in $CaCO_3$ and in SiO_2 differ by an order of magnitude indicates that the excess resonance flux at small r depends upon the slowing-down medium to an appreciable extent.

The experimental result that Ra-Be neutrons produce Gaussian spatial distributions in these media despite their broad energy spectrum[15,16] is to be expected theoretically. From Eq. (1) the spatial distribution of neutrons of energy E about a nonmonoenergetic source is proportional to

$$\int \frac{dS(\tau)}{d\tau} \frac{\exp(-r^2/4\tau)}{\tau^{\frac{1}{2}}} d\tau,$$

where we see that the source spectrum-in-τ is required rather than the specturm-in-E_0. Now the fractional width of the Ra-Be spectrum-in-τ for most moderators will be smaller than that for the spectrum-in-E_0 by roughly the factor[4] $\lambda_s^2/[3\xi(1-\langle\cos\theta\rangle_{Av})\tau_0]$ where τ_0 is evaluated at the peak of the E_0 spectrum. Qualitatively one can see, for example, that all neutrons in a source spectrum which has a lower cut-off at, say, 1 Mev

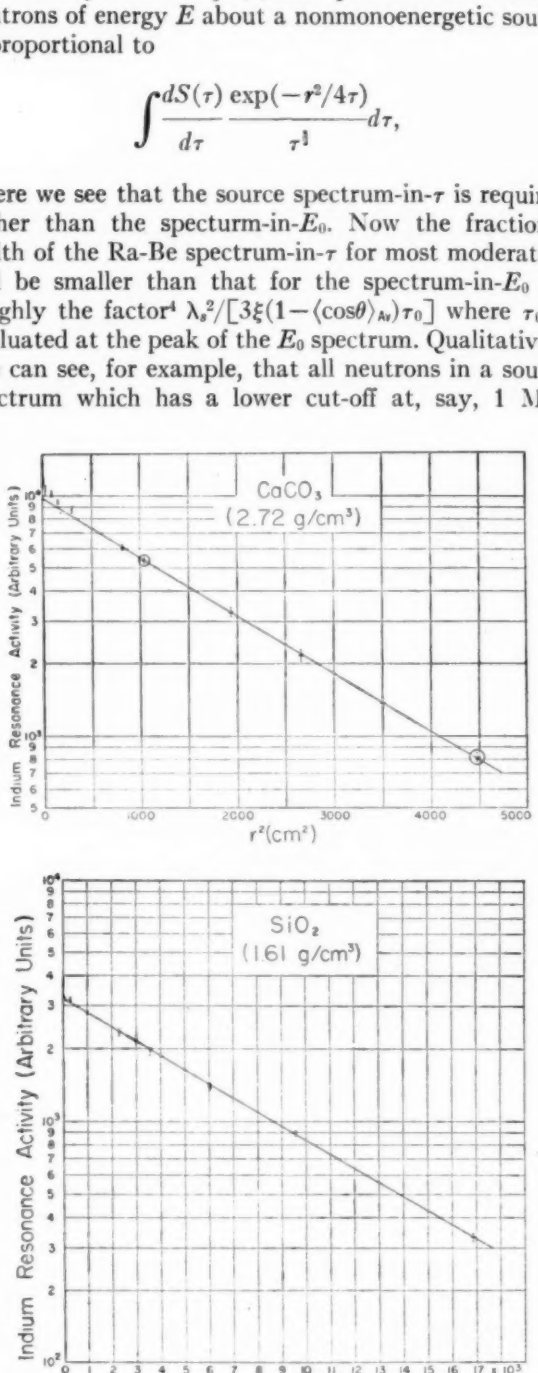

FIG. 3. Indium resonance neutron distributions in SiO_2 and $CaCO_3$. Vertical bars represent standard deviations of several independent measurements; horizontal bars are estimated uncertainties in r^2. Solid curves are age theory Gaussians corrected by Eq. (2) and fit to last six experimental points in $CaCO_3$ and last five in SiO_2. Circled points were corrected for edge effects.

[13] P. R. Wallace and J. Lecaine, *Elementary Approximations in the Theory of Neutron Diffusion*, MT-12 (National Research Council of Canada, Chalk River), p. 63.

[14] The larger value of the source strength given in a preliminary report was due to a numerical error.

[15] Yalow, Yalow, and Goldhaber, Phys. Rev. 69, 253 (1946); D. L. Hill, AECD-1945.

[16] P. Demers, MP-204, Natl. Research Council of Canada Ann. Rept.

suffer energy degradation in common over roughly six decades in E. Hence, if the upper E_0 cut-off of the spectrum is at ~10 Mev, the fractional width of the spectrum-in-τ is of the order 1/7 while that of the spectrum-in-E_0 is of the order unity. A detailed calculation of the expected spatial distribution of In resonance neutrons in $CaCO_3$ about a Ra-Be source yields a Gaussian (to within better than one percent from $r^2=0$ to $r^2=9\tau_0$) having a τ slightly smaller than τ_0. An average of the data of Hill[15] and Demers[16] was taken for the source spectrum-in-E_0. It can be shown rather generally[17] that for a source spectrum-in-τ describable by a peak at τ_0 and a width w, a Gaussian spatial distribution results for $(r^2/\tau_0)^2 \ll 256(\tau_0/w)^2$, a condition which is satisfied easily by the present measurements.

Table II lists the measured dominant τ's for the two media, as well as the calculated[18] values for an assumed $E_0=5$ Mev. Wherever a gap in the cross-section data exists, a smooth connection to data on either side of the gap was made. Further, in the cases of Si and Ca, averages over resonances were used to smooth out $\lambda_s(E)$; in all cases it was assumed that $\lambda_{\text{total}}=\lambda_s$. Because of these approximations, and the likelihood that the appropriate $E_0 \neq 5$ Mev, it is questionable whether the SiO_2 difference is significant. In view of the larger discrepancy in the case of $CaCO_3$, however, it is possible that at least part of the difference is due to inelastic scattering which can reduce the effective age. A further possible manifestation of inelastic scattering is the introduction of an apparent component in the source having a smaller τ than the dominant component. This could account qualitatively for the excess resonance flux at small r in $CaCO_3$ and also explain the apparent dependence of the strength of the low-energy component in the source upon the moderator. The difficulty in making a unique assignment of causes for these effects arises from the lack of exact knowledge of the Ra-Be source spectrum and inelastic scattering data.

The coefficient $(4\pi\tau)^{-\frac{3}{2}}$ in Eq. (1) arises from normalization, since the absence of absorption in the medium requires the space integral of the slowing-down density to equal the source strength. Since the same source and foils were used in both media, we should expect

$$\frac{B(CaCO_3)}{B(SiO_2)}=\frac{(\lambda_s/\xi)_{CaCO_3}}{(\lambda_s/\xi)_{SiO_2}}, \tag{5}$$

where $B=\int_0^\infty r^2 A_{54}dr$ and λ_s and ξ are evaluated at the detection energy. The B's were determined by extending the experimental data to infinity using Eq. (1) and the experimental τ's of Table II. It should be noted that the data at small r, which are subject to the largest corrections, contribute only weakly to the total area because of the r^2 factor in the integrand.

TABLE II. Measured and calculated slowing-down parameters.

Parameter	Measured	Calculated[a]
$\tau(SiO_2)$ (cm²)	1906±90	2130
$\tau(CaCO_3)$ (cm²)	461±23[b]	560
$\frac{B(CaCO_3)}{B(SiO_2)}$[c]	0.36	0.43

[a] Assumes $E_0=5$ Mev, $E_{det}=1.6$ ev (see appendix).
[b] The slight discrepancy between this value and that of an earlier report is caused by the introduction of the correction factor $G(u,r^2/\tau)$ of Eq. (2)
[c] $B=\int_0^\infty r^2 A_{54}dr$.

A comparison of the experimental left-hand side of Eq. (7) with the computed[18] right-hand side yields a measure of the relative integrated absorption in the two media. The values thus obtained are listed in Table II, where we note that $CaCO_3$ shows a 14 percent reduction in In resonance flux relative to that of SiO_2. A calculation of $\exp[-\int_0^u \sigma_a/(\sigma_s\xi)du]$[19] for both media, using an assumed $1/v$ absorption normalized to the known thermal values, accounts for only about 2 percent of the measured effect. The remainder is presumably due to excess resonance absorption in $CaCO_3$ during the slowing down process. Although the appropriate λ's are not known with high accuracy,[18] it seems unlikely that the remaining discrepancy is due to errors in these quantities.

ACKNOWLEDGMENTS

The author wishes to thank the Schlumberger Well Surveying Corporation for permission to publish these results. The measurements and calculations were carried out with the assistance of F. F. Johnson and A. H. Heim. Cooperation of the Vermont Marble Company is gratefully acknowledged.

APPENDIX

Indium Resonance Detection Energy

Since the recent work of Sailor[12] has shown that several In resonances contribute to the 54-min activity, it is of interest to examine how this affects the average energy at which neutrons are detected in these measurements. For this purpose, we took the average detection energy to be

$$\langle E\rangle_{Av}=\frac{\int_0^{10ev} Ef(r^2,E)T_{Cd}[1-T_{In}(E)]dE}{\int_0^{10ev} f(r^2,E)T_{Cd}[1-T_{In}(E)]dE},$$

where f is the age theory flux, T_{Cd} is the transmission through the Cd cassette, and T_{In} is the transmission of

[15] J. Tittman (unpublished).
[18] Cross sections were taken from E. Melkonian, Phys. Rev. **76**, 1750 (1949); Rainwater, Havens, Dunning, and Wu, Phys. Rev. **73**, 733 (1948); Havens, Rainwater, Wu, and Dunning, Phys. Rev. **73**, 963 (1948); AECU-2040. (See reference 11.)
[19] See reference 6, E. Fermi, p. 184.

the In detector foil. In the calculation of T_{In}, twice the measured foil thickness was used to account for the isotropic nature of the flux in which the foils were placed; also the potential scattering cross section was subtracted from the total cross section[20] for In so that $[1-T_{In}(E)]$ is a fairly good representation of the activability of the foils. Since the quality of the slow neutron flux changes with r, it is apparent that $\langle E\rangle_{Av}$ is r dependent. Thus $\langle E\rangle_{Av}$ was evaluated in each medium at $r=0$ and at the r corresponding to the farthest foil. The results are the same for both media to within the precision of the calculation: $r^2=0$, $\langle E\rangle_{Av}=1.80$ ev and $r^2\approx 9\tau$, $\langle E\rangle_{Av}=1.73$ ev. The larger value at $r=0$ is to be expected since the flux in the vicinity of the source is richer in the higher energy neutrons. Actually, the values given above represent rough upper limits on $\langle E\rangle_{Av}$ since no account has been taken of the relative detectability of β-rays originating at different depths in the foil. This latter effect will tend to weight more strongly the importance of the 1.46 ev level. We have thus arbitrarily assumed that the present measurements refer to an energy of approximately 1.6 ev rather than 1.46 ev, corresponding to a reduction in τ by slightly less than one percent in both media.

[20] A detailed experimental curve of $\sigma(E)$ for In was kindly provided by V. L. Sailor.

JOURNAL OF APPLIED PHYSICS VOLUME 26, NUMBER 4 APRIL, 1955

Re-Examination of the Nonsteady Theory of Jet Formation by Lined Cavity Charges*†

R. J. EICHELBERGER
Department of Physics, Carnegie Institute of Technology, Pittsburgh, Pennsylvania
(Received May 26, 1954)

A new type of analysis is applied to observations on jets from lined cavity charges in order to test the nonsteady-state hydrodynamic theory of a jet formation. The results support previous findings that the theory is qualitatively accurate, but give evidence of departures from the ideal situation assumed in the theory. An attempt is made to assess one of the more likely sources of error, the neglect of acceleration of the liner.

SUMMARY OF THE THEORY AND PREVIOUS TESTS

THE nonsteady theory of jet formation[1] is based on the same steady-state hydrodyanmical concepts of streamline flow used by Taylor and Birkhoff in the original steady-state theory.[2] The conservation laws lead to the same equations for jet velocity, jet mass, and other jet characteristics, for a given set of conditions at the stagnation point where the jet is being formed. The important equations are

$$\sin\delta=\frac{V_0\cos\alpha}{2U_D}\ \text{(Taylor's relation)};\qquad(1)$$

$$V_j=V_0\csc\beta/2\cos(\alpha+\delta-\beta/2);\qquad(2)$$

$$dm_s/dm=\cos^2\beta/2;\qquad(3)$$

$$dm_j/dm=\sin^2\beta/2.\qquad(4)$$

δ is the angle between the direction an element of the liner travels after being struck by the detonation wave and the normal to the liner surface; V_0 is the velocity at which the liner element travels toward the axis; α is the half-angle of the conical liner; U_D, the detonation rate of the explosive; V_j, the velocity of the jet element formed; β, the angle between the collapsing liner wall and the axis; m_s, the mass of the slug; m_j, the mass of the jet; and m, the mass of the liner. The masses m_s, m_j, and m are each functions of x. The mass m is that part of the mass of the liner that is included between the top (apex) ($x=0$) of the cone and the plane perpendicular to cone axis at $x=x$. The masses m_s and m_j are the parts of m that end up in the slug and the jet respectively. Except for the differential form of Eqs. (3) and (4), these are identical with the results of the steady-state theory, but all parameters except α and U_D vary with x, the original position of the liner element. The essential difference between the original and the nonsteady theories lies in the fact that variations of V_0 that are taken into account in the latter make the collapsing liner assume a far more complex form, and β, instead of being a constant given by

$$\beta=2\delta+\alpha=\alpha+2\sin^{-1}(V_0\cos\alpha/2U_D),\qquad(5)$$

is variable and is given as a function of x by the far more complex formula

$$\tan\beta=\frac{\sin(2\delta+\alpha)-x\sin\alpha(1-\tan\delta\tan[\alpha+\delta])V_0'/V_0}{\cos(2\delta+\alpha)+x\sin\alpha(\tan[\alpha+\delta]+\tan\delta)V_0'/V_0},\qquad(6)$$

where $V_0'=dV_0/dx$.

* Submitted in partial fulfillment of the requirements for the degree of doctor of philosophy at Carnegie Institute of Technology.

† This work was performed under research contract with the Office of the Chief of Ordnance, U. S. Army, and with the Ballistic Research Laboratories, Aberdeen Proving Ground.

[1] Pugh, Eichelberger, and Rostoker, J. Appl. Phys. **23**, 532 (1952).

[2] Birkhoff, MacDougall, Pugh, and Taylor, J. Appl. Phys. **19**, 563 (1948).

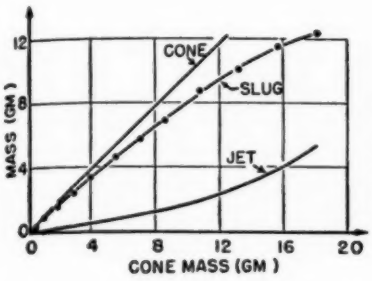

FIG. 1. Mass of slug section as a function of mass of parent liner section. Jet mass is estimated by subtracting observed slug mass from observed cone mass.

In the previous test of the theory,[3] experimental observations of jet mass and velocity were combined with slug mass data to deduce the values of V_0 for various liner elements. Values of β computed from Eq. (6) were then compared with those obtained directly from slug mass data by means of Eq. (3) as a test of the theory. While this procedure is entirely valid, it involves a very difficult and not too precise experiment for the correlation of jet mass and velocity.

A more direct approach would be to measure V_0 directly, but the experimental techniques to accomplish this are extremely difficult and such measurements appear to be still well in the future. An alternative method is to determine β as a function of x by means of slug mass measurements[3] and Eq. (3) and solve the differential equation (6) for V_0. The latter procedure is the one to be described below.

DETERMINATION OF COLLAPSE ANGLES

The slug masses have been redetermined by refined, more precise techniques. The results are shown in Fig. 1. The experimental curve was fitted with a polynomial equation by Birge's method[4] and the polynomial differentitated to obtain values of dm_s/dm and thence, by means of Eq. (3), values of β were obtained. The resulting curve is shown in Fig. 2. It will be noted that this curve is slightly different from that reported previously.[3] There is no systematic difference between the two sets of slug mass measurements, but the slopes are very sensitive to any change in the shape of the experimental curve.

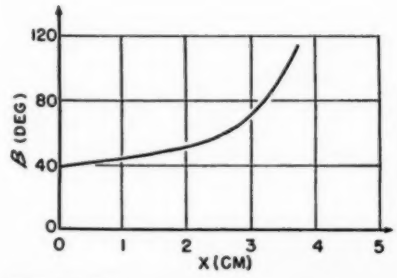

FIG. 2. Collapse angle β as a function of initial position of liner element, measured from top of cone.

[3] R. J. Eichelberger and E. M. Pugh, J. Appl. Phys. **23**, 537 (1952).

[4] Raymond T. Birge, Revs. Modern Phys. **19**, 298 (1947).

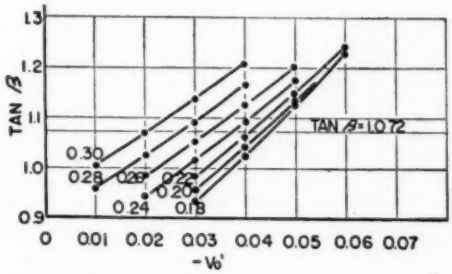

FIG. 3. Illustration of first step in graphical solution. Each curve represents the indicated value of V_0; horizontal line indicates experimental value of tanβ at $x=1.6$ cm.

SOLUTION OF $\tan\beta = f(V_0, V_0')$

Lacking a closed solution of Eq. (6), we resort to a graphical solution. For each value of x at regularly spaced intervals, the value of β is taken from Fig. 2. A series of computations are then made for arbitrarily chosen values of V_0 and of V_0' [δ is evaluated for each V_0 by using Eq. (1)]; the values of tanβ are plotted as functions of V_0' for each value of V_0, as illustrated in Fig. 3. The intersection of each of the resulting families of curves with a horizontal line, representing the experimentally determined β, then represents a combination of V_0 and V_0' that is compatible with the value of β obtained at that value of x. The compatible combinations are then plotted as shown in Fig. 4. The condition required to determine V_0 as a function of x is that

$$\int_{x_1}^{x_2} V_0' dx = V_0(x_2) - V_0(x_1). \tag{7}$$

For the present purpose, we can obtain a sufficiently accurate result by using the approximate form

$$V_0(x_2) \doteq V_0(x_1) + \frac{V_0'(x_2) + V_0'(x_1)}{2}(x_2 - x_1), \tag{8}$$

provided small enough intervals of x are used. Equation (8) is a linear relation between $V_0(x_2)$ and $V_0'(x_2)$, if $V_0(x_1)$ and $V_0'(x_1)$ are known. The point at which the line representing this relation intersects the curve of

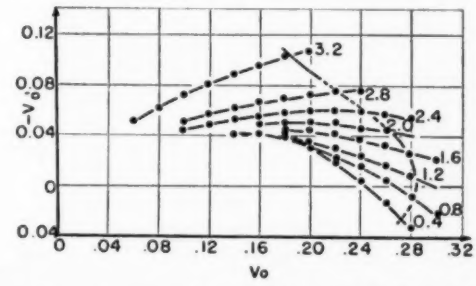

FIG. 4. Curves representing combinations of V_0 and V_0' compatible with the experimentally observed values of β at the indicated values of x. Broken line connects values that are found to be mutually compatible and to yield agreement with observed initial conditions.

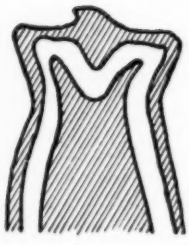

FIG. 5. Photograph of sectioned slug from a bimetallic cone (copper, steel), and sketch of apex end, illustrating evidence of departure from ideal in initial stages of linear collapse.

V_0' *vs* V_0 for x_2 represents a uniquely determined combination of V_0 and V_0' at x_2 that is compatible with the values at x_1. Thus, if either V_0 or V_0' is known for any one position on the liner, all other values can be determined from slug mass measurements. The evaluation of an initial pair amounts to determining the constant of integration, which can be accomplished by an experimental investigation of the initial conditions of liner collapse.

DETERMINATION OF INITIAL CONDITIONS

It would perhaps seem natural to assume that the tip of the jet is formed by the very top of the liner. This has been commonly assumed and would suffice to complete the solution of Eq. (6). There is evidence, however, that the initial stages of collapse are considerably perturbed, at least for flat-topped liners of the type used in these investigations. For example, a sectioned slug from a cone composed of a thick inner layer of copper, a thick layer of steel, and a thin outer layer of copper, is shown in Fig. 5. The jet, of course, was made up of copper from the inner layer, the remainder of which comprises the core of the slug. There is clear evidence that the flat top was forced inward by the pressure of the explosion. Tiny jets traveling backward have been observed in such cases, and the process must certainly interfere with the idealized collapse assumed in the theory.

In order to determine what portion of the liner does produce the front of the jet, we must again resort to the theory. If we assume that the liner element at a point $x_0>0$ is the parent of the front of the jet, and that this liner element approaches the axis at velocity V_0, forming a jet element of velocity V_j, the time between the arrival of the detonation wave and the arrival of the front of the jet at the base of the charge will be given by

$$T=\frac{a+x_0\tan\alpha}{V_0\cos(\alpha+\delta)}+\frac{h-x_0-(a+x_0\tan\alpha)\tan(\alpha+\delta)}{V_j}-\frac{h-x_0}{U_D}, \quad (9)$$

where a is the radius of the flat top of the cone, h is the height of the liner. The value of T can be determined directly by experiment. For the charge used in this investigation, the mean value was found to be

$$T=1.51\ \mu\text{sec}\pm 0.05.$$

Since the velocity of the front of the jet is known, the only remaining unknown quantities in Eq. (9) are x_0 and V_0. But for any value of x there is another restriction, represented by Eq. (2), which, with the values of β from Fig. 2, fix the value of V_0 that must be associated with any value of x to produce the observed V_j. Between the two conditions, then, it is possible to unambiguously determine the values of both x_0 and the associated V_0. The compatible value of V_0' can be determined as illustrated in Figs. 3 and 4, thus completing the determination of an initial set of values.

Under the idealized conditions assumed thus far, the results indicate that the tip of the jet is formed by a liner element initially at a point 0.52 cm from the top of the cone, and the value of V_0 for that element is estimated to be 0.255 cm/μsec. The position appears

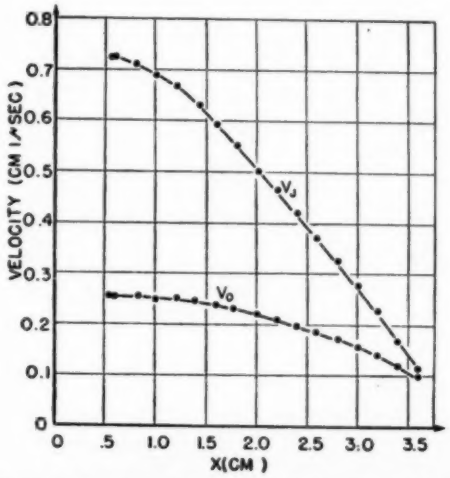

FIG. 6. Computed values of collapse velocity V_0 and jet velocity V_j as functions of initial position of liner element.

quite reasonable from the qualitative observations on initial conditions and the V_0 is in good agreement with observations of the velocity of liners propelled by two-dimensional charges under comparable conditions of charge and liner geometry.

The fact that all further computations depend upon the evaluation of initial conditions causes some concern about the validity of the simplifying assumptions involved in the theory. The effect of a finite acceleration time is considered in detail below. The assumptions of constant velocity and direction of collapse for the liner element and of constant velocity of the jet element can produce only very slight errors so long as this procedure is applied only to the tip of the jet. It is also found that the final results are relatively insensitive to changes in the value of x_0 because of the relatively small departures from the ideal steady state during early stages of jet formation.

CALCULATION OF COLLAPSE VELOCITY, JET VELOCITY

The values of the collapse velocity obtained by carrying out the complete calculation outlined above are plotted as a function of position on the liner in Fig. 6. The values of jet velocity calculated by use of Eq. (2) are also shown. Comparison with the similar curves obtained previously for the same charge[3] shows only slight quantitative differences. There is a definite tendency for both the collapse velocity and the jet velocity to decrease more rapidly from the top of the liner toward the bottom in the newer estimates, because of the difference in the new values of β obtained from the new slug mass measurements.

COMPARISON OF CALCULATED AND OBSERVED VELOCITY AND MASS DISTRIBUTIONS

Having determined the collapse velocities and jet velocities associated with each liner element, as well as the position of the tip of the jet relative to the detonation wave, we can calculate the position of any jet element at an arbitrarily chosen time. Thus, a prediction of the spatial distribution of velocities in the jet can be computed and compared with experimental observations.[3] The results of such a comparison are shown in Fig. 7. A relatively very early time has been deliberately chosen for the comparison in order to exaggerate the differences. At later times, both distributions would be very nearly linear with slopes approaching the reciprocal of the time, and the discrepancies would be relatively much smaller. As is evident in the plot, there is a small, systematic discrepancy between the predicted and the observed distributions. While the difference is certainly not much greater than the errors to be expected of the analysis, it seems that there is at least a small, real error. Consideration of possible sources of error in the experimental observations and in the simplifying assumptions leads, at present, to no conclusion as to the most likely cause.

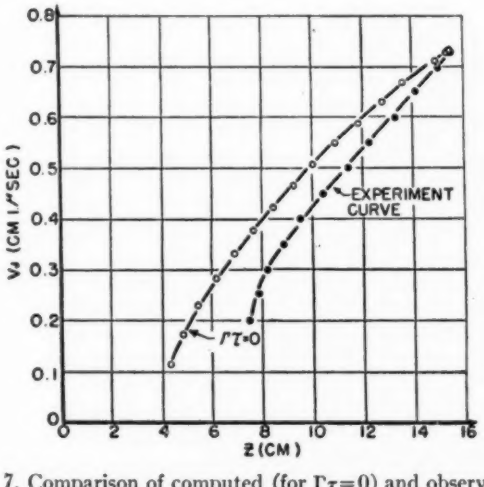

FIG. 7. Comparison of computed (for $\Gamma\tau=0$) and observed distribution of velocities in the jet 35 μsec after initiation of the charge. The early time is chosen in order to exaggerate the discrepancy.

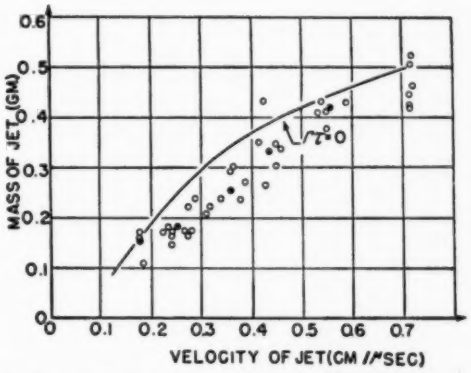

FIG. 8. Comparison of computed distribution of mass in the jet with experimental observations. Curve is computed from slug mass data.

By combining the cone and slug mass measurements from Fig. 1, one can estimate the mass of jet ($m_j=m-m_s$) contributed by each part of the cone. This, together with the computed jet velocities, suffices to calculate the distribution of mass in the jet, which has also been observed experimentally.[3] A comparison of the predicted and observed distributions is shown in Fig. 8. Again, a small but systematic difference is observed. Since the mass of the jet is observed as a function of jet velocity, the error may well be connected with that in the velocity distribution, and probably has no additional significance.

EFFECT OF FINITE ACCELERATION TIME

One of the simplifying assumptions used in the theory and in the above analysis whose effect on the results can be easily determined is the assumption of impulsive acceleration of the liner when it is struck by the detonation wave. Theoretical treatments of the acceleration of an inert liner by an explosive charge, based on shock wave theory, have been carried out for one-dimensional

situations. They are of no use here, however, because they predict much longer acceleration times than are observed for conditions comparable with those encountered in the charges concerned. The available experimental observations also fail to provide a good estimate of the acceleration time or of the rate of acceleration, but they do fix an upper limit of 2 μsec for the acceleration time of at least the upper part of the liner. The actual value is more likely of the order of 1 μsec or less.

The first concern in considering the effect of acceleration time is whether or not a given liner element attains its final velocity (or a velocity sufficiently close to it) before entering the stagnation point at the axis. Fortunately, the values of acceleration time and of collapse velocity that apply in the present case indicate that every liner element will have attained its terminal velocity before reaching the axis. This is one advantage of the flat-topped cone used. Under these circumstances, it is permissable to ignore the details of the acceleration period. We need only use the time τ during which appreciable acceleration occurs, and the average velocity during the period of acceleration, for which we shall use $(1-\Gamma)V_0$. The parametric equations for a liner element at a time after its acceleration period but before it reaches the axis, are

$$z=x+V_0\sin(\alpha+\delta)\left[t-t_0-\frac{x}{U_D}-\Gamma\tau\right] \tag{10}$$

and

$$r=a+x\tan\alpha-V_0\cos(\alpha+\delta)\left[t-t_0-\frac{x}{U_D}-\Gamma\tau\right], \tag{11}$$

where z and r locate the liner element in a cylindrical coordinate system at a time t after initiation of the charge; t_0 is the time required for the detonation wave to reach the top of the liner. The equations apply only during the time interval after the acceleration ceases and before the element reaches the axis. We have assumed that the liner element follows the direction of the vector V_0 even during the acceleration period. Evaluating $\tan\beta$ by means of[1]

$$\tan\beta=\left.\frac{dr/dx}{dz/dx}\right]_{\tau=0}, \tag{12}$$

we obtain

$$\tan\beta=\frac{N+V_0\cos(\alpha+\delta)\cdot(\Gamma\tau)'}{D-V_0\sin(\alpha+\delta)\cdot(\Gamma\tau)'}; \tag{13}$$

the primes indicate differentiation with respect to x; N and D are, respectively, the numerator and the denominator of Eq. (6). Unless $\Gamma\tau$ depends on x, neither the collapse angle nor any of the characteristics of the jet is affected by the finite acceleration time. In this case, only the time at which the jet element having a given velocity is observed at a given position is altered. The velocity distribution plot shown in Fig. 7 would still be valid, but would represent conditions at a time $\Gamma\tau$ later than indicated. For any reasonable acceleration time, the change would be very small. If a correction were applied, it would be in such a direction as to increase the discrepancy between theory and and experiment.

If $\Gamma\tau$ does depend on x for the charge configuration considered, the computed values of the collapse velocity and of the jet velocity may vary over a wider range. By suitable arbitrary choices of $\Gamma\tau$ and $(\Gamma\tau)'$ the agreement between the computed and observed distribution of mass in the jet can be improved, although the distribution of velocities is not significantly changed for any reasonable values. We shall not present any detailed results here because of the lack of any basis, at present, for specific values of the parameters. We are concerned only with the conclusion that the comparison of the theory with experimental observations in the preceding sections, in which the acceleration of the liner was completely neglected, would not be appreciably affected by the approximation used.

CONCLUSIONS

The results of the re-examination of the experimental test of the theory of jet formation support completely the earlier conclusions.[3] The approach used in the more recent analysis is completely different from that used earlier, and the primary experimental observations (i.e., the slug mass measurements) are new and more precise. The results differ slightly, quantitatively, from those published earlier, and expose what appears to be a systematic discrepancy between predicted and observed values of jet velocity. The difference, while very small, appears to be real. An attempt has been made to assess one of the more obvious approximations used in the theory, the neglect of the acceleration of the liner by the products of detonation. While the acceleration can be treated only in a qualitative manner, it seems unlikely that the observed discrepancy is due entirely, or even largely, to the acceleration. Other probable sources of error, which include interactions within the liner during collapse, interactions within the jet after its formation, and errors in the basic hydrodynamic pictures due to the nonsteady character of the phenomenon, have yet to be evaluated.

The author is indebted to E. M. Pugh for encouragement and support in carrying out this work.

Relation to Diffusion Measurements of Some Beta-Ray Absorption Phenomena*

A. E. BERKOWITZ†
Randal Morgan Laboratory of Physics, University of Pennsylvania, Philadelphia, Pennsylvania
(Received May 28, 1954)

The absorption in thin layers of nickel, aluminum, and cobalt of beta rays from Co^{60} was measured in connection with the use of the surface counting method of determining diffusion coefficients. Data was obtained for foils and for evaporated and electroplated layers. In all cases the activity increased between 0 and 4 mg/cm². A discrepancy was noted between the data for foils and those for evaporated and electroplated layers. It is shown that this general behavior is predicted by simple scattering and absorption expressions. The implications of these data for the use of the surface counting method are discussed.

INTRODUCTION

THE surface-counting method of measuring diffusion coefficients involves the deposition of a thin layer of radioactive material on one face of a sample and the measurement of the activity of this face before and after the diffusion anneal. The fraction of surface activity, F, remaining after the diffusion anneal, depends on the diffusion coefficient, D, the duration of the diffusion anneal, t, and the characteristics of the absorption of the radiation by the sample. Usually it is experimentally determined or calculated that the radiation is absorbed according to the relation

$$N/N_0=\epsilon^{-\mu x},$$

where μ is a constant and N and N_0 are, respectively, the activities with and without an absorbing layer of thickness x. With this type of absorption it can be shown[1] that, for a planar active face

$$F=F(\mu^2 Dt).$$

ABSORPTION MEASUREMENTS

In some recent measurements[2] of the diffusion of Co^{60} in some Ni—Al alloys the surface counting method was used. Co^{60} emits two gamma rays, of energies 1.16 and 1.3 Mev, and a beta spectrum with a maximum energy of 0.31 Mev. The geiger tube used in these experiments had a thin (1.4 mg/cm²) mica end window and counted less than one percent of gamma rays. The sources used were $\frac{1}{8}$-in. thick Ni—Al samples onto which Co^{60} had been evaporated. The geiger tube was mounted in an aluminum housing and the source was placed beneath the tube in a lead collimator-holder. The active area of the source was circular with a $\frac{7}{16}$-in. diameter. The collimator was 1 in. long with a $\frac{3}{8}$-in. diameter opening. The active surface of the source was $\frac{1}{8}$ in. from the bottom of the collimator; the top of the collimator was $\frac{3}{8}$ in. from the geiger tube window.

For the absorption measurements, particular effort was made to adhere to the diffusion geometry as closely as possible. The ideal experiment would have been to measure the absorption in thin films of the Ni—Al alloys which fitted tightly to the source. Unfortunately, the Ni—Al alloys are hard and often very brittle. This made it impossible to fabricate foils of the alloys which were sufficiently thin to make useful absorption measurements. Therefore, it was decided to measure the absorption in nickel and aluminum foils and combine these data to obtain the absorption in the alloys, making the appropriate corrections for lattice spacing and composition. Since beta-ray absorption is mass dependent, such a procedure seemed valid.

The absorption data were obtained by placing the aluminum and nickel foils directly on top of the source. The resulting curves are shown in Figs. 1 and 2. Neither of the curves indicates a linear extrapolation to zero at zero thickness as would be expected if the absorption were exponential. Both curves show a maximum activity between 0 and 4 mg/cm². The two thinnest Al foils were obtained by evaporating aluminum onto a zapon substrate and their thicknesses are uncertain by at least 10 percent. A number of absorption measurements were made and the reproducibility was better than two percent.

When reproducibility was established, several possible origins for this behavior were considered. First, it

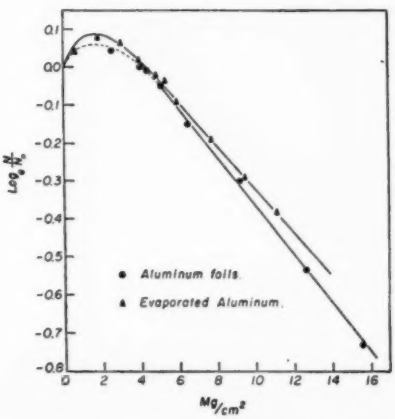

FIG. 1. The absorption of beta-radiation from Co^{60} by aluminum foils and evaporated aluminum layers.

* Supported by the Office of Naval Research. This work is part of a doctoral dissertation presented by the author to the University of Pennsylvania.
† Now at The Franklin Institute Laboratories for Research and Development, Philadelphia 3, Pennsylvania.
[1] For example, Steigman, Shockley, and Nix, Phys. Rev. **56**, 13 (1939).
[2] Berkowitz, Jaumot, and Nix, Phys. Rev. **95**, 1185 (1954).

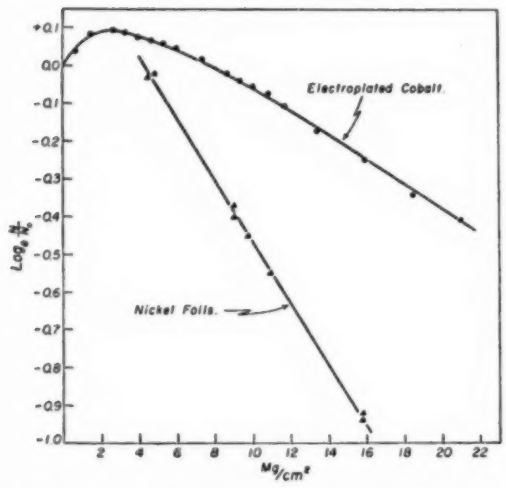

FIG. 2. The absorption of beta-radiation from Co^{60} by nickel foils and electroplated cobalt layers.

was possible that the accompanying gamma rays ejected electrons from the foils by Compton scattering and photoelectric emission. These mechanisms were rejected since their cross sections are negligibly small for the thickness involved. Second, there was the possibility that Co^{60} gamma rays traveling back into the thicker Ni—Al substrate might produce a lower energy radiation background that would have a more favorable cross section for the production of secondary electrons in the foils. To check this, a new source was prepared by evaporating Co^{60} onto a thin aluminum foil and additional absorption measurements were made. These new data agreed, within the experimental error, with the data for foils in Figs. 1 and 2. It was then concluded that the maxima in the absorption data were the result of changes in the angular distribution of the beta rays when a thin foil is placed over the source. In the usual absorption measurements, the foils are placed close to the geiger tube in order to minimize the effect of the change in angular distribution.[3] In the present case, it was necessary to simulate the diffusion geometry and thus the absorption geometry was the poorest possible. When absorption curves were obtained with the foils closer to the geiger tube, they showed a monotonic decrease with thickness.

Inasmuch as geometry was so critical, it seemed advisable to obtain absorption data for layers that fitted tightly to the source. This was accomplished for aluminum by evaporating the metal directly onto the active surface. The results are shown in Fig. 1. It should be noted that although the general characteristics for the foils and evaporated layers are similar, there is a decided difference in the details of the curves. In the case of nickel, it proved to be extremely difficult to evaporate a sufficient quantity of the metal. Also, nickel could not be electroplated onto the Co^{60} since cobalt replaces nickel in solution. Therefore, cobalt was electroplated onto the source. Since cobalt and nickel are very similar chemically, there should be no appreciable error involved in substituting the cobalt absorption data for those of nickel. These data are shown in Fig. 2. In this case, although both curves have maxima, there is much less agreement in detail than for aluminum. Occasionally, the electroplated cobalt layers do not adhere tightly to the source. In those instances, the data were much more similar to the nickel foils data. This is reasonable since poorly adhering layers approximate the geometry of foils more closely than do tightly plated layers.

It was found that both the evaporated aluminum and the electroplated cobalt data could best be fitted to curves representing the differences between two exponential terms. The fits in both cases is better than two percent. The equations for the curves of best fit were, for evaporated aluminum,

$$N/N_0 = 1.29e^{-56.8\sigma} - 0.29e^{-700\sigma}, \tag{1}$$

and for electroplated cobalt,

$$N/N_0 = 1.31e^{-32.1\sigma} - 0.31e^{-390\sigma}, \tag{2}$$

where $\sigma = \text{gm/cm}^2$.

When Eq. (1) and Eq. (2) are properly combined to give the absorption in the Ni—Al alloys, a function is obtained which is the sum of four exponential terms. The function may be used to derive a new expression for $F(\mu^2 Dt)$ as follows:

If the absorption for the alloys is

$$N/N_0 = \sum_{i=1}^{4} A_i e^{-\mu_i x}, \tag{3}$$

where A_i and μ_i are constants, then, if the sample is appreciably thicker than the mean diffusion depth, it can be shown that

$$F(Z) = \sum_{i=1}^{4} A_i G\left(\frac{\mu_1^2}{\mu_2^2} Z\right),$$

where $Z = (\mu_1)^2 Dt$. $G[(\mu_i^2/\mu_1^2)Z]$ is obtained from a

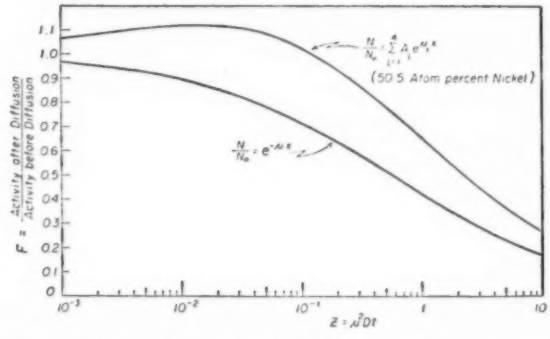

FIG. 3. The fraction of surface activity (F) remaining after diffusion as a function of ($\mu^2 Dt$) for simple and complex absorption functions.

[3] E. Bleuler and G. J. Goldsmith, *Experimental Nucleonics* (Rinehart and Company, Inc., New York, 1952), p. 85.

large-scale plot of

$$G(Z)=e^{-Z}\left[1-\frac{2}{\pi^{\frac{1}{2}}}\int_0^{Z^{\frac{1}{2}}}\exp(-y^2)dy\right].$$

Curves of F *versus* (μ^2Dt) are plotted in Fig. 3 for both the complex and simple types of absorption functions. It is apparent that an appreciable error in D can arise, particularly for the higher values of F, if the simple type of absorption function is used in an experiment that is correctly represented by a complex absorption function.

DISCUSSION

A satisfactory explanation of the general features of the absorption curves may be made along lines suggested by Novey and Elliot.[4] The absorption process may be considered to take place in two stages. First, the primary beta rays are scattered; this may be represented by the usual exponential term with a scattering coefficient μ_1. This scattered radiation is degraded in energy and consequently has an absorption coefficient $\mu_2(>\mu_1)$. μ_2 is an average absorption coefficient since the degradation of the beta-ray energy is a continuous process. By using the same approach employed when considering the degradation of gamma radiation by Compton scattering, it can be shown that the amount of scattered radiation counted is

$$N=\frac{N_0\mu_1}{\mu_2-\mu_1}(e^{-\mu_1 x}-e^{-\mu_2 x}). \tag{4}$$

Equation (4) is added to the amount of unscattered primary radiation; namely,

$$N=N_0e^{-\mu_1 x},$$

giving, for the total activity,

$$N=N_0[(1+A)e^{-\mu_1 x}-Ae^{-\mu_2 x}], \tag{5}$$

where

$$A=\mu_1/(\mu_2-\mu_1). \tag{6}$$

Equations (5) and (6) imply that the scattered radiation emerges isotropically. Actually, Elliot and Shapiro[5] have presented evidence that the radiation is scattered with an approximately cosine distribution in the forward direction. In addition, it has been shown[6] that an appreciable part of the radiation from the source has been back-scattered and has a distribution favoring the forward direction. These factors would have the effect of increasing the amount of scattered radiation which is counted. Thus Eq. (6) would be replaced by

$$A=K(\mu_1/\mu_2-\mu_1), \tag{7}$$

where K is a constant greater than unity.

Comparing Eq. (1) and Eq. (2) with Eq. (5) and Eq. (7), we find that

$$A_{\mathrm{Ni}}\approx A_{\mathrm{Al}},$$

which makes

$$K_{\mathrm{Ni}}\approx K_{\mathrm{Al}}, \tag{8}$$

since

$$(\mu_1/\mu_2)_{\mathrm{Ni}}\approx(\mu_1/\mu_2)_{\mathrm{Al}}.$$

Since "K" has been defined as essentially a geometrical factor, it is quite reasonable that (8) should hold. Therefore the experimental data represented by Eq. (1) and Eq. (2) are seen to behave in accord with the predictions of Eqs. (5) and (7).

The absorption behavior encountered in these experiments indicates several precautions which should be observed when the surface counting technique is used. First, the necessary absorption measurements should be made with geometries which are, as closely as possible, identical to the diffusion geometry. Consequently, absorbing layers which are evaporated or electroplated are preferable to foils. Second, the distance from the source to the geiger tube should be as small as possible; this has the effect of reducing K. This distance is usually limited by the necessity for collimating the radiation in order to minimize the effects of surface diffusion. It is possible that the advantages of minimizing the effects of surface diffusion are less important than those from the minimization of K. When $K>1$, F has a maximum; and the resulting double-valued range of D could be troublesome in cases of very slow diffusion rates. It is possible to avoid the absorption region containing the maximum by making all measurements with a foil between the geiger tube and the sample. To use such a method one would have to make certain that the position and condition of this foil remained constant for all measurements.

ACKNOWLEDGMENTS

The author is indebted to Dr. Sherman Frankel for many valuable discussions.

[4] C. D. Coryell and N. Sugarman, *Radiochemical Studies: The Fission Products* (McGraw-Hill Book Company, Inc., New York, 1951), Book 1, p. 44.

[5] Reference 4, p. 36.

[6] H. H. Seliger, Phys. Rev. **88**, 408 (1952).

Measurement of the Elastic Constants of Single Crystal Cobalt

H. J. McSkimin
Bell Telephone Laboratories, Inc., Murray Hill, New Jersey
(Received June 14, 1954)

The 5 elastic constants of hexagonal cobalt have been determined using pulse modulated ultrasonic waves which are reflected back and forth within the crystal. Frequencies between 10 and 30 Mc/sec were used. Values of the constants were derived from 11 measurements of wave velocities for longitudinal and shear modes in 3 crystals, using a phase comparison technique. At 25°C the constants (all in 10^{12} dynes/cm^2) are: $c_{11}=3.071\pm0.5$ percent, $c_{12}=1.650\pm0.5$ percent, $c_{13}=1.027\pm1.5$ percent, $c_{33}=3.581\pm0.5$ percent, $c_{44}=0.755\pm0.5$ percent. These are based on a density of 8.836.

1. INTRODUCTION

CRYSTALS with hexagonal symmetry—such as cobalt—require five independent elastic constants to specify the relationships between stresses and strains at a point. In terms of stiffness coefficients, they may be listed as c_{11}, c_{12}, c_{13}, c_{33}, and c_{44}.[1]

These five quantities can be determined by sending ultrasonic waves through properly oriented crystal specimens and measuring the wave velocities, which depend on the elastic constants and the density. Obviously at least five measurements must be made for hexagonal crystals.

Relations between wave velocities and elastic constants are given by Cady.[2] If measurements for arbitrary directions are made (i.e., not along the simpler crystallographic directions), a third degree equation results. Neighbours and Smith[3] have described a perturbation method for calculating elastic constants from measured velocities in arbitrary directions. Other aspects relating to ultrasonic techniques are to be found in the paper by Price and Huntington.[4]

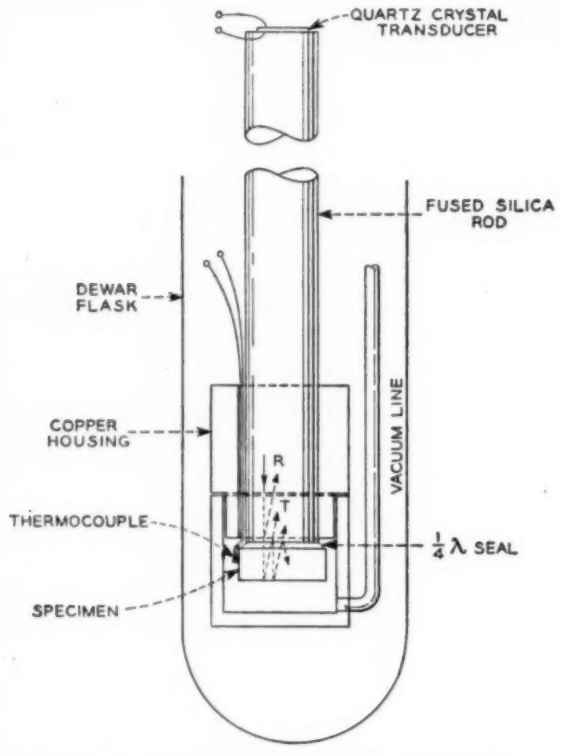

FIG. 1. Apparatus for measuring elastic constants.

2. METHOD USED

The method used for measuring wave velocities has been described previously,[5,6] but will be reviewed briefly here.

Pulse modulated ultrasonic waves in the frequency range 10–30 mc/sec are transmitted down a fused silica rod, through a plastic one-quarter wavelength seal, and into the specimen as shown by Fig. 1. There they reflect back and forth within the specimen and give rise to components transmitted back through the seal. At discrete frequencies (with a sufficiently long pulse duration) these waves will be in phase and give rise to a distinct pattern observed on the viewing oscilloscope, as seen in Fig. 2. Thus, by measuring a number of these frequencies accurately, the wavelength can be determined, and hence the velocity of propagation which is given by

$$V_0=2tf_0/n_0, \tag{1.1}$$

where t is the thickness of the specimen, f_0 is a frequency for "in-phase" condition, and n_0 is the number of wavelengths in the path as given by f_0 divided by the frequency separation between successive "in-phase"

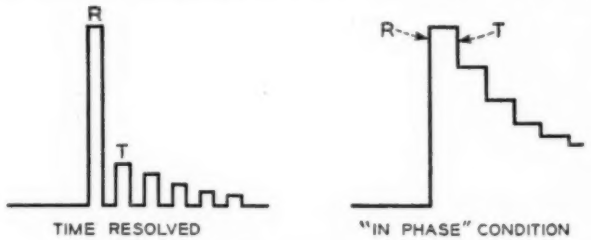

FIG. 2. Oscilloscope patterns (envelopes).

[1] W. G. Cady, *Piezoelectricity* (McGraw-Hill Book Company, Inc., New York, 1946), first edition, p. 55.
[2] See reference 1, p. 105.
[3] J. R. Neighbours and C. S. Smith, J. Appl. Phys. **21**, 1338 (1950).
[4] W. J. Price and H. B. Huntington, J. Acoust. Soc. Am. **22**, 32 (1950).
[5] H. J. McSkimin, J. Acoust. Soc. Am. **22**, 413 (1950).
[6] H. J. McSkimin, J. Appl. Phys. **24**, 988 (1953).

frequencies. For details of construction, preparation of specimens, and further analysis, see references 5 and 6.

3. FORMULAS FOR VELOCITIES OF PROPAGATION AND ELASTIC CONSTANTS

3.1 Crystal Cuts Used

Three cobalt single crystals were made available,[7] with orientations which are shown in Figs. 3–5. Formulas for velocities and elastic constants are summarized in Table I. As can be seen, all the elastic constants with the exception of c_{13} can be obtained from crystal cuts A and B. Measurements on crystal C, involving propagation of waves in two directions, are in themselves sufficient to determine all five constants. Thus, with 11 measurements possible, numerous cross checks could be made.

Since the matrix of c constants remains invariant for rotation of x and y axes about z, data equivalent to those obtained from crystal B, for example, could be obtained by propagating waves in *any* direction perpendicular to the z axis.[8] Similarly, instead of crystal C, one could have used any cut such that the propagation direction was 45° with respect to the z axis. The direction of z must, of course, be accurately known so that proper orientation of shear particle motion can be effected.

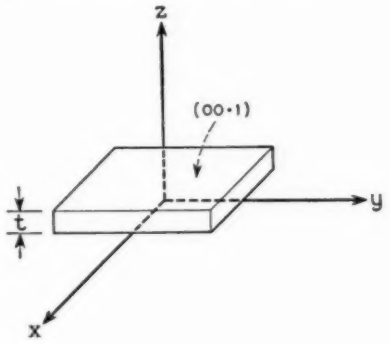

FIG. 3. Crystal A—thickness parallel to z axis.

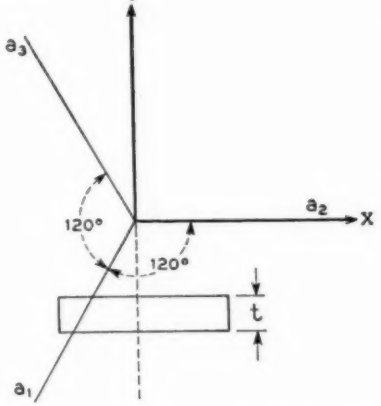

FIG. 4. Crystal B—thickness parallel to y axis (z axis is ⊥ plane of paper).

[7] These crystals were made available through R. M. Bozorth, and were originally purchased from Horizons, Inc., 2891 E. 79th Street, Cleveland 4, Ohio. Preparation of specimens, including x-ray orientation, was done by A. J. Williams. Maximum probable error in alignment of surfaces was estimated to be ±10′.

[8] L. Gold, J. Appl. Phys. **21**, 541 (1950).

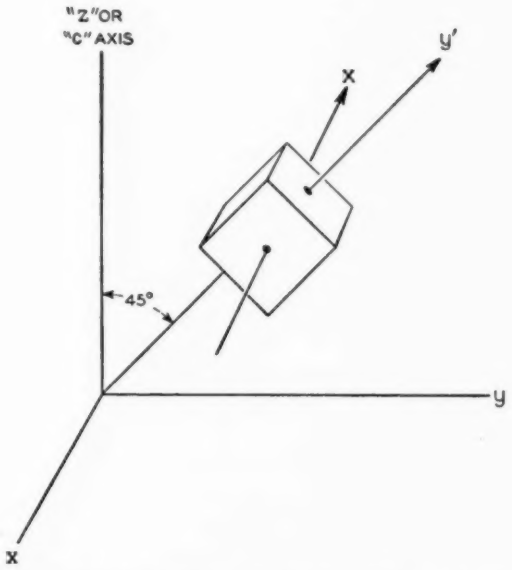

FIG. 5. Crystal C—propagation along x yields c_{11}, c_{12}, c_{44}; propagation along y' yields c_{13}, c_{33}, plus one check measurement.

3.2 Velocities of Propagation for 45° Rotation Around x (Crystal C, Fig. 5)

It can be shown that the $x'y'$ shear mode propagated along a direction making 45° with respect to y and z is not coupled to the other two modes because the cross couplings c_{26}' and c_{46}' are zero. (See Appendix A.)

Thus the velocity for the $x'y'$ shear mode is given by

$$V_8=\left(\frac{c_{66}'}{\rho}\right)^{\frac{1}{2}}=\left[\frac{(\frac{1}{4}c_{11}-\frac{1}{4}c_{12}+\frac{1}{2}c_{44})}{\rho}\right]^{\frac{1}{2}}. \qquad (3.1)$$

The other two velocities[9] (V_6 and V_7) are found by solving the quadratic equation

$$(c_{22}'-\rho V^2)(c_{44}'-\rho V^2)-c_{24}'^2=0. \qquad (3.2)$$

In terms of the elastic constants with respect to the unrotated axes, Eq. (3.2) yields the following for V_6^2 or

TABLE I. Formulas for elastic constants.

Crystal	Type mode	Direction of propagation	Direction of particle motion	Velocity symbol	Elastic constant
A	Long.	z	z	V_1	$c_{33}=\rho V_1^2$
	Shear	z	in xy plane	V_2	$c_{44}=\rho V_2^2$
B	Long.	y	y	V_3	$c_{11}=\rho V_3^2$
	Shear	y	x	V_4	$c_{66}=\frac{1}{2}(c_{11}-c_{12})=\rho V_4^2$
	Shear	y	z	V_5	$c_{44}=\rho V_5^2$
C	Quasi-Long.	y'	y'	V_6	(see text)
	Quasi-Shear	y'	z'	V_7	(see text)
	Shear	y'	$x'=x$	V_8	$\frac{1}{4}c_{11}-\frac{1}{4}c_{12}+\frac{1}{2}c_{44}=\rho V_8^2$
	Long.	x	x	V_9	$c_{11}=\rho V_9^2$
	Shear	x	y	V_{10}	$c_{66}=\frac{1}{2}(c_{11}-c_{12})=\rho V_{10}^2$
	Shear	x	z	V_{11}	$c_{44}=\rho V_{11}^2$

[9] For cobalt, c_{24}' is quite small for the 45° rotation, so that effects of acoustic birefringence were not observed experimentally. That is, the two modes were essentially uncoupled. For a 35.5° rotation about x (i. e., angle between y and $y'=35.5°$), $c_{24}'=0$.

TABLE II. Measured velocities of propagation for cobalt single crystals at 25°C.

V_1	$=6.361\times10^5$ cm/sec
V_2	$=2.919$
V_3	$=5.890$
V_4	$=2.833$
V_5	$=2.924$
V_6	$=5.773$
V_7	$=3.597$
V_8	$=2.878$
V_9	$=5.900$
V_{10}	$=2.838$
V_{11}	$=2.925$

V_7^2 depending on whether the plus or negative sign precedes the radical:

$$V^2=\frac{(\frac{1}{2}c_{11}+\frac{1}{2}c_{33}+c_{44})\pm\left[\left(\frac{c_{11}-c_{33}}{2}\right)^2+(c_{13}+c_{44})^2\right]^{\frac{1}{2}}}{2\rho}. \tag{3.3}$$

In Eq. (3.3), ρ is the density.

3.3 Elastic Constants as Functions of Wave Velocities

Table I lists formulas from which c_{11}, c_{12}, c_{33}, and c_{44} may be calculated. With these quantities known (or more specifically, with V_1, V_2, and V_3 known), either V_6 for the quasi-longitudinal waves or V_7 for the coupled quasi-shear wave can be used to determine c_{13}. Putting values for c_{22}', c_{24}', and c_{44}' into Eq. (3.2) (see Appendix A), and solving for c_{13}/ρ, one obtains

$$c_{13}/\rho=-V_2^2+(V_2^4-Q)^{\frac{1}{2}}, \tag{3.4}$$

with

$$Q=-V_1^2V_3^2-V_2^2V_3^2-V_2^2V_1^2+(2V_3^2+2V_1^2+4V_2^2)V^2-4V^4. \tag{3.5}$$

V is either V_6 or V_7.

3.4 Elastic Constants from Measurements on Crystal C Only

From Eq. (3.2), using both V_6 and V_7, two expressions involving c_{11}, c_{13}, c_{33}, and c_{44} are obtained. These may be solved simultaneously for c_{33} and c_{13} with the following results:

$$\begin{aligned} c_{33}/\rho&=2(V_6^2+V_7^2-\tfrac{1}{2}V_9^2-V_{11}^2)\\ c_{13}/\rho&=-V_{11}^2+(V_{11}^4-Q')^{\frac{1}{2}}, \end{aligned} \tag{3.6}$$

with

$$Q'=-2V_6^2V_9^2+4V_6^2V_7^2-2V_6^2V_{11}^2-2V_7^2V_9^2-2V_7^2V_{11}^2+V_9^4+2V_9^2V_{11}^2+2V_{11}^4. \tag{3.7}$$

3.5 Cross Checks for Velocities

In addition to the direct checks listed in Table I, two other useful relations may be derived:

$$V_8^2=\tfrac{1}{2}V_2^2+\tfrac{1}{2}V_4^2, \tag{3.8}$$

$$V_6^2+V_7^2=\tfrac{1}{2}V_1^2+V_2^2+\tfrac{1}{2}V_3 \tag{3.9}$$

4. RESULTS

4.1 Velocities of Propagation

Table II lists velocity data for the three crystals used. These are for a temperature of 25°C (obtained from a plot of velocity *versus* temperature over a −30° to +25° range).

Illustrative data are shown in Fig. 6. These velocities are *not* corrected for changes in length as a function of temperature. A correction of approximately −13 parts/10^6/°C for directions perpendicular to the z axis and a somewhat higher value for directions parallel to z is indicated.[10]

4.2 Elastic Constants

Using the results listed in Table II, the elastic constants were calculated with $\rho=8.836$ as determined from unit cell dimensions and atomic weight. They are listed in Table III with estimated limits of probable error.

These results were obtained by averaging, respectively, values for elastic constants as obtained from the formulas of Table I. Values for c_{13} were calculated as described in Secs. 3.3 and 3.4, and the results averaged.

4.3 Compressibilities

The volume compressibility for hydrostatic pressure is given by

$$2s_{11}+2s_{12}+4s_{13}+s_{33}=0.526\times10^{-12}\ \text{cm}^2/\text{dyne}. \tag{4.1}$$

This value is to be compared with 0.520 obtained by extrapolating Bridgman's data to zero pressure.[11] A further check can be obtained from a calculation of compressibilities parallel and perpendicular to the c axis (i.e., unit linear compression per unit pressure).

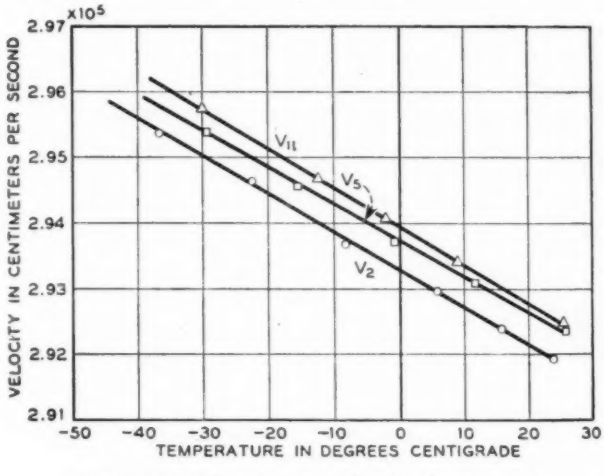

FIG. 6. Velocities of propagation for shear waves in cobalt single crystal.

[10] L. Marick, Phys. Rev., **49**, 831 (1936).
[11] P. W. Bridgman, Proc. Am. Acad. Arts Sci. **77**, 187–234, (1949).

TABLE III. Elastic constants of single crystal cobalt at 25°C.[a]

$c_{11}=3.071\times10^{12}\pm0.5\%$	
$c_{12}=1.650$	0.5%
$c_{13}=1.027$	1.5%
$c_{33}=3.581$	0.5%
$c_{44}=0.755$	0.5%

[a] Values in the table are based on a density of 8.836 g/cm³.

They are, respectively,

$$2s_{13}+s_{33}=0.180\times10^{-12}\ \text{cm}^2/\text{dyne}$$

and

$$s_{11}+s_{12}+s_{13}=0.169\times10^{-12}\ \text{cm}^2/\text{dyne}. \quad (4.2)$$

These are to be compared with Bridgman's data which yield values at zero pressure of 0.177 and 0.169, respectively.

APPENDIX A

Elastic Constants for 45° Rotation of Axes Around x

$$c_{22}'=\tfrac{1}{4}c_{11}+\tfrac{1}{2}c_{13}+\tfrac{1}{4}c_{33}+c_{44}$$
$$c_{24}'=-\tfrac{1}{4}c_{11}+\tfrac{1}{4}c_{33}$$
$$c_{26}'=0$$
$$c_{44}'=\tfrac{1}{4}c_{11}-\tfrac{1}{2}c_{13}+\tfrac{1}{4}c_{33}$$
$$c_{46}'=0$$
$$c_{66}'=\tfrac{1}{4}c_{11}-\tfrac{1}{4}c_{12}+\tfrac{1}{2}c_{44}$$

Equation for Velocities of Propagation in y' Direction

$$\begin{vmatrix} (c_{22}'-\rho v^2) & c_{24}' & c_{26}' \\ c_{24}' & (c_{44}'-\rho v^2) & c_{46}' \\ c_{26}' & c_{46}' & (c_{66}'-\rho v^2) \end{vmatrix}=0$$

JOURNAL OF APPLIED PHYSICS VOLUME 26, NUMBER 4 APRIL, 1955

Theory of Frequency Modulation Noise in Tubes Employing Phase Focusing*

JOHN L. STEWART
Department of Electrical Engineering, University of Michigan, Ann Arbor, Michigan
(Received May 12, 1954)

Oscillators employing phase focusing such as magnetrons have fairly well defined spokes whose rotational speed is proportional to the oscillation frequency. Each spoke is composed of a finite number of electrons having random velocities and consequently is subject to random fluctuations about a mean position. This spoke "jitter" leads to fluctuations in the oscillation frequency resulting in frequency modulation noise. It is the theoretical evaluation of the parameters of this noise as affecting the power spectrum of the oscillator output that is of interest here. The theoretical results compare favorably with the measured power spectrum of a voltage-tunable magnetron. The application of the formulas require an estimate of electron temperature although no attempt is made to evaluate this temperature. Amplitude fluctuation noise appears to be relatively unimportant in continuous-wave phase-focused oscillators.

1. INTRODUCTION

IT has been observed that two types of noise exist in the output of magnetrons and other tubes employing phase focusing.[1] As would be expected, amplitude-modulation noise is present due to shot and flicker effects. In addition to this, there exists frequency modulation noise, part of which is correlated to the amplitude noise. The study here is restricted to the FM noise, and, in particular, to that component of FM noise introduced because the charge in the tube[2] consists of discrete particles having random velocities. There also exist components of FM and AM noise due to flicker and other low frequency effects which will not be analyzed here.

As necessary background, some results of a previous analysis will be stated.[3] If a carrier is modulated in frequency with a rectangular band of Gaussian noise extending from a radian frequency of zero to B such that the instantaneous frequency deviation of the carrier is directly proportional to the amplitude of the noise, then the power spectrum of the resulting modulated carrier will have the asymptotic forms

$$W(\omega)=\begin{cases}\dfrac{1}{(2\pi D^2)^{\frac{1}{2}}}\exp\left[\dfrac{(\omega-\omega_0)^2}{2D^2}\right], & \dfrac{D}{B}\gg1, \quad (1)\\[2ex] \dfrac{1}{\pi B}\cdot\left[\dfrac{\pi D^2/2B^2}{(\pi D^2/2B^2)^2+(\omega-\omega_0)^2/B^2}\right], & \dfrac{D}{B}\ll1, \quad (2)\end{cases}$$

where ω_0 is the carrier frequency and D is the rms frequency deviation. The three decibel half bandwidth of these power spectra are

$$B_F=\begin{cases}(2\log2)^{\frac{1}{2}}D=1.18D, & \dfrac{D}{B}\gg1, \quad (3)\\[2ex] \dfrac{\pi D^2}{2B}=1.57D^2/B, & \dfrac{D}{B}\ll1. \quad (4)\end{cases}$$

* This work was sponsored by the Signal Corps, Department of the Army.

[1] "Microwave noise study," Quarterly Progress Report Nos. 1, 2, and 3, February 1, 1953 to November 1, 1953, Raytheon Manufacturing Company, Contract AF 19(604)-636.

[2] Magnetrons will be considered specifically because more data are available.

[3] J. L. Stewart, Proc. Inst. Radio Engrs. 42, 1539 (1954).

For small D/B, the power spectrum falls off quite slowly with the difference frequency $\omega-\omega_0$.

2. THE MECHANISM OF FM NOISE

In a magnetron, the space charge exists in the form of spokes that rotate at an angular velocity ω_r.[4] If the magnetron operates in the π mode and has N anode segments, there are $N/2$ spokes and $\omega_0=N\omega_r/2$ where ω_0 is the generated frequency in radians per second.

The current induced in the anode segments is due mainly to the rotational motion of the spokes, their radial motion having only a second-order effect which will be neglected here. The electrons that comprise the spoke were at one time emitted from the cathode with random velocities. The probability density function of the velocity tangential to the cathode is assumed to be Gaussian with a variance kT/m where k is Boltzmann's constant, T is the electron temperature, and m is the mass of the electron.[5]

Although even the approximate variance of the velocity distribution of electrons in the cathode-anode region is not known, it is believed that because of electron-electron interaction, growing wave amplification, and relatively high random velocities of secondary electrons, the mean-square electron random velocity between anode and cathode is very much larger than that at the cathode. This random motion can be approximately specified in terms of a temperature. Although the temperature of the electrons upon emission is only about 1000°K, in the interaction space between cathode and anode it may be on the order of millions of degrees Kelvin.[6]

There are a certain number of electrons in the spokes at any given instant. It is the average rotational velocity of all these electrons, suitably weighted in accordance with their relative effectiveness in inducing anode current, that gives the instantaneous frequency of the magnetron. New electrons are continually being removed at the anode and entering the spokes at the cathode. It can be concluded that the instantaneous frequency will vary in an approximately Gaussian fashion about the average frequency. The correlation function $R(\tau)$ of these frequency variations will decrease to zero at $\tau=T'$, where T' is the average cathode-to-anode transit time of the electrons.

Because of the averaging effect of the large number of electrons in the spokes at any instant, "jitter" of the spokes will be much smaller than that accountable to a single electron. However, the small transit times found in practice indicate that the rate of change of instantaneous frequency is rather high. Consequently, it is apparent that the output spectrum of the magnetron will have the form of Eq. (2) for D/B very small.[7]

The calculation of the equivalent D and B, and especially of the half bandwidth B_F, for the type of noise described above are of primary concern here. There appears to be no reason why any correlation should be expected between this type of FM noise and AM noise.

Some magnetrons have an appreciable pushing figure. In such tubes, current fluctuations produced by the shot effect result in a component of FM noise that is highly correlated with the AM noise. This induced FM noise is more important than that produced by spoke jitter in some conventional magnetrons. The discussion here will be confined to FM noise resulting from spoke jitter which is an irreducible component of noise existing in all magnetrons regardless of the pushing figure.

3. INDUCED CURRENT IN THE MAGNETRON

Visualize a diagram of spokes of space charge rotating in a magnetron. An impedance Z is connected between the positive and negative anode segments and alternate segments are connected together. The induced current flows through the impedance Z resulting in a voltage between adjacent anode segments. The magnetron will be assumed axially symmetric and of length L.

Let it be assumed that the total charge in the spokes is constant and that all induced current is caused by rotation of the spokes rather than by the radial motion of the electrons. Then, the space charge density function of the spokes ρ and the function ψ_k giving indirectly the potential of the field in the cathode-anode region can be expanded into Fourier series.

$$\psi_k=\sum_k A_k \cos\frac{kN\theta}{2}, \tag{5}$$

$$\rho=\sum_j\left[B_j\cos\frac{jN\theta'}{2}+C_j\sin\frac{jN\theta'}{2}\right]. \tag{6}$$

The angle θ is the angle in a fixed coordinate system and θ' is the angle in a system rotating with the spokes. $\theta'=0$ is assumed to correspond to the center line of a spoke. It is assumed that at the reference time $t=0$, $\theta=\theta'$ from which $\theta'=\theta-\omega_r t$.

Welch[4] has shown that the magnitude of the fundamental component of induced current in the magnetron is given by[8]

$$|i_1|=\pi L\omega_0\int_{r_c}^{r_a} A_1B_1 r\,dr, \tag{7}$$

[4] H. W. Welch, Jr., Proc. Inst. Radio Engrs. 41, 1631 (1953).

[5] All units are in the M.K.S. system.

[6] P. Guénard and H. Huber, Ann. radioélec. compagn, franç. assoc. T.S.F. 7, 252 (1952). Guénard and Huber report temperatures on the order of one-half million degrees Kelvin in non-oscillating tubes. Although no published data seem to be available, it would appear that temperatures in the oscillating magnetron are much larger than this.

[7] In an analogous fashion, one can postulate the existence of a similar kind of FM noise in backward wave and other types of beam tubes.

[8] The lower limit r_c can be interpreted as either the radius of the cathode or the radius of the subsynchronous swarm, whichever is applicable.

in which it is assumed that the spokes are symmetric such that all the C_k are zero.

If it is assumed that the space charge has a negligible effect upon the potential in the anode-cathode region by comparison with that caused by the voltage between anode segments, then the coefficients A_k are functions only of the radius r and are obtainable through a solution of Laplace's equation in two dimensions. Consequently, it is permissible to assume a normalized function $A(u)$ such that $A_1=A_mA(u)$ and $A(1)=1$ in which A_m is the value of A_1 at $r=r_a$ (which is generally the maximum value of A_1), and where the variable u is the normalized radius r/r_a.

The coefficient B_k of Eq. (6) is defined by the usual Fourier series formula as

$$B_k=\frac{N}{2\pi}\int_{-2\pi/N}^{2\pi/N}\rho(r,\theta')\cos\frac{kN\theta'}{2}d\theta'. \tag{8}$$

Let it be assumed that each spoke has a uniform charge density in $-\beta<\theta'<\beta$ and zero charge density for $|\theta'|>\beta$. Then, $\rho(r,\theta')=\rho(r)\rho(\theta')$ and

$$\int_{-2\pi/N}^{2\pi/N}\rho(\theta')d\theta'=\int_{-\beta}^{\beta}\rho(\theta')d\theta'=2\beta, \tag{9}$$

where it should be noted that $\rho(\theta')$ is dimensionless.

The above assumption may be unrealistic in some cases. However, some equivalent rectangular spoke can be hypothesized and some equivalent β obtained.

Using Eqs. (8) and (9) in Eq. (7) and integrating, there is obtained

$$|i_1|=N\beta L\omega_0\left[\frac{\sin(N\beta/2)}{N\beta/2}\right]\int_{r_c}^{r_a}A_mA(u)\rho(r)rdr. \tag{10}$$

If V is the volume of one spoke and q is the total charge in the magnetron

$$\int_V\rho(r,\theta')dV=q\frac{2}{N}. \tag{11}$$

Since $dV=Lrdrd\theta'$, Eq. (11) becomes

$$\int_{-2\pi/N}^{2\pi/N}\int_{r_c}^{r_a}\rho(r,\theta')Lrdrd\theta'=2L\beta\int_{r_c}^{r_a}\rho(r)rdr=q\frac{2}{N}, \tag{12}$$

from which

$$\int_{r_c}^{r_a}\rho(r)rdr=\frac{q}{L\beta N}=r_a^2\int_{r_c/r_a}^{1}u\rho(u)du. \tag{13}$$

The function $\rho(r)$ gives the manner in which the electron density varies with r. This can be normalized to a function $B(r)$ and $B(r/r_a)$ as

$$\rho(r)=qB(r)/L\beta N,$$
$$\rho(r/r_a)=\rho(u)=\frac{qB(u)}{L\beta Nr_a^2}, \tag{14}$$

such that

$$\int_{r_c}^{r_a}rB(r)dr=\int_{r_c/r_a}^{1}uB(u)du=1. \tag{15}$$

Using the definition of Eq. (14), Eq. (10) may be written

$$|i_1|=A_m\omega_0q\left[\frac{\sin(N\beta/2)}{N\beta/2}\right]\int_{r_c/r_a}^{1}uA(u)B(u)du. \tag{16}$$

The maximum (but unrealizable) current is given when the spokes are very narrow and the total charge is located very close to the anode in which case $A(u)=1$ and the integral over $B(u)$ is unity giving a current $A_m\omega_0q$.

As a specific approximation, assume that $B(u)$ varies as $1/u$—the constant of proportionality is found from Eq. (15) to be $1/(1-r_c/r_a)$. Also, assume that $A(u)$ varies as u^k where k is some positive number. Then, Eq. (16) becomes

$$|i_1|=\frac{A_m}{k+1}\omega_0q\left[\frac{\sin(N\beta/2)}{N\beta/2}\right]\frac{1-(r_c/r_a)^{k+1}}{1-r_c/r_a}\cong\frac{A_m}{k+1}\omega_0q. \tag{17}$$

The charge dq in the volume element dV (which includes the corresponding element in every spoke) is found from Eq. (12) as

$$\frac{N}{2}\rho(r,\theta')dV=dq. \tag{18}$$

But $\rho(r,\theta')=\rho(r)$ for $|\theta'|\leqslant\beta$ and $dq=ne$ where n is the number of electrons in dV. Thus,

$$n=\frac{qB(u)dV}{2L\beta er_a^2}=\frac{qB(r)dV}{2L\beta e}. \tag{19}$$

It can be easily shown that the relative effectiveness of any given electron in inducing current in the anode is proportional to $A(u)$ and to $\cos(N\theta'/2)$.

4. MEAN-SQUARE DEVIATION OF FM NOISE

The probability density function of the transverse velocity of one electron is assumed to be Gaussian with a variance kT/m. At a radius r, the velocity v is $\omega_r=v/r$. Thus, the variance of the density function for ω_r is $kT/(mr^2)$. In one revolution of the spoke, there are $N/2$ cycles of the carrier; hence, the variance of the generated frequency due to a single electron is

$$\langle(\Delta\omega_c)^2\rangle_{1e}=(N/2)^2kT/mr^2, \tag{20}$$

which can be considered to refer to an electron in the most favorable position for inducing current in the anode. For any other electron, Eq. (20) must be multiplied by the square of the relative effectiveness of the electron, $A(u)\cos N\theta'/2$.

The variance due to the n electrons in the volume element dV is less than that of a single electron. In order to obtain the appropriate average, Eq. (20) must be divided by n as given by Eq. (19) to give

$$\frac{1}{\langle(\Delta\omega_n)^2\rangle_{Av}}=\left(\frac{2}{N}\right)^2\left(\frac{mr^2}{kT}\right)\frac{qB(r)dV}{[A(r)\cos(N\theta'/2)]^2 2L\beta e}. \quad (21)$$

The average for all electrons in the magnetron is obtained by summing Eq. (21) for the n electrons in each volume element dV. This integration yields the reciprocal of the variance D^2 of the FM noise as

$$\frac{1}{D^2}=\left(\frac{2}{N}\right)^2\frac{mq}{2\beta ekT}\int_{-\beta}^{\beta}\frac{d\theta'}{\cos^2(N\theta'/2)}\int_{r_c}^{r_a}\frac{r^3B(r)}{A^2(r)}dr. \quad (22)$$

Integrating over θ', inverting, and substituting for q from Eq. (16), we find

$$D^2=\left(\frac{N}{2}\right)^2\frac{ekT\omega_0}{m|i_1|r_a^2}\cos\frac{N\beta}{2}F\left(\frac{r_c}{r_a}\right), \quad (23)$$

where $F(r_c/r_a)$ is a geometrical constant given by

$$F\left(\frac{r_c}{r_a}\right)=\frac{\int_{r_c/r_a}^{1}uA(u)B(u)du}{\int_{r_c/r_a}^{1}\frac{u^3B(u)}{A^2(u)}du}. \quad (24)$$

In order to have some (albeit rough) estimate of $F(r_c/r_a)$, we assume $B(u)$ varies as $1/u$ as before and that $A(u)=u^k$. Then,

$$F(r_c/r_a)=\begin{cases}\left(\frac{3-2k}{k+1}\right)\left[\frac{1-(r_c/r_a)^{k+1}}{1-(r_c/r_a)^{3-2k}}\right], & k\neq 1.5,\\ \frac{1-(r_c/r_a)^{2.5}}{2.5\log(r_a/r_c)}, & k=1.5,\end{cases} \quad (25)$$

which is plotted as a function of r_c/r_a for several values of k in Fig. 1.

The induced current can be estimated if the power of the oscillations of the tube is known. Let R be the shunt resistance of the loaded cavity. Then,

$$|i_1|=(2P/R)^{\frac{1}{2}}. \quad (26)$$

If the induced current is not in phase with the voltage between spokes, the above relation is somewhat in error. This could be taken into account if necessary.

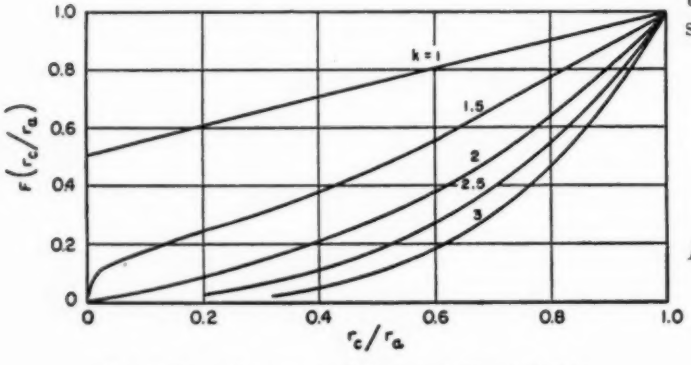

FIG. 1. Geometric constant for calculating deviation.

5. ESTIMATE OF NOISE BANDWIDTH

It would appear feasible to obtain an analytic expression for the bandwidth of the noise by setting up a picture of the electrons moving from cathode to anode and computing a correlation function for the "instantaneous" frequency. However, many of the parameters in the magnetron are known only vaguely; in particular, the transit time. Rather than obtaining an analytical solution, an estimate will be made. If T' is the electron transit time, the correlation function $R(\tau)$ is zero at $\tau=T'$. In order to get a simple estimate, we will assume that

$$R(\tau)=\begin{cases}1-\left|\frac{\tau}{T'}\right|, & \left|\frac{\tau}{T'}\right|\leqslant 1,\\ 0, & \left|\frac{\tau}{T'}\right|>1.\end{cases} \quad (27)$$

The power spectrum of the equivalent low-pass modulator producing the FM noise can be calculated from this assumption as

$$W(\omega)=4\int_0^{\infty}R(\tau)\cos\omega\tau d\tau=T'\left[\frac{\sin(\omega T'/2)}{\omega T'/2}\right]^2, \quad (28)$$

which has a half-power radian bandwidth of

$$B=2.74/T'=C_B/T'. \quad (29)$$

Because the electrons most effective in inducing current are fairly close to the anode, the bandwidth given above is probably too small. If one assumes a C_B of about three or four the error should not be excessive.

Let it be assumed that the radial velocity of the electrons is constant. Then it is possible to relate the transit time to the dc anode current I_0 and the total space charge q as

$$T'=\frac{q}{2\pi\times 10^{18}I_0e}. \quad (30)$$

Combining Eqs. (30) and (17), we find

$$B=\frac{C_B}{T'}=\frac{2\pi\times 10^{18}I_0e\omega_0C_B}{|i_1|}\left[\frac{\sin(N\beta/2)}{N\beta/2}\right]\times\int_{r_c/r_a}^{1}uA(u)B(u)du. \quad (31)$$

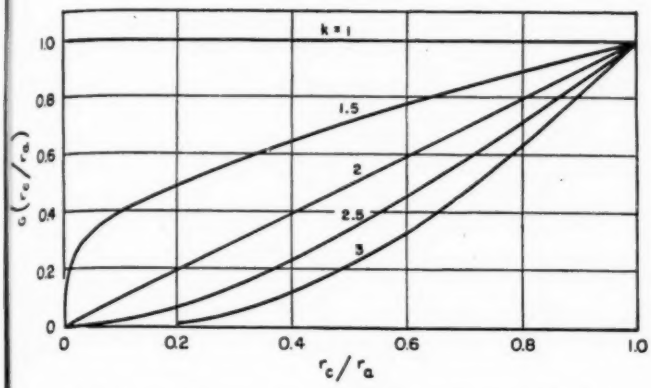

FIG. 2. Geometric constant for calculating spectrum width.

Assuming that $B(u)$ varies as $1/u$ and that $A(u)=u^k$, we can obtain an approximate expression as

$$B\cong\frac{2\pi\times10^{18}I_0e\omega_0C_B}{(k+1)|i_1|}\left[\frac{\sin(N\beta/2)}{N\beta/2}\right]\frac{1-(r_c/r_a)^{k+1}}{1-(r_c/r_a)}. \quad (32)$$

6. BANDWIDTH OF THE MAGNETRON SPECTRUM

Relative to unity at the center frequency, the power spectrum of the magnetron output is given by

$$W_M(\Delta\omega)=\frac{B_F^2}{B_F^2+\Delta\omega^2}, \quad (33)$$

where B_F is the half bandwidth given by Eq. (4) for $D/B\ll1$.

If D^2 from Eq. (23) and B from Eq. (31) are substituted into Eq. (4), it is found that the bandwidth B_F is neither a function of the induced current $|i_1|$ nor the generated frequency ω_0:

$$B_F=\left(\frac{N}{2}\right)^2\frac{kT}{4\times10^{18}I_0mC_Br_a^2}\left[\frac{N\beta/2}{\tan(N\beta/2)}\right]G(r_c/r_a). \quad (34)$$

The geometric constant $G(r_c/r_a)$ is given by

$$G(r_c/r_a)=\frac{1}{\int_{r_c/r_a}^1\frac{u^3B(u)}{A^2(u)}du}. \quad (35)$$

Using the approximations used before,

$$G(r_c/r_a)=\begin{cases}\dfrac{(1-r_c/r_a)(3-2k)}{1-(r_c/r_a)^{3-2k}}, & k\neq1.5,\\[2ex] \dfrac{1-r_c/r_a}{\log(r_a/r_c)}, & k=1.5,\end{cases} \quad (36)$$

which is plotted in Fig. 2 as a function of r_c/r_a for various values of k. For the special value $k=2$, $G(r_c/r_a)=r_c/r_a$.

7. APPLICATION TO A VOLTAGE TUNABLE MAGNETRON

The application of the foregoing theory will be made to a small voltage tunable magnetron of the type developed over recent years at the University of Michigan Tube Laboratory. The tube has a broadband (essentially untuned) cavity structure. Approximate dimensions and operating conditions are taken as follows: $N/2=6$, $r_a/r_c=0.7$, $r_a=0.0026$ meters, and $I_0=0.01$ ampere. It will be assumed that $T=2.2\times10^6$ °K (200 electron volts), $C_B=3$, $G(r_c/r_a)=0.8$, and the angle factor $=1.0$.

Using Eq. (34), we find B_F to be 1170 radians per second, or 186 cycles per second. At difference frequencies of 0.1, 1.0, and 10 megacycles, the spectrum is down about 54.6, 74.6, and 94.6 decibels, respectively, from that at $\Delta\omega=0$. These figures compare within a few decibels with observed values, although it must be pointed out that adequate measured values are not yet available. The shape of the spectrum has repeatedly been observed to follow the "single-tuned" response pattern up to difference frequencies large enough to show other components of noise, shot noise in particular.

It is of interest to calculate the deviation D^2 and bandwidth B for the example. For this, Eq. (23) can be used. It will be assumed that $P=0.2$ watts, $R=50$ ohms, $\omega_0=18\times10^9$ radians per second, and $\cos(N\beta/2)F(r_c/r_a)=0.4$.

The value of induced current $|i_1|$ is found to be 0.09 ampere. Then, $D=1.5\times10^6$ radians per second which is 223 kilocycles. Using this result in Eq. (4), $B=3020\times10^6$ radians per second, or 481 megacycles.

Measurement of the Lifetime of Minority Carriers in Germanium

WILLIAM G. SPITZER,* TOMAS E. FIRLE, MELVIN CUTLER, ROBERT G. SHULMAN,† AND MILTON BECKER
Semiconductor Research and Development Department, Hughes Aircraft Company, Culver City, California

(Received May 12, 1954)

Two methods are described for the measurement of lifetime of minority carriers. One depends on pulse injection of carriers in a filament and detection, after a known time, at a collector. The second makes use of the decay of the conductivity modulation caused by minority carriers after injection at a single contact. Both measure the lifetime in a small region rather than the average value over a large part of the sample.

1. INTRODUCTION

THE measurement of the lifetime of minority carriers has become an important problem in semiconductor studies. Several methods for making such measurements have been described in the literature.[1–4] The purpose of this paper is to describe two new methods, which are characterized by the fact that they measure the lifetime in relatively small regions of the semiconductor rather than an average value over the sample. Both methods have the additional advantage of measuring the lifetime directly rather than deriving it from the diffusion length, thus avoiding the necessity of measuring small distances accurately. The first, which we call the Pulse Delay Method (PDM), is a modification of experimental methods described by Haynes and Shockley.[1] The second is more novel, and makes use of conductivity modulation at a point contact. It is referred to as the Conductivity Modulation Method (CMM).

2. PULSE DELAY METHOD

The PDM is a modification of methods used by Haynes, Shockley, and Pearson in measuring lifetime and drift mobility. Minority carriers are injected into a germanium filament by a current pulse at a point-contact emitter. After a time, which can be varied and during which the injected carriers recombine to some extent, they are swept down the filament by another current pulse past a collector contact. The magnitude of the collector response as a function of the time between pulses is observed on an oscilloscope.

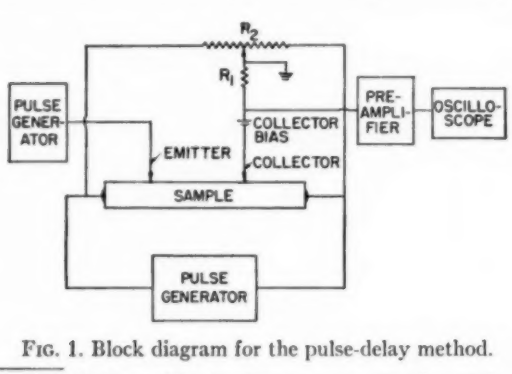

FIG. 1. Block diagram for the pulse-delay method.

Description of Method

Figure 1 is a block diagram of the apparatus used. The emitter and collector are point contacts. The latter is maintained at a dc reverse bias, while the emitter is biased in the forward direction only when the first pulse is applied. In operation, the emitter is pulsed first for about 4 microseconds. (The shape and duration of the emitter pulse are not critical.) The injected holes remain in the vicinity of the emitter, spreading out by diffusion. (In order to fix our ideas, we shall refer to measurements on n-type materials. Both methods can be used with p-type materials, with appropriate changes in current directions.) After a variable time delay, a second pulse generator produces a voltage across the filament which sweeps the holes past the collector; the resulting current pip is observed as a voltage across a resistor R_1 on a synchronized oscilloscope. The impedance of R_1 is small compared to the collector impedance. The potentiometer, R_2, allows one to balance out the sweeping pulse in the collector circuit. This would otherwise appear as a plateau on which the hole-response pip is situated. Removal of most of the plateau permits greater amplification of the pip, and thus greater sensitivity in measuring the collector response. Pulse transformers are used to isolate the grounds of the pulse generators.

A typical oscilloscope pattern is shown in Fig. 2. The time intervals which are noted are bounded, consecutively, by the beginning of the emitter pulse, the end of the emitter pulse, the beginning of the sweeping field pulse, the arrival of the injected holes at the collector, and the end of the sweeping field pulse. During the

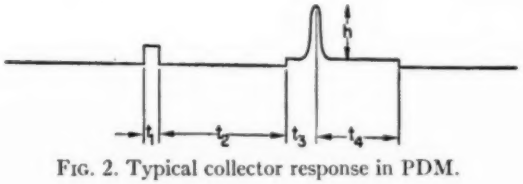

FIG. 2. Typical collector response in PDM.

* Present Address: Physics Department, Purdue University, Lafayette, Indiana.

† Present Address: Bell Telephone Laboratories, Murray Hill, New Jersey.

[1] J. R. Haynes and W. S. Shockley, Phys. Rev. **81**, 835 (1951), Shockley, Pearson, and Haynes, Bell System Tech. J. **28**, 344 (1949).

[2] Navon, Bray, and Fan, Proc. Inst. Radio Engrs. **40**, 1342 (1952).

[3] L. B. Valdes, Proc. Inst. Radio Engrs. 40, 1420 (1952).

[4] E. M. Pell, Phys. Rev. **90**, 278 (1953).

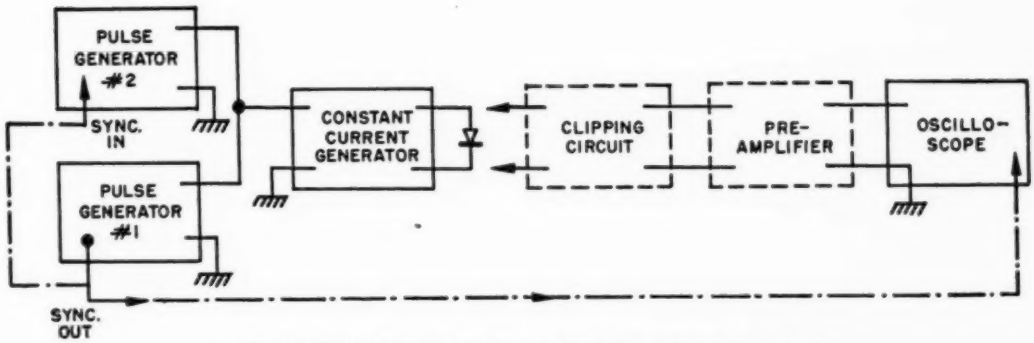

FIG. 3. Block diagram for the conductivity-modulation method.

course of a measurement, t_2 is the only time interval which is varied. As we shall show in more detail below, this has the consequence that the number of holes which reach the collector changes only as the result of recombination which occurs in this time interval, during which the holes are near the emitter. The concentration of excess holes which reach the collector is related to the collector response through the Haynes equation.[1,5,6]

Theory of the Pulse Delay Method

The current I in the collector is related to the excess hole concentration p by the equation

$$I=I_0[1+(\gamma p/n_0)], \tag{1}$$

where I_0, γ, and n_0 are constants for a fixed collector bias. If the smallest value of t_2, which we denote as t_s, is not smaller than the recombination time at the emitter τ_e, one can express the hole concentration at the collector as[6]

$$p=p(t_s)\,\mathrm{xep}[-(t_2-t_s)/\tau_e]\exp(-t_3/\tau_f). \tag{2}$$

The first exponential represents the decay occurring after the arbitrary time t_s in the region of the emitter, and the second exponential represents the decay occurring as the holes are swept to the collector, with an average decay time τ_f.

The time interval t_3 is constant during a measurement, since the sweeping field is not changed. Therefore, $\exp(-t_2/\tau_e)$ is the only factor in Eq. (2) which varies in the course of measurement. On the other hand, the height h of the signal appearing on the oscilloscope is proportional to the current difference $(I-I_0)$ in Eq. (1), if the resistance R_1 in the measuring circuit is small compared to the impedance of the collector. $(I-I_0)$ is, in turn, proportional to p, so that one has, on combining Eqs. (1) and (2),

$$h=\mathrm{const}\exp(-t_2/\tau_e). \tag{3}$$

One sees that τ_e can be computed simply from the measurement of the response h as a function of the delay time t_2, both of which are obtained directly on the oscilloscope. The decay which occurs during the transit of the holes from the emitter to the collector appears in the factor $\exp(-t_3/\tau_f)$, and does not enter into the measurement because t_3 remains constant.

The region in which the measured decay occurs is limited to the distance that the injected carriers diffuse away from the emitter, and is of the order of $(D_p t_2)^{\frac{1}{2}}$, where D_p is the diffusion constant for the holes. For typical measurements in germanium of lifetimes of the order of 100 microseconds, this is about 0.5 mm. The equations relating the measured lifetime to surface and bulk recombination are discussed by Shockley.[6] A consideration of the latter, as well as experimental observations, shows that one obtains the correct exponential-decay curve for h as long as t_s (the minimum value for t_2) is not smaller than the measured τ_e. If one uses smaller values of t_2, Eq. (2) is not valid, and one observes a more rapid decay because of the fact that injected carriers are concentrated near the surface at the emitter.

Diffusion of the carriers along the axis of the filament during the delay period leads to a small error in the use of the formula in Eq. (2). One can make a correction, but this was not done in our experiments.

3. THE CONDUCTIVITY MODULATION METHOD

The second method makes use of the modulation of the spreading resistance of a point contact, which results from the injection of minority carriers.[7] The carriers are injected by a forward-current pulse. After a variable time, during which the carriers recombine and diffuse, a second forward-current pulse is applied. The spreading resistance modulation because of injection of carriers, which appears as a spike on the leading edge of the voltage pulse, is measured as a function of the delay time. The primary advantage of this method is that little preparation is needed, since it requires only a single-point contact on a sample of any size or shape.

Description of Method

A whisker contact is made on a lapped and etched surface on the semiconductor ingot, to which a base

[5] J. Bardeen, Bell System Tech. J. **29**, 469 (1950).
[6] W. S. Shockley, *Electrons and Holes in Semiconductors* (D. Van Nostrand Company, Inc., New York 1950), pp. 319–325.
[7] A. Many, Proc. Phys. Soc. (London) **67B**, 9 (1954).

contact has been made. The diode is pulsed with pairs of rectangular constant-current pulses in the forward direction from zero bias, and the voltage response is observed on an oscilloscope.

Figure 3 shows a block diagram of the experimental arrangement. The voltage pulses of two pulse generators are fed into a constant-current generator. The latter generates pairs of constant-current pulses of equal amplitude and rise time in the diode. The voltage across the diode is observed on a synchronized oscilloscope. The sensitivity is improved by clipping to remove the bottom part of the voltage pulses. The first pulse generator, set at a low repetition rate, provides the synchronizing signal for the oscilloscope and for the delay line into the second pulse generator.

The constant amplitude twin-current pulses applied to the diode with given time delays are shown in Fig. 4(a), while Fig. 4(b) shows the corresponding voltage pulses. The spike on the second voltage pulse is smaller than the first, because some injected carriers still remain from the first current pulse. Figure 4(c) is a multi-exposure photograph of the voltage pulses, for a large number of delay times. It was prepared by photographing on the same plate a number of oscilloscope traces such as in 4b, with different values of t. The length of the second pulse was decreased in order to avoid confusion in the photograph. It is seen that as the delay time increases, the second spike approaches the first in magnitude. A graph of the difference of the voltage peaks (V_1-V_2) *versus* the delay time t results in an exponential curve except near $t=0$. The corresponding plot of $\ln(V_1-V_2)$ against t, as shown in Fig. 5, gives a straight line, for which the reciprocal of the slope is equal in magnitude to the lifetime.

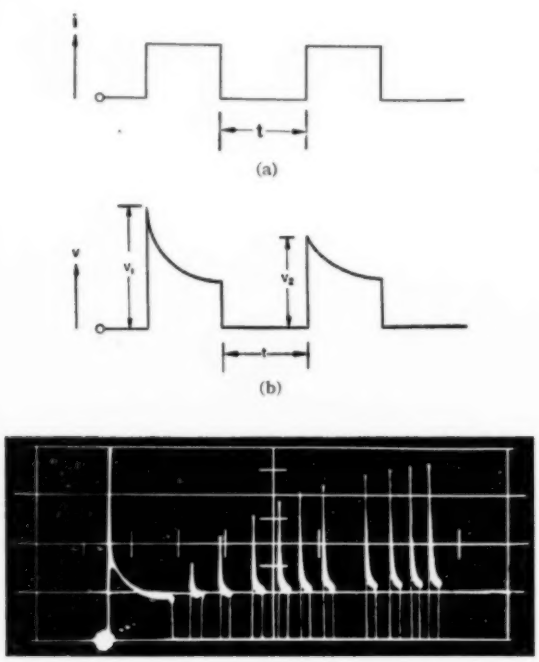

FIG. 4. (a) Applied-current pulses. (b) Voltage pulses across contact. (c) Multi-exposure oscillogram of experimental-voltage pulses.

Theory of the Conductivity Modulation Method

The voltage V resulting from the spreading resistance at a point contact on extrinsic material (assuming a spherical contact) is

$$V(t)=\frac{I\rho}{2\pi}\int_a^\infty \frac{r^{-2}dr}{1+(b+1)(p/bn_0)}, \tag{4}$$

where a is the radius of the contact, ρ is the normal resistivity, b is the ratio of electron mobility to hole mobility, p is the excess concentration of holes, n_0 is the equilibrium concentration of electrons, and I is the current. V is implicitly, through the dependence of p on t, a function of the time t since the end of the previous pulse; p is a function of the radial distance r as well as the delay time t. If t is not too small, then p has a steady state spatial distribution $f(r)$, and can be expressed as

$$p=f(r)\exp(-t/\tau_e), \tag{5}$$

where, as before, τ_e is the lifetime in the point contact region.[6] The peak of the first pulse V_1 can be assumed to be equal to some constant (representing the voltage drop in the barrier region and parts of the circuit external to the diode), plus $V(\infty)$. (We assume that the repetition time is very large compared to τ_e, and is therefore effectively infinite.) The value of V_2 is this

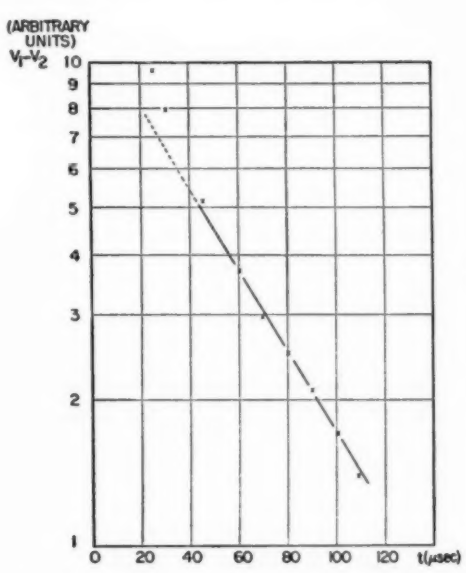

FIG. 5. Experimental plot of $\log(V_1-V_2)$ as a function of time in CMM for n-type germanium with resistivity of 8 ohm cm. The current pulses are 10 ma, and the measured lifetime is 51 microseconds.

TABLE I. Comparison of PDM and CMM values of τ_e for a number of samples.

PDM	CMM
66 microseconds	74 microseconds
72	72
102	100
51	54
40	46
38	42
225	210

same constant plus $V(t)$. Therefore, the difference is

$$V_1-V_2=V(\infty)-V(t)$$

$$=\frac{I\rho}{2\pi}\int_a^\infty\frac{b+1}{br^2}\frac{f}{n_0}$$

$$\times\exp(-t/\tau_e)\left[1+\frac{b+1}{b}\frac{f}{n_0}\exp(-t/\tau_e)\right]^{-1}dr. \quad (6)$$

If the concentration of injected minority carriers is small compared to the majority concentration,

$$(b+1)(f/bn_0)\exp(-t/\tau_e)\ll 1,\ V_1-V_2$$

$$=(I\rho/2\pi)\left[\int_a^\infty drr^{-2}(b+1)(f/bn_0)\right]\exp(-t/\tau_e). \quad (7)$$

The expression in the brackets is a constant independent of the delay time. Thus, one can expect exponential decay of (V_1-V_2) with time, provided that the delay time t is not too small. Consideration of the approximation in Eq. (7) and of the solution of the equations for recombination at the surface, discussed previously, determines what constitutes sufficiently large values of t.

It is not to be expected that the initial voltages, V_1 and V_2, correspond to the spreading voltage of the point contact, with no injection having resulted from the corresponding current pulse. This is because the rise time (t_r) of the current pulse is not zero, in practice, with the consequence that the injected carriers will have penetrated the semiconductor to a distance r_r equal, at least, to the diffusion distance

$$r_r\geq(D_pt_r)^{\frac{1}{2}}. \quad (8)$$

The experimental rise times of the order of 0.5 microsecond correspond to r_r values of about 4×10^{-3} cm; this is a good deal larger than the contact radius. However, the equations derived in the foregoing can be assumed to be valid if one regards the parameter a as representing this penetration distance r_r instead of the actual contact radius; r_r should remain very nearly constant if the rise time is constant with different delay times. The fact that the experimental results conform with Eq. (7) supports this assumption.

TABLE II. Effect of etching on lifetime.

Region	Etching time (sec)	T_e (microsecond)	Surface recombination velocity[a] (cm/sec)
N-type sample, 7.5 ohm-cm resistivity			
A	0	21	>10 000
B	1	59	2 600
C	5	124	330
D	15	152	250
E	60	174	190
P-type sample, 4-ohm-cm resistivity			
A	0	20	>10 000
B	1	40	2 200
C	5	80	650
D	15	160	220
E	60	175	150

[a] This was computed with no correction for bulk recombination.

4. DISCUSSION

The accuracy of the CMM has been checked by comparing the results of measurement against the PDM, using the same whisker contact. This was done by preparing a filament with contacts suitable for PDM measurement and making, as well, the CMM measurement between the emitter and the filament end. The results of the comparison, shown in Table I, show agreement within the experimental error.

As an illustration of the value of measurements of localized lifetime the results of the effect of etching on lifetime of a single filament are shown in Table II. The surface of a lapped filament of germanium was etched in the same solution, different parts of the filament being treated successively for different lengths of time. As a result, measurements of lifetime as a function of etching time were obtained, where the possibility of changes in other variables was minimized.

The PDM has several advantages over the original methods used by Haynes, Shockley, and Pearson:

1. Variables are simply and directly measured.
2. Low-duty cycle in the sweeping pulse cuts down heating.
3. Lifetime is measured in a small region of the sample.

The disadvantages of the PDM consist in the necessity of preparing the sample in the form of a filament, and of making a collector contact. The latter limits the method to the study of extrinsic material. The apparatus which we have used makes measurements of lifetime over the range from 5 to 800 microseconds, and has been used successfully on silicon.

The CDM has the advantage of requiring little sample preparation, which makes it useful in metallurgical studies. The use of a point contact does not seem to be a limitation, since the contact is not used as a collector. One can observe conductivity modulation even when the material is intrinsic, and lifetime values have been obtained[8] which are in agreement with other methods of measurement (using photo-injection).

[8] These are the observations of O. J. Marsh.

Electron Temperature in the Parallel Plane Diode*

T. N. CHIN
University of Illinois, Urbana, Illinois
(Received March 6, 1954)

Chandrasekhar's relaxation time is applied to the electron gas in flow. By determining the relaxation time, t_R, and the mean transit time, t_T, two types of electron flow may be characterized: anisotropic flow if $t_T \ll t_R$, and isotropic flow if $t_R \ll t_T$. It is shown that the electron temperature along the flow decreases as the mean velocity of the electrons increases in a parallel plane diode. In the given examples, the boundary conditions are obtained for a particular model which has been recommended in the study of thermionic emission.

IN view of the fact that the velocity in a physical electron stream is not single valued, thermal velocities have been of interest in the study of the electron flow for some time. In recent studies an electron stream has been pictured as a flow of the electron gas. Applying the kinetic theory of gases, W. C. Hahn[1] analyzed the possible influence on the electron flow after taking into account the hydrostatic pressure of the electrons. Later, Parzen and Goldstein[2] indicated that the hydrostatic pressure in an electron beam may cause reduction in gain and noise figure in a travelling wave tube.

In formulating a general theory of nonuniform gases, Chapman and Cowling[3] discussed in detail the concepts and definitions that are essential in this field. Based on their definition of temperature, the velocity spread in the electron flow can readily be expressed in terms of an electron temperature Θ, i.e.,

$$\Theta=\frac{m}{nk}\int \mathbf{u}\mathbf{u}\varphi(\mathbf{u},\mathbf{r},t)d\mathbf{u}, \tag{1}$$

where m and n are the mass and number density of the electrons, k is Boltzmann's constant, $\mathbf{u}$ is the peculiar velocity,† and $\varphi(\mathbf{u},\mathbf{r},t)$ denotes the velocity distribution function at $\mathbf{r}$ and t. For the electron beam in a field free space, H. M. Mott-Smith[4] treated the problem by allowing the velocity distribution to be expanded into a Maclaurin series with respect to a point where the function is known.

The present work is intended to show the change of electron temperature in relation to the mean velocity of the electrons in a parallel plane diode. Neglecting the effect of magnetic fields, we shall assume that the process discussed in this paper is adiabatic. All equations, except when explicitly noted otherwise, are written in cgs electrostatic units.

MACROSCOPIC EQUATIONS

In considering a group of particles in the flow, it is possible to obtain three macroscopic equations with the aid of the summational invariants[3] for encounters. They are:

$$\nabla(n\langle\mathbf{c}\rangle)+\frac{\partial n}{\partial t}=0 \tag{2}$$

$$\nabla\cdot(kn\Theta)-mn\left[\mathfrak{F}-\langle\mathbf{c}\rangle\cdot(\nabla\langle\mathbf{c}\rangle)-\frac{\partial\langle\mathbf{c}\rangle}{\partial t}\right]=0 \tag{3}$$

$$\nabla\cdot\left[\left(\Sigma\frac{kn\Theta_i}{2}\right)\langle\mathbf{c}\rangle\right]+\frac{\partial}{\partial t}\left(\Sigma\frac{kn\Theta_i}{2}\right)+\langle\mathbf{c}\rangle\cdot[\nabla\cdot(kn\Theta)]+kn\Theta\cdot(\nabla\langle\mathbf{c}\rangle)-mn\langle\mathbf{c}\rangle\cdot\left[\mathfrak{F}-\langle\mathbf{c}\rangle\cdot(\nabla\langle\mathbf{c}\rangle)-\frac{\partial\langle\mathbf{c}\rangle}{\partial t}\right]=0. \tag{4}$$

In these equations the four macroscopic quantities are (1) number density n, (2) mean velocity $\langle\mathbf{c}\rangle$, (3) external force $\mathfrak{F}$, and (4) electron temperature Θ. Due to the fact that $k\Theta\ll m\langle\mathbf{c}\rangle^2$ in the electron flow, the third moment[5] of the velocity distribution function is supposed to be zero in deriving the last equation.

The external forces[6] acting on the particles are those resulting from sources outside the location of particles in consideration, whereas the internal forces acting on the particles are the interactions between the close particles. Since the effect of the internal forces is included in the encounter process, these equations are applicable in general to the case of the electron flow. The electron temperature Θ in this paper consists of three components—Θ_1, Θ_2, and Θ_3, which correspond to the velocity spread in the three mutually perpendic-

* This paper is a portion of the Ph.D. thesis submitted by the author at the University of Illinois. A preliminary report of this was presented at the Conference on Electronic Devices at Durham, New Hampshire, June 21–22, 1951.

[1] W. C. Hahn, Proc. Inst. Radio Engrs. **36**, 1115 (1948).

[2] P. Parzen and L. Goldstein, J. Appl. Phys. **22**, 398 (1951).

[3] Chapman and Cowling, *The Mathematical Theory of Non-Uniform Gases* (Cambridge University Press, Cambridge, England 1939).

† The peculiar velocity is defined as the velocity relative to axes moving with the mean velocity of the gas at the point (see reference 3, p. 26).

[4] H. M. Mott-Smith, J. Appl. Phys. **24**, 249 (1953).

[5] A. Hald, *Statistical Theory with Engineering Applications* (John Wiley and Sons, Inc., New York, 1952), pp. 105, 625.

[6] Herein, the concept of potential becomes one from which only the external forces are derivable. See, for instance, H. Goldstein, *Classical Mechanics* (Addison-Wesley Press, Inc., Cambridge, Massachusetts, 1950), p. 8.

ular directions. In the molecular gas, where these three components are always equal, the temperature may be degenerated into one component, thus a scalar.

For the sake of simplicity, we shall confine ourselves to the steady-state case. For the electron flow in a parallel plane diode, where the variations of the macroscopic quantities n, $\langle \mathbf{c} \rangle$, $\mathfrak{F}$, and Θ_i's, are only in the direction of the flow, the general equations derived for the electron flow can be reduced to simpler forms:

$$\frac{d}{dx}(nv)=0, \quad (5)$$

$$\frac{d}{dx}(kn\Theta_1)-mn\left(F-v\frac{dv}{dx}\right)=0, \quad (6)$$

$$\frac{d}{dx}\left[\frac{knv}{2}(3\Theta_1+\Theta_2+\Theta_3)\right]-mnv\left(F-v\frac{dv}{dx}\right)=0. \quad (7)$$

where v, F, and x are used instead of $\langle \mathbf{c} \rangle$, $\mathfrak{F}$, and $\mathbf{r}$. The first two equations are identical with the equations of continuity and momentum derived for a continuous fluid in hydrodynamics. The third equation[7] expresses essentially the conservation of energy in the electron flow. If Θ is zero, the third equation reduces to the second equation which, in losing its term $d/dx(kn\Theta_1)$, would precisely become the classical differential equation[8] of motion.

Another equation at our disposal is Poisson's equation,

$$\frac{dF}{dx}=4\pi\frac{e^2}{m}n, \quad (8)$$

which correlates two of the four macroscopic quantities under consideration. Since Θ has three components, the number of unknowns involved in this case is six. Thus, two more conditions besides these four equations are necessary for determining completely the desired macroscopic quantities.

A general form of the velocity distribution function may be written as

$$\varphi(\mathbf{u})=n\left(\frac{m}{2\pi k}\right)^{\frac{3}{2}}(\Theta_1\Theta_2\Theta_3)^{-\frac{1}{2}} \times\exp\left[-\frac{m}{2k}\left(\frac{u_1^2}{\Theta_1}+\frac{u_2^2}{\Theta_2}+\frac{u_3^2}{\Theta_3}\right)\right] \quad (9)$$

where n and Θ_i's may be functions of $\mathbf{r}$. This function is generally known as Schwarzschild's law[9] of ellipsoidal distribution of velocities.

[7] With the expression (6), Eq. (7) is often written in another form. See reference 3, Eq. 4, on p. 52.

[8] I. Langmuir and K. T. Compton, Revs. Modern Phys. **13**, 191 (1931); also L. Page and N. E. Adam, Phys. Rev. **76**, 381 (1949).

[9] S. Chandrasekhar, *Principles of Stellar Dynamics* (University of Chicago Press, Chicago, 1942), p. 7.

TWO CHARACTERISTIC TYPES OF FLOW

In this treatment, the transit time is extended to apply to a group of electrons. An appropriate definition of what we may call a "mean transit time" can be given by

$$t_T=\int_a^b\frac{dx}{v(x)} \quad (10)$$

for a spatial interval between points a and b in which the electron gas is under consideration. Since the mean velocity, v, is a single-valued function of x and greater than zero provided there is any flow of electrons, formula (10) is applicable to any section of the electron flow in a diode.

If a group of electrons is allowed sufficient time to complete its mutual interactions, this group of electrons must reach its equilibrium condition. From this, one can immediately infer that the three temperature components for this group of electrons should be equal to each other. Here we shall follow Chandrasekhar's[10] extensive work on the problem of encounters in stellar systems. The analogy with the electron gas is rather obvious if one considers that in both cases the interaction forces drop with the inverse square of mutual distances between the particles in question. Since each encounter will result in an exchange of energy, ΔE, between the two particles taking part in the encounter, the sum, $\sum(\Delta E)^2$, over all possible encounters will certainly increase with time. Chandrasekhar therefore defines a relaxation time for a star cloud as the time required for $[\langle\sum(\Delta E)^2\rangle]^{\frac{1}{2}}$ to become equal to the initial kinetic energy of the stars. Accepting this definition and converting the quantities appropriate for the electron gas, one finds the so determined relaxation time,

$$t_R=\frac{9}{16(\pi)^{\frac{1}{2}}}\frac{m^{\frac{1}{2}}(k\Theta)^{\frac{3}{2}}}{ne^4\ln(3k\Theta/2e^2n^{\frac{1}{3}})}. \quad (11)$$

In a situation where the group of electrons emitted from the cathode are so swiftly drawn to the anode ($t_T \ll t_R$), the group of particles under consideration will not reach their equilibrium conditions. An observer, moving with the mean velocity along the electron flow, should not observe any essential change of the velocity components perpendicular to the axis of the flow. Thus, the temperature components perpendicular to the direction of the flow become constant in the flow, namely,

$$\partial\Theta_2/\partial x=\partial\Theta_3/\partial x=0. \quad (12)$$

Since the temperature components in this case are not necessarily equal to each other, this type of flow may be called the "anisotropic flow."

In a contrary situation where the relaxation time of the electron gas is much shorter than the transit time in consideration ($t_R \ll t_T$), all three temperature compo-

[10] S. Chandrasekhar, Astrophys. J. **93**, 285; **94**, 511 (1941).

nents in this case are equal to each other, namely,

$$\Theta_1=\Theta_2=\Theta_3. \tag{13}$$

Since the temperature components are independent of direction in this case, this type of flow may be called the "isotropic flow."

These conditions, together with the four general equations derived above, enable us to solve completely all the macroscopic quantities of the electron flow. Since the relaxation time is about inversely proportional to the number density of the electrons under consideration, the above conditions indicate that the number density in the anisotropic flow is generally much lower than that in the isotropic flow. More particularly, if the number density is low enough so that the space charge effect can be neglected, Poisson's equation will then be reduced to Laplace's equation in the case of the anisotropic flow.

Now, integrating Eq. (5) with respect to x, Eq. (5) becomes

$$nv=j, \tag{14}$$

where j is an integration constant of the equation. Since the displacement current is zero in the steady-state case, je becomes the actual electric current density in the diode circuit.

Another possibility of establishing a functional relationship valuable for both cases would be to eliminate the external force, F, from Eqs. (6) and (7). Eliminating F from these equations and making use of Eq. (5), one obtains

$$\frac{d}{\Theta_1 dx}(\Theta_1+\Theta_2+\Theta_3)+\frac{2}{v}\frac{dv}{dx}=0. \tag{15}$$

In the case of the "anisotropic flow," where the temperature components Θ_2 and Θ_3 are independent of x, Eq. (15) yields[11]

$$\Theta_1 v^2=\text{constant}. \tag{16}$$

Similarly, in the case of the "isotropic flow," where the components of the electron temperature are equal, Eq. (15) then yields

$$\Theta_1^3 v^2=\text{constant}. \tag{17}$$

These two equations indicate that the electron temperature along the flow decreases as the mean velocity of the electrons increases in a parallel plane diode. If one could find the mean velocity as a function of x in the electron flow under consideration, the variation of the electron temperature along with the electron flow could be determined from Eqs. (16) and (17).

ANISOTROPIC FLOW

In the case of the anisotropic flow, Laplace's equation for the field between two parallel planes merely implies that

$$F=eE/m, \tag{18}$$

where E is the applied electric field, independent of the coordinate, x. With Eq. (18), and Eqs. (14) and (16) just derived, one is able to replace n, Θ_1, and F of Eq. (6) in terms of the mean velocity, v, and the applied electric field, E. Equation (6) then reads

$$v\frac{dv}{dx}-\frac{A}{v^3}\frac{dv}{dx}-\frac{eE}{m}=0, \tag{19}$$

where

$$A=3k\Theta(0)[v(0)]^2/m.$$

After the equation is integrated with respect to x, we have

$$v^2+\frac{A}{v^2}-\frac{2eEx}{m}=G, \tag{20}$$

where

$$G=v^2(0)+\frac{A}{v^2(0)}.$$

With the constants A and G, determined as above, Eq. (20) can be written as

$$\left\{\left[\frac{v(x)}{v(0)}\right]^2-1\right\}-\frac{3k\Theta_1(0)}{m[v(0)]^2}\times\left\{1-\left[\frac{v(0)}{v(x)}\right]^2\right\}=\frac{2eEx}{m[v(0)]^2}. \tag{21}$$

From Eq. (21), one may calculate the mean velocity, v, as a function of the coordinate x for an electric field, E.

Although our understanding of the thermionic emission[12] has been advanced considerably in the last decade, we are still unable to calculate the quantities n, v, and Θ_1 accurately at the emission surface. Here we use a reasonable model from which these values can be evaluated. The accepted model is as follows: All of the electrons which arrive at the anode are collected by the anode without causing any stray disturbances. The emission surface can be simulated by a uniform surface of work function, W, with a velocity-dependent transmission coefficient D of the simple form (Fig. 1). Based on the empirical reflection factor,[13] this is designed to approximate the actual coefficient by a simpler form

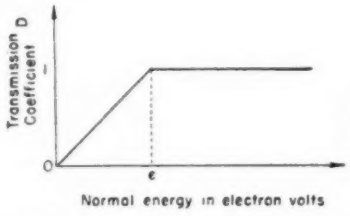

FIG. 1. Associate transmission coefficient of a thermionic cathode.

[11] See M. E. Hines, J. Appl. Phys. **22**, 1385 (1951); and Philip Parzen, J. Appl. Phys. **22**, 1386 (1951).

[12] C. Herring and M. H. Nichols, Revs. Modern Phys. **22**, 398 (1951).

[13] W. B. Nottingham, Phys. Rev. **49**, 78 (1936); also C. S. Hung, J. Appl. Phys. **21**, 37 (1950).

in which the normal energy ϵ is of the order of half an electron volt. Then the velocity distribution function at the emission surface becomes

$$f(0)=\frac{2m^3}{h^3}D\exp\left[-\frac{eW}{kT}\right]\times\exp\left[-\frac{m(c_1^2+c_2^2+c_3^2)}{2kT}\right],\quad c_1>0 \quad (22)$$

$$=0,\quad c_2<0$$

where T is the temperature of the emission surface. With this velocity distribution function at the emission surface, one is able to evaluate[14] the boundary values,

$$n(0)=\frac{(2\pi mkT)^{\frac{3}{2}}}{2h^3}\left(\frac{kT}{e\epsilon}\right)\exp\left[-\frac{eW}{kT}\right] \quad (23)$$

$$v(0)=2\left(\frac{2kT}{\pi m}\right)^{\frac{1}{2}}\left[1-\exp\left(-\frac{e\epsilon}{kT}\right)\right] \quad (24)$$

$$\Theta_1(0)=\frac{3\pi-8}{\pi}T. \quad (25)$$

As compared with the equation of motion in the single-valued velocity theory, Eq. (21) contains an additional term—the second term on the left-hand side of Eq. (21). Since the factor $3k\Theta_1(0)/mv^2(0)$ in this term is usually of the order of unity, this additional term is actually a correction term to calculate the mean velocity of the electrons close to the emission surface. After the mean velocity of the electrons in the diode is obtained, the number density and the electron temperature can easily be determined from the functional relationships, Eqs. (14) and (16), derived above.

Now, a typical example for the anisotropic flow may be cited here. Suppose the work function[15] of the emission surface is 1.2 volts. The value of t_R (Fig. 2) is calculated from Eqs. (11) and (23) against the cathode temperature. In the case of an operation where

cathode temperature = 700°K,

cathode anode spacing = 0.5 cm,

anode voltage with respect to the cathode = 300 volts, one obtains from Eqs. (23) and (11)

$$t_R=1.8\times10^{-7}\text{ second},$$

but from Eqs. (21) and (10)

$$t_T=1.9\times10^{-9}\text{ second}.$$

The result $t_T\ll t_R$ agrees with the specification given to this type of flow.

[14] T. N. Chin, "Thermodynamics and statistics of the electron gas," Tech. Report No. 3-3, ONR contract (unpublished).

[15] G. Herrmann and S. Wagener, *The Oxide-Coated Cathode* (Chapman and Hall Ltd., London, England, 1951), Vol. II, p. 165.

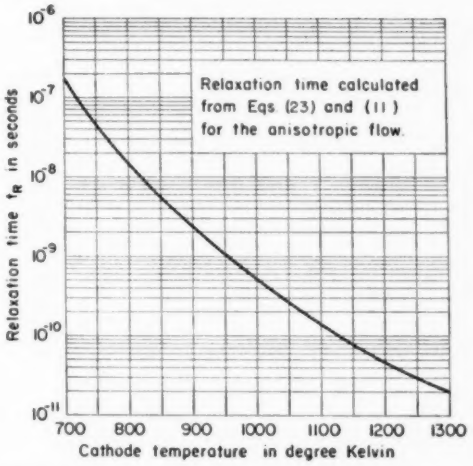

FIG. 2. The plot of relaxation time close to the emission surface against the cathode temperature.

ISOTROPIC FLOW

As mentioned earlier, the number density is generally high in the isotropic flow. This may be due to a weak applied field which does not draw all the emitted electrons away quickly enough. Also, it may occur if the emission current is too high for the applied voltage on the anode. Hence, Poisson's Eq. (8) reduces to

$$\frac{dF}{dx}=4\pi\frac{je^2}{mv} \quad (26)$$

after the relation (14) between the number density, n, and the mean velocity, v, is used. Through Eqs. (14) and (17), n and Θ_1 of Eq. (6) can be put in terms of the mean velocity, v. Then

$$v\frac{dv}{dx}-\frac{B}{v^{5/3}}\frac{dv}{dx}-F=0, \quad (27)$$

where

$$B=\frac{5k\Theta_1(0)}{3m}[v(0)]^{\frac{2}{3}}.$$

Eliminating F from Eqs. (26) and (27), one obtains

$$\left(1-\frac{B}{v^{5/3}}\right)v\frac{d^2v}{dx^2}+\left(1+\frac{5B}{3v^{8/3}}\right)\left(\frac{dv}{dx}\right)^2-\frac{4\pi je^2}{mv}=0. \quad (28)$$

This equation does not involve the independent variable x explicitly[16] and it may therefore be simplified to a first-order linear differential equation by suitable transformations. The solution[14] can be written as

$$x+L=\int\left\{M-\frac{8\pi je^2v}{m}\left(1+\frac{3B}{5v^{8/3}}\right)\right\}^{-\frac{1}{2}}\times\left(1-\frac{B}{v^{8/3}}\right)vdv, \quad (29)$$

[16] E. L. Ince, *Ordinary Differential Equations* (Dover Publications, New York, 1926), p. 43.

where L and M are to be determined by boundary conditions.

In the isotropic flow, the expression for the cathode emission

$$j_i=\frac{4\pi m}{h^3}(kT)^2\frac{kT}{e\epsilon}\left\{1-\exp\left(-\frac{e\epsilon}{kT}\right)\right\}\exp\left[-\frac{eW}{kT}\right] \quad (30)$$

remains the same; but a large portion of the emitted current is compensated by the returning component of the current at the emission surface. Thus the actual current density, j, of the isotropic flow is one such that

$$j/j_i=R_S\ll 1.$$

This parameter, R_S, is the ratio of the number of electrons actually drawn to the anode and the number of emitted electrons per unit area in unit time. In this situation, the electron gas at the emission surface would not follow the half Maxwellian velocity distribution function, Eq. (22), but rather would approach a nearly symmetric Maxwellian velocity distribution function. This nearly Maxwellian electron gas may expand to a great extent away from the cathode. In other words, one can then assume the electron gas at the emission surface to be in equilibrium with the emitter.

$$\Theta_1(0)=T. \quad (31)$$

Since the electron gas at the emission surface is nearly Maxwellian, the returning component of current is

$$n(0)[kT/2\pi m]^{\frac{1}{2}}.$$

With the above description of this model, the boundary values of n and v can be determined at the cathode surface. They are:

$$n(0)=j_i(1-R_S)[2\pi m/kT]^{\frac{1}{2}} \quad (32)$$

$$v(0)=[kT/2\pi m]^{\frac{1}{2}}R_S/(1-R_S) \quad (33)$$

in which j_i, T, and R_S are considered as known quantities for the determination.

To evaluate the two constants, L and M, another boundary value of v must be determined for this problem. Because the relaxation time is about inversely proportional to the number density of the electrons, it is apparent that the isotropic flow may become anisotropic if the electrons in the flow are accelerated to reach sufficiently high velocities. In the region where the mean velocity reaches a sufficiently high value, the percentage difference of the mean velocities calculated from Eqs. (20) and (29) for the two types of flow is much smaller than the difference in the region of low mean velocity. Because of this fact, a good approximate value of $v(x_2)$ can be calculated from Eq. (20) for the anisotropic flow, provided that a sufficiently long distance, x_2, is selected for the calculation.

Using the same example given above, one may raise the cathode temperature to 1100°K for the isotropic flow. When the anode voltage is about 300 volts, the parameter R_S has the value of 0.005. From Eqs. (29) and (10), the mean transit time of the flow is obtained

$$t_T=2.4\times10^{-8}\text{ second},$$

for an interval from $v(0)$ to $10v(0)$. However, from expressions (32) and (11), one may calculate the relaxation time (Fig. 3) to be

$$t_R=3.4\times10^{-11}\text{ second}.$$

The result $t_R\ll t_T$ justifies the condition adopted to specify this type of flow.

CONCLUDING REMARKS

Some progress has been made on the electron flow problems taking into account the effect of the particle encounters. For the cumulative effect of feeble encounters,[17] it is generally difficult to determine the encounter term in the Boltzmann equation. But this effect does not introduce a significant error in calculating the relaxation time[10] for gases.

Since Eq. (28) indicates that v is a slowly varying function when v is small, the assumption of constant temperature made by Hahn may be justified only in the region very close to the cathode.

In the present study two types of flow are characterized by the order of the magnitudes of the transit time and the relaxation time. Equations (16) and (17) give the velocity dependence of the electron temperature for the two types of flow. Although it is not yet possible to determine exactly the velocity dependence of the electron temperatures in the flow lying between these two characteristic types, one may conclude that the electron

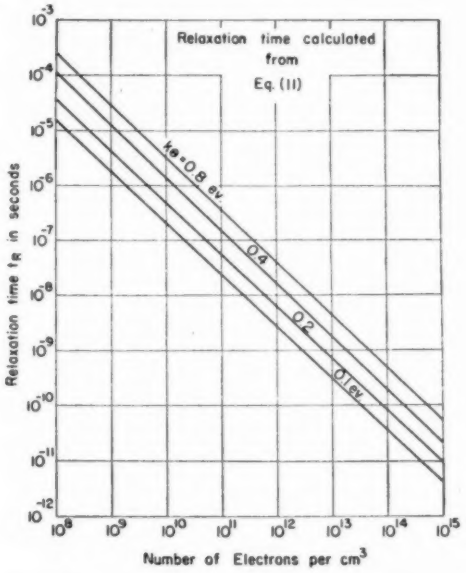

FIG. 3. Relaxation time of the electron gas as a function of the number density with the electron temperature as a parameter.

[17] J. H. Jeans, *Astronomy and Cosmogony* (Cambridge University Press, Cambridge, England, 1929), p. 319.

temperature along the flow decreases as the mean velocity of the electrons increases in the parallel plane diode.

For the case of a travelling wave tube, the conditions assumed by Parzen and Goldstein are $n=10^9$ and $\Theta=1000°K$ (corresponding to 0.09 electron-volt). In the relaxation time (Fig. 3) of this condition, the drift space is found to be 1870 cm for the electrons having a mean velocity of 1000 volts. This agrees reasonably well with the results obtained by Mott-Smith.

However, if the region between the cathode and the drift space is considered as a parallel plane diode and the electron temperature at the cathode is assumed to be the cathode temperature, the foregoing results obtained for the drift space in a travelling wave tube will be altered by a large factor.

ACKNOWLEDGMENT

The author wishes to express his gratitude to Professor Nelson Wax for the inspiring guidance received during the course of this work. He is also indebted to Professor H. Von Foerster for constant encouragement and valuable suggestions. This work was completed in the Electron Tube Research Laboratory of the University of Illinois on funds provided by the Office of Naval Research.

JOURNAL OF APPLIED PHYSICS VOLUME 26, NUMBER 4 APRIL, 1955

X-Ray Diffraction Study of Silver Iodide Aerosols

JAMES E. MANSON
Geophysics Research Directorate, Air Force Cambridge Research Center, Cambridge, Massachusetts
(Received May 20, 1954)

A source of silver iodide aerosols has been studied to determine the effect of the temperature of generation on the crystal structure of the particles in the aerosol output. Sampling was done by use of a novel thermal precipitator which gave samples in the proper form for direct analysis in a Debye-Scherrer x-ray diffraction camera. Patterns were obtained indicating the presence of both cubic and hexagonal modifications (ZnS and ZnO type). As the source temperature was raised, an increase of the proportion of hexagonal particles was observed, 95 percent hexagonal particles resulted when the source was operated at 800°C. An explanation of this behavior is proposed.

INTRODUCTION

THE discoveries of Schaefer[1,2] and Vonnegut[3,4] concerning the effects of various particulate additives on a supercooled water cloud have stimulated considerable activity in cloud physics. The cold-box technique developed by Schaefer for the laboratory investigation of these effects has been exploited by a number of investigators[5,6] to determine the relative effectiveness of smokes formed from many chemical compounds in causing the water cloud to ice cloud transformation. Some compounds are better than others for this purpose; one of the best is silver iodide. It has been proposed by Vonnegut[3] that the effectiveness of this substance is based on the close agreement between its crystal structure and that of ice. Weickmann[7] has also studied the effect of similarity of substrate crystal structure on the initiation of freezing in supercooled water, and has applied the Volmer[8] nucleation theory to show that the degree of similarity may be used to calculate the temperature to which water may be supercooled in contact with a crystalline surface.

The application of this type of argument to cloud physics depends on a knowledge of the crystal structure of the particles which are injected into the supercooled cloud. There have been many investigations of the crystal structure of silver iodide,[9–12] both natural mineral and laboratory preparation. However, only that conducted by Trillat and Laloeuf[13] was so designed as to be applicable to cloud physics, and their research was of an exploratory nature. They reported the presence of the room-temperature hexagonal modification in all smokes examined by electron diffraction, although in only one case was this modification present alone.

EXPERIMENTAL APPARATUS

Aerosol Source

In order to control the conditions of formation of the smoke a source was constructed of Pyrex and Vycor glass, sealed from the atmosphere, and flushed with

[1] V. J. Schaefer, Science **104**, 457 (1946).
[2] V. J. Schaefer, Part 1. Final Report, Project Cirrus, March 1953.
[3] B. Vonnegut, J. Appl. Phys. **18**, 593 (1947).
[4] B. Vonnegut, Occasional Report No. 5, Project Cirrus, September 1948.
[5] C. C. Hosler, J. Am. Meteorol. Soc. **8**, 326 (1951).
[6] S. J. Birstein, Bull. Am. Meteorol. Soc. **33**, 431 (1952).
[7] H. K. Weickmann, Arch. Meteorol. Geophys. u Bioklimatol. Ser. A. **4**, 309 (1951).
[8] M. Volmer, *Kinetik der Phasenbildung* (Steinkopf, Dresden and Leipzig, 1939).
[9] R. B. Wilsey, Phil. Mag. **42**, 262 (1921); *ibid.* **46**, 487 (1923).
[10] N. H. Kolkmeijer and J. W. A. von Hengel, Z. Krist. **88**, 317 (1934).
[11] R. Block and H. Moller, Z. physik. Chem. (A)**152**, 245 (1930).
[12] L. Helmholtz, J. Chem. Phys. **3**, 740 (1935).
[13] J. J. Trillat and A. Laloeuf, J. chim. phys. **46**, 168 (1949).

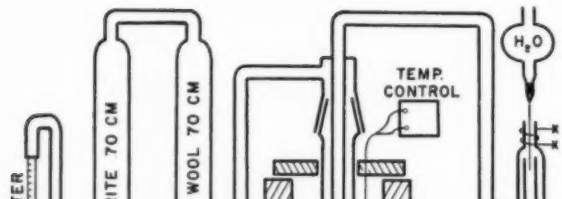

FIG. 1. General view of apparatus. (A) Smoke source. (B) Thermal precipitator.

dried and filtered nitrogen. This is shown in Fig. 1. The source tube had an inside diameter of 20 mm. A six gram sample of silver iodide prepared from reagent grade silver nitrate and potassium iodide was heated in the Vycor tube to 650, 800, and 1000°C, each ±5°C, as measured in oven air. The nitrogen passed over the hot surface of the salt, carrying off vapor. This vapor condensed on emerging from the oven, partly on the walls of the tube and partly in the nitrogen stream. The latter condensate formed the smoke which was carried through the glass tubing without appreciable further loss to the walls.

Typical operating data were, with a six gram sample of silver iodide in the source: nitrogen flow, 160 cc/min at STP; oven temperature 800°C; output 0.5 micrograms/cc of smoke with root mean cube particle diameter of 1100 A and number concentration of 1.3×10^8 particles/cc calculated from this. These data on the output were determined from electron microscope photographs and direct weighing of the precipitated smoke.

Capillary Precipitator

The sampling precipitator was designed around commercially available[14] thin-walled glass capillaries for x-ray analysis, 0.2 mm o.d., 0.01 mm wall thickness. The precipitator is shown in detail in Fig. 2. Water flows by gravity through the capillary, and the 3 mm i.d. tube surrounding the capillary is heated by the nichrome helix to 150°C. The smoke passing through the thermal gradient between these coaxial cylinders is deposited on the cool outer surface of the capillary. Under the foregoing source conditions, and with the flow divided in half to sweep vapor from the coolant out of the sampling region, this precipitator put down 4 micrograms of smoke/mm of capillary length in one-half hour of collection. The aperture of the x-ray camera further limited the sample to 0.5 mm of the capillary length, thus the active sample weight was of the order of 2 micrograms under the foregoing conditions. A sample of this weight has a diametric transmission of 0.72 for CuK_α radiation, hence no correction for absorption in the specimen was made.

[14] The Norelco Reporter **1**, 29 (1953).

Diffraction Apparatus

A copper anode tube excited at 40 kvp and 10 ma, full wave rectified, with 0.025 mm Ni filter was used as source of radiation. Exposures of the order of 20 hours were required using a Norelco 114.6 mm Powder Camera and No-Screen film. The angular positions of the lines were determined within $\pm0.1°2\theta$ visually with a standard film measuring device. The intensities were determined from peak readings of traces obtained with a Leeds and Northrup recording microphotometer with an effective slit size of 0.35×1.0 mm. The film-development-microphotometer system was checked for overall linearity in the optical density-exposure curve by preparation of a step exposure film. Linearity within ±2 percent was verified.

RESULTS

Analysis of Data

The data obtained for twenty-three observed lines are presented in Table I. No lines were observed which could not be accounted for by calculations based on the two room temperature modifications of Ag I reported by Wyckoff.[15] These are face-centered cubic ZnS structure with $a_0=6.473$A, and hexagonal ZnO structure with $a_0=4.580$A, $c_0=7.494$A, and $u=0.625$.

Four films were analyzed, one from the chemical precipitate used as charge for the smoke source and one each from samples obtained from the source at temperatures of 650, 800, and 1000°C. X-ray exposures were

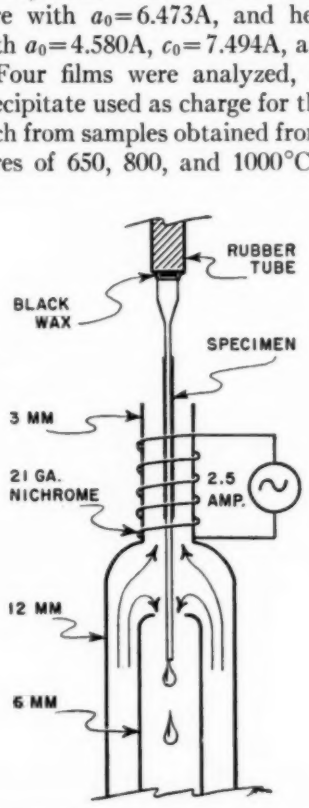

FIG. 2. Thermal precipitator detail.

[15] R. W. G. Wyckoff, *Crystal Structures* (Interscience Publishers, Inc., New York, 1948), Vol. 1, Chap. 3.

TABLE I. Comparison of observed and calculated diffraction intensities.[a]

Miller indices Hex.	Cubic		Relative intensities: Chem. ppt. observed	C_{25}^{0} calc.	650°C observed	C_{75}^{0} calc.	800°C observed	C_{95}^{4} calc.	1000°C observed
10.0		*	25	21	80	70	144	144	153
00.2	111	*	100	100	100	100	100	100	100
10.1		*	11	15	41	47	94	98	96
10.2		*	5	8	15	24	46	50	46
11.0	220	*	90	85	92	89	127	123	109
10.3		*	15	19	40	49	108	107	93
20.0			6	3	14	8	24	17	22
11.2	311	*	60	51	56	48	73	70	62
20.1			4	3	9	7	16	14	12
20.2			1	2	4	5	11	10	11
	400	*	8	11	2	4	0	1	0
20.3		*	4	7	9	13	27	32	23
12.0			4	2	4	5	7	10	8
	331	*	14	16	3	6	0	2	0
12.1			4	2	4	3	7	9	6
10.5 12.2			2	6	6	11	17	28	12
30.0	422		17	24	8	11	10	15	6
12.3			4	3	6	4	17	12	15
00.6 30.2	333 511		10	15	7	8	11	13	8
20.5			0	3	0	4	7	10	6
10.6			0	1	0	1	3	2	0
22.0	440		4	9	3	4	3	7	0
11.6 22.2	531		7	15	5	6	7	12	6

[a] Rows marked (*) were used in the least squares calculations. C_p^B refers to the calculated relative intensities for (p) percent hexagonal smoke and (1-p) percent cubic smoke, with $B\times10^{-16}$ cm² Debye-Waller temperature coefficient. Chem. ppt. refers to precipitate used as charge in the smoke source. Temperatures above columns of observed data refer to the temperature of the smoke source. X-ray exposures were made at room temperature.

made at room temperature. The films corresponding to a source temperature of 800 or 1000°C exhibited an effect ascribed to slight preferred orientation. The intensity of the 00.2–111 line was 10 percent higher on the equator than it was a few millimeters off the equator. For these films the microphotometer traces were taken 2 or 3 mm above or below the equator.

The limits of accuracy on the determination of the composition of each sample were calculated by using the least squares criterion on the differences between calculated and observed relative intensities for ten selected lines (marked with asterisks in Table I). An estimate of experimental error was made for each line and the sum of the squares calculated. The sum of the squares of the differences between observed and calculated intensities were tabulated against p, the percent by volume of hexagonal crystals, and B, the coefficient in the temperature correction, $\exp(-B\sin^2\theta/\lambda^2)$. The

TABLE II.[a]

Sample	$\Sigma\epsilon^2$	$(\Sigma D^2)_{min}$	p(%)	B(cm²)
Chem. ppt.	98	185	36±8	0
650°C	110	370	73±5	6×10^{-16}
800°C	200	88	95±2	4×10^{-16}
1000°C	215	115	95±2	7×10^{-16}

[a] ϵ = estimated experimental error. D = difference between calculated and observed intensity. Σ = sum over ten lines marked with (*) in Table I.

value of B was chosen under which the minimum tabular value occurred. This minimum value was added to the sum of the squares of the experimental errors. The range of p, for which the tabulated values were less than this combined sum, was taken as the uncertainty in determination of p. It will be noted from Table II that this uncertainty decreases as p increases.

Proposed Interpretation

It is believed that the source temperature affects the structure of the smoke through its effect on the relative concentrations of silver and iodine vapor in the source tube. Silver iodide decomposes at its melting point (552°C), and the rate of decomposition will increase with the temperature. Since silver has a very low vapor pressure at 1000°C, it will condense within the source tube to a large extent; whereas iodine, which boils at 183°C, will be carried out in the effluent. The relative concentration of iodine vapor will thus increase with increasing source temperature. Kolkmeijer and von Hengel[10] report that in crystallization of silver iodide from solution an excess of iodide ion yields the hexagonal modification, whereas an excess of silver ion yields the room-temperature cubic modification. As a working hypothesis it has been assumed that analogous behavior may be expected in sublimation. The data reported above supports such an analogy.

CONCLUSIONS

In preparing crystalline aerosols for a use which depends on the crystal structure of the individual particle, it is necessary to ascertain carefully the effect of the method of preparation on the structure. In the case of silver iodide it is possible to vary the proportion of the smoke which consists of crystals of hexagonal structure by varying the temperature of the smoke source, substantially pure hexagonal smoke being obtained when the source is heated to 800–1000°C under the conditions reported above.

Measurement of Detonation Velocity by Doppler Effect at Three-Centimeter Wavelength*

MELVIN A. COOK, RAY L. DORAN, AND GLEN J. MORRIS
Explosives Research Group, University of Utah, Salt Lake City, Utah
(Received June 7, 1954)

This article describes the application of the Doppler principle to the measurement of detonation velocity with three-centimeter electromagnetic radiation. The method makes use of the ionized wave front in detonation as a moving reflecting surface for electromagnetic waves. Detonation velocities for four different solid explosives were calculated from the observed Doppler frequencies and the indices of refraction, which were measured by a microwave interferometer. Complexities in the observed Doppler patterns come about because the cylindrical charges act as multimode dielectric wave guides.

IT is well known that the detonation wave in condensed and gaseous explosives has associated with it sufficient ionization to make it relatively conducting. This is used as the basis for the "pin oscillograph" and similar techniques used extensively in measuring the detonation velocity. The ionization in the detonation wave makes the wave front reflective to E.M. waves of appropriate wavelength. Considerations of the ion density in the detonation wave indicate, however, that the critical upper-limit wavelength for reflection from detonation fronts may be close to the centimeter wave region. Intense shock waves are known to reflect centimeter waves, and the use of microwave radiation has thus provided an important method in the measurement of the velocities of rapidly moving particles through air. Considerable work has been done also on the measurement of the velocities of projectiles, as well as meteor particles.[1,2]

In the case of a detonation wave in a solid explosive the reflection of the electromagnetic wave from the detonation front was measured by making use of the change in frequency due to the moving reflector. This is the well-known Doppler effect applied to the microwave region. This method has been used for gaseous and solid explosives in the region of 23-cm wavelength of the transmitted microwave energy.[3] Although it is understood that several investigations in other frequency regions have been carried out in this country, the results of these have not yet become available.

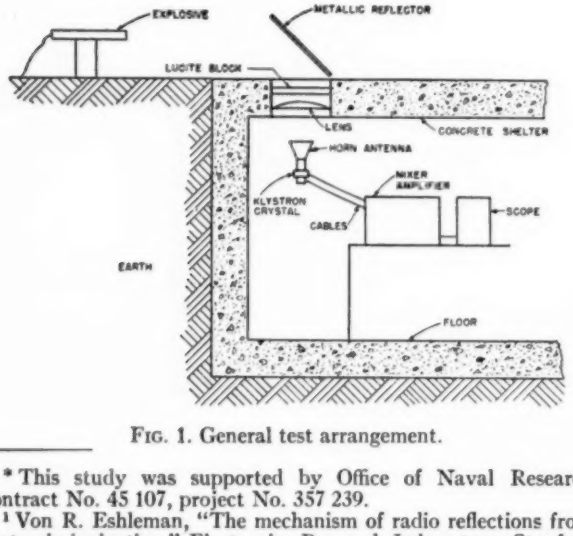

FIG. 1. General test arrangement.

The calculation of the velocity of the detonation wave advancing toward the observer can be made from the well-known application of the Doppler principle to radar echo measurements, namely

$$f=\frac{c+v}{c-v}f_0.$$

Where f_0 is the transmitted frequency of velocity c and v is the velocity of the target. Inasmuch as the radiation in this problem travels through a medium of index of refraction n, the velocity of the radiation is no longer c but c/n, and the expression becomes

$$f=\frac{(c/n)+D}{(c/n)-D}f_0$$

from which

$$D=\frac{(f-f_0)C}{2nf_0}$$

represents the velocity of the wave front toward the observer.

EXPERIMENTAL METHODS

The microwave radiation used in this investigation was 3.3 cm or 9415 megacycles. The radiation was directed into the end of a cylindrical charge, and the reflection from the forward moving shock wave front was mixed with the incident wave. The resulting beat frequency gave a measure of the rate at which the discontinuity of the wave front was advancing. In this case, the electromagnetic wave undergoes a reflection

* This study was supported by Office of Naval Research contract No. 45 107, project No. 357 239.

[1] Von R. Eshleman, "The mechanism of radio reflections from meteoric ionization," Electronics Research Laboratory, Stanford University, Palo Alto, California, Technical Report No. 29, July 15, 1952.

[2] Bennett Bovarnick, "Microwave detection of shock waves," Upper Atmosphere Research Laboratory, Boston University, Technical Note 5, August 24, 1949.

[3] Technical Report ONRL-130-51, Report of Basic Research on Combustion, Detonation, and Shock Waves at the Laboratoire de Recherches Techniques de Saint Louis.

within the explosive medium from the discontinuity formed by the interface between the undetonated explosive and the gaseous products at the detonation front.

The experimental arrangement used in this investigation is illustrated schematically in Fig. 1. The source of radiation, a klystron, fed the 3-cm waves from a microwave horn antenna through a wave-guide lens. The output beam, now nearly parallel, passed from the interior of a concrete blockhouse through a porthole containing a one-inch shock proof Lucite layer. The radiation was reflected through an angle of 90° by a metallic reflector and into the explosive. The reflection from the wave front traversed this path in the opposite direction entered the horn antenna and was beat against the output signal from the klystron. The beat frequency from the mixer and amplifier was presented on a fast-sweep oscilloscope and photographed.

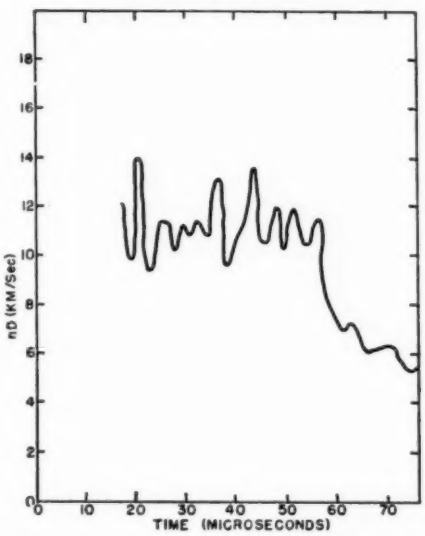

FIG. 2. Apparent velocity *vs* distance plot for TNT.

To make calculations of the velocity of the detonation wave, one must measure the wavelength for each or any particular wave in the train representing the travel of the wave front through the explosive. In this study only the dominant frequency curve in the complex pattern was selected for study. With these values of wavelength, one can then calculate the apparent velocity for various points along the explosive. This method thus gives an instantaneous plot of apparent velocity *versus* distance along the explosive charge. A representative plot of one explosive is shown in Fig. 2.

Since the preliminary results obtained with several granular and cast explosive charges showed the same general characteristics, measurements were made on a number of cast charges of (1) TNT, (2) 50/50 Pentolite, (3) 50/50 Amatol, and (4) 80/20 Tritonal. From the films of each of these shots, the average value was found for the detonation velocity throughout the charge.

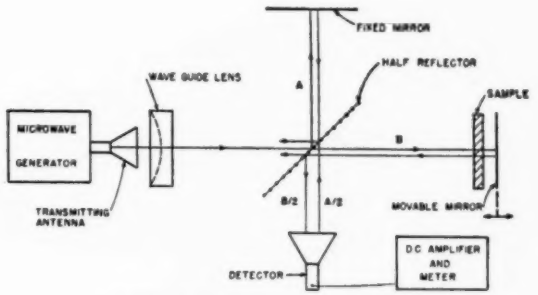

FIG. 3. Microwave interferometer.

To obtain values for the index of refraction of the explosives used, a sample of known thickness was inserted in one arm of a microwave interferometer of the Michelson type (Fig. 3). The introduction of a sample of material substance in the path of one beam causes a change in path length due to the difference in index of refraction of the material used and air for 3-cm waves. By this means it was possible to check the indices of refraction of various substances such as lucite, window glass, pine wood, plywood, etc., to values within two percent of accepted values.[4]

EXPERIMENTAL RESULTS

The results of the firing of a series of explosives were recorded on films showing wave forms of the resulting Doppler frequency measurements. These wave forms all showed the same general characteristics. Two wave forms measured from cylindrical charges of granular TNT 5 cm in diameter and 30 cm and 50 cm in length, respectively, are shown in Figs. 4(a) and 4(b). From these figures one can observe the time required for the cap to fire the charge, the regular pattern representing the travel of the detonation wave through the explosive, and the irregular pattern obtained from the region beyond the end of the charge. Also observable is the modulation of the wave form during the time the charge is detonating. From the wave form shown in Fig. 4(c) of a cast charge of Pentolite 5 cm in diameter and 27 cm long, one can observe all of the aforementioned characteristics.

The "indexes of refraction" for the explosives in the four groups used in the program are shown in Table I. It should be pointed out that the charges sometimes were not entirely homogeneous. As a result, the values of the "index of refraction" obtained varied somewhat. The index of refraction of Pentolite, for example, was measured in samples whose diameters were 2 inches, 5 inches, and 8 inches, respectively. This was done in an attempt to provide better uniformity of density, as well as to investigate the possibility of effects due to other modes of transmission of the electromagnetic wave through the sample. The values obtained in this experiment show a slight increase with diameter.

[4] T. Moreno, *Microwave Transmission Design Data* (McGraw-Hill Book Company, Inc., New York, 1948), p. 201–207.

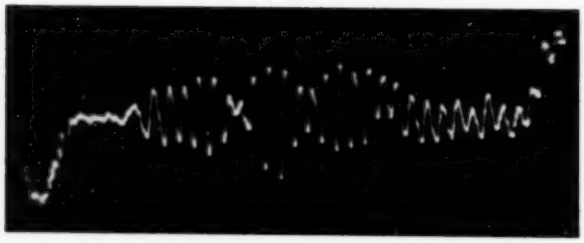

(a)

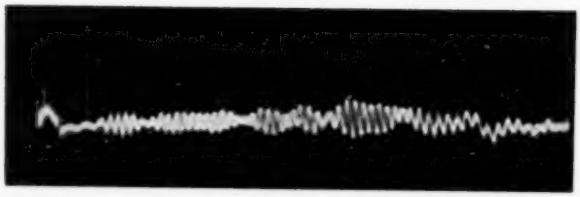

(b)

(c)

(d)

FIG. 4. (a) Doppler pattern for 5×30 cm charge showing no oscillations at beginning. (b) Doppler pattern for 5×30 cm charge of TNT showing high peaks at beginning. (c) Doppler pattern for 5×27 cm Pentolite charge. (d) Doppler pattern for 12.5×65 cm charge showing complex pattern.

The plots of the apparent instantaneous velocity of the wave front as it travels through the explosive were made for each shot. A sample plot of TNT is shown in Fig. 2 made from the data in Table II. From these it may be seen that the difference between the average velocities determined by the Doppler and pin oscillograph methods varied from 0.3 percent for TNT to 5.9 percent for Pentolite. The average deviation of results, however, was between one and two percent. The discrepancy in the case of Pentolite is attributed to unavoidable charge irregularities (cavities) existing along the charge axis in the charges used in this study.

TABLE I. Index of refraction for 3.3-cm E.M. waves.

Diameter	TNT	Pentolite	Amatol	Tritonal
5 cm	1.688	1.736	2.10	2.10
12.5 cm		1.78		
20.0 cm		1.82		

TABLE II. Detonation velocity in cast charges (5 cm diameter, 30 cm length).

	TNT	Amatol	Tritonal	Pentolite
Number of shots	12	12	13	13
Average measured velocity (M/sec)	6520(±125)[a]	5390(±70)	6900(±135)	6960(±110)
Velocity ("pin oscillograph")	6540	5300	6800	7400

[a] Values in ( ) are average deviation.

DISCUSSION

The complexity of the oscillographs of the Doppler frequency obtained in most cases can be interpreted as the result of excitation of multiple modes of transmission within the explosive charge. This interpretation arises from a suggestion by E. F. Pound of this group that it is logical to treat the explosive charge as a dielectric wave guide. From the general theory of cylindrical wave guides,[5] it is known that several modes of transmission may be excited within a wave guide of this type due to the discontinuities that face the microwave radiation. The number of modes theoretically should increase as the diameter of the charge is increased beyond a critical diameter for any particular wavelength. Although the higher modes will naturally have very much less energy than the fundamental hybrid mode, the presence of two modes, if of sufficient energy, is enough to cause modulation similar to that observed in the photographic records.

The propagation of multiple modes gives an explanation of the increased irregularity of modulation shown in Fig. 4(d), which is a record of a five-inch-diameter charge. It is expected that an increased number of modes would be excited in a larger diameter charge.

[5] S. Ramo and J. R. Whinnery, *Fields and Waves in Modern Radio* (John Wiley and Sons, Inc., New York, 1944), p. 332–353.

JOURNAL OF APPLIED PHYSICS VOLUME 26, NUMBER 4 APRIL, 1955

Reflection of Sound in the Ocean from a Continuous Stratum Containing a Velocity Extremum

E. O. Cook, *Naval Research Establishment, Dartmouth, Nova Scotia, Canada*

AND

H. S. Heaps, *Nova Scotia Technical College, Halifax, Nova Scotia, Canada*

(Received June 11, 1954)

The reflection of a plane wave of sound from a layer separating regions of different sound velocities, the layer itself containing a velocity variation through an extremum, is considered in terms of its dependence upon the angle of incidence, the layer thickness, and the velocity variation through the layer. It is found that the power reflection coefficient may differ significantly from its value for the corresponding abrupt or monotonic velocity transition. Numerical results are tabulated for various types of layers of thickness from zero to ten wavelengths and with a total velocity transition of ±5 and ±10 ft/sec.

I. INTRODUCTION

In the ocean, when physical conditions favor horizontal stratification, there may be found thermal strata of thickness comparable to the wavelength of sound. Carhart[1] has discussed the reflection of obliquely incident sound from an inhomogeneous layer in which the sound velocity changes monotonically with depth. The occurence of a layer containing a transition through a velocity extremum is also possible.[2,3] A discussion of the acoustical reflection from such a layer is presented in this paper. It is found that (i) the power reflection coefficient may be significantly higher than it is for the corresponding monotonic transition, (ii) for a given glancing angle of incidence and velocity variation there exists a layer thickness, expressed in terms of wavelength, for which the reflection coefficient is a maximum, and (iii) the amount of reflected energy may exceed the amount reflected from a similar but discontinuous change in sound velocity.

A rigorous solution of the scalar form of the wave equation has been given by Eckart[4] in the case of normal incidence and by Epstein[5] in the case of oblique incidence. The type of stratum to which their solution applies is not unrestricted in form but has a velocity-depth variation which, by a suitable choice of parameters, may be made to approximate to almost any practical example of a layer containing either a monotonic velocity dependence or a transition through a velocity extremum. For plane waves incident upon the layer, the reflection coefficient is a function of the glancing angle of incidence, the layer thickness measured in wavelengths, the total velocity difference across the layer, and a constant which describes the form of the velocity transition. A formula for the reflection coefficient arising from an "exponential" velocity variation has been obtained by Wait,[6] while Hines[7] has given a qualitative discussion of reflection from a medium in which the spatial rate of change of velocity is gradual.

II. THEORETICAL BASIS

For plane waves incident upon the layer, application of the results of Epstein[5] enables the power reflection coefficient to be found from a rigorous solution of the wave equation*

$$\nabla^2 p + k^2 p = 0, \tag{1}$$

where p is the sound pressure. Throughout the layer extending from $z=-s\lambda$ to $z=s\lambda$ the velocity variation is determined by k, which is assumed to have the form

$$k^2=(4\pi^2 f^2/c^2)[1-(2\Delta c/c)\exp\zeta/(1+\exp\zeta) +\epsilon\exp\zeta/(1+\exp\zeta)^2], \tag{2}$$

where c = the sound velocity below the layer; $c+\Delta c$ = the sound velocity above the layer; $2\Delta c/c$ = an approximation to the exact factor $1-(1+\Delta c/c)^{-2}$ with negligible error; f = the frequency of the incident wave; ϵ = a parameter which determines the form of the velocity variation within the layer and is here termed the "velocity structure factor"; λ = the wavelength of the sound at $z=-\infty$; and $\zeta=2\pi z/s\lambda$.

In terms of the glancing angle of incidence θ, put $a'=s\sin\theta$, $b'=s[c^2/(c+\Delta c)^2-\cos^2\theta]^{\frac{1}{2}}$, $d=\frac{1}{2}-(\frac{1}{4}+s^2\epsilon)^{\frac{1}{2}} =\frac{1}{2}-id'$. The power reflection coefficient is then

$$R^2=[\sin^2\pi d+\sinh^2\pi(a'-b')]/\times[\sin^2\pi d+\sinh^2\pi(a'+b')] \tag{3}$$

if d is real, and

$$R_1^2=[\cosh^2\pi d'+\sinh^2\pi(a'-b')]/\times[\cosh^2\pi d'+\sinh^2\pi(a'+b')] \tag{4}$$

if d is complex.

The sound velocity at the height z in the layer is

$$c[1-(2\Delta c/c)\exp\zeta/(1+\exp\zeta) +\epsilon\exp\zeta/(1+\exp\zeta)^2]^{-\frac{1}{2}}. \tag{5}$$

* This form of the wave equation occurs on assuming the density to be constant—an assumption which can be realized to a certain extent in underwater acoustics.

[1] R. R. Carhart, J. Appl. Phys. **24**, 929–934 (1953).
[2] R. K. Brown, J. Acoust. Soc. Am. **26**, 64–67 (1954).
[3] H. F. P. Herdman, Nature **172**, 275–276 (1953).
[4] C. Eckart, Phys. Rev. **35**, 1303–1309 (1930).
[5] P. S. Epstein, Proc. Natl. Acad. Sci. **16**, 627–637 (1930).
[6] J. R. Wait, J. Appl. Phys. **23**, 1403–1404 (1952).
[7] C. O. Hines, Quart. Appl. Math. **11**, 9–31 (1953).

TABLE I. Power reflection coefficient when $\Delta c = 5$ ft/sec ($\theta_c = 2.56°$).

ϵ	s	3°	4°	5°	6°	7°	8°	9°	10°
−0.02	1	0.1525	0.0411	0.0196	0.0114	0.0072	0.0050	0.0036	0.0003
	2.5	0.3691	0.1451	0.0709	0.0374	0.0204	0.0114	0.0064	0.0037
	5	0.7290	0.3571	0.1357	0.0461	0.0150	0.0049	0.0024	0.0005
	7.5	0.9023	0.5190	0.1467	0.0290	0.0053	0.0010	0.0002	
	10	0.9660	0.6372	0.1327	0.0146	0.0015	0.0007		
−0.01	1	0.1114	0.0223	0.0089	0.0046	0.0026	0.0016	0.0011	0.0008
	2.5	0.1707	0.0454	0.0192	0.0094	0.0050	0.0027	0.0015	0.0008
	5	0.3263	0.0852	0.0251	0.0078	0.0025	0.0008	0.0004	0.0001
	7.5	0.4875	0.0978	0.0169	0.0030	0.0005	0.0001		
	10	0.6216	0.0915	0.0087	0.0008	0.0001			
0	0	0.0995	0.0172	0.0058	0.0025	0.0013	0.0007	0.0004	0.0003
	1	0.0971	0.0162	0.0054	0.0024	0.0010	0.0006	0.0003	0.0002
	2.5	0.0891	0.0127	0.0035	0.0012	0.0005	0.0002	0.0001	
	5	0.0639	0.0058	0.0009	0.0002				
	7.5	0.0387	0.0018	0.0002					
	10	0.0208	0.0005						
0.01	1	0.1110	0.0222	0.0088	0.0045	0.0025	0.0016	0.0011	0.0008
	2.5	0.1555	0.0390	0.0161	0.0078	0.0041	0.0022	0.0012	0.0007
	5	0.1810	0.0365	0.0099	0.0030	0.0009	0.0003	0.0001	
	7.5	0.1176	0.0126	0.0019	0.0003	0.0001			
	10	0.0436	0.0020	0.0002					
0.02	1	0.1487	0.0393	0.0186	0.0108	0.0068	0.0046	0.0033	0.0025
	2.5	0.2823	0.0974	0.0455	0.0235	0.0127	0.0070	0.0039	0.0022
	5	0.2932	0.0728	0.0211	0.0065	0.0020	0.0007	0.0003	0.0001
	7.5	0.1035	0.0105	0.0015	0.0003				
	10	0.0208	0.0005						

When $\epsilon = 0$ the expressions (3) and (5) may be reduced, respectively, to the forms (8) and (6) of Carhart.[1]

For a layer of infinitesimal thickness in which the sound velocity changes abruptly from c to $c+\Delta c$ the amplitude reflection coefficient is given by

$$r = [(c+\Delta c)\sin\theta - c\sin\theta'] / [(c+\Delta c)\sin\theta + c\sin\theta'] \quad (6)$$

(constant density) where θ' is the angle of emergence measured from the horizontal, and the angles θ and θ' are related by

$$c/(\cos\theta) = (c+\Delta c)/\cos\theta' \quad \text{(Snell's law)}. \quad (7)$$

As a consequence of Snell's law, the critical angle is the same for Eqs. (3), (4), and (6), and is $\theta_c = (2\Delta c/c)^{\frac{1}{2}}$ when $\Delta c/c$ is small.

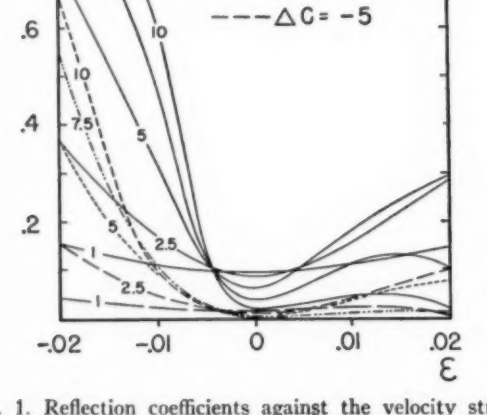

FIG. 1. Reflection coefficients against the velocity structure factor with stratum thickness as parameter for the 3° ray and velocity difference ±5 ft/sec.

III. NUMERICAL AND GRAPHICAL RESULTS

The power reflection coefficient R^2 or R_1^2 is tabulated to four decimal places in Tables I to IV for a glancing angle θ which varies in intervals of 1° from 1° to 10°, for $s = 0$, 1, 2.5, 5, 7.5, and 10, $c = 5000$ ft/sec, $\Delta c = \pm 5$, ± 10 ft/sec, and $\epsilon = 0$, ± 0.01, ± 0.02. The tables give R^2 when $s^2\epsilon > -0.25$ and R_1^2 when $s^2\epsilon < -0.25$. From Table I it is seen that Fig. 9 of Carhart[1] contains an error; in this figure the curve $2d = 10\lambda$ should be labeled $2d = 5\lambda$.

The ranges of values chosen for ϵ, s, and θ are considered to be adequate for most practical purposes; the values that are assumed for the net velocity change across the layer are more or less arbitrary but fall within the range encountered in practice. A value of ± 5 ft/sec, which corresponds to a temperature difference of approximately 1°F, would lead, for example, to an average velocity gradient of ± 4 sec^{-1} at a frequency of 20 kc/sec and $s = 5$, and to a gradient of ± 0.1 sec^{-1} at 1 kc/sec and $s = 2.5$. The value of the absolute velocity which is adopted lies within the normal small relative variation found in the ocean. Although an angle of 3° is used for convenience in plotting, neither

TABLE II. Power reflection coefficient when $\Delta c = -5$ ft/sec.

ϵ	s	1°	2°	3°	4°	5°	6°	7°	8°	9°	10°
−0.02	1	0.2869	0.0983	0.0433	0.0229	0.0138	0.0088	0.0061	0.0043	0.0032	0.0023
	2.5	0.5278	0.2803	0.1514	0.0839	0.0475	0.0271	0.0157	0.0090	0.0052	0.0030
	5	0.8408	0.6255	0.3727	0.1750	0.0701	0.0256	0.0091	0.0031	0.0009	0.0004
	7.5	0.9538	0.8338	0.5448	0.2115	0.0535	0.0119	0.0025	0.0005	0.0001	
	10	0.9865	0.9291	0.6675	0.2163	0.0346	0.0044	0.0005	0.0001		
−0.01	1	0.2364	0.0660	0.0240	0.0108	0.0058	0.0033	0.0021	0.0014	0.0010	0.0007
	2.5	0.3093	0.1121	0.0480	0.0234	0.0122	0.0067	0.0037	0.0021	0.0012	0.0008
	5	0.5020	0.2263	0.0908	0.0337	0.0121	0.0042	0.0015	0.0005	0.0001	0.0001
	7.5	0.6855	0.3379	0.1076	0.0261	0.0056	0.0012	0.0002			
	10	0.8144	0.4296	0.1034	0.0156	0.0020	0.0003				
0	0	0.2180	0.0567	0.0185	0.0075	0.0034	0.0018	0.0010	0.0006	0.0004	0.0002
	1	0.2155	0.0550	0.0175	0.0068	0.0031	0.0015	0.0008	0.0004	0.0003	0.0002
	2.5	0.2048	0.0488	0.0139	0.0047	0.0017	0.0007	0.0003	0.0001	0.0001	
	5	0.1670	0.0308	0.0064	0.0015	0.0003	0.0001				
	7.5	0.1235	0.0158	0.0021	0.0003						
	10	0.0841	0.0070	0.0006							
0.01	1	0.2357	0.0656	0.0237	0.0106	0.0057	0.0032	0.0020	0.0014	0.0010	0.0007
	2.5	0.2906	0.1001	0.0414	0.0196	0.0102	0.0055	0.0031	0.0017	0.0010	0.0006
	5	0.3318	0.1130	0.0390	0.0136	0.0047	0.0016	0.0005	0.0002	0.0001	
	7.5	0.2587	0.0624	0.0140	0.0030	0.0006	0.0001				
	10	0.1349	0.0178	0.0023	0.0003						
0.02	1	0.2823	0.0953	0.0415	0.0217	0.0131	0.0083	0.0057	0.0040	0.0029	0.0022
	2.5	0.4380	0.2040	0.1021	0.0543	0.0300	0.0169	0.0097	0.0056	0.0032	0.0019
	5	0.4662	0.1993	0.0777	0.0285	0.0102	0.0035	0.0012	0.0004	0.0001	
	7.5	0.2361	0.0539	0.0118	0.0025	0.0005	0.0001				
	10	0.0841	0.0070	0.0006							

the general features of the various curves nor the major conclusions are affected by this choice of value.

Figure 1, taken from the tables, illustrates the dependence of the power reflection coefficient upon the velocity structure factor with the stratum thickness, expressed as the number of wavelengths in a half-thickness, as parameter, for a glancing angle of incidence of 3° and a net velocity change of ±5 ft/sec. The continuous lines refer to $\Delta c = 5$ and the broken lines to $\Delta c = -5$. The appropriate values of s are as indicated upon each curve. The transition of reflection coefficient from R^2 to R_1^2 occurs on the curve corresponding to $s = 7.5$ when $\epsilon = -0.005$ and on the curve corresponding to $s = 10$ when $\epsilon = -0.0025$. The vertical velocity structure for each value of ϵ is shown sketched at the top of the figure.

Figure 2, in which the continuous curves apply to the case of $\Delta c = 5$ and the broken curves to $\Delta c = -5$, shows the variation of the power reflection coefficient with s for $\theta = 3°$ and the various values of the parameter ϵ.

IV. DISCUSSION

Equations (3), (4), and (7) indicate that conditions for total reflection obtain either for a glancing angle of zero or for an angle equal to or less than the critical angle. That is, the power reflection coefficient for the type of velocity transition under consideration becomes unity under the same conditions as for the corresponding monotonic ($\epsilon = 0$) and discontinuous ($s = 0$) transitions. In regard to the critical angle, it follows immediately from Snell's law that its magnitude is not affected by the structure of the layer, but that it is determined solely by the absolute values of the velocity of sound at the upper and lower boundaries of the layer.

Figure 1 shows (for the range of values considered) that the power reflection coefficient of sound waves for a stratum containing a velocity extremum as defined

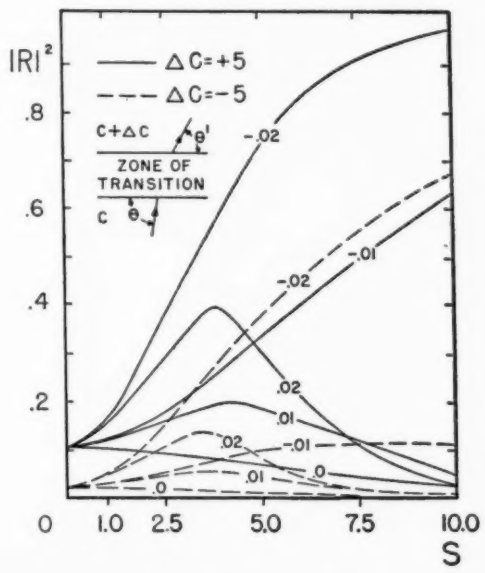

FIG. 2. Reflection coefficients against half-stratum thickness measured in wavelengths with the structure factor as parameter for the 3° ray and velocity difference ±5 ft/sec.

TABLE III. Power reflection coefficient when $\Delta c = 10$ ft/sec ($\theta_c = 3.62°$).

ϵ	s	4°	5°	6°	7°	8°	9°	10°
−0.02	1	0.1929	0.0487	0.0217	0.0119	0.0074	0.0048	0.0034
	2.5	0.3201	0.1079	0.0509	0.0255	0.0136	0.0075	0.0041
	5	0.5882	0.2063	0.0653	0.0201	0.0063	0.0020	0.0006
	7.5	0.7822	0.2584	0.0482	0.0081	0.0014	0.0002	
	10	0.8911	0.2796	0.0290	0.0039	0.0002		
−0.01	1	0.1684	0.0359	0.0140	0.0068	0.0038	0.0023	0.0015
	2.5	0.1875	0.0427	0.0167	0.0076	0.0038	0.0020	0.0011
	5	0.2356	0.0456	0.0120	0.0035	0.0011	0.0003	
	7.5	0.2850	0.0349	0.0051	0.0008	0.0001		
	10	0.3263	0.0220	0.0017	0.0002			
0	0	0.1645	0.0339	0.0128	0.0060	0.0033	0.0020	0.0012
	1	0.1600	0.0317	0.0115	0.0051	0.0027	0.0014	0.0009
	2.5	0.1398	0.0224	0.0066	0.0023	0.0009	0.0004	0.0002
	5	0.0881	0.0077	0.0013	0.0003	0.0001		
	7.5	0.0454	0.0018	0.0002				
	10	0.0208	0.0004					
0.01	1	0.1680	0.0358	0.0139	0.0068	0.0038	0.0022	0.0014
	2.5	0.1784	0.0387	0.0147	0.0053	0.0032	0.0017	0.0009
	5	0.1484	0.0220	0.0052	0.0014	0.0001		
	7.5	0.0770	0.0054	0.0007	0.0001			
	10	0.0273	0.0007					
0.02	1	0.1905	0.0474	0.0209	0.0114	0.0071	0.0046	0.0032
	2.5	0.2590	0.0761	0.0339	0.0165	0.0087	0.0047	0.0026
	5	0.2144	0.0395	0.0102	0.0029	0.0009		
	7.5	0.0711	0.0046	0.0007	0.0001			
	10	0.0208	0.0004					

TABLE IV. Power reflection coefficient when $\Delta c = -10$ ft/sec.

ϵ	s	1°	2°	3°	4°	5°	6°	7°	8°	9°	10°
−0.02	1	0.3667	0.1535	0.0658	0.0342	0.0194	0.0119	0.0078	0.0052	0.0038	0.0028
	2.5	0.5062	0.2700	0.1408	0.0782	0.0441	0.0253	0.0146	0.0085	0.0049	0.0029
	5	0.7586	0.5240	0.2853	0.1316	0.0534	0.0202	0.0072	0.0026	0.0009	0.0003
	7.5	0.9010	0.7198	0.3915	0.1367	0.0352	0.0080	0.0017	0.0004	0.0001	
	10	0.9616	0.8419	0.4664	0.1201	0.0190	0.0026	0.0003			
−0.01	1	0.3390	0.1309	0.0507	0.0239	0.0123	0.0068	0.0041	0.0025	0.0017	0.0012
	2.5	0.3638	0.1471	0.0604	0.0285	0.0142	0.0075	0.0041	0.0023	0.0013	0.0007
	5	0.4319	0.1867	0.0702	0.0264	0.0099	0.0035	0.0012	0.0004	0.0001	
	7.5	0.5179	0.2193	0.0632	0.0160	0.0037	0.0008	0.0002			
	10	0.6053	0.2401	0.0484	0.0078	0.0011	0.0001				
0	0	0.3361	0.1272	0.0488	0.0221	0.0111	0.0061	0.0035	0.0022	0.0014	0.0009
	1	0.3294	0.1232	0.0456	0.0205	0.0099	0.0051	0.0029	0.0018	0.0010	0.0006
	2.5	0.3070	0.1040	0.0347	0.0133	0.0054	0.0023	0.0010	0.0005	0.0002	0.0001
	5	0.2369	0.0610	0.0141	0.0036	0.0012	0.0003	0.0001			
	7.5	0.1619	0.0282	0.0041	0.0006	0.0001					
	10	0.1023	0.0114	0.0010	0.0001						
0.01	1	0.3386	0.1306	0.0505	0.0237	0.0122	0.0067	0.0041	0.0025	0.0017	0.0011
	2.5	0.3531	0.1387	0.0553	0.0255	0.0125	0.0065	0.0034	0.0019	0.0011	0.0006
	5	0.3224	0.1114	0.0354	0.0121	0.0044	0.0014	0.0005	0.0002	0.0001	
	7.5	0.2207	0.0519	0.0105	0.0022	0.0005	0.0001				
	10	0.1190	0.0158	0.0017	0.0002						
0.02	1	0.3641	0.1513	0.0644	0.0332	0.0187	0.0114	0.0075	0.0050	0.0036	0.0026
	2.5	0.4431	0.2126	0.1019	0.0537	0.0292	0.0164	0.0093	0.0054	0.0031	0.0018
	5	0.4066	0.1681	0.0613	0.0227	0.0085	0.0029	0.0010	0.0004	0.0001	
	7.5	0.2101	0.0475	0.0092	0.0019	0.0004	0.0001				
	10	0.1023	0.0114	0.0010	0.0001						

by Eq. (2), (i) is never less than for the case of $\epsilon = 0$, (ii) may be significantly higher than for either of the two corresponding simpler cases $\epsilon = 0$ and $s = 0$; this is particularly evident in the case of an increase in velocity across the layer and the higher numerical values of ϵ, (iii) is generally greater for negative values of ϵ than for positive values, (iv) generally increases more rapidly with negative ϵ than with positive ϵ, especially for

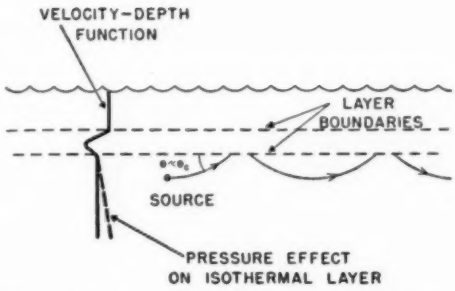

FIG. 3. Alternate reflection and refraction of sound from a source situated below a stratified layer in the ocean.

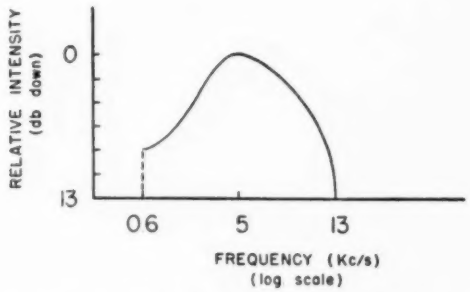

FIG. 4. Loss in decibels of the spectral intensity of white sound due to a single reflection from a stratum of the type described in Part V.

positive Δc, but may decrease when ϵ and Δc are positive and s is large.

The data are presented in the form shown in Fig. 2 to illustrate the possibility of obtaining a maximum value of the intensity of the reflected sound for a given angle of incidence and stratum thickness by choosing a frequency corresponding to an appropriate value of s. In contrast with the monotonic transition curve, the reflected intensity curve for a layer possessing an extremum attains a maximum value for a value of s which depends upon the sign of the total velocity change and the structure factor. Figure 2 also provides a clear indication of the range of s over which the reflected energy exceeds that for the $\epsilon=0$ and $s=0$ cases.

Consideration of the tables shows, in addition, that (i) the maxima of reflection for negative values of ϵ occur at higher values of s than the corresponding maxima for positive ϵ, and that, as the glancing angle increases, (ii) the maxima occur at smaller values of s, (iii) the rate of displacement of the peaks for the negative values of ϵ is greater than for the positive values; in the latter case the value of s for maximum is almost independent of θ, (iv) the reflected intensity decreases rapidly over the first two or three degrees and the maxima become progressively less well defined.

It may be of interest to note that the intensity maxima appear because of the periodicity of the trigonometric term which occurs in Eq. (3) for real values of the radical. The intensities of the higher-order maxima are, however, of no practical consequence.

V. APPLICATION OF RESULTS

There are two applications of interest which may be mentioned here; the first relates to the possibility of propagation to super distances by the mechanism of total reflection, and the second to the dependence on range of the spectral character of complex sounds due to the action of quasi-selective reflection and/or transmission at the complex velocity stratum.

Consider the hypothetical case of a white sound source situated below a stratum bounded by the ocean surface on one side and on the other by a thick isothermal layer as shown in Fig. 3. As a consequence of this situation all rays suffer a slight upward refraction because of the increase in velocity with pressure; these rays which are incident on the complex layer at angles less than the critical angle will alternately be completely reflected, then refracted upward with transmission losses due only to the semispherical divergence and attenuation of the sound energy. If the source is above the stratum, energy loss may also be suffered on reflection at the ocean surface.

Figure 4 shows the loss in decibels of the spectral intensity of a white sound source for a single reflection relative to the frequency, in this case 5 kc/sec, for which the reflection coefficient is a maximum for the particular velocity transition chosen. The chosen values of θ, ϵ, Δc, and the layer thickness were, respectively, 3°, 0.02, 5 ft/sec, and 7.8 feet.

ACKNOWLEDGMENTS

The authors wish to thank Miss M. Hachey and Mr. E. Ripley for assistance in the numerical work. Thanks are due the Defence Research Board of Canada for granting permission to publish this paper.

Dependence of the Electric Strengths of Liquids on Electrode Spacing

A. H. SHARBAUGH, J. K. BRAGG,* AND R. W. CROWE
General Electric Research Laboratory, Schenectady, New York

(Received June 23, 1954)

Using a reproducible pulsed voltage technique, the electric strengths of liquid hexane, heptane, and tetradecane have been measured with small electrode spacings (approximately 2 to 200 microns). The electric strengths are found to change inversely with the logarithm of the separation in accord with theoretical expectation. On the basis of an approximate model of the breakdown process, the measurements on heptane yield values of 9×10^{-7} cm for the electron mean free path in the liquid and 9 for the number of multiplications per electron required for breakdown.

I. INTRODUCTION

FOR some twenty-five years the decrease in the measured electric strength of liquids with increasing electrode spacing has been an important subject of study because of its practical as well as theoretical significance. Early investigators were handicapped by the lack of reproducibility of electric strength values as well as by inability to measure accurately small electrode spacings. With the recent development of a reproducible pulsed-voltage technique[1] and a means of determining small electrode separations (1–10μ) by capacitance measurement, we have re-examined this phenomenon using several carefully purified hydrocarbons as the liquid dielectric. Our measurements extend and, in some cases, differ from those of Edwards[1] and Goodwin and Macfadyen.[2]

Qualitatively, the electric field necessary to cause breakdown at small electrode spacings is higher than that at large spacings because it is necessary to accelerate electrons more rapidly in order that they may make ionizing collisions a suitable number of times before they are lost to the anode. This assumption differs from that of Fröhlich[3]; he requires only a distance large enough for an appreciable fraction of the electrons to make *one* ionizing collision. The experimental results to be given unfortunately do not provide an entirely unambiguous decision regarding the two hypotheses, which in any case give the same equation relating the breakdown field and the electrode separation, with different values predicted for a constant appearing therein.

II. EXPERIMENTAL PROCEDURE

A hard tube modulator was used to generate rectangular pulses of amplitude 0–15 kv, while a pulse-forming network and thyratron switch supplied the pulses having amplitudes between 15 and 50 kv. These two generators deliver pulses having a duration of 1.6 and 3.3 μsec, respectively. Since the critical breakdown time is of the order of 1 μsec for the liquids, the observed electric strength is independent of the length of the applied pulse.[1] The electrodes were highly polished steel. With the exception of these changes, and the new technique for setting small gaps which will be described below, the experimental procedure was essentially that described elsewhere.[4]

At electrode spacings less than one-tenth of the electrode radius, the relation between the capacitance of two hemispheres and the logarithm of their separation becomes very nearly linear.[5] Thus, a given electrode configuration may be "calibrated" at large gaps where mechanical settings of good percentage accuracy may be made; an extrapolation of the straight line so obtained will determine the capacitance at any smaller electrode spacing. In this way a simple capacitance measurement and a knowledge of the dependence of capacitance upon electrode separation yields the spacing of gaps in the range 1–10μ with an experimental error of less than 5 percent.

III. THEORY

We will use a very simple model to relate the electrode spacing to the observed electric strength, one often invoked for semiquantitative discussions. Let λ be the mean free path of an electron (assumed independent of energy); the fraction of electron paths in the liquid of length greater than x is $\exp(-x/\lambda)$. The fraction of paths over which the electron reaches some critical energy ϵ_0 is then $\exp(-\epsilon_0/eE\lambda)$. Each electron makes $1/\lambda$ "tries" per centimeter, so that the mean multiplication distance is

$$d=\lambda \exp(\epsilon_0/eE\lambda).$$

The assumption is made here that the electron collisions are totally inelastic. In reality, an electron may retain some energy after its pre-ionization collisions; the mean multiplication distance may be somewhat shorter than that given here. It should also be noted that the assumption about energy-independence of the mean free path is not so severe as may be supposed: extensive work with gases has shown that the functional form of $d(E)$ is preserved for a variety of assumptions regarding

* Present address: Operations Research, Inc., 8485 Fenton Street, Silver Spring, Maryland.

[1] W. D. Edwards, Can. J. Phys. **29**, 310 (1951).

[2] D. W. Goodwin and K. A. Macfadyen, Proc. Phys. Soc. (London) **B66**, 85 (1953).

[3] S. Whitehead, *Dielectric Breakdown of Solids* (Oxford University Press, New York, 1951), p. 84.

[4] Crowe, Sharbaugh, and Bragg, J. Appl. Phys. **25**, 1480 (1954).

[5] A. H. Sharbaugh and R. M. Fuoss (to be published).

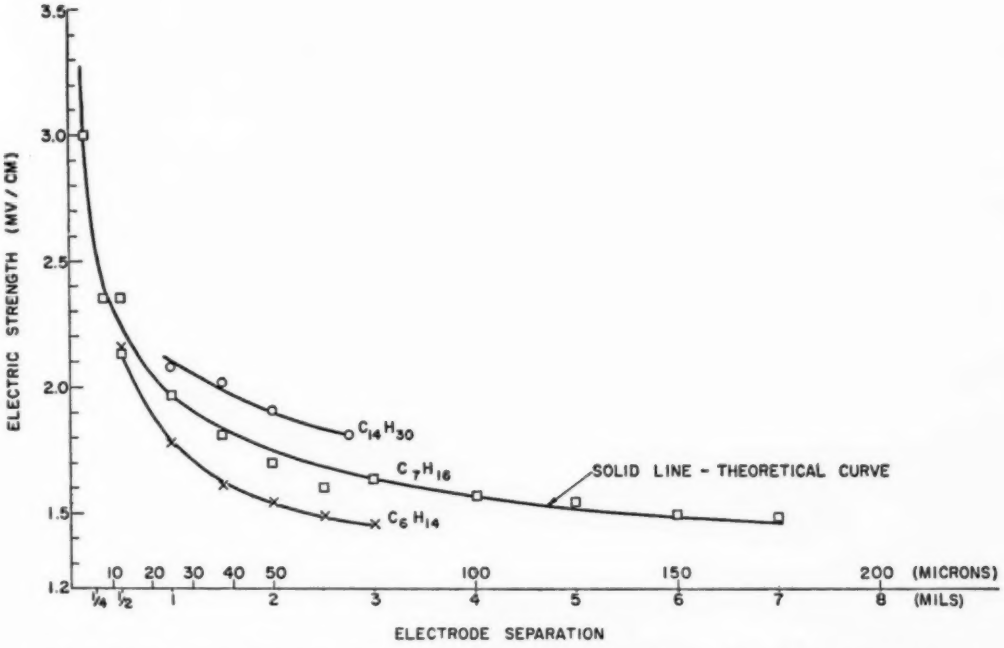

FIG. 1. Electric strength as a function of electrode separation for hexane, heptane, and tetradecane. Steel electrodes, 1.6 μsec pulse width.

λ.[6] If an average number of multiplications n is required for breakdown, the gap must be

$$\delta = nd = n\lambda \exp(\epsilon_0/eE\lambda).$$

Finally, the breakdown strength may be written

$$E = \epsilon_0/e\lambda \log(\delta/n\lambda).$$

The most rapid variation occurs when $\delta/n\lambda$ is not much larger than unity.

The theory of breakdown in liquids is not sufficiently advanced to permit a more precise criterion of breakdown. Townsend-like theories of breakdown in gases are sufficiently detailed not only to show that n is a slowly varying function of the electric field, but also to give the form of the variation. This is possible because specific secondary mechanisms are introduced, which prescribe the relationship of n to the electric field. Nevertheless, many investigators[7] have successfully used the criterion n = constant to calculate the dependence of electric strength upon electrode spacing in studies of breakdown in gases. The Townsend theory shows that this success depends upon the strength of the variation of α (the number of ionizing collisions per centimeter of travel of an electron in the direction of the field) with the electric field, and the weak dependence of n upon the field. It is expected that α will vary even more strongly with field in liquids.

IV. RESULTS AND DISCUSSION

We have tested the model described in Sec. III by measuring the electric strength of heptane over the range of electrode spacing 3–175μ. The results are shown

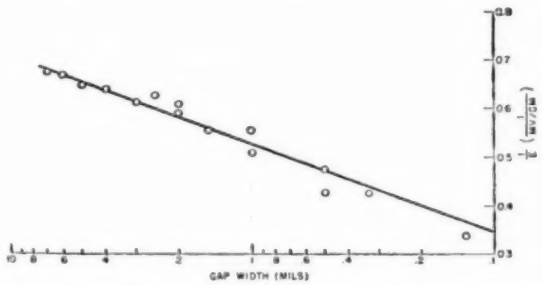

FIG. 2. Reciprocal of electric strength *vs* logarithm of the electrode separation for heptane. Steel electrodes, 1.6 μsec pulse length.

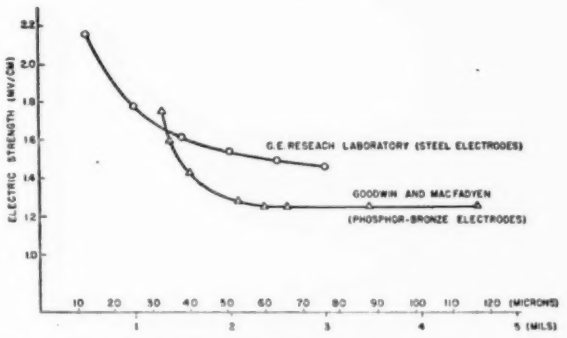
ELECTRIC STRENGTH (MV/CM)
G.E. RESEACH LABORATORY (STEEL ELECTRODES)
GOODWIN AND MACFADYEN
(PHOSPHOR-BRONZE ELECTRODES)
10 20 30 40 50 60 70 80 90 100 110 120 (MICRONS)
1 2 3 4 5 (MILS)

FIG. 3. Electric strength as a function of electrode separation—hexane. A comparison of the results of Goodwin and Macfadyen with those of the General Electric Research Laboratory.

[6] See, for example, Crowe, Bragg, and Thomas, RL-1011, General Electric Research Laboratory.

[7] See, for example, H. Raether, Ergeb. exakt. Naturw. **22**, 73 (1949).

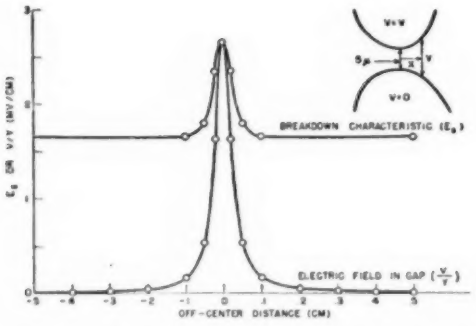

FIG. 4. The breakdown characteristic and imposed electric field for electrodes which have a separation of five microns.

in Fig. 1 along with those for hexane and tetradecane, which were measured over a smaller range of electrode separation. The test plot of $1/E$ *vs* $\log\delta$ is given in Fig. 2 for heptane and shows that the experimental results are consistent with the theory. The product $n\lambda$ has the value 8×10^{-6} cm while λ itself is 9×10^{-7} cm. The latter is an upper limit to the mean free path, obtained by taking ϵ_0 to be the ionization energy. Thus the number of multiplications per electron is greater than 9. It should be cautioned that this number may be in error for two important reasons; first, the product $n\lambda$ is sensitive to small experimental errors, and second, the theoretical model is an oversimplification.

Our hexane results measured with steel electrodes are compared in Fig. 3 with those measured by Goodwin and Macfadyen with phosphor-bronze electrodes. Since Goodwin and Macfadyen found electric strengths measured with steel electrodes to be about 20 percent higher than those measured with phosphor-bronze, the two sets of results are in satisfactory agreement as to magnitude. At 75μ electrode spacing, Edwards' results show the logarithmic decay of the electric field predicted by our simple model, as do ours, in contrast to the lack of dependence found by Goodwin and Macfadyen in this region.

The use of hemispherical electrodes at spacings small compared to their radii insures the existence of the maximum electric field along the axis joining their centers. Normally, such geometry would lead to breakdown along the path of closest approach. However, at very small electrode separation the measured electric strength is strongly dependent on the available length of breakdown path; we are confronted with the possibility that the preferred path of breakdown may be along some longer path. We have examined this phenomenon; the results of an analysis are pictured in Figs. 4 and 5. The lower curve of Fig. 4 shows the dependence of the applied electric field on distance from the line of centers for electrodes spaced 5μ apart. For simplification of the calculations, it has been assumed that all the electric flux lines are parallel. Because of the neglect of transverse component of the electric field, these fields, calculated for regions away from the symmetry axis, will be slightly larger than those present in practice. The upper curve of Fig. 4 shows the variation in the measured electric strength of the liquid as a function of the distance away from the gap center as constructed from the experimentally determined curve of Fig. 1. It is to be noted that the applied electric field decreases more rapidly than the breakdown characteristic curve, and so our breakdowns are occurring along

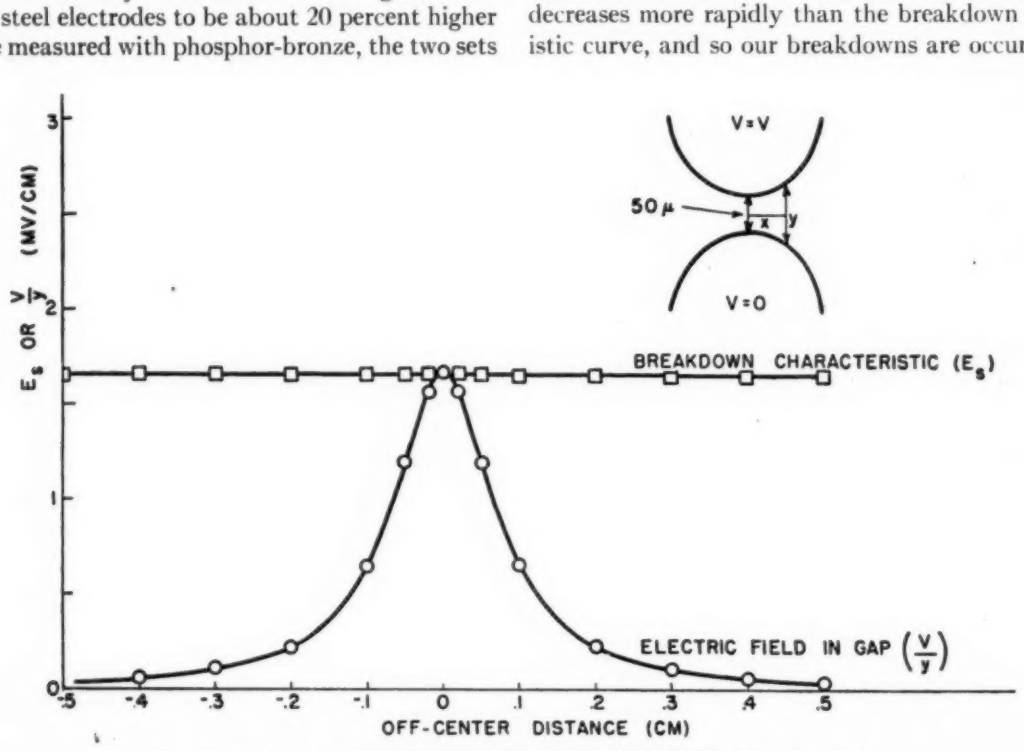

FIG. 5. The breakdown characteristic and imposed electric field for electrodes which have a separation of fifty microns.

the shortest available path. Figure 5 shows the same relations for a 50μ gap. At these large spacings the electric strength is substantially independent of the electrode spacing and so the possibility of off-center breakdown paths is eliminated.

The dependence of electric strength on electrode spacing that is often observed in the testing of commercial oils is to be associated with another phenomenon such as the number of suspended dirt particles in the strong field region. It is likely that the processes considered in this paper are basically different because of the following experimental observations: (1) Our electric strengths are almost an order of magnitude higher than those measured in practical tests; (2) the rapid change in electric strength occurs in our measurements at much smaller electrode separations; (3) our measurements[4] are independent of the length of the applied pulse (beyond 1 μsec).

JOURNAL OF APPLIED PHYSICS VOLUME 26, NUMBER 4 APRIL, 1955

Barium Getters in Carbon Monoxide

J. MORRISON AND R. B. ZETTERSTROM
Bell Telephone Laboratories, Inc., Murray Hill, New Jersey
(Received May 7, 1954)

The effects of pressure, temperature, and physical state on the ability of a barium getter to sorb carbon monoxide are presented. At pressures in the 10^{-5}-mm range, a five-milligram getter is exhausted in about one thousand hours. Temperatures ranging from room temperature to 150°C did not affect greatly the rate of gettering or the capacities of the getters. The observed gettering rates or capacities do not obey any simple law over an extended time.

I. INTRODUCTION

THE role of the getter in a vacuum tube is to maintain residual gas at a satisfactorily low level. In a study of getters the choice of getter material and gases presents a problem. This report confines itself to the behavior of a five milligram Kemet iron clad barium getter in carbon monoxide. Carbon monoxide was found, by mass spectrometric analyses, to be the predominant gas evolved in many vacuum tubes.

A common method of evaluating getter materials used by many is to introduce a sample of gas at high pressure, 10^{-3} to 10^{-2} mm, to a closed system. The time required to reduce this pressure to a somewhat lower pressure is a measure of the ability of the material to sorb the gas. However, this method is not analogous to the gas conditions in a vacuum tube. In a tube one would expect the gas to be evolved at much lower pressures for long periods of time. The method we have employed is similar to one used by S. Wagener[1]; however, we have extended the time scale by a large factor by means of a variable leak.

II. APPARATUS

The apparatus used in this study is shown in Fig. 1. It consists of a ceramic leak system,[2] the performance of which has been checked by a mass spectrometer. This ceramic leak system employs a liter flask containing the carbon monoxide at nearly atmospheric pressure. The plunger of the first or faster leak is raised magnetically, thus lowering the mercury level and exposing part of the ceramic. The second liter flask is filled to some intermediate pressure (a few tenths of a millimeter) as measured by the Pirani gauge. The plunger of the second leak is raised to expose a portion of the tapered ceramic allowing the gas to flow through the system at the desired pressure. The gas flows through the header and is continually pumped away, and also flows into the getter tester through a variable impedance called the leak control tube.[3] This leak control tube (see Fig. 2) has four holes. Total calculated speeds of 10, 50, 285, and 1275 cubic centimeters per second are obtained by opening these holes in sequence. Associated with the main header is an ionization gauge (P_1) and a similar gauge (P_3) is sealed closely to the getter tester. The gauge (P_3) is operated at an emission current of 0.3 milliampere instead of the normal 8 milliamperes in order to minimize its pumping ability. The ion collectors of these gauges are connected to dc amplifiers which in turn operate Esterline-Angus recorders so that continuous records of the pressure changes are obtained.

III. THEORY OF METHOD

Knudsen's law for the flow of gases at low pressures is used to determine the equation for the gettering rate. Referring to Fig. 1, we find that

$$\frac{1}{S}=\frac{1}{S_1}+\frac{1}{S_2},$$

[1] S. Wagener, Brit. J. Appl. Phys. **1**, 225 (1950).
[2] J. Morrison, Rev. Sci. Instr. **24** 230–231 (1953).
[3] J. Morrison, Rev. Sci. Instr. **24**, 546(L) (1953).

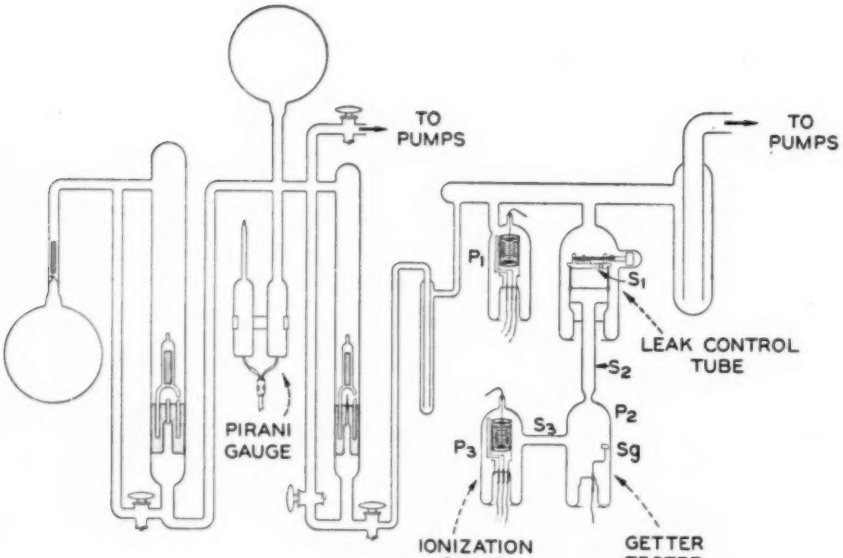

FIG. 1. Schematic of system.

where S is the effective pump speed between the header and the getter tester. For the two smaller holes in the leak control tube $S=S_1\pm 3$ percent, since the conductance of S_2 is approximately 1600 cc/sec. Furthermore,

$$SgP_2=S(P_1-P_2)+S_3(P_3-P_2)-V\frac{dp}{dt},$$

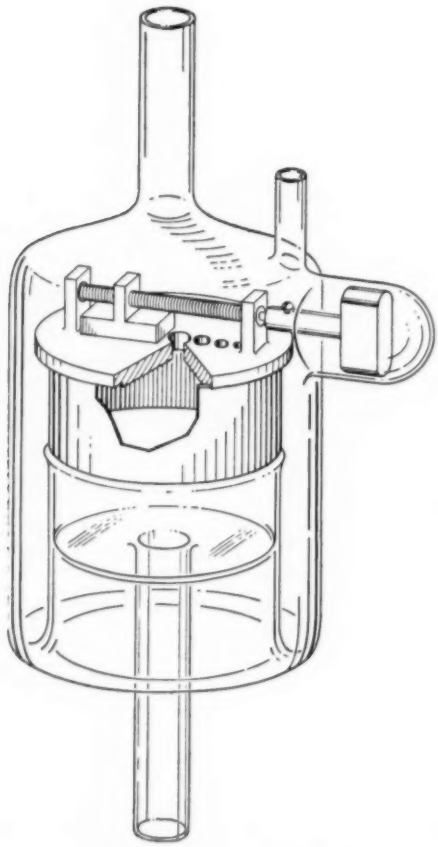

FIG. 2. Leak control tube.

where dp/dt is the rate of change in pressure in volume V on the getter side of the leak control tube. $S_3(P_3-P_2)$ is very small compared to $S(P_1-P_2)$ since the gauge measuring P_3 is not a source of gas; its gettering is minimized and P_2 is essentially equal to P_3; dp/dt is also very small as the data for a typical run (Fig. 3) shows. dp/dt is initially about 1×10^{-6}, and decreases rapidly, whereas $S(P_1-P_2)$ is of the order of 10^{-3}. The equation used for determining the getter rate is therefore

$$SgP_2=S(P_1-P_2).$$

The total quantity of gas sorbed by the getter is determined by

$$C=S\int_0^t (P_1-P_2)dt.$$

When $t=\infty$ this would be the total capacity of the getter. However, we have measured partial capacities for certain time intervals. The capacities were determined by mechanically integrating the area between the P_1 and P_2 curves and multiplying by the appropriate value of S.

The leak control tube or variable impedance may be regarded as an amplifier. The amplification is in the sensitivity of measurement of the gettering rate. For maximum sensitivity, the conductance of the gas to the getter should approximate the gettering rate. In a typical test the difference between P_1 and P_2 becomes steadily smaller and the measurement of pressure difference eventually becomes insensitive. Then S or the speed of the flow of gas to the getter is reduced by closing off a hole. This reduces S by approximately a factor of three, and the difference P_1-P_2 is increased. As each hole is closed in turn, with the accompanying gain in sensitivity, we obtain an over-all increase of approximately 75 in the sensitivity of measurement

over one fixed impedance such as a length of capillary tubing.

IV. TYPICAL RUN

The tube containing the getter and the associated system, Fig. 1, are evacuated. They are baked, excluding the ceramic leaks, for several hours at 400°C resulting in a low pressure of the order of 10^{-8} mm. The getter is flashed and the gas is admitted at a rate which has been carefully set. The gas flows constantly through the manifold at the preset pressure and is continually removed by the pumps. The gas also flows into the section to which the getter is sealed through the leak control tube.

Initially there is a large difference in pressure between the getter pressure and the manifold pressure. As soon as the getter pressure approaches the manifold pressure for the first time, the impedance is changed by closing off the fourth hole thus obtaining more sensitivity in the measurements. As the getter pressure again approaches the manifold pressure, the third hole is closed off; this procedure is repeated until only the smallest hole is open. A graphic representation of these pressure changes is shown in Fig. 3.

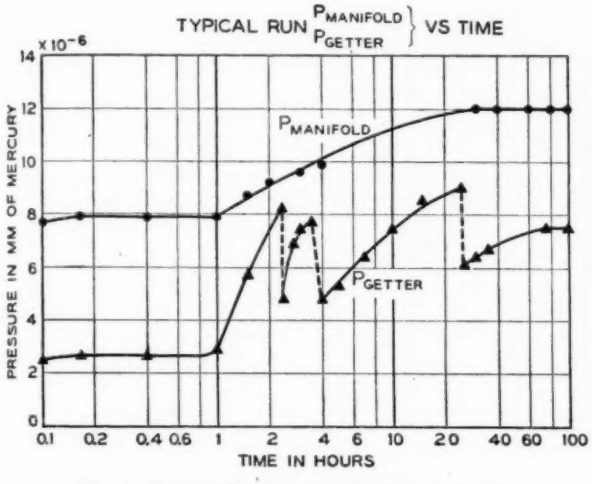

FIG. 3. Changes in pressure as holes are closed.

After a group of curves were obtained at 25°C several were repeated at 150°C. After the getter was flashed, a small oven was raised around the tube containing the getter and the temperature was held at 150°C by means of a Leeds & Northrup micromax recorder.

V. RESULTS

The results of studies on the behavior of a five milligram KIC getter in carbon monoxide are presented in Figs. 4 and 5. The gettering rates at 25° and 150° are shown *versus* the exposure time in hours on logarithmic scales. A pressure, which was the initial manifold pressure, is indicated for each curve. Since this pressure is the most constant one throughout the test and is not much greater than the average pressure at the getter, the curves have been identified by these starting pressures.

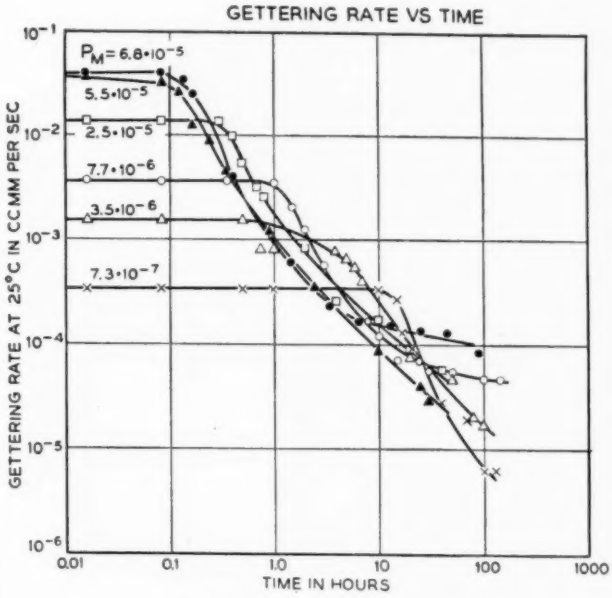

FIG. 4. Gettering rate at 25°.

A significant characteristic of these curves is the initial flat portion, the length of which is clearly dependent on pressure. The time interval for this flat portion ranged from 0.1 hour for pressure of 5 to 6×10^{-5} mm to 10 hours for a pressure of 7.3×10^{-7} mm. This flat portion represents a condition in which the speed of the getter is higher than that of the conductance S (710 cc/sec of the tubing); therefore, the limiting rate $SgP_2=SP_1$ is determined by the conductance S.

As the gettering rate decreases, the curves show a

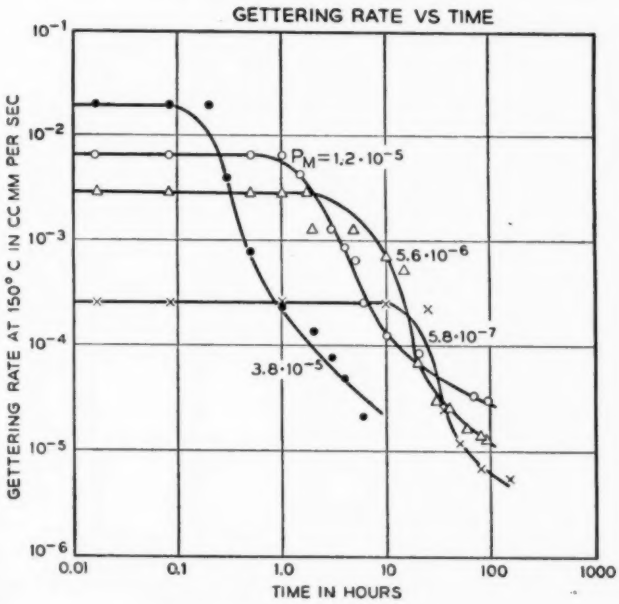

FIG. 5. Gettering rate at 150°.

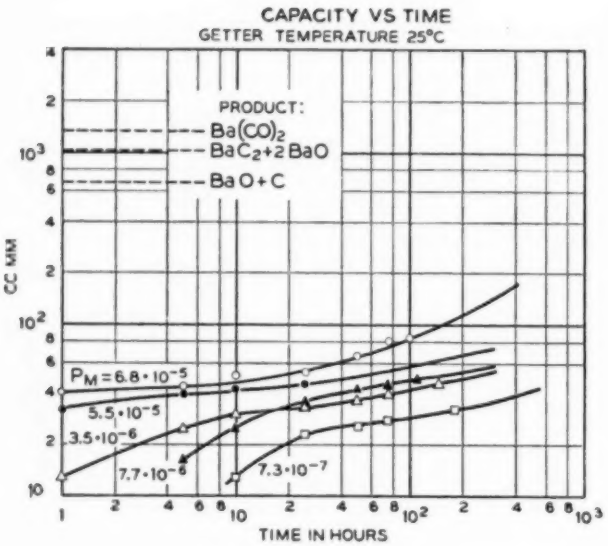

FIG. 6. Capacity at 25°.

tendency to approach a low value which in all cases would continue for many hours longer than the time recorded, but the sensitivity of the equipment was not sufficient to measure this range accurately.

The curves for 150° are similar to those for 25° except that at 150° the flat portion extends for a slightly longer time interval. An increase of the temperature by 125°C does not increase the rate by a large factor. The results at 150° are of interest since this temperature is nearer to actual operating temperatures of some vacuum tube envelopes.

Figure 6 shows other properties of these getters obtained from the data. The capacities or total quantities of gas sorbed are shown for the various pressures. On the curves the points are indicated for the computed capacities and the curves are extrapolated to show the general form of the curves.

Several reactions may be considered such as the formation of barium oxide, barium carbide, or barium carbonyl. These possibilities are listed as follows:

$$\mathrm{Ba+CO\rightarrow BaO+C}$$

$$\mathrm{3\,Ba+2\,CO\rightarrow BaC_2+2\,BaO}$$

$$\mathrm{Ba+2\,CO\rightarrow Ba(CO)_2}.$$

Dotted lines have been drawn showing the equivalent quantity of gas for the five milligrams of available barium and each of these reactions. If barium and carbon monoxide combined in a 1:1 ratio, the five milligrams of barium would be equivalent to 674 cc mm of carbon monoxide. At 25°C and a pressure of 6.8×10^{-5} mm, an extrapolation would indicate that the getter material would be completely used in about 1000 hours.

Several tests were made by varying the treatments of the getters. One of these variations was to bake the getter flash at 350° for fifteen minutes prior to admitting the gas. It was thought that a recrystallization of the barium at this temperature might have a noticeable effect on the properties of the getter. Another reason for baking the getter at 350° was that in the pumping of tubes the glass bulb is often at that temperature when the getter is flashed. At room temperature following the 350° bake the flat portion of the curve was noticeably shorter than for the curves in Fig. 4. This would indicate a considerably smaller capacity for the getter. After a period of approximately 100 hours at room temperature, the getter temperature was raised to 150° and it was observed that the gettering ability was increased for several hours.

Another condition studied was that of flashing the getter on to a thin magnesium oxide film on the glass envelope. The magnesium oxide was sprayed on an area large enough so that all of the getter material was deposited on it. The thought was that possibly a large gain would be obtained in the capacity of the getter due to a greater surface area. However, based on one run at room temperature there was no appreciable gain in the getter capacity. A further comparison was to bake the barium on magnesium oxide at 350° before admitting the carbon monoxide. Again there was no appreciable gain in the gettering rate or the capacity.

Several getters were flashed in argon to obtain a finely divided or black surface resulting in greater surface area. The barium does not react with the argon and pressures of argon ranging from one to five millimeters will produce diffuse deposits of barium. The general results of flashing in argon indicated that surface area is an important factor in getter behavior since those getters flashed in argon possessed the same properties as those flashed *in vacuo* but to a different degree. The gettering rate after flashing in argon was the same, but the initial flat portion of the curve was extended by a factor of two or three, with the resultant large increase in the initial capacity.

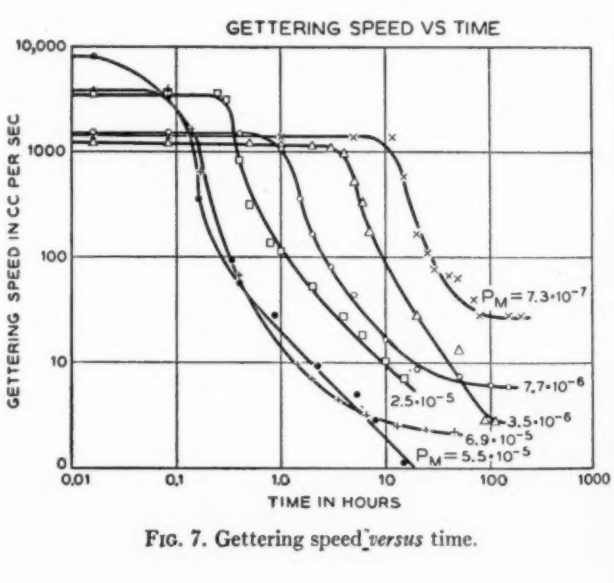

FIG. 7. Gettering speed *versus* time.

VI. DISCUSSION

A significant quantity that is characteristic of a getter is its pumping speed. These speeds in cubic centimeters per second *versus* the times of exposure are shown in Fig. 7. The pressures are the same as those shown in Fig. 4.

From the equation for the gettering rate, we find

$$\text{(pumping speed) } Sg = S\left(\frac{P_1 - P_2}{P_2}\right).$$

The initial pumping speeds of the getters are shown in Table I. The averaged value is 3.2×10^2 cc/sec/cm², probably accurate within a factor of about 2.

This pumping speed is dependent on the sticking probability[4] of the gas, which is the fraction, which do not escape, of the total number of molecules striking the surface.

To determine the sticking probability, we find that

$$KS_gP_2 = rP_2sA_g,$$

where

$K = 3.2\times10^{16}$ molecules in 1 cc at 1 mm pressure,

S_g = speed of getter,

A_g = area of getter,

r = collisions at 1 mm/cm²/sec,

$= 3.8\times10^{20}$ for N_2 at 300°K,

s = sticking probability,

$$s = \frac{KS_g}{rA_g},$$

$$= \frac{3.2\times10^{16}\times3.2\times10^3}{3.8\times10^{20}\times10},$$

$= 2.7\times10^{-2}$ initial sticking probability for the visible area.

This value of s seems low because one expects nearly every molecule striking a freshly flashed getter to stick.

If we assumed a sticking probability of 0.5 as for nitrogen on tungsten, then the number of collisions at 1 mm/cm²/sec $= 3.8\times10^{20}$ for 10 cm² (area of getter) $= 3.8\times10^{21}$; 1 cc mm $= 3.2\times10^{16}$ molecules; 3.8×10^{21} molecules striking the surface $= 6\times10^4$ cc/sec removed for a sticking probability of 0.5. This value is about 20 times the average observed pumping speed.

The characteristic flat portions of the rate curves have been described and attributed to the condition that the gas is being gettered at near the maximum delivery rate, that is, that Sg is equal to or larger than S. The length of the flat portion is determined by the chosen pumping impedance as well as the getter. It is only when the ability of the getter to sorb gas is reduced to a value equal to or less than the quantity passing through the impedance that we obtain values on the curve other than the flat portion. In some types of vacuum tubes S is quite small because of mica structures, in others it is relatively large. Thus the initial gettering conditions in different types of tubes may vary widely.

TABLE I. Initial pump speed of the getter.

P_1	P_2	S_g (S = 710 cc/sec)
6.8×10^{-5}	1.1×10^{-5}	3730
5.5×10^{-5}	4.5×10^{-6}	7960
2.5×10^{-5}	4.0×10^{-6}	3550
7.7×10^{-6}	2.45×10^{-6}	1520
3.5×10^{-6}	1.25×10^{-6}	1280
7.3×10^{-7}	2.4×10^{-7}	1450
		Av = 3248 cc/sec

Our results as shown in Fig. 4 agree fairly well with a result quoted by Wagener who gives an initial value for carbon monoxide of 1250 cc/sec at a pressure of 2×10^{-7} mm for an average area of 10 cm². This value of 125 cc/sec/cm² may be compared to our value of 145 cc/sec/cm² at a starting pressure (P_2) of 2.4×10^{-7} mm.

In view of previous work and of this work on the gettering of a gas, one can readily draw the conclusion that the removal of gas by a film of barium is a complex reaction. There are several processes which must be considered in the removal of the gas: for example, surface adsorption, diffusion of barium, and chemical reaction. It is probable that all three of these are active in the gettering process.

That the area of the surface is an important factor is conclusively demonstrated by the increase in capacity when the getter is flashed in argon. Here a threefold increase in capacity indicates the effect of increased surface area as sites for the sorption of the gas. The fact that we have obtained high gettering rates for more than one hundred hours, in which time very many monolayers are formed, is evidence that there must be a diffusion of the gas into the barium or of barium through a reaction product to the gas.

There are a number of theories[5] of the mechanism of oxidation of a metal:

(1) The linear law expected at higher temperatures and pressures. Oxides of porous structure (physically discontinuous), of which barium oxide is one, offer no resistance to the passage of oxygen to the surface of the metal. As a result the rate of growth of the layer of oxide is expected to be constant at any given temperature. Denoting the increase in weight per unit area by W, the linear law states that for a given temperature

$$W = k_1t,$$

where t = time elapsed, and k_1 is a constant.

[4] J. A. Becker and C. D. Hartman, J. Phys. Chem. **57**, 153 (1953).

[5] S. Dushman, Sci. Foundations of Vac. Tech.

(2) Another law, the parabolic law, applies to metals for which the oxide coating is compact (the oxide forms as a homogeneous layer) and the rate of oxidation depends on the rate of diffusion of oxygen through the layer already formed. It is found that $W^2=k_2t$ where k_2 is a constant for any given temperature. This relation was first observed by G. Tammann[6] and was confirmed by Pilling and Bedworth.[7]

(3) A third law, the logarithmic law, was proposed by G. Tammann[8] and is of the form

$$W=k_4\log(at+1),$$

where k_4 and a are constants for any given temperature. This relation was found to be in agreement with observations on the oxidation of zinc. For temperatures above 225°C the logarithmic law was found to be in very good agreement with the experimentally observed values of W and t; for temperatures below 225°C, the agreement was not so good.

From our curves in Figs. 4 and 5, it would be difficult to claim adherence to any one of these laws over a wide range. For the greater part of the curve, that is the initial flat segment and the following slope to the point where we are using but one hole in the impedance and the pressure difference is small, the data is considered to be quite accurate. Because of the initial limitations due to the impedance of the connecting tube, and possible variations in the location of the final points when the sensitivity is diminished, we are not able at this time to apply any more elaborate theory to the experimental data. However, from an engineering point we believe the data to be of real value in that it reveals getter behavior under conditions which might be encountered in a vacuum tube.

[6] G. Tammann, Z. anorg. Chem. **111**, 78 (1920).
[7] Pilling and Bedworth, J. Instr. Metals **29**, 529 (1923); J. Ind. Eng. Chem. **17**, 372 (1952).
[8] G. Tammann, Z. anorg. Chem. 124 (1922); **42**, 169 (1928).

SUMMARY

The initial speed at which barium getters carbon monoxide was observed to be about 300 cc/sec/cm^2 and is roughly independent of pressure in the range from 10^{-5} mm to 10^{-7} mm. The time interval during which this initial rate is maintained is inversely proportional to the pressure.

The capacities of individual getters should be roughly the same over a sufficiently long period. However, the higher the pressure, the shorter the time interval in which the ultimate capacity is reached.

At a pressure of 7×10^{-5} mm of carbon monoxide, a five milligram getter might be completely used in a thousand hours. At a pressure of 7×10^{-7} mm the useful life of the same getter would be ten to one hundred times greater.

Flashing the getters in argon to obtain a diffuse deposit increased the quantities sorbed by the getters by factors of two or three for the first hundred hours. Flashing the barium on a layer of magnesium oxide in an attempt to obtain greater surface area did not produce any increase in quantity sorbed or rate.

Temperature in the range from 25° to 150° did not affect greatly the rate of gettering or the quantities sorbed.

Our observed initial pumping speed of the getter is one-fortieth of that which would be obtained if the sticking probability were unity.

Gettering rates or capacities do not obey any simple law over an extended time.

ACKNOWLEDGMENTS

We wish to thank J. J. Lander and J. A. Becker for their help and advice on this study.

JOURNAL OF APPLIED PHYSICS VOLUME 26, NUMBER 4 APRIL, 1955

Crystallization Kinetics in High Polymers. II. Polymer-Diluent Mixtures*

LEO MANDELKERN
National Bureau of Standards, Washington, D. C.
(Received June 3, 1954)

The rates of crystallization of two polymer-diluent mixtures, poly-(ethylene oxide)-diphenyl ether and poly-(decamethylene adipate)-dimethyl formamide were studied at various temperatures ranging from 6° to 15° below the melting points of the mixtures. The various mixtures investigated encompassed a wide range of compositions; the volume fraction of the diluent v_1 ranged from about 0.10 to 0.70. The crystallization behavior observed was strikingly similar to that previously reported for bulk polymers in the first paper of this series. The results are interpreted by making the necessary modifications to the treatment previously employed wherein steady-state nucleation and growth were assumed to occur simultaneously throughout the process. Agreement obtained between theory and experiment is similar to the corresponding results for the bulk polymer.

INTRODUCTION

IN the initial paper in this series,[1] paper I, the results of a study of the crystallization kinetics of several bulk polymers were discussed. The experimental observations were limited to temperature intervals in the vicinity of the respective equilibrium melting temperatures T_m^0 of the polymers, and reproducible experimental results were obtained. The crystallization rate was found to be strongly dependent on temperature in the region investigated, and the temperature coefficient was uniform throughout the crystallization process. Thus, for any given polymer the isotherms, which relate the amount of crystallinity to time, were superposable merely by rescaling the time. The shape of the experimental isotherms and the temperature coefficient of the rate could be quantitatively explained by assuming that steady-state nucleation and growth occur simultaneously, i.e., from zero time to the end of the process. Both the nucleation and growth rate depend on temperature, each of course in a different manner. The strong temperature coefficient of the crystallization process, in the vicinity of T_m^0, is a manifestation of the temperature coefficient of the nucleation rate in this region. Other features of crystallization behavior of polymers, such as the occurrence of a temperature at which the rate of crystallization is a maximum and the subsequent decrease in rate as the glassy state is approached, can qualitatively be explained on the basis of the assumed mechanisms.

The crystallization rate can, of course, be influenced by other factors besides temperature, the over-all effect of any external influences being a resultant of the effect on both the nucleation and growth. In general, low molecular weight diluents affect the physical properties and behavior of polymers. In particular, it has been demonstrated[2–7] that diluents depress T_m^0 in a systematic manner in accord with the theormodynamic principles governing two-phase equilibria. Since the nucleation rate depends both on the melting temperature and the "apparent activation energy" of diffusion and since the growth rate has been assumed to depend on segmental mobility, it may be expected *a priori* that the addition of diluent will have a marked effect on the over-all crystallization rate. To assess the effect of the amount and type of diluent that is mixed with the polymer, the theory previously derived is further generalized in this paper. Experimental studies of the crystallization kinetics of polymer-diluent mixtures are presented and discussed in terms of the theory. Two polymers, poly-(ethylene oxide) and poly-(decamethylene adipate), were chosen and mixtures with diluent covering a wide range of composition were employed. For each of the polymers detailed studies were made with only one diluent type, PEO with diphenyl ether and PDA with dimethyl formamide; less detailed though qualitatively adequate results were obtained with the other diluents. To study the rate at which crystallinity develops, volume dilatometers were again used because of their simplicity and sensitivity to changes in the amount of crystallinity.

EXPERIMENTAL

Materials

The polymers used, poly-ethylene oxide, "PEO" and poly-decamethylene adipate, "PDA," were characterized in the previous paper.[1] The diluents, dimethyl formamide, tetralin, and diphenyl ether, were of reagent grade and the first two named were redistilled before use. The polymer-diluent mixtures were prepared by heating the ingredients with stirring in an atmosphere of nitrogen. This procedure has been previously described in greater detail.[3,4,6] The densities of the diluents were measured at two temperatures and were assumed to vary linearly with temperature.

* A portion of this work was supported by the Office of Naval Research.

[1] Mandelkern, Quinn, and Flory, J. Appl. Phys. **25**, 830 (1954).
[2] P. J. Flory, J. Chem. Phys. **17**, 223 (1949).
[3] Evans, Mighton, and Flory, J. Am. Chem. Soc. **72**, 2018 (1950).
[4] Flory, Mandelkern, and Hall, J. Am. Chem. Soc. **73**, 2352 (1951).
[5] A. M. Bueche, J. Am. Chem. Soc. **74**, 65 (1952).
[6] Mandelkern, Garrett, and Flory, J. Am. Chem. Soc. **74**, 3949 (1952).
[7] Flory, Garrett, Newman, and Mandelkern, J. Polymer Sci. **12**, 97 (1954).

Dilatometry

The dilatometric procedures have also been described elsewhere.[1,3,4,6] The studies of crystallization kinetics were carried out in a manner similar to that described in the previous paper.

RESULTS

Melting Temperatures and Heats of Fusion

For PDA the values of the equilibrium melting temperature, T_m^0 and the heat of fusion per mole of repeating unit, ΔH_u, have been reported.[6] These are 79.5°C and 10 500 cal/mole of repeating unit, respectively. The value of T_m^0 for PEO was determined by studying the dependence of the specific volume on temperature and the results are illustrated in Fig. 1. T_m^0 is defined as that temperature at which the last traces of crystallinity disappear and is 66°C for PEO. In the determination of T_m^0, the thermal history of the sample consisted only in the gradual uncontrolled cooling of the melt. Volume equilibrium was attained in one to two hours at all temperatures except in the range less than 10° below T_m^0. In this interval the temperature was raised in 0.5° or 1° increments and held at each temperature from twelve to twenty-four hours within which time volume equilibrium appeared to be established. The major portion of the melting process takes place over a comparatively narrow temperature range; 90 percent of the volume change occurred in a five degree interval.

The heat of fusion per mole of repeating unit ΔH_u can be determined by studying the lowering of T_m^0 by diluent according to methods previously demonstrated.[2-7] By applying the thermodynamic equation applicable to two-phase equilibrium it has been shown that for polymers of appreciable molecular weight

$$(1/T_m - 1/T_m^0)/v_1 = (RV_u/V_1\Delta H_u)(1 - BV_1v_1/RT_m) \quad (1)$$

where T_m is the melting point of the polymer-diluent mixture, R is the gas constant, V_u the molar volume of the repeating unit, V_1 the molar volume of the diluent, v_1 the volume fraction of the diluent, and B the molar free energy change brought about by first neighbor interactions.[8] The values of T_m of binary mixtures of PEO with either diphenyl ether or tetralin as diluents were determined over a composition range of approximately $v_1 = 0.10$–0.70. Some typical specific volume-temperature plots for these diluent mixtures are included in Fig. 1. The data are plotted in Fig. 2 in the manner suggested by Eq. (1), and are well represented by straight lines. From the intercepts in these plots, the values of ΔH_u obtained are 1825±85 cal/mole of repeating unit with diphenyl ether as diluent and 2130±40 cal/mole of repeating unit with tetralin as diluent.

Crystallization Kinetics

The isothermal rates of crystallization of the supercooled binary mixtures were investigated in a temperature interval below T_m, so chosen that the times τ_i at which crystallization became detectable were in the range of from 5 to 5×10^2 min. Since sufficient information could be obtained from studies in this interval, for convenience the studies of the complete

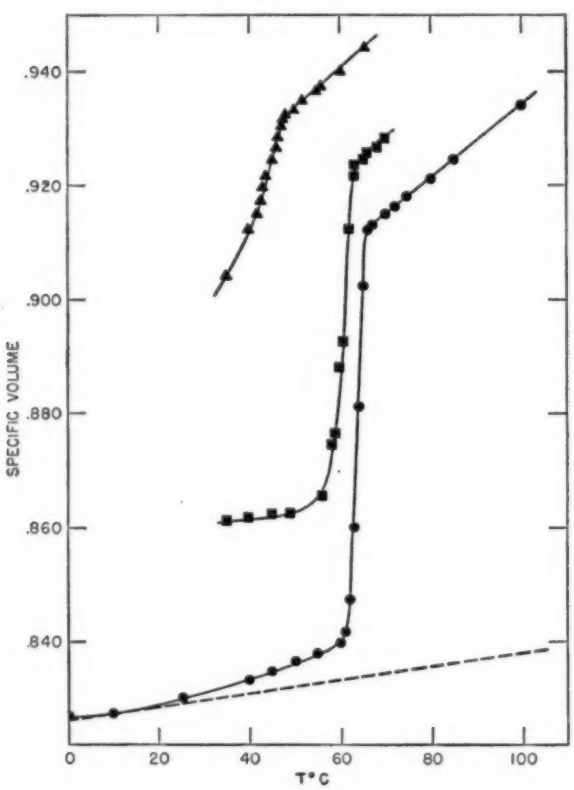

FIG. 1. Specific volume *vs* temperature for poly-(ethylene oxide) and its mixture with diluents. Pure polymer ●; with tetralin, $v_1 = 0.098$ ■; with diphenyl ether, $v_1 = 0.602$ ▲.

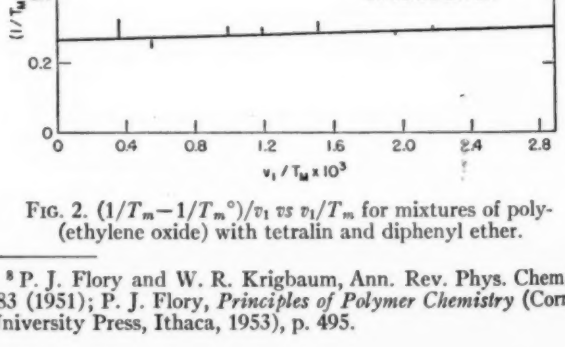

FIG. 2. $(1/T_m - 1/T_m^\circ)/v_1$ *vs* v_1/T_m for mixtures of poly-(ethylene oxide) with tetralin and diphenyl ether.

[8] P. J. Flory and W. R. Krigbaum, Ann. Rev. Phys. Chem. 2, 383 (1951); P. J. Flory, *Principles of Polymer Chemistry* (Cornell University Press, Ithaca, 1953), p. 495.

TABLE I. Apparent induction times τ_i (in minutes) at various values of ΔT for the polymer-diluent mixtures.

Poly-(ethylene oxide)—diphenyl ether

$v_1=0.094$		$v_1=0.182$		$v_1=0.295$		$v_1=0.388$		$v_1=0.494$		$v_1=0.601$		$v_1=0.689$	
ΔT	τ_i	ΔT	τ_i	ΔT	τ_i	ΔT	τ_i	ΔT	τ_i	ΔT	τ_i	ΔT	τ_i
10.5–11.5	15	11.5–12	6–9	12–13	3–5	12–13	7–8	12–13	8–9	15–15.5	6	14–14.5	13
9.5–10.5	39	10.5–11	11	11–12	6–7	11–12	15	11–12	12	14–14.5	10	13.5–14	24
8.5–9.5	92	9.5–10	38	10–11	14	10–11	30	10–11	28	13–13.5	18	12.5–13	53
7.5–8.5	329	8.5–9	250	9–10	30–35	9–10	65	9–10	55	12–12.5	42	11.5–12	124
		7.5–8	315	8–9	85	8–9	220	8–9	210	11–11.5	103	10.5–11	162–202
				7–8	220	7–8	470–585	7–8	450	10–10.5	231		
				6–7	440	6–7	2070–2880			9–9.5	>420		

Poly-(ethylene oxide)—tetralin

$v_1=0.098$		$v_1=0.205$		$v_1=0.321$		$v_1=0.536$		$v_1=0.686$	
ΔT	τ_i	ΔT	τ_i	ΔT	τ_i	ΔT	τ_i	ΔT	τ_i
12–12.5	5	12–12.5	5–6	12.5–13	8	13–13.5	4	14–14.5	5
11–11.5	10	11–11.5	13	11.5–12	12	12–12.5	8	13–13.5	8
10–10.5	20	10–10.5	38	10.5–11	25	11–11.5	17–18	12–12.5	13
9–9.5	54	9–9.5	111	9.5–10	34	10–10.5	34	11–11.5	39
8–8.5	195	8–8.5	220	8.5–9	100			10–10.5	111
7–7.5	626	7–7.5	325	7.5–8	325				

Poly-(decamethylene adipate)—dimethyl formamide

$v_1=0.202$		$v_1=0.422$		$v_1=0.603$	
ΔT	τ_i	ΔT	τ_i	ΔT	τ_i
11.0±0.5	7	14.2±0.5	15	12.5±0.5	23
10.0±0.5	15	13.2±0.5	25	11.5±0.5	40
9.0±0.5	32	12.2±0.5	38	10.5±0.5	53
8.0±0.5	102	11.2±0.5	88	9.5±0.5	103
7.0±0.5	220	10.2±0.5	120	8.5±0.5	230
6.0±0.5	679	9.2±0.5	350	7.5±0.5	731

crystallization process were limited to this temperature range. The dilatometers were identical in construction with those previously employed so that volume changes of the order of 0.02 percent were detected.

If a plot is made of the variation of the specific volume with time at any given temperature the curves that are obtained display general characteristics which are independent of composition and are very similar to those obtained for bulk polymers. After the attainment of temperature equilibrium, the volume remains constant for a well-defined "apparent induction time," τ_i. Crystallization becomes observable at τ_i as is indicated by the decrease in volume, and the process then proceeds at an accelerating rate until a pseudo-equilibrium degree of crystallization is approached. The experiments are again highly reproducible and the results are independent of the temperature at which the samples were initially held above T_m, provided that care is taken to insure that all the crystallinity has disappeared.

As is indicated in Table I, a very strong effect of temperature on the crystallization rate is observed in these systems. There are given in Table I the values of τ_i at various values of ΔT, the difference between T_m and the temperature at which the observations were made for the three systems studied. The marked dependence of τ_i on temperature in the region near T_m is reminiscent of the behavior of bulk polymers and suggests that in the neighborhood of T_m the steady-state nucleation rate is still the rate-determining step.

Typical results illustrating the entire crystallization process are shown in Fig. 3. In this figure the ratio $(V_\infty - V_0)/(V_\infty - V_t)$ is plotted against the log of time, for the various temperatures studied for a mixture of PEO and diphenyl ether, having a volume fraction of diluent equal to 0.388. V_0 is the initial volume per unit mass, V_t this volume at time t, and V_∞ the apparent equilibrium volume. The characteristic "apparent induction time" and subsequent acceleration of the crystallization rate are well illustrated in these plots. The isotherms of Fig. 3 are very similar to those obtained for all the polymer-diluent mixures studied.

DISCUSSION

The experimental isotherms, can be brought into coincidence merely by the shifting of each of the curves an appropriate amount along the horizontal axis. The isotherms are superposable over the entire crystallization process, indicating that the temperature dependence of the process is invariant with time. This phenomenon has been observed[1] for a wide variety of bulk polymers and is characteristic of all the polymer-diluent mixtures of the present investigation.

The isothermal crystallization kinetics of a polymer-diluent mixture can then be represented by a composite curve obtained by shifting all the isotherms to a common one. The solid curves of Figs. 4 and 5 represent the composite curves for each of the polymer-diluent mixtures studied; also included in the figures are the composite curves for the corresponding bulk polymers. It can be seen that there is no major effect of composition on the isothermal rate of crystallization. However, as the diluent concentration in the mixtures increases,

sufficient differences in the crystallization process are observed to preclude the possibility of constructing a realistic composite which is independent of composition.

The superposability of the isotherms and the accompanying invariance of the temperature coefficient of the crystallization rate lends strong support to the concurrence of the nucleation and growth processes, in close analogy to the situation for bulk polymers. The excellent reproducibility of the observations and the absence of an effect of the temperature of superheating on the subsequent crystallization rate indicate a homogeneous nucleation process. The nucleus is assumed to be disk shaped and comprised of a bundle of portions of polymer chains that are oriented parallel to the axis of the disk. Since there is no direct evidence as to the detailed nature of the growth mechanism, it is assumed for simplicity that the radius of a growing center increases linearly with time so that the rate of volume change of a growing center is proportional to its surface area. The disk-shaped nuclei are allowed to develop either along their radii, with the polymer chain normal to the plane of the disk, or to develop spherically, i.e., grow in all directions.

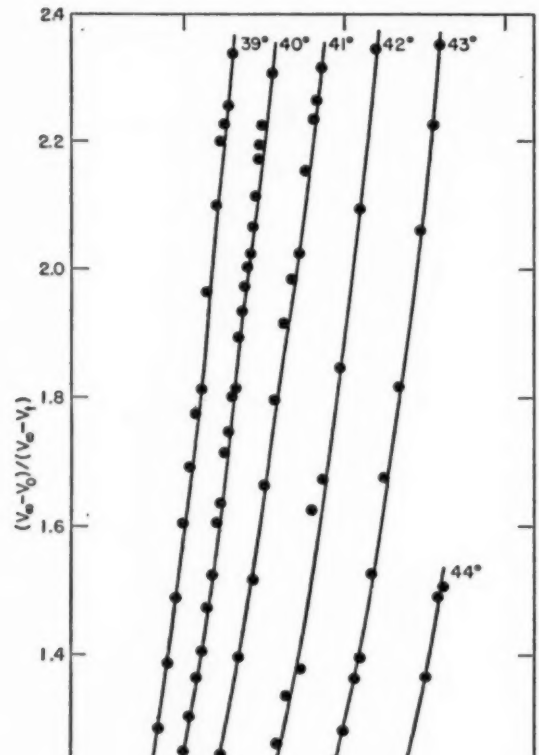

FIG. 3. $(V_\infty-V_0)/(V_\infty-V_t)$ *vs* log*t* for a mixture of poly(ethylene oxide) with diphenyl ether, $v_1=0.388$, at various temperatures.

The isothermal rate at which crystallinity develops can be calculated from these assumptions following the procedures developed by Avrami[9] and previously adapted for bulk polymers. Again, a hypothetical analog is assumed wherein nuclei are allowed to form and grow throughout the entire mass. The actual crystallization rate is calculated by considering only that portion of the increase of mass of an average growing center that takes place in space actually available for the transformation. The growth of a center is retarded as it encounters regions already transformed (impingement); it is also retarded by the fact that the polymers, in general, do not crystallize completely even at equilibrium so that not all the amorphous region can be transformed, and also by the fact that part of the total mass is occupied by regions of diluent into which the crystallite cannot grow.

Let dW_c' be the mass that is transformed during time dt and assume that there are no restraints to the growth of a center. The actual mass transformed dW_c will, of course, be less than dW_c' because of the retardation to growth discussed above. Since nuclei, both real and hypothetical, have been formed at random throughout the entire mass, the shells of transformed material are in random regions. Therefore, in the vicinity of the growing centers the fraction of the mass that is available for transformation is the same as the total fraction available. Then the expected actual mass transformed is given by

$$dW_c=dW_c'[1-U(t)], \tag{2}$$

where $U(t)$ is the "effective fraction" of the mass transformed at time t; it is that fraction of the total mass in which further crystal growth can not occur. This effective fraction transformed is assumed proportional to the actual fraction transformed. The proportionality factor is $1/\lambda_w'$, where λ_w' is the fraction of the total mass, polymer and diluent, that is crystalline at equilibrium. Since

$$U(t)=(W_c/W_0)(1/\lambda_w'), \tag{3}$$

where W_c is the mass crystalline at time t, and W_0 is the total mass, then

$$dW_c/dW_c'=[W_0-(1/\lambda_w')W_c]/W_0. \tag{4}$$

Since the growth and nucleation processes are identical with those previously assumed for bulk polymers, the analysis proceeds in a manner identical to that in paper I with the result that

$$\int_0^{W_c} dW_c/[W_0-(1/\lambda_w')W_c]=(\pi/3\delta)AG^3t^4=k_st^4 \tag{5}$$

[9] M. Avrami, J. Chem. Phys. **7**, 1103 (1939); **8**, 212 (1940).

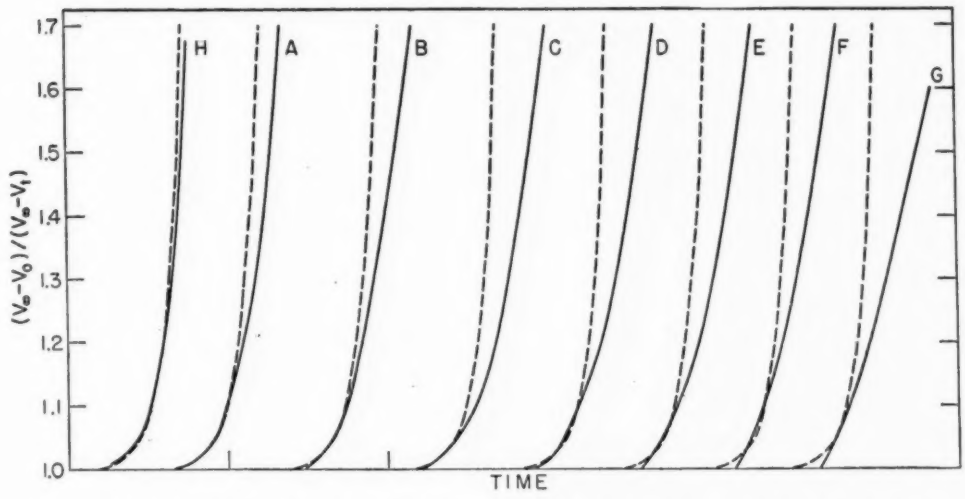

FIG. 4. Fit of experimental data to theoretical curves. Plot of $(V_\infty - V_0)/(V_\infty - V_t)$ *vs* log t for mixtures of poly-(ethylene oxide) with diphenyl ether. Solid lines composite isotherm for each mixture. Curve A—$v_1 = 0.094$; curve B—$v_1 = 0.182$; curve C—$v_1 = 0.295$; curve D—$v_1 = 0.398$; curve E—$v_1 = 0.494$; curve F—$v_1 = 0.601$; curve G—$v_1 = 0.689$; curve H—$v_1 = 0.000$. Dashed line theoretical isotherm for spherical growth. Position of each isotherm relative to abscissa is arbitrary; short vertical marks along abscissa indicate length of one decade.

for spherical growth and

$$\int_0^{W_c} dW_c/[W_0 - (1/\lambda_w')W_c] = (\pi/3\delta)l_c A G^2 t^3 = k_d t^3 \quad (6)$$

for disk growth. A is the rate of formation of nuclei per unit volume G, the growth rate constant, is the rate of change of the radius with time, δ is the ratio of the density of the liquid to crystalline polymer, and l_c is the thickness of the disk. Further integration yields

$$\ln\{W_0/[W_0 - (1/\lambda_w')W_c]\} = (1/\lambda_w')(\pi/3\delta)AG^3t^4 = (1/\lambda_w')k_s t^4 \quad (5')$$

and

$$\ln\{W_0/[W_0 - (1/\lambda_w')W_c]\} = (1/\lambda_w')(\pi/3\delta)l_c AG^2t^3 = (1/\lambda_w')k_d t^3. \quad (6')$$

Substituting

$$\lambda_w' = W_c(\infty)/W_0; \quad W_c = \rho_c V_c; \quad W_c(\infty) = \rho_c V_c(\infty)$$

and $V_c(t) = (\delta/\delta - 1)[V_t - V_0]$, we obtain

$$\ln\{[V_\infty - V_0]/[V_\infty - V_t]\} = (1/\lambda_w')k_s t^4 \quad (5'')$$

and

$$\ln\{[V_\infty - V_0]/[V_\infty - V_t]\} = (1/\lambda_w')k_d t^3. \quad (6'')$$

The arguments of the logarithm suggested the plots that are made in Figs. 3 to 6. Equations (5″) and (6″) are in agreement with the observed superposition of the isotherms, and reduce to the equations previously developed when there is no diluent present. The isotherm, as defined by plots of $[V_\infty - V_0]/[V_\infty - V_t]$ against t, are describable by use of only one arbitrary parameter, $(1/\lambda_w')k_s$ or $(1/\lambda_w')k_d$. Thus, if a theoretical or master plot is made of $[V_\infty - V_0]/[V_\infty - V_t]$ against $\log(\tau^4)$ or against $\log(\tau^3)$, respectively, where τ is a time variable defined as either $(1/\lambda_w')k_s t^4$ or $(1/\lambda_w')k_d t^3$, the experimental isotherms can be fitted to the universal isotherm, and the value of the arbitrary parameter that governs the crystallization rate can be determined. This procedure has been followed for the two polymer-diluent systems studied in detail, PEO-diphenyl ether and PDA-dimethyl formamide; the values of the "effective rate constants," $(1/\lambda_w')k_s$ and $(1/\lambda_w')k_d$, thus obtained are found to decrease enor-

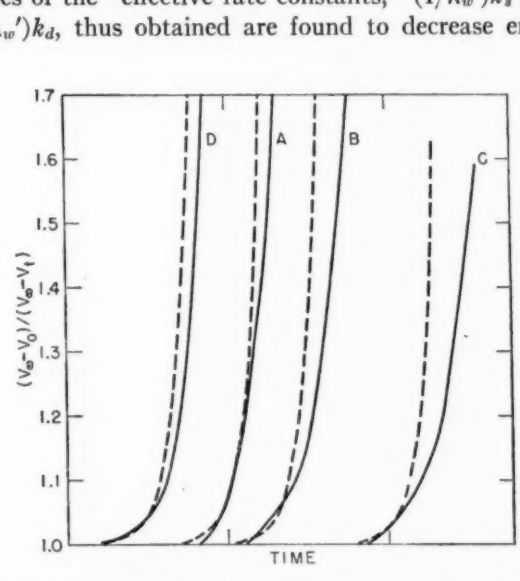

FIG. 5. Fit of experimental data to theoretical curves. Plot of $(V_\infty - V_0)/(V_\infty - V_t)$ *vs* log$t$ for mixtures of poly-(decamethylene adipate) with dimethyl formamide. Solid lines are composite isotherms for each mixtures. Curve A—$v_1 = 0.202$; curve B—$v_1 = 0.422$; curve C—$v_1 = 0.603$; curve D—$v_1 = 0.000$. Dashed line theoretical isotherms for spherical growth. Position of each isotherm relative to abscissa is arbitrary; short vertical marks along abscissa indicate length of one decade.

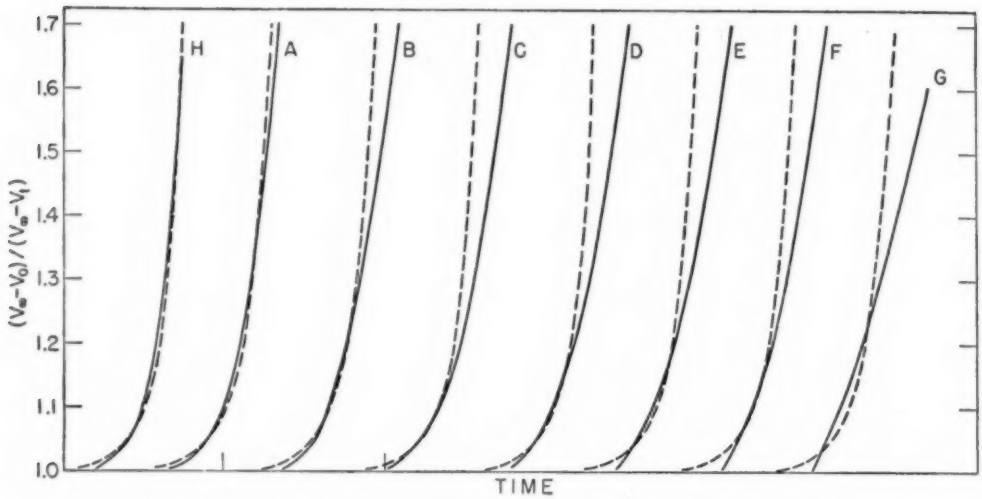

FIG. 6. Fit of experimental data to theoretical curves. Plot of $(V_\infty - V_0)/(V_\infty - V_t)$ *vs* log t for mixtures of poly-(ethylene oxide) with diphenyl ether. Solid lines are composite isotherms for each mixture, and are identical to those in Fig. 5. Dashed lines are theoretical isotherms for disk growth. Position of isotherm relative to abscissa is arbitrary; short vertical marks along abscissa indicate length of one decade.

mously with temperature in a manner strikingly similar to the behavior in bulk polymers, as was suggested by the observed dependence of the apparent induction time on temperature.

The fit that is obtained between the theoretical and experimental isotherms is illustrated in Figs. 4 to 7. In each figure the solid lines represent the composite isotherm for each of the mixture studied in detail. In Figs. 4 and 5 the dashed lines represent the theoretical isotherms for spherical growth, while in Figs. 6 and 7 the dashed lines represent the corresponding theoretical isotherms for disk growth. Quantitative agreement is obtained for the initial stages of the process for either type of growth, the experimental observations not being sufficiently precise to distinguish between them. Since there are no gross differences between the isotherms for bulk polymers and polymer-diluent mixtures, the agreement obtained is similar to that for bulk polymer. As the crystallization progresses, the agreement becomes only qualitative. As the concentration of diluent increases, these deviations become more marked; at the highest concentrations of diluent the agreement is only superficial for the complete process. The reasons for the changes in the shape of the experimental isotherm as the diluent concentration increases are not at present understood. The simple nucleation and growth processes that appear to be adequate to explain the isotherms for bulk polymers and polymer-diluent mixtures up to moderate concentrations will have to be modified to explain the behavior at higher diluent contents. However, even for the mixtures containing the higher amounts of diluent the crystallization rate depends markedly on temperature in the vicinity of T_m, indicating that the process is still nucleation-controlled.

The time τ_i at which crystallinity is first observed, corresponds to a critical value of the argument of the logarithm in Eqs. (5″) and (6″), depends, of course, on the nucleation rate, the growth rate, and the sensitivity of our crystallinity detector.[1,10] These times are inversely related to the "effective" rate constants, so the τ_i must be inversely proportional to either $(1/\lambda_w')^{\frac{1}{4}}k_s^{\frac{1}{4}}$ or $(1/\lambda_w')^{\frac{1}{4}}k_d^{\frac{1}{4}}$. Up to moderate diluent concentrations, when comparison is made at the same values of ΔT the "effective rate constants" are practically independent of composition. However, as the amount of diluent increases at comparable values of ΔT, the "effective" rate constants decrease; these observations are reflected in the data of Table I in that longer times are necessary for crystallization to be first observed in mixtures containing the higher amounts of diluent.

It can be shown that

$$1/\lambda_w' = [\bar{V}_c - \bar{V}_1]/[\bar{V}_\infty - \bar{V}_0], \qquad (7)$$

where $\bar{V}_c$ and $\bar{V}_1$ are the specific volumes of the all-crystalline and all-liquid bulk polymers, and $\bar{V}_0$ and $\bar{V}_\infty$ are the initial and equilibrium values, respectively, of the specific volumes of the mixtures. Thus, using the data obtained from the specific volume-temperature studies and approximating the specific volume of the all-crystalline polymer in the manner indicated by the dotted line of Fig. 1, the effective rate constants can be transformed to actual rate constants. The values of k_s and k_d thus obtained are less than the corresponding "effective rate constants" but their variation with temperature and composition has not been altered.

The variation of the rate constant with either temperature or composition is governed by the dependence

[10] D. Turnbull, Acta Met. 1, 684 (1953).

of the growth and nucleation rate on these variables. In order for crystallization to occur in a supercooled liquid or binary liquid mixture, stable nuclei exceeding a definite critical size must be formed by means of statistical thermal fluctuations. Though at a given temperature nuclei of critical size are formed through growth of smaller subcritical sized nuclei, a steady-state rate of production of critical size nuclei is quickly reached.

The steady-state rate of nucleation (formation of nuclei of critical size in layer) in condensed systems can be expressed as[11,12]

$$A = A_0 \exp\{-E_D/RT - \Delta F^*/RT\}, \qquad (8)$$

where A_0 is a constant that is only slightly temperature dependent and E_D, the apparent activation energy of viscous flow, serves as an approximation for the energy of activation for transport across the liquid-crystal interface. The free energy change in forming a nucleus possesses a maximum with respect to the nucleus size. The maximum value of the free energy of formation is ΔF^*; it is the height of the free energy barrier that must be surmounted in order for stable nuclei to be formed. Nuclei larger than the size corresponding to ΔF^* can grow spontaneously while smaller nuclei are thermodynamically unstable and disappear. In order to calculate ΔF^* one must first obtain an expression for ΔF_d, the free energy change that occurs in forming from a supercooled polymeric liquid a nucleus comprised of polymer segments. Although our major interest is in polymer-diluent mixtures, it will be advantageous to consider also the analogous calculation for a system consisting only of polymer molecules.

Consider a disk of length L and radius R comprised of portions of ρ polymer chains, the chains being all aligned parallel to the length of the disk. If ζ is the number of repeating units comprising the length of the disk, $\zeta\rho_s$ the number of repeating units on the surface, and γ_u the surface free energy per repeating unit, then the free energy of forming such a disk from either the supercooled polymer or polymer-diluent mixture can be written as

$$\Delta F_d = \zeta\rho_s\gamma_u - \Delta F_f(\zeta,\rho), \qquad (9)$$

where ΔF_f, the free energy of fusion, includes both the bulk free energy of fusion and the surface free energy of the ends of the disk.[13] By considering the volume and surface area of each unit, it can be shown that ρ_s is equal $2(\pi\rho)^{\frac{1}{2}}$. Equation (9) can then be written as

$$\Delta F_d = 2\zeta\gamma_u(\pi\rho)^{\frac{1}{2}} - \Delta F_f(\zeta,\rho). \qquad (10)$$

Using for ΔF_f an explicit formula calculated by Flory[3] one has for a system composed of N polymer molecules, each of x repeating units,

$$\Delta F_f/xN = (\zeta\rho/xN)\Delta f_0 + RT\{(1/x)\ln[1-\zeta\rho/xN] + \rho/xN[\ln D + \ln[(x-\zeta+1)/x]]\}, \qquad (11)$$

[11] R. Becker and W. Doring, Ann. Physik **24**, 719 (1935).
[12] D. Turnbull and J. C. Fischer, J. Chem. Phys. **17**, 71 (1949).
[13] See reference 2, Eq. (19).

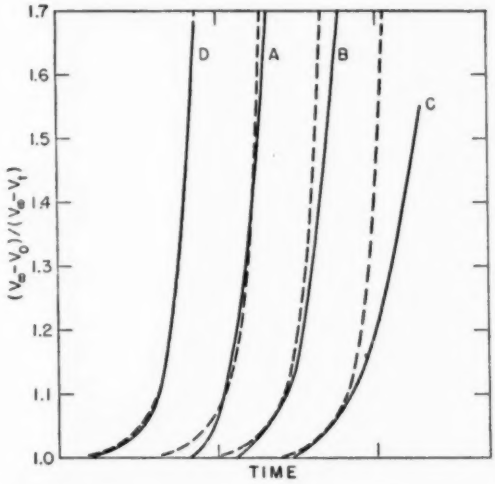

FIG. 7. Fit of experimental data to theoretical curves. Plot of $(V_\infty - V_0)/(V_\infty - V_t)$ *vs* log$t$ for mixtures of poly-(decamethylene adipate) with dimethyl formamide. Solid lines are composite isotherms for each mixture and are identical to those in Fig. 6. Dashed lines are theoretical isotherms for disk growth. Position of isotherm relative to abscissa is arbitrary; short vertical marks along abscissa indicate length of one decade.

where Δf_0 is the bulk free energy per mole of repeating unit and D is a parameter whose value is constrained to lie between zero and one.[2] Since in polymeric systems the length of a crystallite is much less than the molecular length, the number of repeating units comprising the length of a nucleus ζ must be much less than x. Then, for a high molecular weight polymer Eq. (11) reduces to

$$\Delta F_f = \zeta\rho\Delta f_0 + RT\rho\ln D, \qquad (12)$$

so that

$$\Delta F_d = 2\zeta\gamma_u(\pi\rho)^{\frac{1}{2}} - \zeta\rho\Delta f_0 + RT\rho\ln D. \qquad (13)$$

ΔF^* is the value of ΔF_d at the saddle point of the free energy surface described by Eq. (14). In the conventional manner the coordinates of the saddle point are obtained by equating $(\partial\Delta F_d/\partial\rho)_\zeta$ and $(\partial\Delta F_d/\partial\zeta)_\rho$ to zero and solving the resultant simultaneous equations for ρ and ζ. It is found that

$$\Delta F_d{}^* = 4\pi\gamma_u{}^2\gamma T_m{}^2/\Delta H_u{}^2(\Delta T)^2 \qquad (14)$$

where γ is defined as $-RT\ln D$ and Δf_0 equals $(\Delta T/T_m)\Delta H_u$. Equation (15) has the identical form as the expression previously obtained,[14] where the polymeric nature of the supercooled liquid was not specifically taken into account in calculating the free energy of nucleus formation.

The above calculation can be easily extended to the case where a nucleus composed only of polymer segments is formed from a supercooled polymer-diluent mixture. From the reference previously cited,[2] we find

[14] See reference 1, Eq. (13).

when x is large and ζ is less than x, that

$$\Delta F_f/xN=(\zeta\rho/xN)\Delta f_0 + RT\{(V_u/V_1)(-v_1)+(1/\zeta)\ln v_2 D + (V_u/V_1)\chi_1(1-v_2)^2/[1-v_2(1-\zeta\rho/xN)]\}, \quad (15)$$

where $\chi_1=BV_1/RT_m$. Since $\zeta\rho/xN\ll 1$, Eq. (15) can be expressed as

$$\Delta F_f=\zeta\rho[\Delta f_0'+(1/\zeta)\ln v_2 D], \quad (16)$$

where

$$\Delta f_0'\equiv\Delta f_0-RTV_u/V_1\{v_1-\chi_1(1-v_2)^2\}. \quad (17)$$

The saddle point in the expression for the free energy of nucleus formation is

$$\Delta F_d^*=4\pi\gamma_u^2\gamma_{v_2}/(\Delta f_0')^2 \quad (18)$$

where $\gamma_{v_2}\equiv -RT\ln v_2 D$.

Substituting $\Delta f_0=\Delta H_u(1-T/T_m^0)$ into Eq. (17) and recalling that

$$1/T_m-1/T_m^0=(R/\Delta H_u)(V_u/V_1)[v_1-\chi_1 v_1^2],$$

we find that

$$\Delta f_0'=\Delta H_u[(T_m-T)/T_m] \quad (19)^{15}$$

so that

$$\Delta F_D^*=4\pi\gamma_u^2\gamma_{v_2}T_m^2/\Delta H_u^2(\Delta T)^2. \quad (20)$$

If the temperature coefficient of the growth process is assumed to be the same as for diffusion, then the growth rate can be expressed as

$$G=G_0\exp\{-E_D/RT\}. \quad (21)$$

For polymer-diluent mixtures E_D and G_0 are functions of composition, while E_D will also vary with temperature over any extended range. Both E_D and G_0 can be assumed to be temperature independent over the small temperature interval of present interest, but both parameters will vary with composition. For the formation of disk nuclei accompanied by disk growth it is found from Eqs. (6′), (8), (20), and (21) that

$$k_d^d=(\pi l_c/3\delta)A_0G_0^2\exp\{-3E_D/RT - 4\pi\gamma_u^2\gamma_{v_2}T_m^2/\Delta H_u^2(\Delta T)^2RT\}. \quad (22)$$

For the formation of disk nuclei accompanied by spherical growth

$$k_s^d=(\pi/3\delta)A_0G_0^3\exp\{-4E_D/RT - 4\pi\gamma_u^2\gamma_{v_2}T_m^2/\Delta H_u^2(\Delta T)^2RT\}. \quad (23)$$

Aside from minor differences in the first terms in the exponential, both growth mechanisms lead to the same temperature coefficient of the rate constants, which is identical to that previously derived for bulk polymers. For the small temperature range of the present experiments we may write

$$\log k_d^d=B_d-4\pi\gamma_u^2\gamma_{v_2}T_m^2/\Delta H_u^2(\Delta T)^2RT2.3 \quad (24)$$

and

$$\log k_s^d=B_s-4\pi\gamma_u^2\gamma_{v_2}T_m^2/\Delta H_u^2(\Delta T)^2RT2.3, \quad (25)$$

where

$$B_d=\log(\pi l_c/3\delta)A_0G_0^2-3E_D/2.3RT$$

and

$$B_s=\log(\pi/3\delta)A_0G_0^3-4E_D/2.3RT.$$

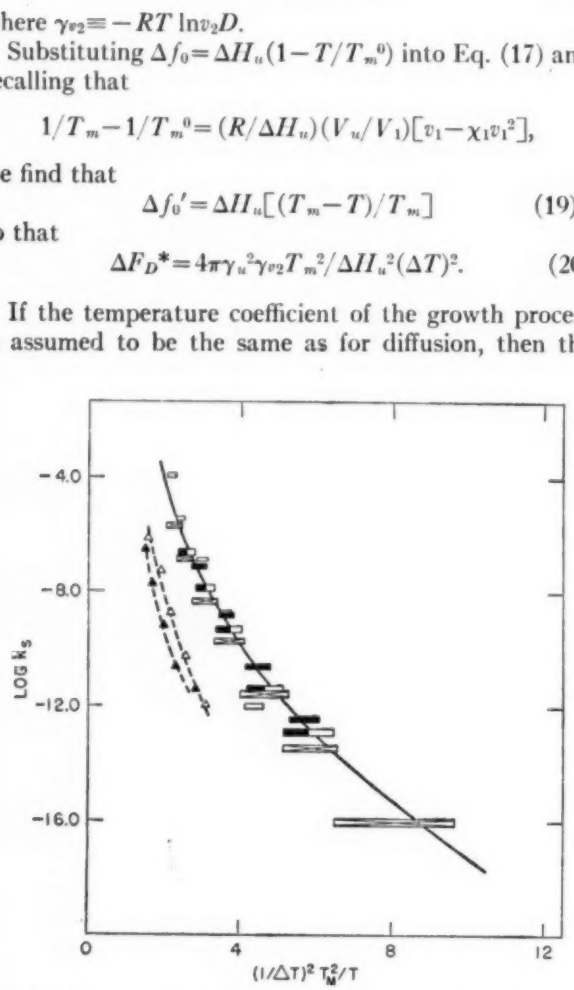

FIG. 8. Plot of $\log k_s^d$ against temperature variable $(1/\Delta T)^2\times(T_m^2/T)$ for poly-(ethylene oxide)-diphenyl ether mixtures. $v_1=0.094$ ■; $v_1=0.182$ □; $v_1=0.383$ ⊠; $v_1=0.494$ ■□; $v_1=0.601$ △; $v_1=0.689$ ▲. Solid curve is plot for bulk polymer.

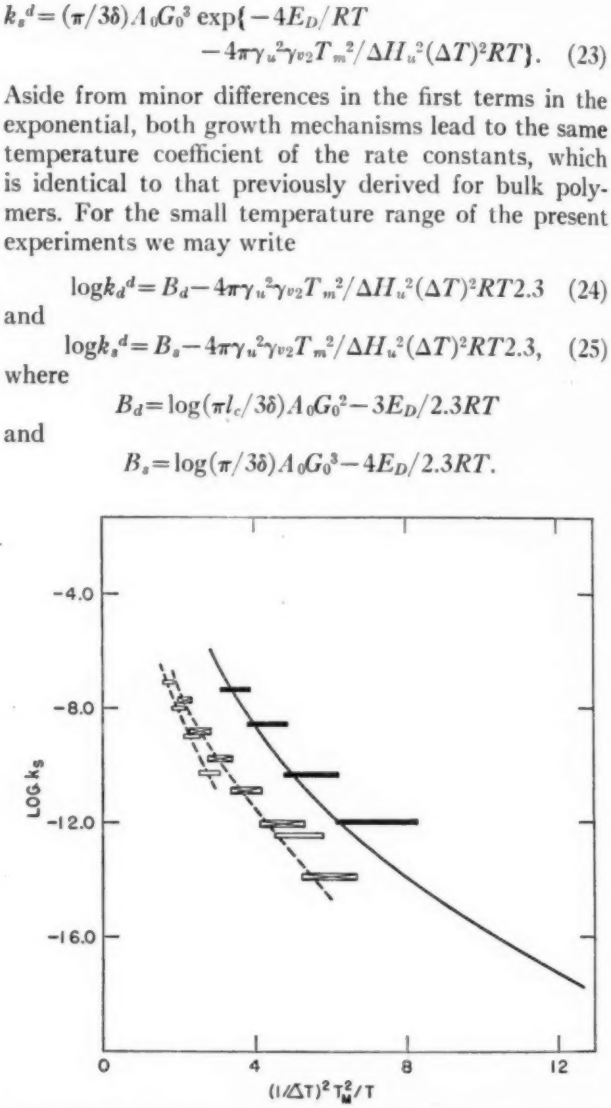

FIG. 9. Plot of $\log k_s^d$ against temperature variable $(1/\Delta T)^2\times(T_m^2/T)$ for poly-(decamethylene adipate)-dimethyl formamide mixtures. $v_1=0.202$ ■; $v_1=0.422$ □; $v_1=0.603$ ⊠. Solid curve is plot for bulk polymer.

[15] Strictly speaking Eq. (19) is correct only when $\chi_1=0$. More exactly, $\Delta f_0'=[\Delta H_u+BV_u v_1^2][(T_m-T)/T_m]$. The second term of the first bracket will usually be only several percent of ΔH_u; hence, Eq. (19) is a good approximation for the more general case where $\chi_1\neq 0$. The author wishes to thank J. Bischopps for bringing this matter to his attention.

Plots of $\log k_s^d$ against $T_m^2/T(\Delta T)^2$ are shown in Figs. 8 and 9 for the polyethylene oxide-diphenyl ether mixtures and the PDA-dimethyl formamide mixtures, respectively. Similar plots are obtained if $\log k_d^d$ is plotted against the same temperature variable. Also included in these plots are the results for the corresponding bulk polymers, which are represented by the solid lines. From these plots it would appear that neither $\log k_d^d$ nor $\log k_s^d$ are linear functions of $T_m^2/T(\Delta T)^2$ as required by the theory just developed; a similar situation also exists for bulk polymers.[1] However, for the bulk material it has been shown that there is an uncertainty of about three degrees in the correct value to assign to T_m^0 and thus to ΔT. When due allowance is made for this uncertainty in polymer-diluent mixtures, the resulting plots are linear within experimental error. Thus the mechanisms proposed can explain the very marked variation of the crystallization rate with temperature.

The crystallization rate constants vary with composition in an interesting manner in the temperature interval investigated. For a given value of the variable $T_m^2/T(\Delta T)^2$, the rate constants have the same value as that of the bulk polymer up to relatively high diluent concentrations. For example, in the PEO-diphenyl ether mixtures this invariance of the rate constant is maintained up to a volume fraction of diluent equal to 0.494. A further increase in the concentration of diluent results in a marked decrease in the magnitude of the rate constant. This effect is qualitatively independent of the nature of the solvent and of its thermodynamic interaction with the polymer.

As diluent is added to a polymeric liquid the viscosity of the medium is decreased and this would be expected to result in an increase in the crystallization rate. However, the steady-state nucleation rate will decrease with increasing diluent concentration because of the variation of γ_{v2} with concentration. These opposing effects appear to counteract each other over the range in which the rate constant is independent of concentration. As the amount of diluent increases the nucleation term dominates in causing the marked decrease in rate constant. Due to the difficulty of quantitatively predicting the concentration dependence of all the terms entering into Eqs. (5) and (6), a more exact analysis of the variation of rate constant with composition is difficult. The decrease with concentration of the nucleation rate appears to be the only factor that can qualitatively explain the experimental observations.

For bulk polymers the crystallization rate passes through a maximum at a temperature well below T_m^0. It has been shown[1] that for a wide range in values of the molecular parameters that are involved, the temperature at which the rate is a maximum $T_{max}=0.8$ or $0.9T_m^0$. Formally, the expression for T_{max} in polymer-diluent mixtures is identical to that for bulk polymers. E_D can be written more generally as $E_D=E_D^0/T^n$, where n ranges from one to five and E_D^0 will depend on composition. For disk nucleation accompanied by spherical growth it is found that

$$4(n+1)E_D^0(v_2)/\kappa(v_2) = T_m^2(3T_{max}-T_m)T_{max}^n/(T_m-T_{max})^3, \quad (26)$$

where $\kappa=4\pi\gamma_u^2\gamma_{v2}/\Delta H_u^2$. For illustrative purposes it is simpler to consider the case where $n=0$, so that

$$4E_D^0(v_2)/\kappa(v_2)=(3T_{max}/T_m-1)/(1-T_{max}/T_m)^3. \quad (27)$$

The ratio of T_{max}/T_m depends on the ratio of E_D^0/κ; the greater this latter ratio, the greater the ratio of T_{max}/T_m. There is no experimental evidence available at present for the crystallization kinetics of polymer-diluent mixtures over any extended temperature range, so that deductions based on Eqs. (26) and (27) can not at present be subject to experimental verification. It would be expected that the ratio of T_{max}/T_m would not be independent of concentration; E_D is known to depend very markedly on composition,[16] while observed variation of the rate constants with composition indicates that E_D and κ vary in quite different ways.

ACKNOWLEDGMENT

The experimental portion of this paper was undertaken during the author's tenure as a Research Associate at Cornell University. He would like to acknowledge his gratitude to Paul J. Flory for his most helpful advice and stimulating discussions.

[16] F. Bueche, J. Appl. Phys. **24**, 423 (1953).

Surface Matching of Dielectric Lenses

E. M. T. JONES AND S. B. COHN
Stanford Research Institute, Stanford, California

(Received June 14, 1954)

Two methods of cancelling the surface reflections of dielectric lenses are described in this paper. The first utilizes a simulated quarter-wave matching layer, and the second a reactive wall embedded within the dielectric. The reactive wall may take a variety of physical forms, such as arrays of thin conducting disks which have a capacitive reactance, or arrays of thin wires which have an inductive reactance. Surface matching is obtained when the disks are placed approximately $\frac{3}{8}$ wavelength inside the lens, or the wires $\frac{1}{8}$ wavelength. Curves are presented that show how the reflections at the air and dielectric boundary are reduced for various angles of incidence and polarization when quarter-wave layer and reactive-wall matching are employed.

The reactance of the array of disks for waves incident at various angles and polarizations is computed by means of Bethe's small aperture theory, and Babinet's principle. Measurements in wave guide of the reactance of an array of circular disks for various angles of incidence and for both E- and H-plane polarization show close agreement with the theory.

INTRODUCTION

THE use of ordinary natural dielectric lenses as focusing elements for microwave-antenna systems has the disadvantage of the loss of a portion of the energy incident on the air-dielectric interfaces due to reflection. This decrease in transmission results in a net decrease in the power gain of the system, while the reflected energy raises the input standing-wave ratio and can cause various anomalies in the far-zone diffraction pattern. If the surface of the lens is matched in some fashion, these difficulties disappear and the lens becomes a much more useful microwave antenna. Two basic methods of achieving a surface match are considered in this paper.

The first method requires a quarter-wave layer having a dielectric constant intermediate to that of air and the main body of the lens. The quarter-wave layer may be simulated by perturbing the surface of the dielectric lens, as illustrated in Fig. 1. T. Morita and S. B. Cohn have determined by theoretical and experimental means that these surface perturbations behave similarly to a homogeneous dielectric.[1]

In the second method a reactive wall is placed inside the surface of the lens. This wall can assume a variety of forms. A rectangular grid of thin wires or an array of thin conducting disks are typical physical elements. The wires have an inductive reactance, and therefore, must be embedded about $\frac{1}{8}$ wavelength within the dielectric to match the surface. The disks on the other hand, have a capacitive reactance and, therefore, must be embedded about $\frac{3}{8}$ of a wavelength in the dielectric to cancel surface reflections. A practical method of construction for the reactive wall is to print conducting obstacles or inductive strips on the lens surface, and then to cement over this the necessary additional layer of dielectric material.

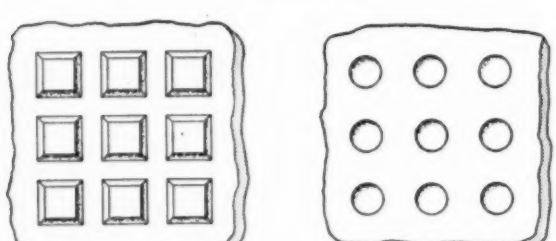

FIG. 1. Simulated quarter-wave sheets.

THEORETICAL PERFORMANCE OF VARIOUS MATCHING METHODS

The relative performance of various matching techniques can be evaluated most easily in terms of the power reflection coefficient of the air-dielectric interface. For quarter-wave matching sheets let the external region be region 1, the quarter-wave sheet region 2, and the lens region 3. Then R_{12} and R_{23} the reflection coefficients[2] measured at the interfaces of regions 1 and 2 and regions 2 and 3 are both real. The power reflection coefficient R^2 becomes

$$R^2=\frac{(R_{12}+R_{23})^2-4R_{12}R_{23}\sin^2\phi}{(1+R_{12}R_{23})^2-4R_{12}R_{23}\sin^2\phi}, \tag{1}$$

while the electrical length ϕ of the quarter-wave sheet is

$$\phi=\frac{2\pi L}{\lambda}(n_2^2-\sin^2\theta_1)^{\frac{1}{2}}, \tag{2}$$

where λ is the free-space wavelength, θ_1 the angle of incidence in region 1, n_2 the index of refraction of the quarter-wave sheet, and L the thickness of the quarter-wave sheet. When reactive wall matching is used, let the region outside the lens be region 1, the region between the lens surface and the matching wall be region 2, and the region within the matching wall be region 3. Then

[1] T. Morita and S. B. Cohn, "Simulated quarter-wave matching sheet," Presented at U.R.S.I. Meeting, Washington D. C., May 4, 1954.

[2] J. A. Stratton, *Electromagnetic Theory* (McGraw-Hill Book Company, Inc., New York, 1941), p. 492.

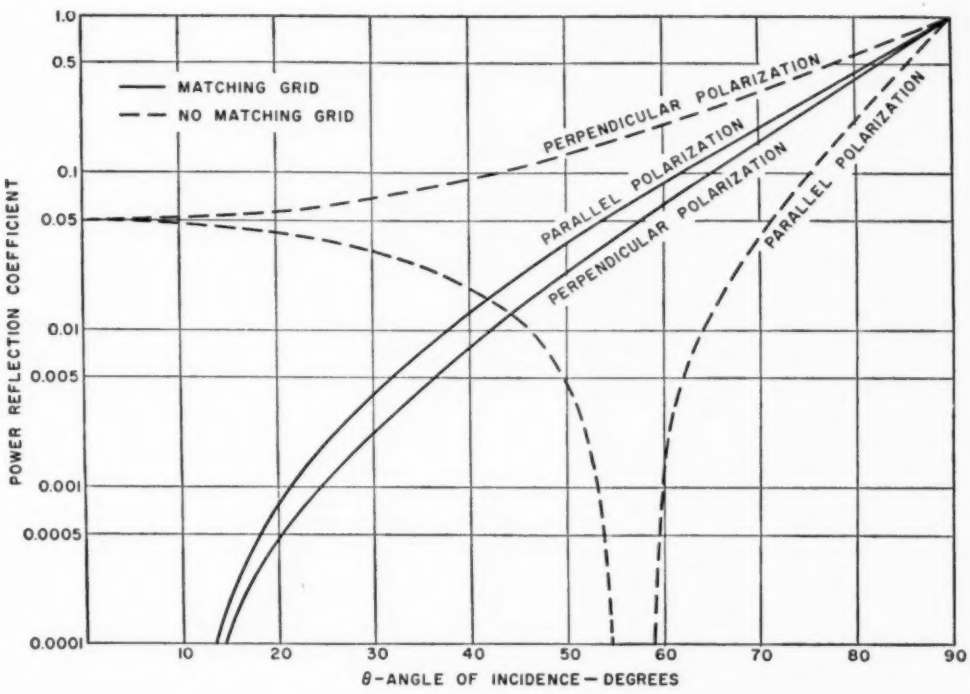

FIG. 2. Single-boundary power reflection coefficient for a dielectric lens of refractive index 1.57 with and without a quarter-wave matching sheet.

R_{12} is real, and $R_{23}=a_{23}+jb_{23}$. The power reflection coefficient in this case becomes

$$R^2=\frac{R_{12}^2+2R_{12}(a_{23}\cos 2\phi+b_{23}\sin 2\phi)+a_{23}^2+b_{23}^2}{1+2R_{12}(a_{23}\cos 2\phi+b_{23}\sin 2\phi)+R_{12}^2(a_{23}^2+b_{23}^2)}, \quad (3)$$

while the electrical spacing ϕ of the reactive wall from the lens surface is

$$\phi=\frac{2\pi L}{\lambda}(n^2-\sin^2\theta_1)^{\frac{1}{2}}, \quad (4)$$

and the reflection coefficient R_{23} is

$$a_{23}+jb_{23}=\frac{-(B/Y_2)^2-j2(B/Y_2)}{4+(B/Y_2)^2}.$$

Y_2 is the characteristic admittance of the dielectric in region 2 (i.e., the ratio of the components of magnetic to electric field that are parallel to the reactive wall), B the susceptance of the reactive wall, n the refractive index of the lens, and L the separation of the reactive wall from the lens surface.

The conditions for matching a lens with a quarter-wave layer on its surface are seen from (1) to be that $R_{12}=R_{23}$ and $\phi=90°$. When a reactive wall is used for surface matching, it can be determined from (3) that the spacing of the wall from the dielectric surface is determined by

$$Y_2/Y_1=\tan^2\phi, \quad (5)$$

while the normalized susceptance of the wall is given by

$$B/Y_2=\cot 2\phi, \quad (6)$$

where Y_1 is the characteristic admittance of free space (i.e., the ratio of the components of magnetic to electric field that are parallel to the lens surface).

The single-boundary power reflection coefficient for a dielectric lens of refractive index 1.57 matched by a quarter-wave sheet at normal incidence is plotted in Fig. 2 by means of (1) and (2). For comparison the power reflection coefficient for an unmatched surface is also shown. For perpendicular polarization the quarter-wave matching sheet reduces the reflected power for all angles of incidence while for parallel polarization it reduces the reflected power up to angles of 51 degrees and increases it above 51 degrees.

A rectangular array of wires, as shown in Fig. 3, will appear inductive to plane waves incident upon it because the inductive susceptance of the wires running in the x direction is orders of magnitude greater than that of the capacitive susceptance of the wires running in the y direction. Therefore, this capacitive susceptance will be neglected in the following discussion. For the values of susceptance needed to match the surface of ordinary dielectric lenses the required wire diameter D will be so small that in the analysis (and also in practice) it will be permissible to replace the wires of diameter D by flat strips of width $2D$.

The reactance of an array of thin strips of width $2D$ (oriented in the x direction) to a wave polarized in the plane of incidence, can be obtained by use of Babinet's transformation from the solution for a capacitive slit in a wave guide operating in a TE_{10} mode. The solution for the capacitive slit is given by Marcuvitz.[3] Applying the

[3] N. A. Marcuvitz, *Wave-Guide Handbook* (McGraw-Hill Book Company, Inc., New York, 1951), p. 218, Eq. (2A).

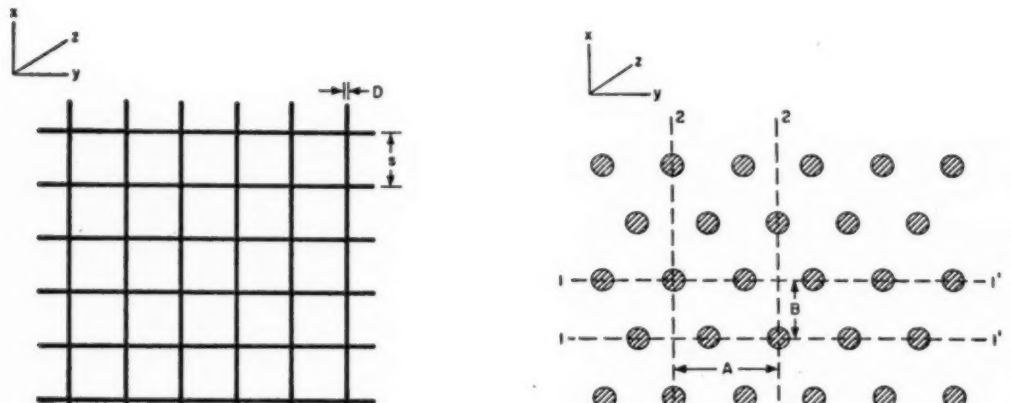

FIG. 3. Reactive walls.

transformation, the inductive reactance of the wires becomes

$$\frac{X}{Z_2}=\frac{s}{\lambda_2}\cos\theta_2\left[\ln\left(\csc\frac{\pi D}{s}\right)+F\left(\theta_2,\frac{s}{\lambda_2}\frac{D}{s}\right)\right], \quad (7)$$

where $Z_2=1/Y_2$, s is the center-to-center spacing of the wires, and λ_2 is the wavelength in the dielectric medium surrounding the wires. The correction term F has a small value for normal incidence, and its value decreases further as the angle of incidence increases.

The reactance of this array of wires (or thin strips) for an incident wave polarized perpendicular to the plane of incidence has been computed by MacFarlane.[4] He obtains

$$\frac{X}{Z_2}=\frac{s}{\lambda_2}\cos\theta_2\left[\ln\frac{s}{\pi D}+F'\left(\theta_2,\frac{s}{\lambda_2}\right)\right]. \quad (8)$$

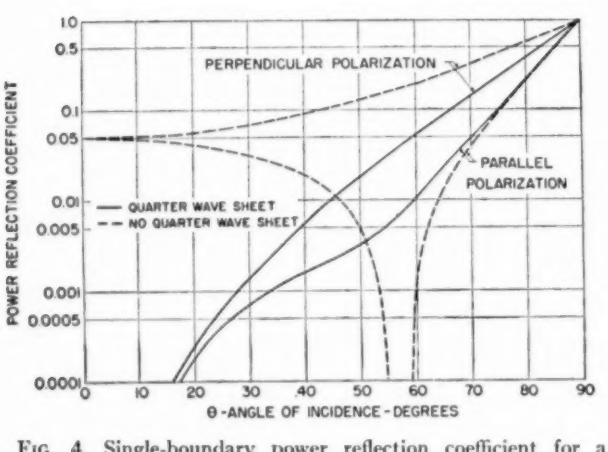

FIG. 4. Single-boundary power reflection coefficient for a dielectric lens of refractive index 1.57 with and without a wire grid matching wall.

[4] G. G. MacFarlane, J. Inst. Elec. Engrs. (London) **94**, 1523–1526 (1947).

The correction term F' has the same value as F for normal incidence but has much greater values for angles off the normal.

In Fig. 4, the single-boundary power reflection coefficient is plotted from (3), (4), (7), and (8) for a wave incident on a dielectric lens of refractive index 1.57 matched at normal incidence by a grid of wires spaced 0.45 wavelength between centers. The power reflection coefficient of an unmatched lens is also included in Fig. 4. Here it is seen that with matching the power reflection is always greater for parallel polarization than for perpendicular polarization. This grid does not give as small a power reflection at angles off the normal as does the quarter-wave section.

The susceptance of a reactive wall composed of thin circular disks arranged in hexagonal array, as shown in Fig. 3b, will be analyzed later in this paper. The single-boundary power reflection coefficient of a dielectric lens with a refractive index of 1.57 that has been matched by such an array of disks spaced on half-wavelength centers, together with the power reflection coefficient for the unmatched lens, is shown in Fig. 5. Here it is seen that for perpendicular polarization, matching reduces the power reflection for all angles of incidence, while for parallel polarization the power reflection is reduced for angles up to 42°, and is increased for angles greater than 42°.

THEORETICAL CALCULATION OF THE SUSCEPTANCE OF AN INFINITE ARRAY OF THIN CIRCULAR DISKS

The susceptance of an array of small, thin metal obstacles can be computed for various angles of incidence with the help of Bethe's small-aperture theory, and Babinet's principle as follows.

Consider an array of obstacles immersed in a uniform dielectric medium, of relative permeability μ_2 and relative permittivity ϵ_2, lying in the plane $z=0$ (as shown in Fig. 3b) with two plane waves incident on it at angles θ_2

and $-\theta_2$, each wave being polarized perpendicular to the plane of incidence. Imagine for the moment another wave incident on the array identical to that described above but propagating in the negative z direction. It then becomes obvious that a magnetic wall can be inserted in the plane of the obstacles, since the sum of the tangential H field of the two waves in this plane is zero. With the magnetic wall in place, the array of metal obstacles appears as a pure susceptance to the wave traveling in the positive z direction. The value of this susceptance is equal to one-half the value of the susceptance of the metal obstacles before the magnetic wall was inserted.

Babinet's principle states that if a solution $E(x,y,z)$ and $H(x,y,z)$ to Maxwell's equation in a medium is known, then another solution may be obtained by replacing $E(x,y,z)$ by $(\mu_2/\epsilon_2)^{\frac{1}{2}}H'(x,y,z)$ and $H(x,y,z)$ by $-(\epsilon_2/\mu_2)^{\frac{1}{2}}E'(x,y,z)$. Obviously for this solution to hold at boundaries, it is also necessary to replace all electric walls by magnetic walls and conversely. As a corollary, it is seen that all susceptances are replaced by reactances.

Applying Babinet's principle to the case of a wave terminated by the reactive wall, one sees that the magnetic wall is replaced by the electric wall and the electric-wall obstacles are replaced by magnetic-wall obstacles. The reactance $2X'/Z_2'$ of this composite wall is equal to the susceptance $B/2Y_2$ of the previous wall.

The field components in Gaussian units of the incident wave after the Babinet transformation are

$$\begin{aligned} H_z' &= E_0 \cos(k_2 y \sin\theta_2)\epsilon^{j(\omega t - k_2 z\cos\theta_2)}, \\ E_y' &= -\left(\frac{\mu_2}{\epsilon_2}\right)^{\frac{1}{2}} E_0 \cos\theta_2 \cos(k_2 y \sin\theta_2)\epsilon^{j(\omega t - k_2 z\cos\theta_2)}, \\ E_z' &= -j\left(\frac{\mu_2}{\epsilon_2}\right)^{\frac{1}{2}} E_0 \sin\theta_2 \sin(k_2 y \sin\theta_2)\epsilon^{j(\omega t - k_2 z\cos\theta_2)}, \end{aligned} \tag{9}$$

where

$$k_2 = (2\pi/\lambda)(\mu_2\epsilon_2)^{\frac{1}{2}}.$$

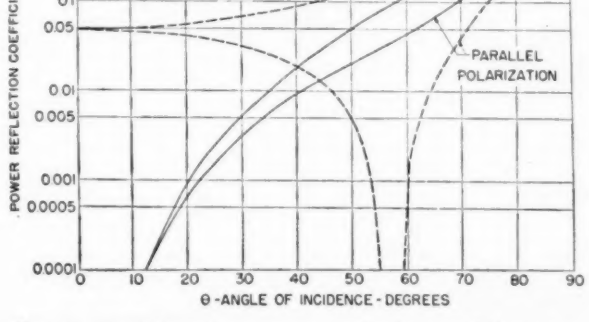

FIG. 5. Single-boundary power reflection coefficient for a dielectric lens of refractive index 1.57 with and without a circular disk matching wall.

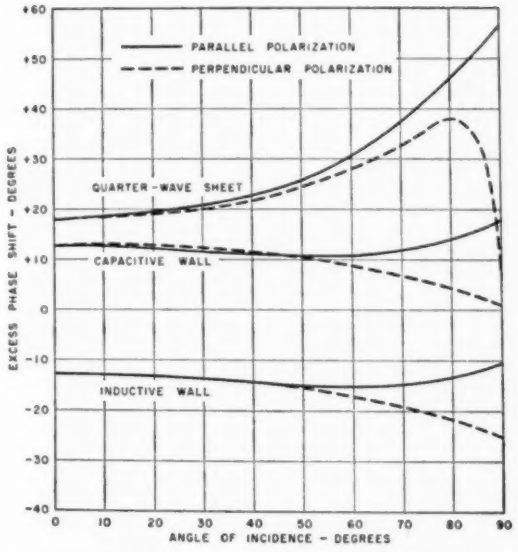

FIG. 6. Single-boundary excess phase shifts for a lens matched at normal incidence by various methods ($n=1.57$).

Now the magnetic wall can be removed by the reverse procedures used to insert it, and there remains an electric wall with small apertures. The reactance X' of the apertures is related to the susceptance B of the obstacles according to the relation

$$\frac{-Y_2'}{B'} = \frac{1}{4}\frac{B}{Y_2}. \tag{10}$$

In order to have the array of apertures excite a transmitted wave traveling only in the direction θ_2, it is necessary that the center-to-center spacing s be related to the angle of incidence θ_2 by the relation

$$s \leq \frac{\lambda_2}{1+|\sin\theta_2|}. \tag{11}$$

If s were to exceed this limit, one or more undesired waves in other directions would emanate from the array of apertures.

Because there is no variation of H_z' in the x direction, magnetic walls can be inserted at the planes $11'$ without affecting the incident wave. It can also be seen from (9) that there are planes parallel to the xz plane a distance $A=\lambda_2/2\sin\theta_2$ apart where H_z' is zero. Therefore, magnetic walls also can be inserted here. The behavior of the cell bounded by these walls will be the same as that of the infinite array.

Bethe[5] has given a formula for the normalized susceptance B'/Y_2' of a single small aperture in a thin metal wall of such a cell. His formula can be extended to the present case of m identical small apertures by summing up the contributions from the m apertures.

[5] H. A. Bethe, "Lumped constants for small irises," Radiation Laboratory Report 43-22, March 24, 1943.

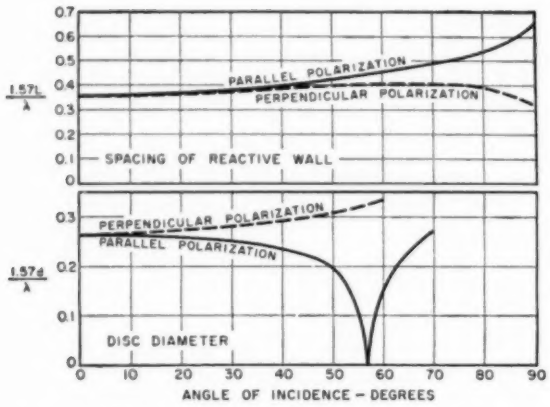

FIG. 7. Disk diameters and spacing of disk array from lens surface for a match ($n=1.57$) $s=\lambda/3.14$.

One obtains

$$\frac{Y_2'}{B'}=\frac{-2\pi}{\lambda_2 S}\sum_m (M_x H_{xm}'^2+M_y H_{ym}'^2+P_z E_{zm}'^2), \quad (12)$$

where M_x and M_y are the magnetic polarizabilities and P_z the electric polarizabilities of an aperture the same size as the obstacle. H_{xm}' and H_{ym}' are the tangential components of magnetic field at the mth aperture, and E_{zm}' the normal component of electric field at the mth aperture. The normalization factor S is given by

$$S=\int_0^B\int_0^A \hat{n}\cdot\bar{E}'\times\bar{H}'\cdot dxdy. \quad (13)$$

For an integral number of apertures within the cell, substitution of (9) and (10) in (12) gives

$$\frac{B}{Y_2}=\frac{16\pi}{\sqrt{3}\lambda_2 s^2\cos\theta_2}(M_x-P_z\sin^2\theta_2). \quad (14)$$

Proceeding in the same fashion, it can be shown that the susceptance of the array of obstacles for an incident wave polarized in the plane of incidence is

$$\frac{B}{Y_2}=\frac{16\pi\cos\theta_2}{\sqrt{3}\lambda_2 s^2}M_y. \quad (15)$$

The value of the electric and magnetic polarizabilities of a circular aperture of diameter d have been computed by Bethe.[5] He finds

$$M_x=M_y=2P_z=d^3/6.$$

The values for other shapes have been measured by electrolytic tank means.[6,7] A correction formula for the polarizability of wave-guide irises whose diameter is an appreciable fraction of the wavelength has been found to give good agreement with theory.[8] This correction method can also be applied to an array of obstacles, with the aid of Babinet's transformation. When a wave is incident on the array with the electric field perpendicular to the plane of incidence, the normalized susceptance becomes, using this correction method,

$$\frac{B}{Y_2}=\frac{16\pi}{\sqrt{3}\lambda_2 s^2\cos\theta_2}\left[\frac{M_x}{1-(\lambda_{c1}/\lambda_2)^2}-\frac{P_z\sin^2\theta_2}{1-(\lambda_{c2}/\lambda_2)^2}\right]. \quad (16)$$

When a wave incident on the array with the magnetic vector is perpendicular to the plane of incidence, the normalized susceptance is

$$\frac{B}{Y_2}=\frac{16\pi\cos\theta_2}{\sqrt{3}\lambda_2 s^2}\cdot\frac{M_y}{1-(\lambda_{c1}/\lambda_2)^2}. \quad (17)$$

Here λ_{c2} is the cutoff wavelength of the TE_{11} mode in a circular wave guide having the same radius as the obstacle, and λ_{c2} is the cutoff wavelength of the TM_{01} mode in a circular wave guide having the same radius as the obstacle.

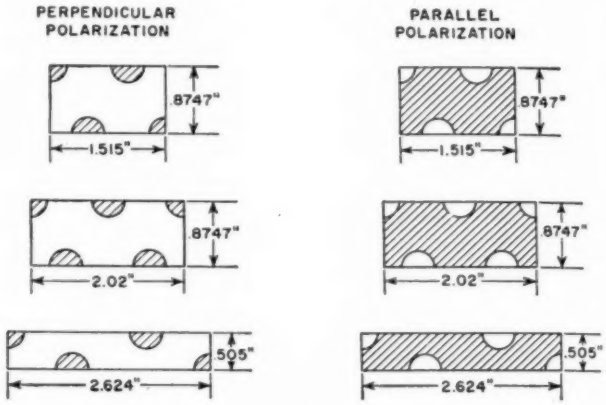

FIG. 8. Cross section of wave-guide test sections with obstacles and apertures in place used in determining the susceptance of disks for various angles of incidence and polarizations.

The phase shift introduced by the matching means is also of interest. For both quarter-wave-sheet and reactive-wall matching, multiple reflections cause a difference in the phase of the transmitted wave from that predicted from simple geometric optics. Also, the addition of a quarter-wave sheet to a lens results in a slightly increased effective pathlength. Figure 6 shows the total excess phase shift computed for a lens matched for normal incidence by three methods. In each case the excess phase shift varies by less than $\lambda/16$, except for the quarter-wave sheet when $\theta>73$ deg. The defocusing resulting from such a small phase variation should be of negligible importance.

DESIGN INFORMATION FOR CIRCULAR DISK WALL

In order to achieve a perfect match at various incident angles and polarizations, it is necessary to vary the spacing of the reactive wall from the lens surface as well

[6] S. B. Cohn, Proc. Inst. Radio Engrs. **39**, 1416–1421 (1951).
[7] S. B. Cohn, Proc. Inst. Radio Engrs. **40**, 1069–1071 (1952).
[8] S. B. Cohn, Proc. Inst. Radio Engrs. **40**, 696–699 (1952).

as the reactance of the wall. Figure 7 shows the spacing of a capacitive wall necessary to achieve a match as computed from (5) as well as the disk diameters necessary to achieve a match as computed from (6) and the experimental data presented below.

MEASUREMENT OF DISK SUSCEPTANCE IN WAVE GUIDE

As already discussed, the field pattern and the reflection and transmission coefficients for a wave incident obliquely on a planar array of obstacles can be simulated exactly in a wave guide. To do so, it is necessary that the wave-guide walls lie in planes of symmetry of the array. The angle of incidence of the fundamental-mode wave is given by $\theta=\sin^{-1}(\lambda/2a)$, where a is the width of the wave-guide cross section. A TE_{10}-mode wave incident on a transverse array of obstacles corresponds to the perpendicular-polarization case. On the other hand, if a thin transverse diaphragm containing an array of apertures is utilized in the experiment, and if Babinet's transformation is then applied to the data, the measurement corresponds to parallel polarization on an array of obstacles having the same dimensions as the aperture.

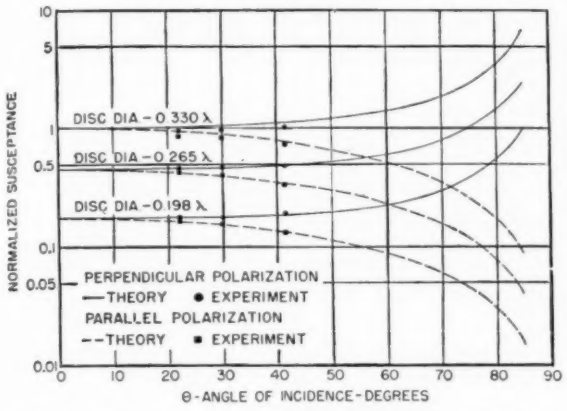

FIG. 9. Normalized susceptance of a hexagonal array thin circular disks on half wavelength centers.

Figure 8 shows the nonstandard wave-guide cross sections, with obstacles and apertures in place, used in determining the susceptance of a hexagonal array of circular disks for various angles of incidence and polarization. In each case the center-to-center spacing of the disks and apertures is 1.010 in. Disk and aperture radii of 0.202 in., 0.267 in., and 0.333 in. were used, with thicknesses of 0.002 in., 0.005 in., 0.010 in., and 0.020 in., in all cases. From the measurements for these different thicknesses, the data corresponding to zero-obstacle thickness were obtained. It is estimated that any individual measurement of obstacle susceptance is within 2 percent of the true value. A curve drawn through the measured points for various angles of incidence should be within 1 percent of the true value.

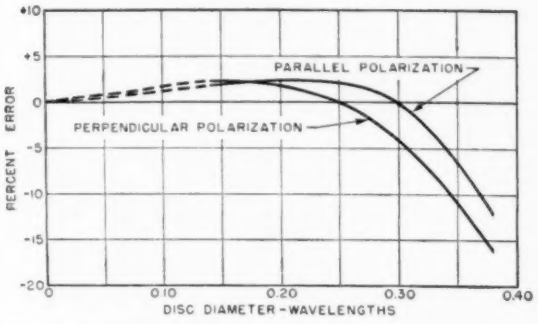

FIG. 10. Percent difference between the measured and theoretical susceptance of an array of circular disks. The ordinate is the measured susceptance minus the theoretical expressed in percent of the theoretical susceptance.

In Fig. 9 are shown typical measured values at one frequency of disk susceptance for various disk radii and polarizations. It is seen that for the two smaller disk radii the measured points lie very close to the theoretical curves. For the largest disk radius the experimental points are considerably below the theoretical values, indicating that the high-frequency corrections proposed in (16) and (17) are not valid for a disk diameter of 0.330λ.

Measurements of the susceptance of these disks have been made at a number of frequencies. As shown previously, each frequency corresponds to a different angle of incidence in each wave-guide cross section. It has been found that the error between experiment and theory does not depend on the center-to-center spacing of the disks in terms of wavelength or on the angle of incidence, but only on the disk radius in terms of wavelength. In Fig. 10 is shown the average difference between the theoretical curves and experimental points as a function of disk diameter for each polarization.

ACKNOWLEDGMENT

The work reported in this paper was supported by the Signal Corps of the U. S. Army.

Field Produced by an Arbitrary Slot on an Elliptic Cylinder

JAMES R. WAIT
Radio Physics Laboratory, Defence Research Board, Shirley Bay, Ottawa, Canada
(Received June 23, 1954)

A derivation is given for the electromagnetic field produced by an arbitrary slot cut in the surface of an elliptic cylinder of perfect conductivity and infinite length. The electric field tangential to the slot is assumed to be a prescribed function. The integrals in the formal solution are evaluated by the saddle point method for the far zone fields which when specialized to thin transverse or axial slots agree with known results. As illustrative examples, patterns of thin axial and transverse slots on a strip are computed.

INTRODUCTION

THE radiative properties of slots cut in metal conducting surfaces are now being extensively utilized in microwave radiating systems. It is often assumed that the metal surface can be regarded as infinite in extent, and thus the radiation diffracted around the edges to the rear is neglected.

The theoretical treatment of radiation from antennas and slots near obstacles of finite size is very difficult except for cases where the obstacle can be approximated by some regular shape. When the slots are cut in the surface of a circular wave guide it is reasonable to assume that the guide can be represented by an infinite cylinder of circular cross section. This problem has been treated under various restrictive conditions of the geometry of the slot, by Sinclair,[1] Papas,[2] and others. Silver and Saunders[3] have developed a solution for the fields or an arbitrary slot on the circular cylinder, and their results have been applied to the calculation of radiation patterns of slotted cylinder antennas.[4]

When the conducting surface is in the form of a sheet or a plate, it is reasonable to expect that a cylinder of elliptic cross section is a good representation if the eccentricity is quite large. Sinclair[5] has calculated the far fields of electric and magnetic dipoles near elliptic cylinders by an application of the reciprocity theorem. His results have been extended by Wong[6] to calculate the radiation conductance of thin axial and transverse slots on elliptic cylinders.

It is the purpose of this paper to derive expressions for the fields produced by a slot of arbitrary shape on the surface of an elliptic cylinder of infinite length and perfect conductivity. The tangential components of the electric field in the slot are assumed to be prescribed. The integrals in the formal solution are then evaluated approximately for the far zone fields by a direct application of the saddle point method. When these far field solutions are specialized to thin axial and transverse slots, agreement is obtained with known results.

[1] George Sinclair, Proc. Inst. Radio Engrs. **36**, 1487 (1948).
[2] C. H. Papas, J. Math. Phys. **28**, 227 (1950).
[3] S. Silver and W. K. Saunders, J. Appl. Phys. **21**, 153 (1950).
[4] S. Silver and W. K. Saunders, J. Appl. Phys. **21**, 745 (1950).
[5] George Sinclair, Proc. Inst. Radio Engrs. **33**, 660 (1951).
[6] J. Y. Wong, Proc. Inst. Radio Engrs. **41**, 1172 (1953).

STATEMENT OF PROBLEM

The perfectly conducting cylinder is taken to be of infinite length with major axis $2a$ and minor axis $2b$. If the cylinder axis is coincident with the z-axis of a rectangular (x,y,z) coordinate system, the surface of the cylinder is specified by

$$x^2/a^2+y^2/b^2=1. \tag{1}$$

Elliptic cylindrical coordinates (u,v,z) are most useful in developing the general solution, and they can be defined by the following transformation:

$$x=d\cosh u\cos v, \quad y=d\sinh u\sin v, \quad z=z, \tag{2}$$

where $2d$ is the distance between the foci of the ellipse.[7] The foci are located at the points $(x=\pm d,\ y=0)$. The surfaces, $u=$constant, represent a family of confocal cylinders of elliptic cross section. The semi-major and semi-minor axis of the ellipse $u=u_0$ are given by

$$a=d\cosh u_0, \quad b=d\sinh u_0. \tag{3}$$

A slot of arbitrary shape is located on the cylinder bounded in the axial direction by the planes $z=z_1$ and $z=z_2$ and confined circumferentially by the curves $v_1(z)$ and $v_2(z)$. The tangential electric field in the slot will in general have components in both the v and z directions. The prescribed electric field in the slot is defined in the following manner:

$$E_v(u_0,v,z)=e_v(v,z), \quad E_z(u_0,v,z)=e_z(v,z)$$

for $v_1\leq v\leq v_2$ and $z_1\leq z\leq z_2$, whereas (4)

$$E_v(u_0,v,z)=0, \quad E_z(u_0,v,z)=0$$

for points (u_0,v,z) outside the slot.

THE FORMAL SOLUTION

A solution of Maxwell's equations is now constructed which assumes the prescribed value of the tangential electric field on the cylinder and gives rise to outgoing waves at infinity. The fields in the region external to the cylinder $(u\geq u_0)$ can be generally represented as a superposition of a complete set, ψ_m and ψ_m^*, of TM and

[7] The semifocal distance d is denoted by c_0 in Wong's paper (see reference 6). Our notation follows that of Sinclair (see reference 5).

TE cylindrical waves,[8] respectively, as follows:

$$E_z=\int_{-\infty}^{+\infty}\sum_{m=1}^{\infty}(k^2-h^2)\psi_m(u,v,h)e^{-ihz}dh, \tag{5}$$

$$H_z=\int_{-\infty}^{+\infty}\sum_{m=0}^{\infty}(k^2-h^2)\psi_m^*(u,v,h)e^{-ihz}dh, \tag{6}$$

$$E_u=\int_{-\infty}^{+\infty}\sum_{m=0}^{\infty}\left[-\frac{ih}{h_1}\frac{\partial\psi_m(u,v,h)}{\partial u}-\frac{i\mu\omega}{h_2}\frac{\partial\psi_m^*(u,v,h)}{\partial v}\right]e^{-ihz}dh, \tag{7}$$

$$H_u=\int_{-\infty}^{+\infty}\sum_{m=0}^{\infty}\left[\frac{ik^2}{\mu\omega h_2}\frac{\partial\psi_m(u,v,h)}{\partial v}-\frac{ih}{h_1}\frac{\partial\psi_m^*(u,v,h)}{\partial u}\right]e^{-ihz}dh, \tag{8}$$

$$E_v=\int_{-\infty}^{+\infty}\sum_{m=0}^{\infty}\left[-\frac{ih}{h_2}\frac{\partial\psi_m(u,v,h)}{\partial v}+\frac{i\mu\omega}{h_1}\frac{\partial\psi_m^*(u,v,h)}{\partial u}\right]e^{-ihz}dh, \tag{9}$$

$$H_v=\int_{-\infty}^{+\infty}\sum_{m=0}^{\infty}\left[-\frac{ik^2}{\mu\omega h_1}\frac{\partial\psi_m(u,v,h)}{\partial u}-\frac{ih}{h_2}\frac{\partial\psi_m^*(u,v,h)}{\partial v}\right]e^{-ihz}dh, \tag{10}$$

where the time factor is $\exp(i\omega t)$, $k=2\pi/$free space wavelength, and $\mu=4\pi\times10^{-7}$. The metrical coefficients h_1 and h_2 appropriate to the elliptic coordinates are given by

$$h_1=h_2=d(\cosh^2u-\cos^2v)^{\frac{1}{2}}$$

and should not be confused with the axial propagation constant h.

The field components, E_z, etc., satisfy the wave equation which is expressed in elliptic coordinates as

$$\frac{1}{h_1^2}\left[\frac{\partial^2E_z}{\partial u^2}+\frac{\partial^2E_z}{\partial v^2}\right]+\frac{\partial^2E_z}{\partial z^2}+k^2E_z=0. \tag{11}$$

It then follows that the functions ψ_m and ψ_m^* satisfy

$$\frac{1}{h_1^2}\left[\frac{\partial^2\psi_m}{\partial u^2}+\frac{\partial^2\psi_m}{\partial v^2}\right]+\lambda^2\psi_m=0, \tag{12}$$

where

$$\lambda^2=k^2-h^2.$$

[8] J. A. Stratton, *Electromagnetic Theory* (McGraw-Hill Book Company, Inc., New York, 1941), p. 354.

The solution of this equation is known to be

$$\psi_m(u,v,h)=A_m^e(\lambda)Se_m(\lambda d,\cos v)He_m^{(2)}[\lambda d,\cosh u)+A_m^o(\lambda)So_m(\lambda d,\cos v)Ho_m^{(2)}(\lambda d,\cosh u), \tag{13}$$

where Se_m and So_m are the even and odd angular Mathieu functions[9] and where $He_m^{(2)}$ and $Ho_m^{(2)}$ are the even and odd radial Mathieu functions[9] of the fourth type. The solution for ψ_m^* is of the same form with coefficients $B_m^e(\lambda)$ and $B_m^o(\lambda)$.

The formal solution of the problem is obtained when the coefficients A_m^e, A_m^o, B_m^e, B_m^o are expressed in terms of the specified tangential electric field on the the surface of the elliptic cylinder.

The electric field components E_z and E_v are written out in full as follows:

$$E_z=\sum_{m=0}^{\infty}\int_{-\infty}^{+\infty}(k^2-h^2)[A_m^{e,o}(\lambda)Se,o_m(\lambda d,\cos v)\times He^{(2)},o_m(\lambda d,\cosh u)]e^{-ihz}dh, \tag{14}$$

and

$$h_1E_v=\sum_{m=0}^{\infty}\int_{-\infty}^{+\infty}[i\mu\omega B_m^{e,o}(\lambda)Se,o_m(\lambda d,\cos v)\times\partial He^{(2)},o_m(\lambda d,\cosh u)/\partial u-ihA_m^{e,o}(\lambda)\partial Se_m,o(\lambda d,\cos v)/\partial v\times He,o_m^{(2)}(\lambda d,\cosh u)]e^{-ihz}dh, \tag{15}$$

where the summation is over both even and odd Mathieu functions. It should be noted that the angular odd Mathieu function for $m=0$ is zero.

To match these expressions for the fields with the prescribed slot field at $u=u_0$, it is necessary to expand $h_1e_v(v,z)$ and $e_z(v,z)$ in a series of angular Mathieu functions as follows:

$$h_1e_v=\sum_{m=0}^{\infty}f_m^{e,o}(z)Se,o_m(\lambda d,\cos v), \tag{16}$$

and a similar expansion for e_z. As a result of orthogonality the coefficients are given by

$$f_m^{e,o}(z)=\frac{1}{N_m^{e,o}(\lambda d)}\int_0^{2\pi}\times e_v(v',z)Se,o_m(\lambda d,\cos v')h_1'dv', \tag{17}$$

where N_m^e and N_m^o are normalization factors defined by

$$N_m^{e,o}(\lambda d)=\int_0^{2\pi}[Se,o_m(\lambda d,\cos v')]^2dv'. \tag{18}$$

[9] P. M. Morse and H. Feshbach, *Methods of Theoretical Physics* (McGraw-Hill Book Company, Inc., New York, 1953), Vol. 1, p. 563, and Vol. 2, p. 1408.

It is also convenient to represent $f_m^{e,o}(z)$ and $f_m^{o}(z)$ as a Fourier integral as follows:

$$f_m^{e,o}(z)=\frac{1}{2\pi}\int_{-\infty}^{+\infty}dh\int_{z_1}^{z_2}f_m^{e,o}(z')e^{-ih(z-z')}dz'. \quad (19)$$

Combining Eqs. (17) and (19) and noting that the limits of integration of v' in Eq. (17) can be replaced by $v_1(z')$ and $v_2(z')$ we find that

$$h_1E_v(u_0,v,z)$$
$$=\frac{1}{2\pi}\sum_{m=0}^{\infty}\int_{-\infty}^{+\infty}e^{-ihz}dh\Big[\int_{z_1}^{z_2}\frac{1}{N_m^{e,o}}\int_{v_1(z')}^{v_2(z')}e_v(v',z')$$
$$\times Se,o_m(\lambda d,\cos v')h_1'e^{ihz'}dv'dz'\Big]$$
$$\times Se,o_m(\lambda d,\cos v). \quad (20)$$

The representation for the axial field in the slot is obtained in a similar manner and is given by

$$E_z(u_0,v,z)$$
$$=\frac{1}{2\pi}\sum_{m=0}^{\infty}\int_{-\infty}^{+\infty}e^{-ihz}dh\Big[\int_{z_1}^{z_2}\frac{1}{N_m^{e,o}}\int_{v_1(z')}^{v_2(z')}e_z(v',z')$$
$$\times Se,o_m(\lambda d,\cos v')e^{ihz'}dv'dz'\Big]$$
$$\times Se,o_m(\lambda d,\cos v). \quad (21)$$

The expansions for h_1E_v and E_z for $u=u_0$ in Eqs. (14) and (15) should now reduce to the above two equations. This leads to two sets of equations to solve for the coefficients A_m^e, A_m^o, B_m^e, and B_m^o. The result of this algebraic process is

$$(k^2-h^2)A_m^{e,o}(\lambda)=\int_{z_1}^{z_2}\int_{v_1(z')}^{v_2(z')}\frac{e_z(v',z')Se,o_m(\lambda d,\cos v')e^{ihz'}dv'dz'}{2\pi N_m^{e,o}He^{(2)},o_m(\lambda d,\cosh u_0)} \quad (22)$$

and

$$i\mu\omega B_m^{e,o}(\lambda)=\frac{ih}{k^2-h^2}\int_{z_1}^{z_2}\int_{v_1(z')}^{v_2(z')}\frac{e_z(v',z')\partial Se,o_m(\lambda d,\cos v')/\partial v'e^{ihz'}dv'dz'}{2\pi N_m^{e,o}[\partial He^{(2)},o_m(\lambda d,\cosh u)/\partial u]_{u=u_0}}$$
$$+\int_{z_1}^{z_2}\int_{v_1(z')}^{v_2(z')}\frac{h_1'e_v(v',z')Se,o_m(\lambda d,\cos v')e^{ihz'}dv'dz'}{2\pi N_m^{e,o}[\partial He^{(2)},o_m(\lambda d,\cosh u)/\partial u]_{u=u_0}}. \quad (23)$$

These expressions when substituted back into Eqs. (14) and (15) constitute the formal solution of the problem. The integration with respect to h is not readily carried out for the general case. It is possible, however, if certain simplifying assumptions are made that an approximate evaluation can be carried out.

For example, if the fields are to be observed at large distances from the cylinder the integration with respect to h can be carried out by the saddle point method as will be illustrated in the next section.

THE FAR FIELDS

The integrals to be evaluated are of the following form:

$$Pe,o=\int_{-\infty}^{+\infty}He,o_m^{(2)}(\lambda d,\cosh u)Fe,o(\lambda)e^{-ihz}dh, \quad (24)$$

where $Fe(\lambda)$ and $Fo(\lambda)$ are slowly varying functions compared with $He_m^{(2)}$ and $Ho_m^{(2)}$. To avoid difficulty with branch points at $h=\pm k$, it is convenient to let k possess a small negative imaginary part which can later be allowed to vanish. The integration of h is then along the real axes from $-\infty$ to $+\infty$. Since $u\gg 1$ in the far field it is permissible to employ the asymptotic expansion of the radial Mathieu functions which are

$$He,o_m^{(2)}(\lambda d,\cosh u)\simeq(\lambda d\cosh u)^{-\frac{1}{2}}$$
$$\times\exp\Big[-i\Big(\lambda d\cosh u-\frac{2m+1}{4}\pi\Big)\Big]. \quad (25)$$

For large values of u it can be seen that

$$d\cosh u\to(x^2+y^2)^{\frac{1}{2}}=\rho$$

so that

$$Pe,o\simeq\int_{-\infty}^{+\infty}\frac{Fe,o(\lambda)\exp\Big[-i\Big(\lambda\rho-\frac{2m+1}{4}\pi\Big)\Big]}{(\lambda\rho)^{\frac{1}{2}}}e^{-ihz}dh. \quad (26)$$

This integral can be evaluated immediately by employing Van der Waerden's modified saddle point method[10] and thus eliminating the usual and unnecessary deformation of the contour to the path of steepest descent. The result is

$$Pe,o\simeq(2\pi)^{\frac{1}{2}}ie^{-ikR}R^{-1}e^{im\pi/2}Fe,o(k\sin\theta), \quad (27)$$

where

$$R=(\rho^2+z^2)^{\frac{1}{2}},\quad \theta=\tan^{-1}\rho/z$$

and where terms containing R^{-2}, R^{-3}, etc. have been neglected.

The integrals of the form $2P_e/\partial u$ and $\partial Po/\partial u$ are

[10] B. L. Van der Waerden, Appl. Sci. Research **B-2**, 43 (1951).

given to the same approximation by

$$\frac{\partial Pe,o}{\partial u}\simeq(2\pi)^{\frac{1}{2}}k\sin\theta e^{-ikR}R^{-1}\rho e^{im\pi/2}Fe,o(k\sin\theta). \quad (28)$$

The far fields in terms of spherical polar coordinates (R,θ,ϕ) are given by

$$E_\theta\simeq E_u\cos\theta-E_z\sin\theta,\quad E_\phi\simeq E_v,\quad E_R\simeq E_u\sin\theta+E_z\cos\theta,$$

and

$$H_\theta\simeq H_u\cos\theta-H_z\sin\theta,\quad H_\phi\simeq H_v,$$
$$H_R\simeq H_u\sin\theta+H_z\cos\theta.$$

After we employ the results of the asymptotic integration it finally follows that the far fields are given completely by

$$E_\theta\simeq\frac{-ie^{-ikR}}{(2\pi)^{\frac{1}{2}}R\sin\theta}\sum_{m=0}^{\infty}\frac{e^{im\pi/2}}{N_m^{e,o}(c)}\frac{Se,o_m(c,\cos\phi)}{He,o_m^{(2)}(c,\cosh u_0)}\int_{z_1}^{z_2}\int_{v_1(z')}^{v_2(z')}e^{ik\cos\theta z'}e_z(v',z')Se,o_m(c,\cos v')dv'dz', \quad (29)$$

$$E_\phi\simeq\frac{k\sin\theta e^{-ikR}}{(2\pi)^{\frac{1}{2}}R}\left\{\sum_{m=0}^{\infty}\frac{e^{im\pi/2}}{N_m^{e,o}(c)}\frac{Se,o_m(c,\cos\phi)}{[\partial He,o_m^{(2)}(c,\cosh u)/\partial u]_{u=u_0}}\right.$$
$$\left.\times\int_{z_1}^{z_2}\int_{v_1(z')}^{v_2(z')}e^{ik\cos\theta z'}e_v(v',z')Se,o_m(c,\cos v')h_1',dv'dz'\right\}+\frac{i\cot\theta e^{-ikR}}{(2\pi)^{\frac{1}{2}}R}$$
$$\times\sum_{m=0}^{\infty}\frac{e^{im\pi/2}}{N_m^{e,o}(c)}\frac{Se,o_m(c,\cos\phi)}{[\partial He,o_m^{(2)}(c,\cosh u)/\partial u]_{u=u_0}}\int_{z_1}^{z_2}\int_{v_1(z')}^{v_2(z')}e^{ik\cos\theta z'}e_z(v',z')\frac{\partial Se,o_m(c,\cos v')}{\partial v'}dv'dz', \quad (30)$$

$$H_\theta\simeq(-k/\mu\omega)E_\phi\quad\text{and}\quad H_\phi\simeq(k/\mu\omega)E_\theta, \quad (31)$$

where $c=kd\sin\theta$. The field components E_R and H_R vary as R^{-2} in the far field. The radiation field of the arbitrary slot on the elliptic cylinder is now completely specified in terms of the prescribed tangential electric field. The task that remains is to carry out the integrations of e_z and e_v with respect to v' and z'.

An important special case that has been treated before in the literature[5,6] is the thin axial slot of width w. In this case the slot is taken to be of length $2l$ with an assumed distribution of voltage $V(z)$ along the narrow slot, such that

$$e_z(v,z)=0,\quad e_v(v,z)=\frac{V(z)}{w}\delta(v-v_0), \quad (32)$$

where $\delta(v-v_0)$ is such that

$$\int_0^{2\pi}\delta(v-v_0)h_1(u_0,v)dv=1. \quad (33)$$

It then follows that

$$E_\phi=\frac{k\sin\theta S(\theta)e^{-ikR}}{(2\pi)^{\frac{1}{2}}R}\times P_\phi, \quad (34a)$$

where

$$P_\phi=\sum_{m=0}^{\infty}\frac{e^{im\pi/2}}{N_m^{e,o}(c)}\frac{Se,o_m(c,\cos v_0)Se,o_m(c,\cos\phi)}{[\partial He,o_m^{(2)}(c,\cosh u)/\partial u]_{u=u_0}}, \quad (34b)$$

$$S(\theta)=\int_{-l}^{+l}V(z')e^{ik\cos\theta z'}dz',$$

and v_0 is the angular location of the slot on the elliptic cylinder. When the slot is sufficiently thin the voltage distribution is approximately cosinusoidal and can be expressed as

$$V(z)=\frac{V_c\sin k(l-|z|)}{\sin kl}, \quad (35)$$

where V_c is the voltage at the center of the slot. The integrations in Eq. (34b) can now be carried out in closed form to yield

$$S(\theta)=\frac{2V_c[\cos(kl\cos\theta)-\cos kl]}{k\sin kl\sin^2\theta} \quad (36)$$

and if the slot is one-half wavelength in length ($2l=\lambda/2$) the space factor is given by

$$S(\theta)=2V_c\frac{\cos[(\pi/2)\cos\theta]}{k\sin^2\theta}. \quad (37)$$

The far field solution for the thin transverse slot is also easily obtained from Eqs. (29) and (30) and agrees with earlier results.[5,6] For example, for a thin slot whose length dl is small compared to the dimensions of the cylinder and much less than a wavelength, it follows that in Eq. (31)

$$e_v(v,z)=0$$

and

$$e_z(v,z)\simeq\delta(z-z_0)\frac{V(v')}{w}, \quad (38)$$

where $\delta(z-z_0)$ is such that

$$\int_{z_1}^{z_2}\delta(z-z_0)dz=1\quad\text{for } z_2>z_0>z_1. \quad (39)$$

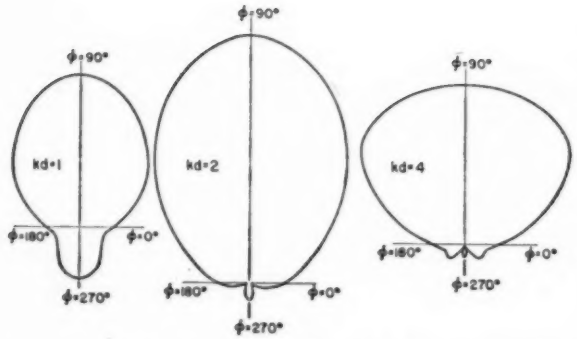

FIG. 1. Intensity patterns in the equatorial plane of a thin axial slot in the center of a strip of width $2d$.

Furthermore

$$\int_{v_1}^{v_2} V(v')Se_{,o_m}(c,\cos v')dv' \simeq Se_{,o_m}(c,\cos v_0)\bar{V}dl/h_1', \quad (40)$$

where

$$\bar{V}dl=\int_{v_1}^{v_2} V(v')h_1'dv' \quad \text{and} \quad v_2>v_0>v_1.$$

The field of the transverse slot can then be written

$$E_\theta=\frac{-\bar{V}dlie^{-ikR}e^{ik\cos\theta z_0}}{(2\pi)^{\frac{1}{2}}R\sin\theta d(\cosh^2 u_0-\cos^2 v_0)^{\frac{1}{2}}}\times P_\theta, \quad (41a)$$

where

$$P_\theta=\sum_{m=0}^{\infty}\frac{e^{im\pi/2}}{N_m^{e,o}(c)}\frac{Se_{,o_m}(c,\cos v_0)Se_{,o_m}(c,\cos\phi)}{He_{,o_m}^{(2)}(c,\cosh u_0)} \quad (41b)$$

and where $\bar{V}$ is the average voltage along the slot which is located at (u_0,v_0,z_0) on the surface of the elliptic cylinder. A similar expression is obtained for the E_ϕ component of the short transverse slot. This component vanishes, however, in the equatorial plane (i.e., $\theta=90°$).

PATTERN CALCULATIONS

The expressions for the radiation fields in Eqs. (34b) and (41b) are in suitable form for computation. The angular and radial Mathieu functions are quite adequately tabulated.[11,12] The computational work becomes somewhat simpler when the eccentricity of the ellipse becomes large. In the limiting case when the minor axis approaches zero, the elliptic cylinder reduces to a strip of width $2d$. The radiation fields for this case are obtained by the above formulas with $u_0=0$, or $\cosh u_0=1$.

The relative radiated intensity $|P_\phi|^2$ for the thin axial half-wave slot at the center of a ribbon ($u_0=0$, $v_0=\pi/2$) is shown plotted in Fig. 1 as a function of ϕ for the equatorial plane ($\theta=90°$). Three values of kd are chosen and it is interesting to note that the diffraction around to the rear of the strip is very significant for the case $kd=1$. The patterns become more directional for the cases, $kd=2$ and 4, with somewhat smaller rear lobes.

The relative intensity in the vertical plane of the half-wave slot at the center of the strip is shown in Fig. 2 where $|P_\phi|^2$ is plotted as a function of θ in the principal planes $\phi=90°$ and $\phi=270°$, while this pattern refers to the case $kd=2$, the vertical patterns for $kd=1$ and 4 are very similar.

An example of a pattern for a short transverse slot at the center of the strip ($v_0=\pi/2$) is shown in Fig. 3, where $|P_\theta|^2$ is plotted as a function of ϕ in the equatorial plane ($\theta=90°$) with $kd=2$. It is noted that the diffraction to the rear of the strip is almost negligible.

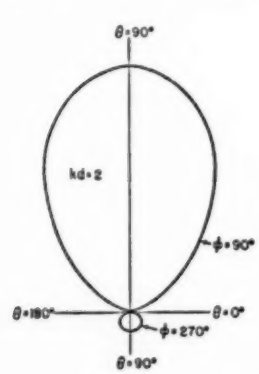

FIG. 2. Intensity pattern in the principal plane of a thin axial half-wave slot in the center of a strip of width $2d$.

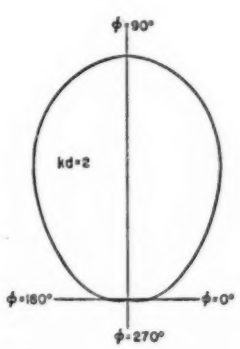

FIG. 3. Intensity pattern in the equatorial plane of a short transverse slot in the center of a thin strip of width $2d$.

In general the rear lobes for the transverse slots are much smaller than for the axial slots.

Finally it seems worthwhile to compare the computed results for an axial slot on a ribbon with some experimental data at a wavelength of 3.2 cm published by Gruenberg.[13] His observed patterns were for a longitudinal half-wave slot offset, $\delta=0.1$ inches, from the center of the broad face of an X-band wave guide. Patterns have been computed for a strip whose width $2d$ is chosen to be the same as the width of the broad face of the wave guide (1.0 inch). The computed field strength patterns, which are proportional to $|P_\phi|$, are shown plotted in Fig. 4 for $kd=2.2$. The angular slot

[11] *Tables Relating to Mathieu Functions* (Columbia University Press, New York, 1951).

[12] Stratton, Morse, Chu, and Hutner, *Elliptic Cylinder and Spheroidal Wave Functions* (John Wiley and Sons, Inc., New York, 1941).

[13] H. Gruenberg, Can. J. Phys. **31**, 55–69 (1953).

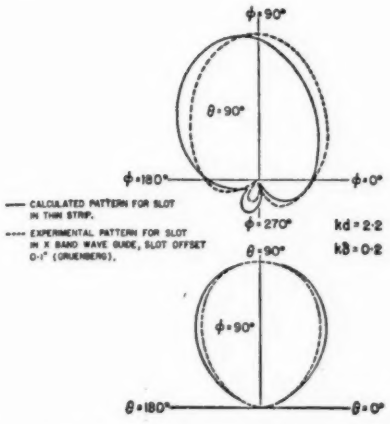

FIG. 4. Computed field strength patterns of a thin axial half-wave slot with offset δ on a strip of width $2d$ and the experimental patterns for an offset longitudinal slot on the broad face of an X-band wave guide.

location is $v_0=77.3°$ which is specified by the amount δ; the slot is offset from the center of the strip (i.e. $k\delta=0.2$). The experimental results are also shown in Fig. 4 and are normalized such that the experimental and computed curves have the same maximum amplitude.

The agreement being the experimental and computed patterns in the principal planes of the slot is quite reasonable. The discrepancy is probably due to the finite width ($\frac{1}{2}$ inch) of the X-band wave guide. Nevertheless, the computed patterns of the slots in thin strips should be an adequate method for predicting the approximate shape of the patterns of slotted waveguide antennas.

Other computations are being carried out for the patterns of slots in strips whose width is somewhat larger than a wavelength and the results are being compared to those predicted by approximate knife-edge diffraction theory.[14] Further work is also being done on calculating the currents on the strip excited by axial and transverse slots where it is not permissible to employ any of the far field assumptions. These results will be reported at a later date.

ACKNOWLEDGMENT

I would like to thank R. Walpole for carrying out the computations. The general problem was suggested by Dr. George Sinclair.

[14] J. R. Wait and R. Walpole, Can. J. Tech. (to be published).

JOURNAL OF APPLIED PHYSICS VOLUME 26, NUMBER 4 APRIL, 1955

Properties of Elastic and Plastic Waves Determined by Pin Contactors and Crystals*†

STANLEY MINSHALL
Los Alamos Scientific Laboratory, University of California, Los Alamos, New Mexico
(Received February 1, 1954)

Experimental techniques are described by which one can observe the separation of a shock wave in a metal into an elastic wave and a slower plastic wave. The plastic-wave velocity was about 15 percent less in steel and 10 percent less in tungsten than the elastic-wave velocity, at pressures imparted by Composition B explosive. Elastic-wave velocities were the same, within experimental error, as the measured sound velocities. The pressure in the elastic wave in SAE 1020 steel, deduced from the material and wave velocities, is independent of the plastic-wave pressure within experimental accuracy, and is about 12 kilobars. SAE 1040 steel, however, does not exhibit a single characteristic elastic-wave pressure. The pressure initially is about 6 kilobars, and increases to about 12 kilobars before the arrival of the plastic wave.

INTRODUCTION

WHEN a metal is subjected to a shock wave, the normal shock-wave velocity, D, is intermediate between the sound velocity, c_0, in the metal ahead of the shock and the local sound velocity, c_c, in the compressed metal behind the shock, i.e., $c_0<D<c_c$. However, it has been observed that some shocks in iron and steel are propagated at a velocity well below sound velocity. In this case it seems clear that the shocks should be preceded by a sonic disturbance. The front-running sonic disturbance has been observed by several experimenters.

Roberts and Nedzel[1] reported experiments with electrical contactors to obtain shock and free-surface velocities of steel plates in contact with high explosives. In their experiments they used a series of contactors spaced at increasing distances from the free surface of the target plate. A time-distance plot of the data in most cases could be fitted by a straight line, and the calculated free-surface velocity was appropriate to the pressure of the shock. However, when the first contactor of the series was placed close enough to a

* Work conducted under the auspices of the U. S. Atomic Energy Commission.
† Presented in part at a meeting of the Division of Fluid Dynamics, American Institute of Physics, July 1–3, 1953, Pennsylvania State College, Pennsylvania.

[1] J. H. Roberts and V. A. Nedzel (private communication, February, 1945).

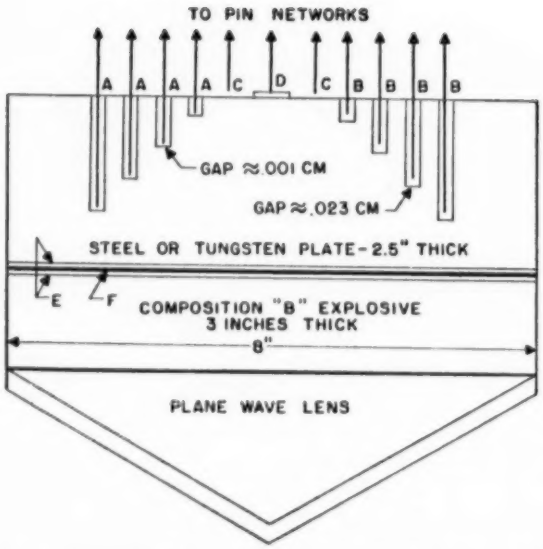

FIG. 1. Schematic cross section of wave-separation target plate. A—A show a group of elastic-wave pins backed off from the bottom of the hole just to break contact. B—B show a group of plastic-wave pins backed off 0.023 cm. C—C show two of a group of six pins used to measure free surface velocity. E—F, cellulose tape-copper foil sandwich, to obtain time at which shock wave entered target plate. D is a Z-cut tourmaline crystal, 0.020 in. thick, 0.375 in. in diameter. The annular space between pins and walls of the holes was filled with plastic spaghetti. The Composition B explosive is 40 percent TNT and 60 percent RDX.

1-in. thick target plate so that it just failed to make electrical contact, it was discharged about 0.5 μsec too early to be on the straight line which best fitted later contactors. The result was attributed to the presence of a faster sonic wave ahead of the shock wave. This wave was sufficiently strong to move the free surface far enough to short the close-set electrical contactor or pin before the shock wave reached the free surface.

The phenomenon was investigated theoretically by Peierls.[2] He concluded that under certain conditions the metal would be compressed by the elastic wave to somewhat above the yield strength. The elastic wave would then be followed by a second compression by which the shock pressure would be reached.

R. W. Goranson[3] reported experiments with steel target plates 1.25 in. thick. He deduced a pressure for the elastic wave of 15 kilobars from electrical-contactor data and of 15.7 kilobars from piezoelectric-crystal data.

Pack, Evans, and James[4] measured the velocity of a plane longitudinal wave through various lengths of steel and lead. The velocity of the wave in steel was essentially independent of the length of the sample and corresponded to the calculated elastic-wave velocity. The velocity of the wave in lead decreased with increasing length of sample; the initial wave velocity corresponded to the calculated shock-wave velocity, and the velocity decreased to the calculated elastic-wave velocity as the length of the sample was increased.

Still other experimental techniques have been used to study the elastic-plastic wave system. A. C. Whiffen[5] found a pressure of about 6.4 kilobars for the dynamic compressive yield stress of mild steels by analyzing the deformation of flat-ended projectiles which had been shot at a steel plate.

J. S. Rinehart[6] studied the scabbing of steel target plates as a result of a short-duration shock. He obtained a value of 11 kilobars for the critical normal fracture stress under tension. The elastic-plastic wave system for a short-duration shock was discussed by D. S. Wood.[7]

An optical-lever and drum-camera technique was used by Allen and McCrary[8,9] to study the spherical motion of the surface of a steel target plate in contact with a small charge of explosive. Assuming, as they did, that their spherical wave can be approximated by a plane wave, one obtains a pressure of 11.4 kilobars in the elastic wave.

Two groups of experiments, made to study the two-wave system, are reported in this paper. Group I experiments were designed primarily to observe the progressive separation of the two waves as they moved through a target plate. Group II experiments were designed to determine the amplitude and profile of the elastic wave, and to determine if the amplitude of the elastic wave depended upon pressure of the plastic wave.[10]

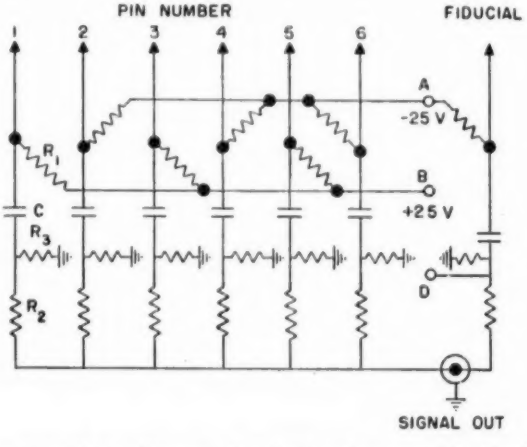

FIG. 2. Wiring diagram of pulse-forming networks. Leads to pins were about 5 ft long and enclosed in braided copper shield. The shield was grounded to the target plate and pulse-forming network. R_1=1 meg, R_2=2000 ohms, R_3=100 ohms, C=0.01 μf. The fiducial was injected onto four other records by the connection at D.

[2] R. E. Peierls (private communication, May, 1945).
[3] R. W. Goranson, *et al.* (to be published).
[4] Pack, Evans, and James, Proc. Phys. Soc. (London) **60**, 1 (1948).
[5] A. C. Whiffen, Proc. Roy. Soc. (London) **A194**, 300 (1948).
[6] J. S. Rinehart, J. Appl. Phys. **23**, 1229 (1952).
[7] D. S. Wood, J. Appl. Mech. **19**, 521 (1952).
[8] W. A. Allen and C. L. McCrary, Rev. Sci. Instr. **24**, 165 (1953).
[9] W. A. Allen, J. Appl. Phys. **24**, 1180 (1953).
[10] For the purpose of this paper, the following definitions will apply: "elastic wave" will refer to a compressional wave, the pressure of which is defined to be the dynamic elastic limit, and "plastic wave" will refer to a high-pressure wave, the pressure of

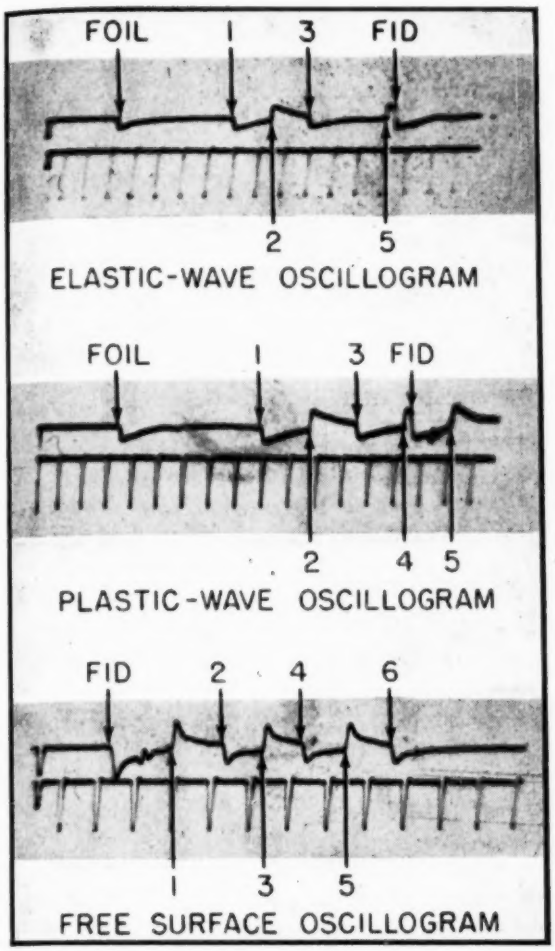

FIG. 3. Three oscillograph records for experiment 5. The pulse from pin 4 of the elastic-wave record is missing, probably because of a premature short. The relatively earlier arrival times of the elastic-wave pin pulses with respect to the plastic-wave pin pulses can be seen by comparing pulses from pin 5 which in each case was on the free surface of the target plate. The fiducial signal is a common time for all records. The timing markers are at 1-μsec intervals.

GROUP I EXPERIMENTS

Contactors were placed in flat-bottom holes in the metal at several distances from an explosive as shown on Fig. 1. One group of five contactors or pins was backed off from the bottom of the holes just far enough ($\approx$0.00076 cm) to break contact. This group of pins, it was expected, would make contact on the passage of the low-pressure elastic wave. A similar group of pins was backed off far enough to discriminate between the elastic and the plastic waves. The gap ($\approx$0.023 cm) was large enough to allow contact only after the plastic wave produced appreciable displacement of the metal. From available data[1-3] it was estimated that the motion of the bottom of the hole, between the time of arrival of the elastic wave and that of the plastic wave, would be about 0.0015 cm per cm of distance over which the two waves had traveled. On the completed target plate there were two groups of elastic-wave pins, two groups of plastic-wave pins, and one group of pins to measure the velocity of the free surface.

The arrival of the emergent wave system was also detected by means of a Z-cut tourmaline crystal located at the free surface of the target plate.

One can see from Fig. 2 how several signals generated at contact of plate and pins were injected onto a single cable. Pin 1, for example, is charged to a potential of +25 v with respect to ground through the resistor R_1. When the target plate moves and makes contact with the pin, the pin is shorted to ground, and the opposite side of the condenser C drops to -25 v with respect to ground. The signal is transmitted to the signal cable by the mixing resistor R_2. The resistor R_3 prevents ringing in the pin leads. Signals were recorded on single-sweep cathode-ray oscillographs manufactured by Hughes Aircraft Company. The equipment is similar to that described by W. C. Elmore.[11]

Three oscillograms from experiment 5 are shown on Fig. 3.

Figure 4 is a graph of the time-distance data of experiment 5 with an arbitrary zero time. The five records are correlated by a fiducial pulse which occurs on all records. When the oscillograms are being converted to time of arrival of the respective waves, consideration must be given to the finite time between arrival of the wave at the bottom of the hole, and contact with the pin, i.e., closing time. The closing time

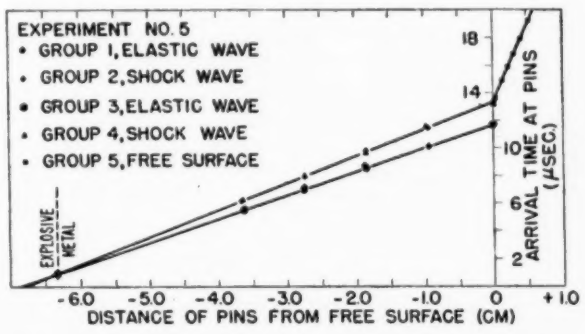

FIG. 4. Data of experiment 5. A separate cellulose tape-copper foil sandwich was used for each of the pin groups at the explosive-target plate interface at -6.35 cm. The use of individual foils for each group resulted in a small variation in the indicated arrival times of the detonation front.

which is above the dynamic elastic limit. "Dynamic elastic limit" will refer to the stress on a dynamic stress-strain diagram where the relation between stress and strain ceases to be linear. "Sound wave" will refer to a compressional wave produced and detected by conventional crystal techniques. Sound- and elastic-wave velocities are expected to be the same because both waves are characteristic of the elastic regime of the metal. "Shock wave" will refer to a wave which, because of the hydrodynamic properties of the metal under investigation, will develop and maintain a pressure discontinuity. All three waves are longitudinal and are assumed to be in a medium of infinite lateral extent. Under the conditions of these experiments the plastic wave is a shock, and the elastic wave has a shock-like profile.

[11] W. C. Elmore and M. Sands, *Electronics* (McGraw-Hill Book Company, Inc., New York, 1949), first edition, National Nuclear Energy Series, Div. V, Vol. 1, Chap. 5.

TABLE I. Summary of experiments for separation of elastic and plastic waves in steel and in tungsten alloy.

Experiment No. and metal	2 Steel	4 Steel	5 Steel	6 W alloy	7 W alloy	8 W alloy
1. Nominal thickness (in.)	1.25	2.50	2.50	2.50	2.50	2.50
2. Density (g/cm³)	···	7.84	7.83	18.34	18.01	18.14
3. Sound velocity, pulsed-crystal technique (cm/μsec)	···	0.588	0.591	0.500	0.492	0.504
4. Elastic-wave velocity, pin technique (cm/μsec)	0.590	0.592	0.589	0.492	0.489	0.496
5. Plastic-wave velocity, pin technique, corrected for pins backed off 0.023 cm (cm/μsec)	0.505	0.510	0.512	0.440	0.445	0.445
6. Plastic-wave velocity, pin technique, corrected for pins backed off 0.045 cm (cm/μsec)	···	···	···	···	0.442	0.446
7. V_p, free-surface velocity caused by plastic wave (cm/μsec)	0.133	0.091	0.091	0.066	0.070	0.068
8. Transit time difference, pin technique (μsec)	0.68	1.66	1.61	1.47	1.17	1.33
9. Transit time difference, crystal (μsec)	···	1.78	1.74	1.74	1.38	1.51
10. Estimated closing time of elastic-wave pins (μsec)	···	0.12	0.13	0.27	0.21	0.18

will depend upon the distance of the pin from the bottom of the hole and the velocity imparted to the bottom of the hole, which in turn will depend upon the pressure of the wave. In the calculation of closing time, the elastic wave pressure was assumed to be the same at all levels.[2,3,7] However, the pressure of the plastic wave is dependent on distance from the explosive. A rarefaction wave necessarily follows the plastic wave because of the finite size of the explosive. Data from these experiments were used to calculate closing times for the plastic-wave pins at different distances from the explosive. This correction ($\approx$0.3 μsec at the 2½ in. level for iron) was made to connect the plastic wave with the free-surface motion it causes. Unless the correction is applied, the free surface appears to move 0.3 μsec before the plastic wave arrives at the free surface. The method of correcting for pin setback was verified with experiments 7 and 8, where the setback of one group of plastic-wave pins was twice the setback of the other group. It can be seen from lines 5 and 6, Table I, that the correlation in velocity is well within experimental error.

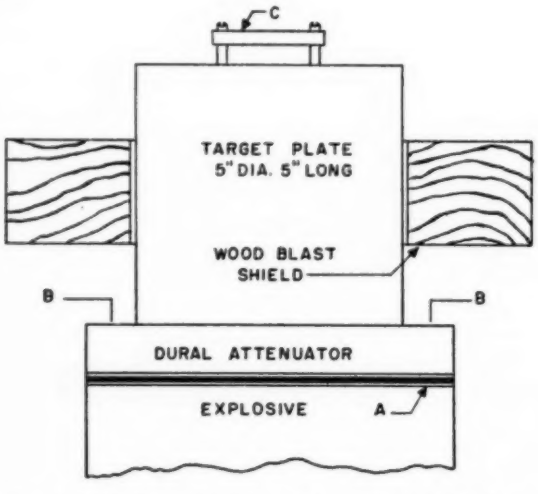

FIG. 5. Schematic cross section of dynamic-elastic-limit experiments. A cellulose tape-copper foil sandwich was located at A on experiment 9 to obtain zero time. For later experiments contactors were at B. The phenolic pin-holding disk was located at C.

Table I is a summary of the data from six experiments. The steel was nominally SAE 1020. The tungsten alloy was sintered tungsten with 5 percent nickel and 3 percent copper as binder.

GROUP II EXPERIMENTS

Group II experiments were designed to study the pressure profile in the wave system. In particular it is desirable to know the pressure in the elastic wave, which is assumed to possess a shock-like profile. Conservation of mass and momentum in one dimension requires that $p=\rho_0 uc$ where p is the pressure in the wave, ρ_0 is the initial density, u is the material velocity produced by the wave, and c is the wave velocity. Therefore, if c and u can be measured for an elastic wave, the dynamic elastic limit can be calculated. In this case $u=\frac{1}{2}V_e$, where V_e is the free surface velocity imparted by the elastic wave.

An experiment was performed with the target plate shown in Fig. 5. The thick target plate was necessary because the velocity imparted to the free surface by the elastic wave was only 0.005 cm/μsec. The free-surface motion over which elastic free-surface velocity could be measured was estimated as 0.015 cm from available data at this Laboratory.[12] A cellulose tape-copper foil sandwich was inserted at A, Fig. 5, in order to obtain an initial time from which to estimate elastic- and plastic-wave velocities. For later experiments transit-time contactors were placed at B instead of the foil. Although one does not obtain good values of initial times from contactors located at B because of curvature of the shock front, they were placed at B rather than on the axis to prevent possible perturbations

[12] The distance over which elastic free-surface velocity can be measured is less than $(d/D-d/c)V_e$, where d is the thickness of the target plate and D is the plastic-wave velocity. When the elastic wave arrives at the free surface of the target plate, it is reflected as a rarefaction wave, leaving the metal between the free surface and the rarefaction as it was before passage of the elastic wave. After the retreating rarefaction and advancing plastic waves collide, a new elastic wave will emerge from the plastic-wave front, with a velocity c greater than D, and further accelerate the free surface. These interactions will continue until the free surface attains the velocity appropriate to the pressure of the shock wave.

from these contactors or foils from affecting the elastic-wave motion. All experiments in this series were made with target plates 5 in. in diameter by 5 in. in height. The purpose of the dural attenuator was to smooth the shock front and remove the von Neumann pressure spike present at the detonation front.[13]

Pin potential was reduced to 4.5 v to minimize the effect of possible arcing. The distance of the pin ends from the surface was measured by setting the axis of a comparator telescope nearly parallel to the surface of the target plate. The cross hairs of the telescope were set first on the pin, then on its reflection. The separation of the pin from the surface is $\frac{1}{2}l(\cos\theta)$ where l is the difference between the two settings and θ is the angle between the axis of the telescope and the surface of the plate. At the angles used, <5 deg, the correction for $\cos\theta$ was much less than the reproducibility of the readings and was ignored. Figure 6 is a plan of the pin arrangements. Figure 7 is a photograph of a completed target plate.

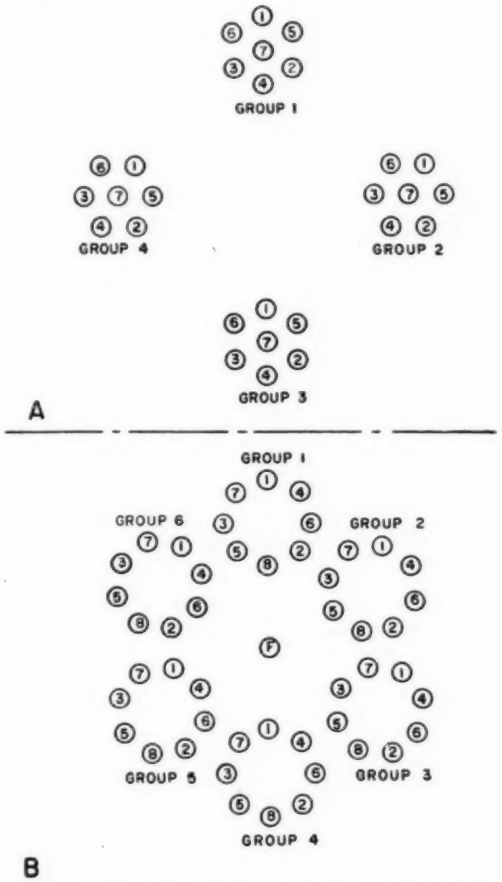

FIG. 6. Lateral location of pins on the free surface of the target plate. The order in which the pins in each group made contact is indicated by the small number in the circles. (A) Pin array used for experiments 9 to 14 inclusive; the pin groups were located on a circle $1\frac{1}{2}$ in. in diameter. (B) Pin array used for experiments 15 and 16; the pin groups were located on a circle 1 in. in diameter.

[13] John von Neumann, "Theory of detonation waves," National Defense Research Council Report No. B 238, Office of Scientific Research and Development Report No. 549, PB 31090 (1942).

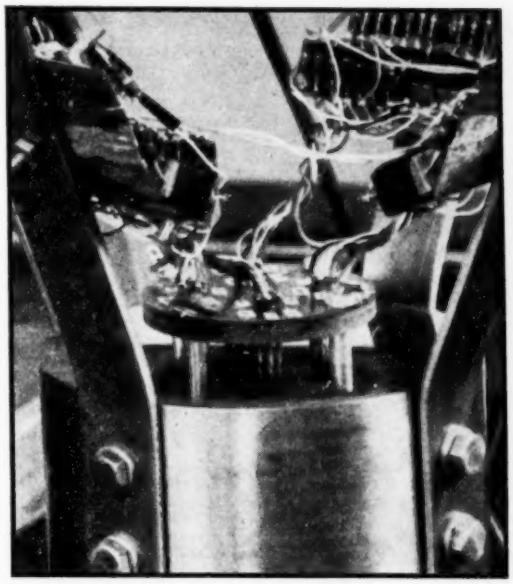

FIG. 7. Photograph of experiment No. 9 with pins connected to pulse-forming networks. The reflection of some of the pins can be seen in the polished surface of the target plate.

A graph of the time-distance data from experiment 9 is shown in Fig. 8. Three more experiments, 10, 11, and 12, were made with SAE 1020 steel at three different pressures (see Table II). No significant difference in the time-distance graphs was observed. The elastic-wave velocity of a sample of SAE 1040 steel, Fig. 9, was 0.564 cm/μsec and was markedly lower than the sound velocity of 0.592 cm/μsec. Had the elastic-wave velocity been the same as the sound-wave velocity, the free surface would have started to move at the time indicated by the X on the ordinate of Fig. 9. Two more experiments were performed so that the discrepancy would be resolved: one with SAE 1020 and one with SAE 1040 steel. Forty-eight pins were

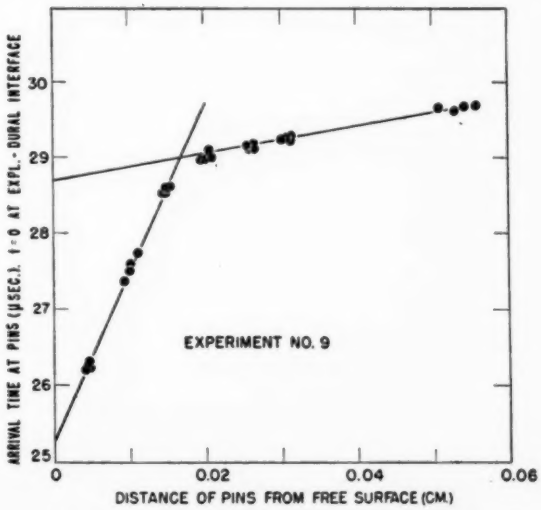

FIG. 8. Data of experiment 9. SAE 1020 steel.

TABLE II. Summary of data of experiments for measurement of dynamic elastic limit.[a]

Experiment No. and metal	9 SAE 1020[b]	10 SAE 1020	11 SAE 1020	12 SAE 1020	13 SAE 1040	14 SAE 1040	15 SAE 1020	16 SAE 1040
1. Density (g/cm³)	7.86	7.84	7.84	7.84	7.83	7.83	7.84	7.82
2. Sound-wave velocity (cm/μsec)	0.591	0.594 ±0.003	0.594 ±0.003	0.594 ±0.003	0.592 ±0.003	0.592 ±0.003	0.591 ±0.003	0.592 ±0.003
3. Elastic-wave velocity (cm/μsec)	0.581	0.602	0.593	0.603	0.555	0.564	0.608	0.597[d] 0.553[d]
4. V_e, elastic free-surface velocity (cm/μsec)	0.0045	0.0048	0.0051	0.0048	0.0061	0.0056	0.0053	0.0025[d] 0.0050[d]
5. Pressure in elastic wave (kilobars)	10.5	11.2	11.9	11.2	...[c]	...[c]	12.3	5.8[d] 11.2[d]
6. Plastic-wave velocity (cm/μsec)	0.498	0.506	0.507	0.509	0.514	0.515	0.509	0.516
7. V_p, plastic free-surface velocity (cm/μsec)	0.055	0.038	0.054	0.034	0.051	0.034	0.049	0.050
8. Pressure in plastic wave (kilobars)	109.	77.	109.	69.	104.	70.	99.	102.

[a] All data were obtained experimentally. The pressure of the elastic wave, line 5, was calculated from the relation $p=\rho uc$. The relation is not correct when the medium ahead of a wave is in motion. A modified relation was used to calculate the pressure in the second "elastic" wave of experiment 16 and the pressure in the plastic wave of all experiments. $1kb=10^9$ dynes/cm².

[b] Physical and chemical properties are not available for this sample.

[c] The pressure in the "elastic" wave has not been calculated because, for these two experiments, the contactors were too far from the free surface for resolution of the early "elastic" wave.

[d] The two values given for "elastic" wave velocity, "elastic" free-surface velocity, and pressure, are based on the interpretation that the data of experiment 16 can be represented by two linear functions.

spaced at levels such that the first 0.005 cm of motion of the free surface could be studied in detail. The data of SAE 1020, Fig. 10, were consistent with the data of former experiments. The presence of what appears to be a low-pressure early elastic wave in SAE 1040 steel can be seen on the graph in Fig. 11. Motion due to the "elastic" wave has been fitted to two straight lines as a convenience. It is not possible to determine from these data whether the free surface undergoes constant acceleration after the initial wave, or whether there are two "elastic" waves at different pressures.

Data from the eight experiments are summarized in Table II.

Physical properties and spectrochemical analyses of the target plate metals are given in Tables III and IV. The steels are representative of SAE 1020 and SAE 1040 steels.

DISCUSSION OF DATA

Data from the wave-separation series with steel and tungsten confirm that the sound- and elastic-wave velocities of each metal are the same. The average difference in the two velocities for tungsten (≈1.4 percent) is of marginal experimental significance.

The elapsed time between the arrival of the elastic and plastic waves can be obtained from both the pin records and the crystal records. That this time interval is larger when measured by crystals than by pins (lines 8 and 9, Table I), is caused by the fact that a closing time correction has been applied to the plastic-wave pin times but not to the elastic-wave pin times. With 0.005 cm/μsec for the elastic free-surface velocity of SAE 1020 steel, and an estimated setback of 0.00076 cm for the elastic-wave pins, one obtains 0.15 μsec as the closing time of the elastic-wave pins. The setback of elastic-wave pins was not measured directly on the experiments, but was estimated from auxiliary experiments. The setback calculated from the elastic free-surface velocity of SAE 1020 steel is 0.00063 cm.

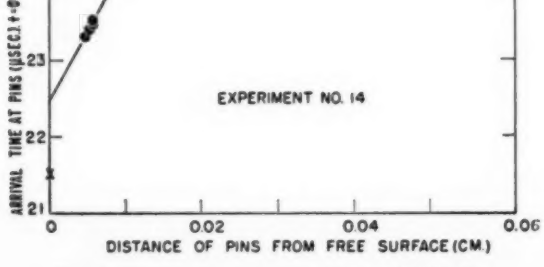

FIG. 9. Data of experiment 14. SAE 1040 steel.

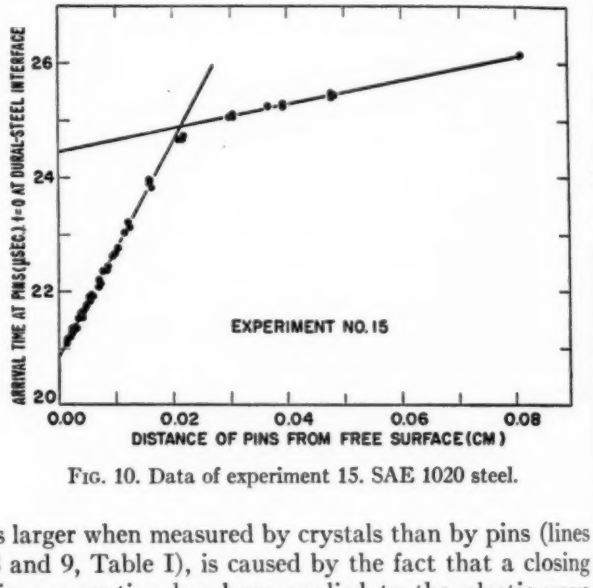

FIG. 10. Data of experiment 15. SAE 1020 steel.

A similar computation of closing time is not possible for the tungsten because elastic free-surface velocity was not measured. However, the process can be reversed to obtain a rough estimate of the dynamic elastic limit of the tungsten alloy. One thus obtains a dynamic elastic limit of about 13 kilobars for a setback of 0.00063 cm, or about 16 kilobars for a setback of 0.00076 cm. It is obvious that little reliance can be put on these numbers.

There is excellent agreement between the values of elastic free-surface velocity and elastic-wave pressure reported here, and those reported by Inyokern workers.[8,9]

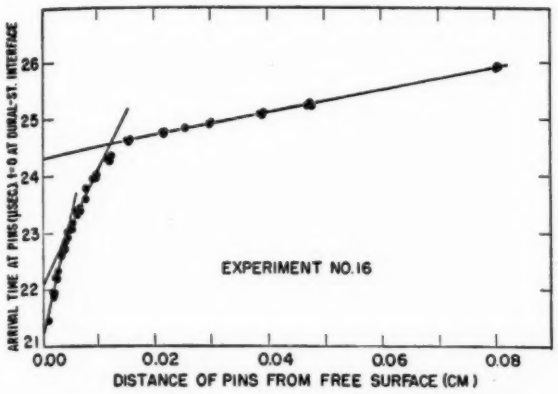

FIG. 11. Data of experiment 16. SAE 1040 steel.

The "elastic" free-surface motion found for SAE 1040 steel is not sufficiently detailed to distinguish between two distinct velocities or continuous acceleration. Two straight lines would imply two dynamic elastic limits, with a different wave velocity for each, whereas an accelerated motion would mean that the pressure of the elastic wave is increasing from the front of the elastic wave to the front of the plastic wave. Only the first wave would come within a strict definition of an elastic wave.[10]

The final elastic-wave pressure of SAE 1040 steel is, within experimental accuracy, the same as the dynamic elastic limit of SAE 1020 steel. A series of experiments is planned, with varying amounts of carbon, to attempt to explain the behavior of SAE 1040 steel.

TABLE III. Physical properties of target plate metals.[a,b]

	Tensile strength (kilobars)	Yield strength 0.2 percent offset (kilobars)	Elongation (percent)	Reduction of area (percent)	Diamond pyramid hardness
SAE 1020 steel	4.79	2.85	37	59.2	143
SAE 1040 steel	5.86	3.96	28	42.3	196

[a] Test sections of the tensile test bars were 1½ in. long and ½ in. diameter.
[b] The microstructure was characteristic of hot-rolled SAE 1020 and SAE 1040 steels.

TABLE IV. Spectrochemical analyses in percent by weight.

	C	Si	Cr	Mn	Ni	Cu
SAE 1020	0.20	0.3	0.07	0.33	0.11	0.08
SAE 1040	0.40	0.2	0.03	0.78	0.1	0.04

Pressure in the elastic wave appears to be independent of plastic-wave pressure for the four samples of steel known to be SAE 1020.

No attempt has been made herein to correlate the dynamic elastic limit with values of yield strength or of ultimate strength, either static or dynamic. This is because there are fundamental differences in the experimental criteria by which these quantities are measured. It has been suggested that "Hugoniot elastic limit" be substituted for "dynamic elastic limit" to emphasize the experimental differences between the phenomenon reported here and the engineering designations of yield stress and ultimate strength.

ACKNOWLEDGMENTS

The writer is indebted to a large number of persons for assistance on this project: B. L. Burton, S. A. Landeen, E. F. Gittings, D. Venable, H. T. Knight, and J. M. Walsh for reading and making constructive criticisms of this manuscript; E. L. Peterson and R. E. Duff for suggesting the interaction of the elastic wave with the free surface and the plastic wave; T. J. Boyd, Jr., and H. L. Laquer for measurements on the sound velocity; A. H. Williams for polishing the target plates; C. G. Hoffman and O. R. Simi for determining the physical and chemical properties of the samples; and R. E. Faudree and L. Hill for assembly of the target plates.

Orientation and Temperature Effects on the Electrical Resistivity of High-Purity Magnesium*

JAMES L. NICHOLS
Metallurgical Laboratories, The Dow Chemical Company, Midland, Michigan
(Received June 25, 1954)

The effect of crystal orientation on the electrical resistivity of high-purity magnesium at 24°C may be represented by the equation:

$$\rho(\phi) = 4.60 - 0.75 \cos^2\phi, \text{ (in microhms/cm}^3\text{)},$$

where ϕ is the angle between the hexagonal axis and the direction of current flow. The effect of temperature on the electrical resistivity for varying orientations shows temperature coefficients of 0.00390 and 0.00408/°C obtained perpendicular and parallel to the hexagonal axis, respectively, for the temperature range of 24° to 200°C. Magnesium shows rotational symmetry about the hexagonal axis with respect to electrical resistivity. Grain size has little or no effect on the electrical resistivity of magnesium.

INTRODUCTION

MAGNESIUM, like other hexagonal metals, is anisotropic with respect to electron flow and hence to electrical resistivity. However, in contrast with cadmium and zinc, previous determinations have shown that the electrical resistivity of magnesium decreases as the angle between the hexagonal axis and direction of current flow decreases. This investigation was undertaken to provide additional insight into the electrical resistivity of magnesium in terms of improvement of metal purity and verification of existing data on the effect of crystal orientation and temperature on the electrical properties of magnesium.

EXPERIMENTAL WORK

In an effort to obtain the highest purity possible, the magnesium used in this investigation was submitted to four sublimations in vacuo and cast under argon. Spectrographic analysis for this material is given in Table I. The cast material in the form of two 3-in. diameter by 8 in. long ingots was extruded into one-half inch rod. The extrusion container was thoroughly cleaned and pickled prior to the extrusion operation so as to prevent any accidental pickup of contaminants.

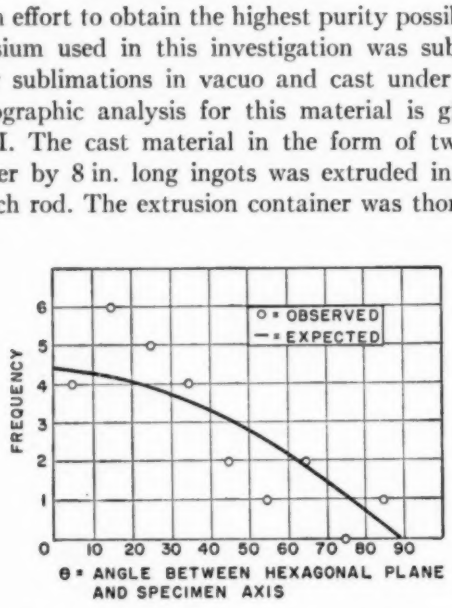

FIG. 1. Orientation angle *versus* frequency of occurrence for 25 magnesium single crystals grown from the melt.

Twenty-five single crystals, ½ inch in diameter and 7 inches long, were grown from the melt from this rod in a gradient furnace similar to that described by Jillson,[1] and modified by Burke and Hibbard.[2] A yield of about 80 percent was obtained in the production of high-purity magnesium single crystals using this method.

The orientations of the twenty-five single crystals were determined using the Laue back-reflection x-ray technique and were the average of two determinations on each crystal at 90° rotation to each other. These invariably checked within 1° when plotted stereographically. A small amount of lineage imperfection was observed (as indicated by a separation of the Laue spots) in a few of the specimens; however, close observations of these crystals in subsequent electrical measurements disclosed no anomalies.

After determination of orientations, the crystals were etched to remove surface oxide and the extreme ends sanded lightly with 3/0 emery paper in order to reduce contact resistance. A Kelvin Double Bridge was used in conjunction with a high-sensitivity D'Arsonval type galvanometer for the resistance measurements. From four to six measurements were made on each bar, and the average of these readings was used as the resistance of the bar. The current clamps were placed on the extreme ends of the rod with a total contact of

TABLE I. Spectrographic analysis of sublimed magnesium.

%C = 0.0036	%Mn = 0.0002	%Ca = 0.0010
%Fe = 0.0005	%Si = <0.001	%K = 0.0019
%Pb = <0.0005	%Cu = <0.0001	%Na = 0.0019
%Zn = <0.01	%Ni = <0.0003	%Sr = <0.0001
%Al = <0.0001	%Sn = <0.001	%B = <0.0001
		%H = 0.0004

* This work was sponsored by the Air Materiel Command, Wright-Patterson Air Force Base under Contract No. AF(600)-19147.

[1] D. C. Jillson, Trans. Am. Inst. Mining Met. Engrs. **188**, 1005 (1950).
[2] E. C. Burke and W. R. Hibbard, Jr., Trans. Am. Inst. Mining Met. Engrs. **194**, 295 (1952).

TABLE II. Comparison of electrical resistivity perpendicular and parallel to the hexagonal axis for high-purity magnesium at 18°C.

	$\rho_\perp$ (10^{-6} ohms/cm^3)	$\rho_{\parallel}$ (10^{-6} ohms/cm^3)
This study	4.48($\sigma=\pm0.01$)	3.74($\sigma=\pm0.01$)
Schmid[a]	4.54	3.77
Bridgman[b]	4.50	3.80

[a] See references 3 and 4.
[b] See reference 6.

approximately 30 percent of the bar circumference, 15 percent on the top and 15 percent on the bottom. The potential clamps were chromium-plated steel knife edges which were held in contact with the upper surface of the specimen by a constant spring tension. The readings were taken in a room in which the temperature was held to $\pm\frac{1}{2}$°C for the duration of measurement.

For the determination of the temperature coefficients of resistivity, ten single crystals were selected having $\cos^2\phi$ values ranging from 0.001 to 0.990, enabling complete coverage of the angular relationships between the hexagonal axis and the direction of current flow. A constant temperature bath was employed for the high-temperature measurements, using peanut oil as the heat exchange medium. In this investigation, an upper temperature limit of 200°C was imposed because of the specimen-holder construction.

RESULTS AND DISCUSSION

The unit hexagonal triangle for each crystal was plotted, enabling a statistical calculation of the probability of growing a magnesium single crystal of a predetermined orientation. Figure 1 shows the expected and observed distributions for twenty-five single crystals as a function of the angle between the specimen axis and the hexagonal plane. The expected frequencies are based on the area of 10° segments of a 30° hemisector on the reference sphere, and not on the areas of the stereographic net, since these areas are not proportional in any perspective projection. From the results obtained, it is observed that the orientation of a magnesium single crystal formed from the melt by the described method is purely a random function of the area of the basic hexagonal triangle and shows no preferred growth orientation. The "goodness of fit" of the observed curve with the expected curve was examined by the "chi-square" test. Standard statistical procedures show the χ^2 value of 4.56 obtained here is associated with a probability range of 0.5–0.75 (depending on the number of degrees of freedom chosen) that χ^2 will be at least as great or greater than the value obtained. This indicates that the hypothesis set forth should be accepted; i.e., that the growth of a single crystal of magnesium by the method described gives a random orientation of the specimen axis with respect to the hexagonal pole in accordance with the area of the spherical triangle on the reference sphere bounded by the hexagonal pole, the [210] and the [100] directions.

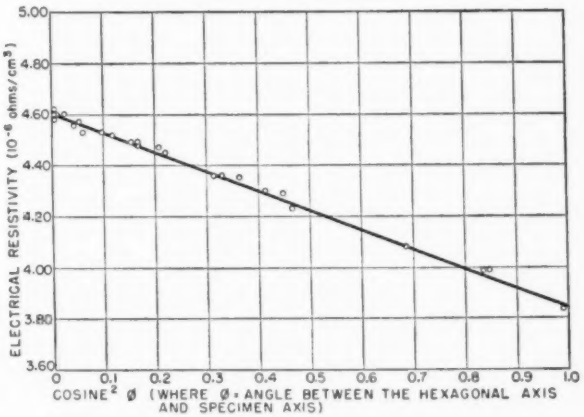

FIG. 2. Electrical resistivity *versus* crystal orientation for high-purity magnesium at 24°C ($\pm\frac{1}{2}$°C).

Figure 2 gives the electrical resistivity, ρ, at 24°C plotted against cosine^2 ϕ where ϕ is the angle between the hexagonal axis and the direction of current flow. This plot shows very little scatter with a standard deviation, σ, of $\pm0.01\times10^{-6}$ ohm/cm^3 for the resistivity. The resistivities perpendicular and parallel to the hexagonal axis for this investigation along with those of Schmid[3,4] and Bridgman,[5] extrapolated to the constant temperature of 18°C, are given in Table II.

From these data it may be deduced that the magnesium used in this investigation was of sufficiently high purity to yield a real difference from previous investigations. It can be seen that magnesium not only varies materially with direction but, unlike almost all other noncubic metals, the resistance is greater perpendicular to the axis of greatest symmetry.

Several attempts were made to find some correlation between resistivity and direction in the basal plane. It was felt that if any effect were to be observed, it should be for angles of ϕ between 45° and 90°; however, the scatter in the data was quite small and further refinement by considering the azimuthal rotation in the basal plane was not possible. Any azimuthal effects around the c axis, of course, would be repetitive for every 60° rotation. The absence of directional changes of resistivity in the basal plane was not unexpected since other investigators[3,4,6] report rotational symmetry around the hexagonal axis. Orientation, then, with respect to electrical resistivity is sufficiently defined by the angle ϕ between the hexagonal axis and the direction of current flow. Since the extreme resistivity values are observed parallel and perpendicular to the hexagonal axis, the resistivity at any particular intermediate angle ϕ is given by the following expression:

$$\rho(\phi)=\rho_\perp \sin^2\phi+\rho_{\parallel}\cos^2\phi. \quad (1)$$

[3] E. Schmid, Z. Elektrochem. **37**, 447 (1931).
[4] E. Goens and E. Schmid, Physik. Z. **37**, 385 (1936).
[5] P. W. Bridgman, Phys. Rev. **37**, 460 (1931).
[6] W. Boas, *Physics of Metals and Alloys* (John Wiley and Sons, Inc., New York, 1949), p. 49.

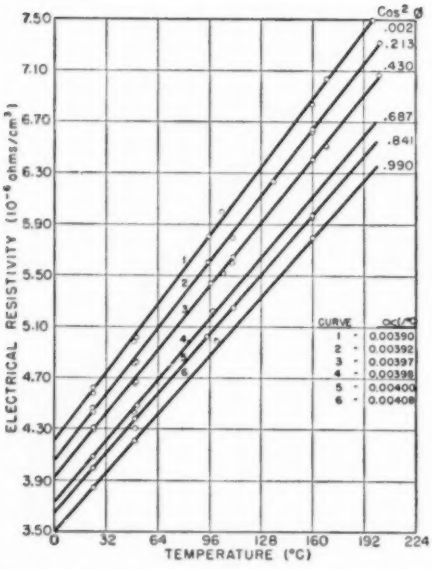

FIG. 3. Electrical resistivity *versus* temperature for high-purity magnesium single crystals of various orientations.

For high-purity magnesium at 24°C this becomes

$$\rho(\phi)=4.60-0.75\cos^2\phi. \qquad (2)$$

A possible source of error was found in the type of specimen clamps used. The sample holder employed spring clamps which undoubtedly incited some twinning in the specimens. However, since subsequent readings on the bars showed no change, it is safe to assume that any twinning which may have occurred was extremely localized in character and caused very minor changes in resistance which were beyond the sensitivity of the bridge.

The results of the temperature coefficient measurements are shown in Fig. 3, a plot of electrical resistivity *versus* temperature for selected orientations. The R_0 values are obtained from the intercepts on the vertical axis in Fig. 3 and the ratio of the slope of the curve to R_0 gives α, the temperature coefficient of resistivity. The resistivity, then, at any temperature in question between 0°C and 200°C is given by the equation $R_T=R_0(1+\alpha T)$. In Fig. 3 there were several duplications of orientations so that only six curves are shown. The results show a small, approximately linear, change in α with orientation, varying from 0.00390/°C ($\sigma=\pm 0.00003$/°C) perpendicular to the hexagonal axis to 0.00408/°C parallel thereto. These values compare very favorably with Schmid's results, being on the order of 0.0002/°C lower but showing a similar relative change with orientation. Bridgman's values are considerably higher than those of this study and of Schmid, which fact tends to favor the acceptance of the coefficients obtained in the latter two studies. These values are recorded for comparison in Table III.

TABLE III. Comparison of temperature coefficients of resistivity for high-purity magnesium from 24°C to 200°C.

	$\alpha_\perp$ (per°C)	$\alpha_{\parallel}$ (per°C)
This study	0.00390	0.00408
Schmid[a]	0.00416	0.00427
Bridgman[b]	0.00428	0.00523

[a] See references 3 and 4.
[b] See reference 5.

It was further observed that there was no significant change in resistivity with varying grain size. This is an expected result, since the "wave" scattering effect of the impurity atoms in solid solution would tend to decrease the mean free electron path much more than the presence of relatively widely-spaced grain boundaries in the metal. It is interesting to note that, assuming grain size has no measureable effect and a random grain orientation is obtained, a polycrystalline aggregate should have an electrical conductivity exactly the same as a single crystal having a specified "average" conductivity, this value being based on Eq. (2). This average conductivity value occurs where $\cos^2\phi=0.333$ or $\phi=55°$. Referring to Fig. 2 at $\cos^2\phi=0.333$, it is calculated that the average conductivity value for high-purity magnesium at 24°C is 23.18 (10^4 Mhos/cm³). At the same temperature, a value of 23.20 (10^4 Mhos/cm³) is measured for polycrystalline high-purity magnesium. Thus, excellent agreement is obtained for the single crystal and the polycrystalline specimens, giving further evidence that the effect of grain size on electrical resistivity is negligible.

CONCLUSIONS

1. The electrical resistivity of high-purity magnesium single crystals is dependent on the crystal orientation. At 24°C, the relationship is represented by the equation $\rho(\phi)=4.60-0.75\cos^2\phi$ where ϕ is the angle between the hexagonal axis and the direction of current flow.

2. Magnesium shows rotational symmetry about the hexagonal axis with respect to electrical resistivity.

3. Magnesium single crystals grown from the melt by the described method show a random orientation according to the area of the unit hexagonal triangle on the reference sphere.

4. Grain size has little or no effect on the electrical resistivity of magnesium.

5. The temperature coefficient of resistivity varies with orientation in magnesium single crystals, varying from 0.00390/°C perpendicular to the hexagonal axis to 0.00408/°C parallel to the axis.

JOURNAL OF APPLIED PHYSICS VOLUME 26, NUMBER 4 APRIL, 1955

Cubic to Orthorhombic Diffusionless Phase Change—Experimental and Theoretical Studies of AuCd†

D. S. LIEBERMAN,‡ M. S. WECHSLER,§ AND T. A. READ‡
Columbia University, New York, New York

(Received February 8, 1954)

A theoretical analysis of the cubic to orthorhombic transformation is presented which predicts for a partly transformed crystal, the interface plane, orientation relationships, and macroscopic distortions from a knowledge only of the lattice parameters of the initial and final phases. Arguments are advanced to show that in order to minimize the strain energy associated with the transformation, the interface plane must be one of zero average distortion. This leads directly to considerations of an inhomogeneous product phase. Experimental studies on an AuCd alloy are described and the observed crystallographic features of the transformation compared with values calculated using the theory. The agreement between calculated and observed results for this alloy system as well as others is strong evidence for the theory of diffusionless phase transformations presented.

INTRODUCTION

IN diffusionless phase changes,[1] a crystalline solid transforms from one structure to another by a process in which individual atoms move less than an atomic distance relative to their nearest neighbors. Some of the pure metals, alloys, and nonmetallic systems that undergo a phase change of this kind are lithium, cobalt, zirconium, uranium, iron and iron-base alloys, Cu-Zn, Cu-Al, Cu-Sn, Au-Cd, Li-Mg, In-Tl, NH_4NO_3, $BaTiO_3$, and $KNbO_3$. The present authors have developed a theory[2] of such phase transformations that permits the calculation of the salient crystallographic features of the transformation; *viz.*, the direction cosines of the normal to the interface plane separating the initial and final phases of a partially transformed specimen, the direction and magnitude of the macroscopic distortion accompanying the transformation, and the orientation relationship between the crystal axes in the two phases. The theory postulates that the total transformation distortion is inhomogeneous and that the interface plane is one of zero distortion when averaged over a region large compared to the scale of the inhomogeneities. The only input data needed are the lattice parameters of the initial and final phases and a specification of the type of inhomogeneity. The two types of inhomogeneity that have been considered are a product phase consisting of twin related domains and a single crystal product in which slip has occurred. Wechsler, Lieberman, and Read[3] have shown that when the slip occurs on the twin plane, the calculated crystallographic features are identical with the twinned product case.

This theory was presented in application to the cubic to tetragonal phase change in a recent paper by Wechsler, Lieberman, and Read.[3] The predicted values of the crystallographic features of the transformation were compared with the results reported in the literature for the austenite-martensite reaction in iron-base alloys. In their paper on the cubic to tetragonal transformation in InTl, Burkart and Read[4] calculated the habit plane normal using the theory. Good agreement was found between theory and experiment in both cases, although in the InTl transformation, the strains involved are so small that comparison of the measured and calculated values of the other crystallographic features does not provide a critical test of the theory.

In this paper, the experimental determination of all the crystallographic features of the cubic to orthorhombic transformation in an alloy of AuCd containing 47.5 atomic percent Cd is described and the mathematical theory is applied to this transformation. Arguments are advanced to show that in order to minimize the strain energy associated with the transformation, the interface plane separating the two phases must be one of zero average distortion and that in general the transformation distortion must be inhomogeneous, in this case resulting in twin-related domains. This alloy is particularly well suited for the critical experiment designed to test the hypothesis concerning the interface plane. A single crystal of the high-temperature cubic phase transforms on cooling by the movement of a single interface that divides the specimen into an orthorhombic and a cubic region and is clearly visible because of the dihedral angle formed upon the polished surfaces. An examination of interference fringes in the region of the interface shows that this plane is indeed one of zero average distortion. Experimental evidence is presented

† Submitted as a thesis by David S. Lieberman in partial fulfillment of the requirements for the degree of Doctor of Philosophy, in the Faculty of Pure Science, Columbia University.

‡ Now at the University of Illinois, Urbana, Illinois.

§ Now at the Oak Ridge National Laboratory, Oak Ridge, Tennessee.

[1] The reader is referred to the following comprehensive reviews: J. S. Bowles and C. S. Barrett, *Progress in Metal Physics*, edited by B. Chalmers, (Interscience Publishers, Inc., New York, 1952), Vol. 3, Chap. 1; and M. Cohen *Phase Transformations in Solids*, edited by Smoluchowski, Mayer, and Weyl (John Wiley and Sons, Inc., New York, 1951), Chap. 17.

[2] The ideas upon which this theory is based were first conceived during studies on the gold-cadmium system and on an indium-thallium alloy (which undergoes a cubic to tetragonal transformation). The cubic to orthorhombic and cubic to tetragonal (martensite) transformations were then developed in detail concurrently.

[3] Wechsler, Lieberman, and Read, Trans. Am. Inst. Mining Met. Engrs. **197**, 1503 (1953).

[4] M. S. Burkart and T. A. Read, Trans. Am. Inst. Mining Met. Engrs. **197**, 1516 (1953).

FIG. 1. Partially transformed AuCd specimen with single interface separating cubic (left) and orthorhombic (right) regions. The heater is at extreme left (1.3×).

that confirms the presence of the twin-related orthorhombic regions postulated. The agreement between calculated and observed crystallographic features for this alloy system as well as the others mentioned above is strong evidence in favor of the theory of diffusionless phase transformations presented.

EXPERIMENTAL INVESTIGATION

I. Description of the Transformation in AuCd Single Crystals

When a single crystal of AuCd containing 47.5 atomic percent Cd is cooled below 60°C in a steep temperature gradient, a single interface forms at the low-temperature end of the specimen and moves slowly toward the other end.[5,6] This interface divides the specimen into two regions that form a dihedral angle and thus cause the interface to be clearly visible. The low-temperature phase grows at the expense of the high-temperature phase and if the crystal is cooled sufficiently, the interface will pass off the end and result in a specimen of the low-temperature phase. If the temperature is raised to 75°C, the same interface will move slowly back, transforming the specimen to the same high-temperature crystal as at the beginning of the transformation cycle. The transformation is thus completely reversible and the specimen may be cycled at will from one phase to the other. Furthermore, the interface may be maintained at any convenient position of the specimen by adjusting the power to the heater. A specimen upon which two flat surfaces have been polished is shown partially transformed in Fig. 1.

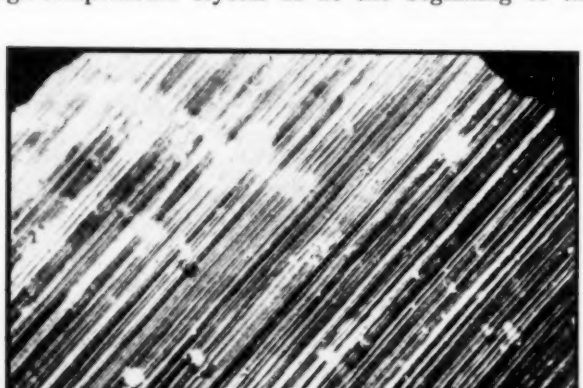

FIG. 2. Microstructure of the orthorhombic phase after single interface transformation. (166×.)

The high-temperature phase of this alloy possesses the CsCl structure,[7,8] The specimens studied were grown from high purity gold and cadmium by a modified Bridgman technique. Back reflection Laue x-ray photograms of the cubic region (to the left of the interface in Fig. 1) showed them to be single crystals of the high-temperature cubic (β_1) phase. The low-temperature (β') phase possesses an orthorhombic unit cell but it is not a single crystal after transformation as evidenced by x-ray photograms of the low-temperature phase (to the right of the interface in Fig. 1).

The specimen was electropolished in the high-temperature phase, cooled through the transformation temperature, and studied metallographically. Figure 2 shows the microstructure as revealed under polarized light at 166×. A stereographic analysis of the markings on two surfaces was made and it was found that these markings determined planes whose unit normal **t** had the direction cosines

$$\mathbf{t}=\begin{pmatrix}0.020\\0.704\\-0.710\end{pmatrix}_{\beta_1} \qquad (1)$$

when expressed in the cubic axis system. By x-ray analysis, Chang[9] has determined the low temperature phase to consist of twin-related orthorhombic domains with a twin plane whose normal agrees with (1) to within experimental error. The observation that the orthorhombic structure consists of twin-related domains demonstrates that the transformation results in an inhomogeneous product phase.

It was observed that the β_1 and β' regions seemed to fit perfectly at the interface. High magnification photographs and interference fringe patterns of the region of the interface revealed that if there is any distortion, it is confined to a region within 10^{-2} mm at the interface. The interference studies were made with a partially silvered optical flat and monochromatic light from a sodium arc which formed fringe systems with the flat surfaces on the high and low temperature phases. Thus it can be concluded that the interface plane is one of zero distortion when averaged over a region that contains many of the twin-related low-temperature domains. These two important observations, *viz.*, that the product phase is inhomogeneous and that the interface plane is one of zero average distortion are intimately related. This is demonstrated below where it is shown

[5] L. C. Chang and T. A. Read, Trans. Am. Inst. Mining Met. Engrs. **191**, 47 (1951).
[6] L. C. Chang, J. Appl. Phys. **23**, 725 (1952).
[7] A. Olander, Z. Krist. **83**, 145–148 (1932).
[8] A. Bystrom and K. E. Almin, Acta Chem. Scand. **1**, 76–89 (1947).
[9] Private communication.

how the mathematical formulation of these physical concepts forms the basis of the theoretical analysis.

II. Determination of the Crystallographic Features of the Transformation

The polished specimen was placed with the heater in a double-circle optical goniometer which could be read to one minute of arc. The power to the heater was adjusted so that part of the crystal transformed to the cubic phase and the interface became fixed at a convenient position, as in Fig. 1. The directions of the normals to the two cubic and two orthorhombic surfaces were obtained relative to axes fixed with respect to the external surfaces of the specimen as shown in Fig. 3.

The system of heater and crystal with its fixed interface was then positioned on a metallograph and the orientation of the interface plane determined relative to the specimen axis system from the traces of the interface in the two polished surfaces in the high temperature cubic region. A back reflection Laue x-ray photogram was taken perpendicular to one of the surfaces of the cubic phase. The normal to this surface

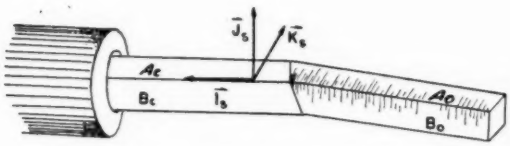

FIG. 3. Surfaces A_c and B_c in the cubic phase transform to A_0 and B_0 in the orthorhombic. The "specimen axis system" is chosen so that the unit vector $\mathbf{i}_s$ coincides with the A_cB_c edge, $\mathbf{j}_s$ coincides with the normal to surface A_c, and $\mathbf{k}_s$ is mutually perpendicular to $\mathbf{i}_s$ and $\mathbf{j}_s$.

was one of the axes of the specimen axis system, and a stereogram was plotted employing this surface as the plane of projection (Fig. 4). The cubic crystal axes were then plotted on the same stereogram from an analysis of the x-ray photogram. In this way, the orientation of the interface was obtained stereographically relative to both the crystal axis system of the cubic phase and the specimen axis system. The direction cosines of the normal to the interface plane relative the crystal axes in the cubic phase were

$$\mathbf{n}=\begin{pmatrix}0.696\\-0.686\\0.213\end{pmatrix}_{\beta_1}. \tag{2}$$

A vector that represents the direction of shear in the specimen was determined by analysis of the data obtained with the optical goniometer. This can be seen most easily by referring to Figs. 3 and 5(a). $\mathbf{C}_c$ is a vector in the direction of the A_cB_c edge (before transformation) and $\mathbf{C}_0$ is a vector in the direction of the A_0B_0 edge (after transformation). These vectors are determined from the vector products of the normals to the surfaces. If the magnitudes of these vectors are adjusted so that their projections on the interface plane normal are both

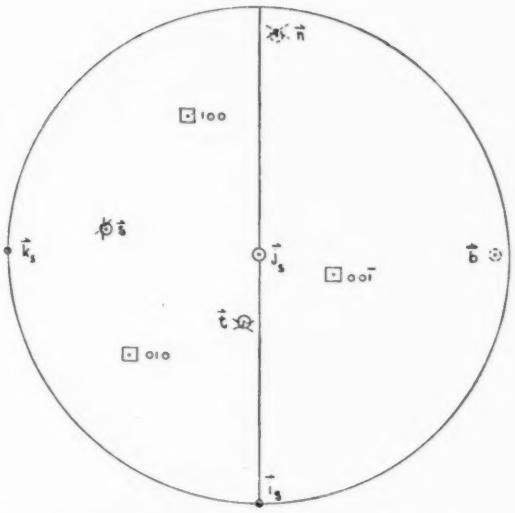

FIG. 4. Stereogram showing the observed (and theoretical) values of interface plane normal, twin plane normal and direction of shear. Legend: ($\mathbf{i}_s$, $\mathbf{j}_s$, $\mathbf{k}_s$)-specimen axis system with $\mathbf{j}_s$ normal to the plane of projection A_c, $\mathbf{i}_s$ along A_cB_c edge and directed toward the heater (see Fig. 3).

⊡—cube edge directions (from x-ray analysis)

b—normal to surface B
n—normal to interface plane
s—shear direction
t—normal to twin plane

} ⊙ size of circle~experimental error
×calculated (theoretical, this paper).

unity, a vector in the direction of shear is given by

$$\mathbf{S}_s=\begin{pmatrix}-0.00690\\0.02294\\0.04525\end{pmatrix}_s, \tag{3}$$

and the magnitude of shear by its absolute value, i.e.,

$$|\mathbf{S}_s|=0.05120. \tag{4}$$

This vector is the same for all before-and-after vector pairs whose end points lie in a plane unit distance from the interface plane.

From an examination of Fig. 5(b), and Eq. (3) it follows directly that the angle of shear is

$$\theta=\tan^{-1}S_s=2°56'. \tag{5}$$

If the shear vector is now normalized to form the unit vector $\mathbf{s}$ and plotted on the stereogram mentioned

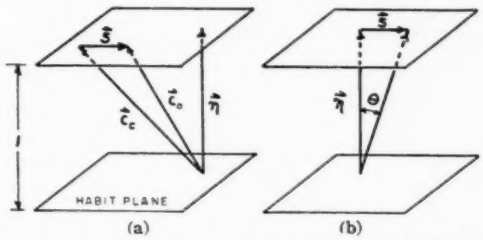

FIG. 5. $\mathbf{C}_c$ and $\mathbf{C}_0$ are vectors in the directions of the A_cB_c and A_0B_0 edges, respectively, and are obtained from the vector products of the unit normals to the polished surfaces. These vectors are intercepted by a plane unit distance from the habit plane. Thus $\mathbf{s}$ is the shear vector and in (b) the angle of shear $\theta=\tan^{-1}|\mathbf{s}|$.

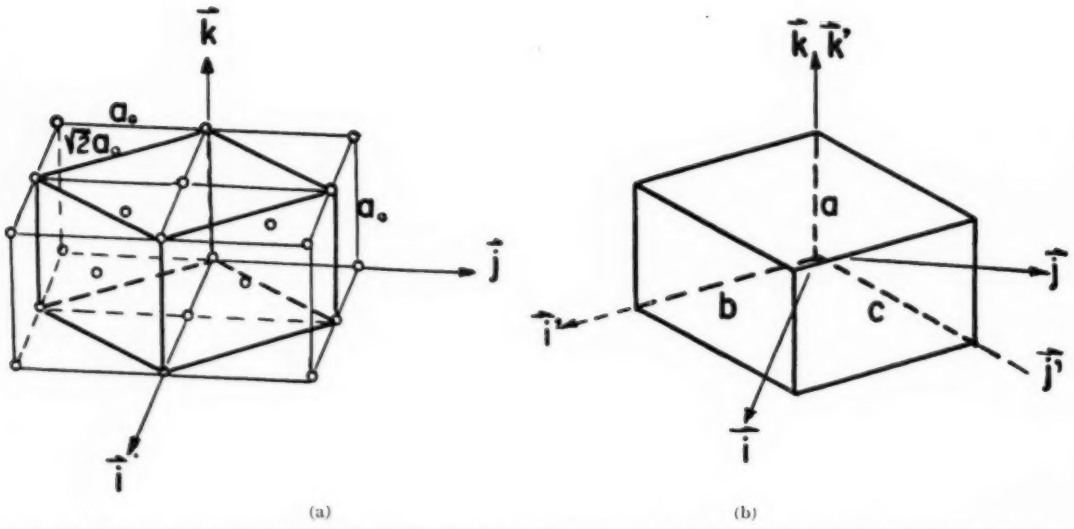

FIG. 6. (a) Untransformed b.c.c. structure in which a f.c.t. cell is delineated. The cubic axis system is (**i**, **j**, **k**). (b) Orthorhombic cell into which the face-centered tetragonal cell is transformed. Principal axes (**i'**, **j'**, **k'**) are obtained by 45° rotation about the **k** axis.

above, its direction cosines relative to the crystal axes are obtained immediately. In this way the direction of shear was found to be

$$\mathbf{s}=\begin{pmatrix}0.660\\0.729\\0.183\end{pmatrix}_{\beta_1}. \tag{6}$$

MATHEMATICAL THEORY

I. Introduction

The mathematical formulation of the theory is based upon the following argument. Provided the lattice parameters permit a solution to exist at all, a plane of zero average distortion which would minimize the strain energy should be present during transformation from one crystal structure to another. This plane is identified with the interface plane. The necessary and sufficient condition for the existence of a plane of zero distortion is that one of the principal distortions be unity, i.e., one of the principal transformation strains vanish. (The proof of this theorem has been given by Wechsler, Lieberman, and Read.[3]) From examination of the lattice parameters of the two phases alone, it can be determined whether or not the product phase must be inhomogenous for this condition to obtain. (Homogeneous distortions which permit a plane of zero distortion are infrequent, e.g., f.c.c. to h.c.p.)

The argument goes as follows. Consider the lattice parameters of the cubic and orthorhombic phases as determined by Chang[10]

$$a_0=3.3165kx,\quad a=3.1476kx,\quad b=4.7549kx,\quad c=4.8546kx\ (\text{all}\ \pm 0.0005kx), \tag{7}$$

where a_0 is the lattice constant of the cubic phase and a, b, and c are the orthorhombic lattice parameters. a differs from a_0 by 5.1 percent while b and c differ from $\sqrt{2}a_0$ by 1.4 percent and 3.5 percent, respectively. Thus the configuration involving the smallest distortion (and hence energetically the most favorable) is shown in Fig. 6 for any (small) region which transforms homogeneously. The matrix which describes this distortion will be diagonal in the (**i'**, **j'**, **k'**) axis system and is written

$$\mathbf{T}_1'=\begin{bmatrix}\dfrac{b}{\sqrt{2}a_0} & 0 & 0\\ 0 & \dfrac{c}{\sqrt{2}a_0} & 0\\ 0 & 0 & \dfrac{a}{a_0}\end{bmatrix}, \tag{8}$$

where $b/\sqrt{2}a_0$, $c/\sqrt{2}a_0$, and a/a_0 are the principal distortions. Substitution of the values of the lattice parameters gives

$$\frac{b}{\sqrt{2}a_0}=1.0138,\quad \frac{c}{\sqrt{2}a_0}=1.0350,\quad \frac{a}{a_0}=0.9491, \tag{9}$$

and since none of these is unity, the transformation distortion must be inhomogeneous if a plane of zero distortion is to exist. The type of inhomogeneity considered here is that of twin-related domains, and it is easy to see how another region of the cubic could transform to an orthorhombic domain which is twin-related to the one previously discussed, as is shown in Figs. 7(a) and (b). These figures show the pure distortion for each region and do not yet take into account the small

[10] L. C. Chang, Acta Cryst. **4**, 320 (1951).

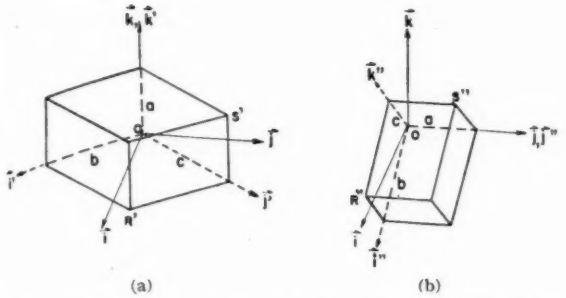

FIG. 7. The pure distortions which (a) region 1 and (b) region 2 undergo during transformation. Unit vectors (**i**, **j**, **k**) are along cube edge directions; (**i'**, **j'**, **k'**) and (**i''**, **j''**, **k''**) are along the principal axes of the pure distortions in regions 1 and 2 respectively.

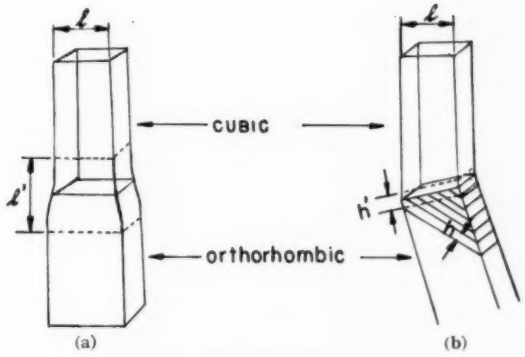

FIG. 8. (a) Homogeneous transformation. (b) Inhomogeneous transformation.

rotations that must be effected to produce coherent twins. Here the distortions are related by a reflection in the cubic face diagonal plane. It will be shown below that the existence of a solution for a plane of zero distortion depends on the values of the lattice parameters.

It can be seen from dimensional and order of magnitude considerations that homogeneous transformation and concomitant distortion at the interface plane involves a larger energy than inhomogeneous transformation with a plane of zero distortion. In Fig. 8(a) is shown the schematic appearance of a square cross section specimen if the transformation were *homogeneous*. The resultant distortion in the region containing the interface is indicated and the strain energy would be of the order

$$W_a = \epsilon^2 Y l^2 l', \tag{10}$$

where Y is Young's modulus, ϵ the strain, l the width of the specimen, and l' the order of l according to Saint Venant's principle. The *inhomogeneous* transformation and the product twin-related domains is shown schematically in Fig. 8(b). Alternate strains at the interface are of opposite sign and thus the average strain vanishes, permitting a plane of zero distortion to exist. The energy now consists of two parts: the energy at the interface and the twin boundary surface energy. Neglecting angular dependence, the energy is now of the form

$$W_b = \epsilon^2 Y l^2 h' + \gamma \frac{l}{h}, \tag{11}$$

where h' is of order h and γ is the twin boundary surface energy. Letting $h' = h$ and differentiating W_b with respect to h yields the result that W_b will be a minimum when the interface strain energy is equal to the twin boundary energy and hence W_b can be written

$$W = 2\epsilon^2 Y l^2 h. \tag{12}$$

Since $l \sim 3$ mm and $h \sim 5\ 10^{-3}$ mm, inhomogeneous transformation with a plane of zero average distortion is energetically the more favorable. Below it will be shown how, from a knowledge of only the lattice parameters of the two phases, the theory permits the calculation of the orientation of the twin plane in addition to the orientation of the interface plane, the magnitude and direction of shear, and the orientation relationships.

II. Mathematical Description of the Transformation Distortion

The pure distortions associated with alternate parallel-sided regions are illustrated in Fig. 7.[11] These distortions are represented by matrices

$$\mathbf{T}_1' = \begin{pmatrix} \frac{b}{\sqrt{2}a_0} & 0 & 0 \\ 0 & \frac{c}{\sqrt{2}a_0} & 0 \\ 0 & 0 & \frac{a}{a_0} \end{pmatrix},$$

and

$$\mathbf{T}_1'' = \begin{pmatrix} \frac{b}{\sqrt{2}a_0} & 0 & 0 \\ 0 & \frac{a}{a_0} & 0 \\ 0 & 0 & \frac{c}{\sqrt{2}a_0} \end{pmatrix}, \tag{13}$$

where the superscripts refer to the reference axes with respect to which the matrices are expressed. Transformation of these matrices to axes aligned along the cube edge directions (**i**, **j**, **k**) of the high temperature

[11] There are other crystallographically equivalent choices of pure distortions, each of which corresponds to a solution. Other choices similar to the choice of the pure distortion enter the analysis; these will be pointed out at appropriate points in the development. The question of multiplicity is treated in more detail in a later section.

(cubic) phase by similarity transformation yields

$$\mathbf{T}_1=\begin{pmatrix} \frac{\sqrt{2}(b+c)}{4a_0} & \frac{\sqrt{2}(-b+c)}{4a_0} & 0 \\ \frac{\sqrt{2}(-b+c)}{4a_0} & \frac{\sqrt{2}(b+c)}{4a_0} & 0 \\ 0 & 0 & \frac{a}{a_0} \end{pmatrix}, \tag{14}$$

and

$$\mathbf{T}_2=\begin{pmatrix} \frac{\sqrt{2}(b+c)}{4a_0} & 0 & \frac{\sqrt{2}(-b+c)}{4a_0} \\ 0 & \frac{a}{a_0} & 0 \\ \frac{\sqrt{2}(-b+c)}{4a_0} & 0 & \frac{\sqrt{2}(b+c)}{4a_0} \end{pmatrix}. \tag{15}$$

The substitution of the values of the lattice parameters (7) in (14) and (15) gives

$$\mathbf{T}_1=\begin{pmatrix} 1.024 & 0.01063 & 0 \\ 0.01063 & 1.024 & 0 \\ 0 & 0 & 0.9491 \end{pmatrix}, \tag{16}$$

and

$$\mathbf{T}_2=\begin{pmatrix} 1.024 & 0 & 0.01063 \\ 0 & 0.9491 & 0 \\ 0.01063 & 0 & 1.024 \end{pmatrix}. \tag{17}$$

However, the distortions to which regions 1 and 2 are subjected are in general *impure*. Therefore, $\mathbf{M}_1$ and $\mathbf{M}_2$, the matrices which describe what happens to vectors in the two regions as a result of transformation, can be written[12]

$$\mathbf{M}_1=\mathbf{\Phi}_1\mathbf{T}_1 \quad \text{and} \quad \mathbf{M}_2=\mathbf{\Phi}_2\mathbf{T}_2. \tag{18}$$

$\mathbf{\Phi}_1$ and $\mathbf{\Phi}_2$ describe the rotations of the principal axes of the pure distortions in regions 1 and 2 relative to an axis system fixed in the untransformed cubic.

A section through the low temperature orthorhombic structure is shown in Fig. 9. A volume of the cubic phase has transformed to a banded twin-related orthorhombic structure of relative amounts x of twin 2 and $(1-x)$ of twin 1. A scratch $\mathbf{r}=\mathbf{OV}$ that was originally a straight line in the cubic phase becomes the broken line $OA'B'C'\cdots U'V'$. However, since the distortion *averaged* over the twin regions is to be considered, it is sufficient to treat the vector sum $\mathbf{OV}'=\mathbf{r}'=\mathbf{OA}'+\mathbf{A}'\mathbf{B}'+\mathbf{B}'\mathbf{C}'+\cdots+\mathbf{U}'\mathbf{V}'$ as describing the transformed position of the vector $\mathbf{r}$. Thus

$$\mathbf{r}'=(1-x)\mathbf{M}_1\mathbf{r}+x\mathbf{M}_2\mathbf{r}=[(1-x)\mathbf{M}_1+x\mathbf{M}_2]\mathbf{r}, \tag{19}$$

or

$$\mathbf{r}'=\mathbf{E}\mathbf{r}, \tag{20}$$

where

$$\mathbf{E}=(1-x)\mathbf{M}_1+x\mathbf{M}_2. \tag{21}$$

$\mathbf{E}$ is called the "total distortion matrix." Equation (20) states that if $\mathbf{r}$ is a vector in the cubic phase, then as a result of the transformation $\mathbf{r}$ goes to $\mathbf{r}'=\mathbf{E}\mathbf{r}$ where $\mathbf{r}$ and $\mathbf{r}'$ are expressed with respect to the cube edge directions in the as yet untransformed cubic phase. From Eq. (19)

$$\mathbf{E}=(1-x)\mathbf{\Phi}_1\mathbf{T}_1+x\mathbf{\Phi}_2\mathbf{T}_2. \tag{22}$$

$\mathbf{\Phi}_1$ and $\mathbf{\Phi}_2$ cannot be determined from the development thus far, but the relative rotation $\mathbf{\Phi}$ can be obtained. This is done by imposing the condition that vectors $\mathbf{OR}'$ and $\mathbf{OS}'$ must coincide with $\mathbf{OR}''$ and $\mathbf{OS}''$, respectively, after transformation to insure coherent twins. This means that the relative rotation must bring the plane $R''OS''$ into coincidence with $R'OS'$ (Fig. 7). Both of these planes were the $(011)_{\beta_1}$ before transformation. The normals to these planes are easily determined from the vector product of two vectors in each plane (such as $\mathbf{OR}'$ and $\mathbf{OS}'$). The axis of rotation is obtained from the vector product of the two plane normals and the magnitude of the rotation from their scalar product. In this way the nonian form of the rotation matrix $\mathbf{\Phi}$ is calculated to be:

$$\mathbf{\Phi}=\begin{pmatrix} 0.9999 & -0.01034 & 0.009585 \\ 0.009585 & 0.9970 & 0.07618 \\ -0.01034 & -0.07608 & 0.9970 \end{pmatrix}, \tag{23}$$

since $\mathbf{\Phi}$ is the relative rotation between $\mathbf{\Phi}_1$ and $\mathbf{\Phi}_2$, and thus (22) may be written as

$$\mathbf{E}=\mathbf{\Phi}_1[(1-x)\mathbf{T}_1+x\mathbf{\Phi}\mathbf{T}_2]. \tag{24}$$

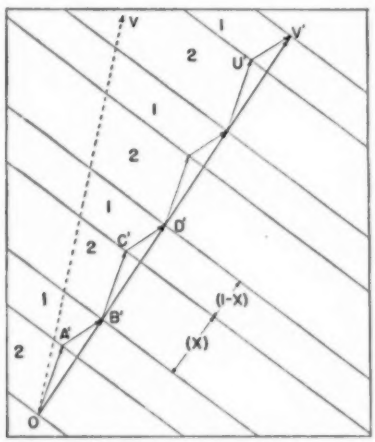

FIG. 9. Section through the orthorhombic region, showing the banded structure of relative amounts x of twin 2 and $(1-x)$ of twin 1. The broken line $OA'B'C'D'\cdots U'V'$ was the straight line OV in the original cubic crystal.

[12] Boldface capital Greek letters are used to denote rotation matrices.

Then $\mathbf{E}$ may be written as

$$\mathbf{E}=\mathbf{\Phi}_1\mathbf{F}, \tag{25}$$

where

$$\mathbf{F}=(1-x)\mathbf{T}_1+x\mathbf{\Phi}\mathbf{T}_2. \tag{26}$$

The substitution of (16), (17), and (23) in (26) gives

$$\mathbf{F}=\begin{pmatrix}1.024 & 0.01063-0.02045x & 0.02045x\\ 0.01063 & 1.024 & -0.07814x & 0.07814x\\ 0 & -0.07221x & 0.9491+0.07221x\end{pmatrix}. \tag{27}$$

III. The Relative Amounts of the Twins

The condition that the habit plane be one of zero average distortion can be satisfied for only certain values of x. These values of x, and subsequently all the crystallographic features of the transformation, can be calculated by using the general properties of matrices. $\mathbf{F}$ is a nonsymmetric matrix and thus may be expressed as the product of a rotation matrix $\mathbf{\Psi}$ and a symmetric matrix $\mathbf{F}_s$

$$\mathbf{F}=\mathbf{\Psi}\mathbf{F}_s. \tag{28}$$

Then $\mathbf{E}$ becomes

$$\mathbf{E}=\mathbf{\Phi}_1\mathbf{\Psi}\mathbf{F}_s. \tag{29}$$

Futhermore, a rotation matrix $\mathbf{\Gamma}$ can be found which diagonalizes the symmetric $\mathbf{F}_s$, so that

$$\mathbf{F}_s=\mathbf{\Gamma}\mathbf{F}_d\mathbf{\Gamma}^*,$$

where $\mathbf{F}_d$ is diagonal and $\mathbf{\Gamma}^*$ is, in this paper, the transpose of $\mathbf{\Gamma}$. Thus

$$\mathbf{E}=\mathbf{\Phi}_1\mathbf{\Psi}\mathbf{\Gamma}\mathbf{F}_d\mathbf{\Gamma}^*. \tag{30}$$

All the matrices in Eq. (30) except $\mathbf{F}_d$ are rotation matrices and $\mathbf{F}_d$ may be written

$$\mathbf{F}_d=\begin{pmatrix}\lambda_1 & 0 & 0\\ 0 & \lambda_2 & 0\\ 0 & 0 & \lambda_3\end{pmatrix}. \tag{31}$$

At this stage of the analysis, the matrix $\mathbf{F}$ is a function of x. However, x can be determined by using the theorem mentioned earlier and proved in reference (3) *viz.*, the necessary and sufficient condition that a plane of zero distortion exist is that one of the principal distortions be unity, i.e., one of the principal strains vanish. This means that when the proper value of x is inserted in the expression for $\mathbf{F}$ (or $\mathbf{E}$), one of the principal distortions will be unity, i.e., one of the λ's in Eq. (31), say λ_3, is equal to unity. Thus

$$\mathbf{F}_d=\begin{pmatrix}\lambda_1 & 0 & 0\\ 0 & \lambda_2 & 0\\ 0 & 0 & 1\end{pmatrix}. \tag{32}$$

In the $(\mathbf{i}_d, \mathbf{j}_d, \mathbf{k}_d)$ axis system in which the distortion is diagonal, Eq. (20) becomes

$$\mathbf{r}_d'=\mathbf{F}_d\mathbf{r}_d, \tag{33}$$

where

$$\mathbf{r}_d=\begin{pmatrix}x_d\\ y_d\\ z_d\end{pmatrix}. \tag{34}$$

Consider those vectors such that

$$\mathbf{r}_d^2=\mathbf{r}_d'^2=(\mathbf{F}_d\mathbf{r}_d)^2. \tag{35}$$

All vectors $\mathbf{r}_d$ which satisfy Eq. (35) suffer no change in length during transformation. The substitution of Eqs. (32) and (34) in Eq. (35) yields

$$\lambda_1x_d^2+\lambda_2y_d^2+z_d^2=x_d^2+y_d^2+z_d^2, \tag{36}$$

and thus

$$(\lambda_1^2-1)x_d^2+(\lambda_2^2-1)y_d^2=0, \tag{37}$$

which is an equation for two planes. The unit matrix is subtracted from $\mathbf{F}_d\mathbf{F}_d^*$ to form the matrix $(\mathbf{F}_d\mathbf{F}_d^*-\mathbf{I})$,

$$\begin{pmatrix}\lambda_1^2 & 0 & 0\\ 0 & \lambda_2^2 & 0\\ 0 & 0 & 1\end{pmatrix}-\begin{pmatrix}1 & 0 & 0\\ 0 & 1 & 0\\ 0 & 0 & 1\end{pmatrix}=\begin{pmatrix}\lambda_1^2-1 & 0 & 0\\ 0 & \lambda_2^2-1 & 0\\ 0 & 0 & 0\end{pmatrix},$$

and it is seen immediately that

$$\det(\mathbf{F}_d\mathbf{F}_d^*-\mathbf{I})=0. \tag{38}$$

Since the determinant of a matrix is invariant under a similarity transformation and $(\mathbf{\Phi}_1\mathbf{\Psi}\mathbf{\Gamma})^*=\mathbf{\Gamma}^*\mathbf{\Psi}^*\mathbf{\Phi}_1^*$, Eq. (38) may be written as

$$\det[\mathbf{\Phi}_1\mathbf{\Psi}\mathbf{\Gamma}(\mathbf{F}_d\mathbf{F}_d^*-\mathbf{I})\mathbf{\Gamma}^*\mathbf{\Psi}^*\mathbf{\Phi}_1^*]=0.$$

If the expression in the square bracket is multiplied out and $\mathbf{\Gamma}\mathbf{\Gamma}^*=\mathbf{I}$ introduced between $\mathbf{F}_d$ and $\mathbf{F}_d$, it becomes

$$\det[(\mathbf{\Phi}_1\mathbf{\Psi}\mathbf{\Gamma}\mathbf{F}_d\mathbf{\Gamma}^*)(\mathbf{\Gamma}\mathbf{F}_d^*\mathbf{\Gamma}^*\mathbf{\Psi}^*\mathbf{\Phi}_1^*)-\mathbf{I}]=0.$$

But from Eq. (30), this is simply

$$\det(\mathbf{E}\mathbf{E}^*-\mathbf{I})=0. \tag{39}$$

By suppressing $\mathbf{\Phi}_1$ and using $\mathbf{\Psi}\mathbf{\Gamma}$ as the transformation matrix, Eq. (38) becomes equivalent to

$$\det(\mathbf{F}\mathbf{F}^*-\mathbf{I})=0, \tag{40}$$

which can be employed immediately to calculate x, whereas Eq. (39) cannot since $\mathbf{\Phi}_1$ is as yet unknown.

The substitution of Eq. (27) into Eq. (40) yields a quadratic equation[13] in x with solutions

$$x=0.7161 \quad \text{and} \quad x=0.2839. \tag{41}$$

The larger value of x will be used in the calculations; the smaller value gives a crystallographically equivalent

[13] The solution up to and including the matrix $\mathbf{F}$ (Eq. 27) was obtained algebraically in terms of the lattice parameters of the two phases (a_0, a, b, and c). Hence the solution to that point is applicable to any cubic to twinned orthorhombic transformation. When $\mathbf{F}(a_0, a, b, c, x)$ was substituted in Eq. (40), it yielded a polynomial in x in which the coefficients of all powers of x higher than the second vanished identically. The roots of the resulting quadratic equation were each positive and less than unity, and their sum unity. This is to be expected on physical grounds. Numerical substitution was made immediately in this presentation because the algebraic expressions are so unwieldly.

solution. The substitution of x into Eq. (27) gives

$$\mathbf{F}=\begin{pmatrix}1.024 & -0.004013 & 0.01464\\ 0.01063 & 0.9685 & 0.05596\\ 0 & -0.05171 & 1.001\end{pmatrix}.$$

IV. The Interface Plane

The interface plane, which is the plane of zero average distortion, can be calculated in the $(\mathbf{i}_d, \mathbf{j}_d, \mathbf{k}_d)$ system if the values of λ_1 and λ_2 are inserted in Eq. (37). The direction cosines of the interface plane normal relative to the cubic axis system can then be determined by employing the rotation matrix Γ.

All the elements of $\mathbf{F}$ can be recovered by matrix manipulation. Thus since

$$\mathbf{F}^*\mathbf{F}=(\Gamma\mathbf{F}_d{}^*\Gamma^*\Psi^*)(\Psi\Gamma\mathbf{F}_d\Gamma^*)=\Gamma(\mathbf{F}_d{}^*\mathbf{F}_d)\Gamma^*,$$

Γ and $\mathbf{F}_d$ may be obtained by diagonalizing $\mathbf{FF}^*$ and extracting the square root. Similarly,

$$\mathbf{FF}^*=(\Psi\Gamma\mathbf{F}_d\Gamma^*)(\Gamma\mathbf{F}_d{}^*\Gamma^*\Psi^*)=(\Psi\Gamma)(\mathbf{F}_d\mathbf{F}_d{}^*)(\Psi\Gamma)^*,$$

and thus Ψ may be recovered by diagonalizing $\mathbf{FF}^*$ and using the matrix Γ found above. In this way it is found that

$$\mathbf{F}_d=\begin{pmatrix}1.027 & 0 & 0\\ 0 & 0.9696 & 0\\ 0 & 0 & 1\end{pmatrix}. \tag{42}$$

The substitution of the eigenvalues of $\mathbf{F}_d$ Eq. (42) in Eq. (37) yields

$$x_d/y_d=\pm 1.044, \tag{43}$$

for the equation of the interface planes of zero distortion in the $(\mathbf{i}_d, \mathbf{j}_d, \mathbf{k}_d)$ axis system. The positive sign gives for the direction cosines of normal in this axis system

$$\mathbf{n}_d=1/[1+(1.044)^2]^{\frac{1}{2}}\begin{pmatrix}1\\ -1.044\\ 0\end{pmatrix}=\begin{pmatrix}0.6916\\ -0.7222\\ 0\end{pmatrix}. \tag{44}$$

(Choice of the negative square root yields another solution, which will be discussed below.) Finally the normal to the interface plane in the cubic axis system is given by

$$\mathbf{n}=\Gamma\mathbf{n}_d=\begin{pmatrix}0.6968\\ -0.6810\\ 0.2250\end{pmatrix}_{\beta_1}. \tag{45}$$

Thus the interface plane has been calculated from a knowledge only of the observed lattice parameters by applying the criterion of zero average distortion to a banded twin-related orthorhombic structure. This treatment gives the result that the interface plane is irrational.

V. Magnitude and Direction of Shear

As far as macroscopic changes in shape are concerned, the total transformation is equivalent to a simple shear on the interface plane plus a contraction in the direction of the interface plane normal, as shown in Fig. 10. It follows then that in the $(\mathbf{i}_d, \mathbf{j}_d, \mathbf{k}_d)$ axis system the direction of shear is given by

$$\mathbf{s}_d=\mathbf{k}_d\times\mathbf{n}_d=\begin{pmatrix}0.7222\\ 0.6916\\ 0\end{pmatrix}, \tag{46}$$

since there is no distortion in the $\mathbf{k}_d$ direction.

Thus in the cubic axis system, a unit vector in the direction of shear is

$$\mathbf{s}=\Gamma\mathbf{s}_d=\begin{pmatrix}0.6510\\ 0.7322\\ 0.2001\end{pmatrix}_{\beta_1}. \tag{47}$$

The angle of shear is defined as the angle between vector $\mathbf{n}$ normal to the interface plane (plane of shear) and this vector after distortion. It is thus the angle between $\mathbf{n}$ and $\mathbf{En}$. To calculate $\mathbf{E}$, Φ_1 must first be determined. When expressed in the cubic axis system Eq. (35) becomes

$$(\mathbf{Fr})^2=\mathbf{r}^2.$$

This insures that all vectors in the interface plane are unchanged in magnitude by the distortion but does not prevent these vectors from being rotated. Φ_1 is the rotation matrix such that

$$\mathbf{Er}=\Phi_1\mathbf{Fr}=\mathbf{r}$$

i.e., such that all vectors $\mathbf{r}$ lying in the interface plane will suffer *neither change in magnitude nor rotation* when operated on by the total distortion matrix $\mathbf{E}$.

If $\mathbf{g}$ is any vector noncollinear with $\mathbf{n}$, then

$$\mathbf{r}=\mathbf{g}\times\mathbf{n}$$

is a vector lying in the interface plane. In particular, two such vectors are

$$\mathbf{q}_1=\mathbf{i}\times\mathbf{n}=\begin{pmatrix}0\\ -0.2250\\ -0.6810\end{pmatrix}_{\beta_1}$$

and

$$\mathbf{p}_1=\mathbf{j}\times\mathbf{n}=\begin{pmatrix}0.2250\\ 0\\ -0.6968\end{pmatrix}_{\beta_1}. \tag{48}$$

The operation of $\mathbf{F}$ on $\mathbf{q}_1$ and $\mathbf{p}_1$ produces two vectors $\mathbf{q}_2$ and $\mathbf{p}_2$. These together with $\mathbf{q}_1$ and $\mathbf{p}_1$ are sufficient to determine the direction cosines of the axis of rotation and the magnitude of the rotation and hence the matrix Φ_1. This is done most easily by employing Euler's theorem in the following form:

$$\frac{(\mathbf{q}_1-\mathbf{q}_2)\times(\mathbf{p}_1-\mathbf{p}_2)}{(\mathbf{q}_1-\mathbf{q}_2)\cdot(\mathbf{p}_1+\mathbf{p}_2)}=\tan\left(\frac{\varphi_1}{2}\right)\mathbf{u}_0, \tag{49}$$

where φ_1 is the magnitude of the rotation and $\mathbf{u}_0$ is a unit vector along the axis of rotation. In this way Φ_1 is calculated and the total distortion matrix $\mathbf{E}$ becomes

$$\mathbf{E}=\begin{pmatrix}1.0240 & -0.02343 & 0.007738\\ 0.03117 & 0.9695 & 0.01006\\ 0.007339 & -0.007172 & 1.002\end{pmatrix}, \tag{50}$$

which is nonsymmetric and therefore represents an impure distortion. A vector in the direction **n** will thus be deformed during transformation, and when normalized this new vector is

$$\mathbf{n}'=\mathbf{En}/|\mathbf{En}|=\begin{pmatrix}0.7331\\-0.6379\\0.2361\end{pmatrix}_{\beta_1}. \qquad (51)$$

Thus θ, the angle of shear, is

$$\theta=\cos^{-1}(\mathbf{n}\cdot\mathbf{n}')=3°17', \qquad (52)$$

n, **n**′, and θ are shown schematically in Fig. 10.

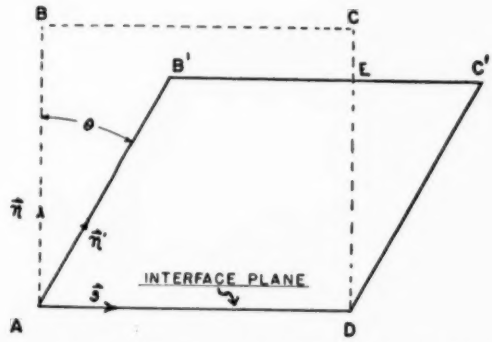

FIG. 10. Schematic drawing of the distortion **E** viewed as a simple shear of $\theta°$ on the interface plane plus a contraction perpendicular to the interface plane. A unit vector **n** perpendicular to the interface plane is transformed to a vector in the direction of **n**′; **s** is a unit vector in the direction of shear. V is the volume ratio of the initial and final phases and is equal to $ED/CD=\det \mathbf{E}=abc/2a_0^3=0.9959$. The volume change $1-V=0.0041$ has been ignored in Fig. 5 and in the treatment of the data presented in the paper which resulted in the experimental value of $\theta=\tan^{-1}0.05120=2°56'$—Eqs. (4) and (5). When the effect of the volume change is included, $\theta=\tan^{-1}0.05141$, a change of less than 1 minute of arc.

VI. The Twin Plane

The plane in the cubic phase which becomes the twin plane after transformation is $(0\bar{1}1)\beta_1$. Two directions in this plane are

$$\mathbf{v}_1=\begin{pmatrix}1\\0\\0\end{pmatrix} \quad \text{and} \quad \mathbf{v}_2=\begin{pmatrix}0\\\frac{1}{\sqrt{2}}\\\frac{1}{\sqrt{2}}\end{pmatrix}$$

The normal to the twin plane is then given by the cross-product of the transformed positions of these vectors, i.e.,

$$\mathbf{t}=\mathbf{v}_1'\times\mathbf{v}_2',$$

where

$$\mathbf{v}_1'=\mathbf{E}\mathbf{v}_1 \quad \text{and} \quad \mathbf{v}_2'=\mathbf{E}\mathbf{v}_2.$$

Upon substitution of equation (50), it is found that the direction of the normal to the twin plane relative to the cubic crystal axis system is given by:

$$\mathbf{t}=\begin{pmatrix}0.01666\\-0.7124\\0.7015\end{pmatrix}_{\beta_1}. \qquad (53)$$

VII. Orientation Relationships

The orientation relationships between the cubic phase and each of the orthorhombic twins depend upon the distortions to which each twin region is subjected separately, i.e., upon

$$\mathbf{M}_1=\mathbf{\Phi}_1\mathbf{T}_1,$$

and

$$\mathbf{M}_2=\mathbf{\Phi}_2\mathbf{T}_2=\mathbf{\Phi}_1\mathbf{\Phi}\mathbf{T}_2.$$

The directions of the orthorhombic axes for each twin are determined by applying $\mathbf{M}_1$ and $\mathbf{M}_2$ to the appropriate edges and face diagonal directions in the cubic (see Fig. 7). Six equations result (three from each twin) from which two transformation matrices can be formed. Thus, given a vector **v** expressed with respect to axes aligned along the cube edge directions of the cubic phase, this same vector expressed with respect to orthorhombic axes in the two twin regions is given by

$$\mathbf{v}_1=\mathbf{\Theta}\mathbf{v}=\begin{pmatrix}\theta_{11}&\theta_{12}&\theta_{13}\\\theta_{21}&\theta_{22}&\theta_{23}\\\theta_{31}&\theta_{32}&\theta_{33}\end{pmatrix}\mathbf{v} \quad \text{for region 1,} \qquad (54)$$

and

$$\mathbf{v}_2=\mathbf{\Omega}\mathbf{v}=\begin{pmatrix}\omega_{11}&\omega_{12}&\omega_{13}\\\omega_{21}&\omega_{22}&\omega_{23}\\\omega_{31}&\omega_{32}&\omega_{33}\end{pmatrix}\mathbf{v} \quad \text{for region 2.} \qquad (55)$$

The rotation matrices $\mathbf{\Theta}$ and $\mathbf{\Omega}$ define the orientation relationships and are calculated to be

$$\mathbf{\Theta}=\begin{pmatrix}0.7213&-0.6920&-0.02777\\0.6926&0.7204&0.03722\\-0.005755&-0.04608&0.9989\end{pmatrix} \qquad (56)$$

and

$$\mathbf{\Omega}=\begin{pmatrix}0.7052&-0.0001548&-0.7090\\-0.03020&0.9991&-0.03025\\0.7084&0.04274&0.7045\end{pmatrix} \qquad (57)$$

For comparison with the experimental results, it is useful to express the orientation relationships in terms of the angles between certain crystallographic planes and directions in the two structures. The conjugate transformation matrices (in this case, $\mathbf{\Theta}^*$ and $\mathbf{\Omega}^*$) are used to transform orthorhomibc planes and directions to the cubic axis system. Thus

$$(100)_{\beta'^1}=\begin{pmatrix}0.7213\\-0.6920\\-0.02777\end{pmatrix}_{\beta_1}$$

is read as "the (100) plane of the orthorhombic twin 1 has the direction cosines

$$\begin{pmatrix}0.7213\\-0.6920\\-0.02777\end{pmatrix}_{\beta_1}$$

when expressed in the untransformed cubic axis system." The angle between the unit vectors

$$\begin{pmatrix} 0.7213 \\ -0.6920 \\ -0.02777 \end{pmatrix}_{\beta_1} \quad \text{and} \quad \begin{pmatrix} 1/\sqrt{2} \\ -1/\sqrt{2} \\ 0 \end{pmatrix}_{\beta_1}$$

is $\cos^{-1}0.9994 = 1°59'$ which is therefore the angle between the normals to $(100)_{\beta'^1}$ and $(1\bar{1}0)_{\beta_1}$. Therefore the orientation relationship for this plane is written as

$$(1\bar{1}0)_{\beta_1} 1°59' \quad \text{from} \quad (100)_{\beta'^1}$$

and similarly for twin 2

$$(10\bar{1})_{\beta_1} 10' \quad \text{from} \quad (100)_{\beta'^2}. \tag{58}$$

The orientation relationship for $\{100\}_{\beta'}$ planes are summarized in Table I(a).

The relationships between important crystallographic *directions* are obtained by a similar analysis. The $\langle 100\rangle_{\beta'}$ directions are the same as the plane normals above. The $[011]_{\beta'^1}$ direction can be written as the unit vector

$$\begin{pmatrix} 0 \\ 0.8391 \\ 0.5440 \end{pmatrix}_{\beta'}$$

by using the lattice parameters of the orthorhombic unit cell. This becomes the unit vector,

$$\begin{pmatrix} 0.5780 \\ 0.5794 \\ 0.5750 \end{pmatrix}_{\beta_1},$$

when expressed in the cubic axis system, and makes an angle of 18 minutes of arc with the vector

$$\begin{pmatrix} 1/\sqrt{3} \\ 1/\sqrt{3} \\ 1/\sqrt{3} \end{pmatrix}_{\beta_1}.$$

Hence the orientation relationship for this direction is written

$$[111]_{\beta_1} 18' \quad \text{from} \quad [011]_{\beta'^1}, \tag{59}$$

and, similarly for twin 2,

$$[111]_{\beta_1} 18' \quad \text{from} \quad [011]_{\beta'^2}.$$

The orientation relationships for $\langle 100\rangle_{\beta'}$ and $\langle 110\rangle_{\beta'}$ directions are listed in Table I(a) and (b), respectively.

TABLE I. Orientation relationships.

(a) $\{100\}_{\beta'}$ planes and directions

Cubic and orthorhombic twin 1	Cubic and orthorhombic twin 2
$(1\bar{1}0)_{\beta_1}$ 1°59′ from $(100)_{\beta'^1}$	$(101)_{\beta_1}$ 10′ from $(100)_{\beta'^2}$
$(10\bar{1})_{\beta_1}$ 2°26′ from $(010)_{\beta'^1}$	$(010)_{\beta_1'}$ 2°27′ from $(010)_{\beta'^2}$
$(001)_{\beta_1}$ 2°40′ from $(001)_{\beta'^1}$	$(101)_{\beta_1}$ 2°27′ from $(001)_{\beta'^2}$

(b) $\langle 110\rangle_{\beta'}$ directions

Cubic and orthorhombic twin 1	Cubic and orthorhombic twin 2
$[111]_{\beta_1}$ 18′ from $[011]_{\beta'^1}$	$[111]_{\beta_1}$ 18′ from $[011]_{\beta'^2}$
$[11\bar{1}]_{\beta_1}$ 4°48′ from $[01\bar{1}]_{\beta'^1}$	$[11\bar{1}]_{\beta_1}$ 2°20′ from $[110]_{\beta'^2}$
$[1\bar{1}1]_{\beta_1}$ 3°24′ from $[101]_{\beta'^1}$	$[1\bar{1}1]_{\beta_1}$ 4°42′ from $[0\bar{1}1]_{\beta'^2}$
$[1\bar{1}\bar{1}]_{\beta_1}$ 2°10′ from $[10\bar{1}]_{\beta'^1}$	$[1\bar{1}\bar{1}]_{\beta_1}$ 2°10′ from $[1\bar{1}0]_{\beta'^2}$
$[100]_{\beta_1}$ 1°49′ from $[110]_{\beta'^1}$	$[100]_{\beta_1}$ 1°49′ from $[101]_{\beta'^2}$
$[0\bar{1}0]_{\beta_1}$ 2°41′ from $[1\bar{1}0]_{\beta'^1}$	$[00\bar{1}]_{\beta_1}$ 1°54′ from $[10\bar{1}]_{\beta'^2}$

VIII. Multiplicity of the Solutions

It can be seen from an examination of Fig. 7a that there are six distinct choices for the pure homogeneous distortion since for each of the three directions of the contraction axis a, the expansions b and c can be interchanged. For each orientation of the distortion in region 1, there are six $\{011\}_{\beta_1}$ planes which reflect this distortion into region 2 and permit regions 1 and 2 to be twin related. However, two of these $\{011\}_{\beta_1}$ planes contain the unique contraction axis a and hence the resulting twins could not produce a plane of zero average distortion. Thus for each choice of the first pure distortion, there are four reflection planes that can result in twin planes which can produce planes of zero average distortion. Since the twinned regions are further distinguishable by the two values of x, the total multiplicity thus far is 24.

In addition, the analysis yields another factor of 2 from the choice of sign in Eq. (43). A particular set (variant) of the crystallographic features has been presented for the choice of the positive sign and the discussion above indicates how the expected multiplicity of 24 for vector quantities (such as the interface plane normal $\mathbf{n}=\begin{pmatrix} h \\ k \\ l \end{pmatrix}$) in structures with cubic symmetry arises. Here it will be shown how the choice of the minus sign results in a different solution for the crystallographic features and thus how this theory predicts the existence of two distinct sets, each consisting of 24 crystallographically equivalent solutions for vector quantities, such as the interface normal.

Choice of the negative sign in Eq. (43) yields for the interface plane in the $(\mathbf{i}_d, \mathbf{j}_d, \mathbf{k}_d)$ axis system

$$\mathbf{n}_d = \begin{pmatrix} 0.6916 \\ 0.7222 \\ 0 \end{pmatrix}. \tag{60}$$

(Solutions for this sign choice will be designated by boldface German.) Since $\boldsymbol{\Gamma}$ does not depend upon the choice of sign, the normal to this interface plane in the cubic axis system is given by

$$\mathbf{n} = \boldsymbol{\Gamma}\mathbf{n}_d = \begin{pmatrix} 0.6202 \\ 0.7610 \\ 0.1907 \end{pmatrix}_{\beta_1}. \tag{61}$$

The magnitude and direction of shear are obtained in the same manner as in section V:

$$\mathbf{s}_d = \mathbf{k}_d \times \mathbf{n}_d = \begin{pmatrix} 0.7222 \\ -0.6916 \\ 0 \end{pmatrix}, \tag{62}$$

and in the cubic axis system

$$\mathfrak{s}=\Gamma\mathfrak{s}_d=\begin{pmatrix}0.7243\\-0.6487\\0.2334\end{pmatrix}_{\beta_1}. \tag{63}$$

The angle of shear gives the same value as in Eq. (53) viz., 3°17′. The twin plane is calculated as in Section VI and is

$$\mathbf{t}=\begin{pmatrix}-0.02315\\-0.7177\\0.6960\end{pmatrix}_{\beta_1}. \tag{64}$$

Discussion of these two distinct solutions for the crystallographic features will be deferred until the next section, where comparison will be made between theory and experiment.

COMPARISON BETWEEN EXPERIMENTAL AND THEORETICAL RESULTS

Before comparing the theoretical calculations and experimental results, the order of magnitude of the errors in measurement will first be considered. The shear direction [Eq. (6)] may be given as

$$\mathbf{s}=\begin{pmatrix}0.660\pm0.007\\0.729\pm0.007\\0.183\pm0.01\end{pmatrix}_{\beta_1}$$

since the major contribution[14] to the possible error arises from the uncertainty in crystal orientation ($\sim\pm1°$). The normal to the interface plane [Eq. (2)] is given as

$$\mathbf{n}=\begin{pmatrix}0.696\pm0.012\\-0.686\pm0.012\\0.213\pm0.015\end{pmatrix}_{\beta_1}$$

since, in addition to the uncertainty in crystal orientation, there is the error arising from the two-surface analysis of planes, and hence the total error $\sim\pm2°$. The twin plane normal [Eq. (1)] is given as

$$\mathbf{t}=\begin{pmatrix}0.020\pm0.040\\0.704\pm0.015\\0.710\pm0.015\end{pmatrix}_{\beta_1},$$

since in addition to the presence of the two previous sources of error, there is another difficulty due to electropolishing. In electropolishing to enable twin markings to be seen, the definitive A_cB_c edge is lost and the surfaces lose their flatness. Hence a larger error is introduced into the analysis of the twin markings making it difficult to accurately assign direction cosines relative to the cubic axis system. The total error will thus be $\sim\pm2.5°$.

In the first place, it can be seen that the experimentally determined twin plane (1) corresponds equally well to both theoretical solutions (53) and (64). Thus there are eight interface planes which correspond to a $(0\bar{1}1)_{\beta_1}$ reflection plane and thus to the same twin plane within experimental error. These fall into two groups of four; one group contains solutions crystallographically equivalent to Eq. (53) and the other those of the type Eq. (64). However, the same ambiguity does not exist for the interface plane normal (and shear direction) as it does for the twin plane normal. The angle between the particular variants Eqs. (45) and (61) is 92.5° and the angle between the closest variants belonging to the *same* $(0\bar{1}1)_{\beta_1}$ reflection plane is 24.8°. (The angle between the closest variants, but belonging to *different* reflection planes is 5.4°.) A similar analysis obtains for the shear direction.

A comparison of the experimental results and the theoretical calculations [e.g. Eqs. (2), (45), and (61) for the interface plane normal and Eqs. (6), (47), and (63) for the shear direction] indicates unequivocally that the first solution describes the crystallographic features of this transformation. No observations on single-interface transformations of AuCd single crystals containing 47.5 atomic percent Cd are known which correspond to the second solution. It would appear that the first solution is energetically more favorable for this type of transformation, although the second solution may play a part in the more complex types of transformation which have not as yet been studied in detail. In what follows, all references to theoretical results will be to the first solution only.

The theoretical results and observations on a typical specimen are collected in Table II. The theoretical values of the habit plane normal, twin plane normal, and direction of shear have also been plotted in Fig. 4 to facilitate a qualitative comparison.

From the table and the figure, the predicted and observed values are seen to agree within experimental

TABLE II. Comparison of experimental and theoretical results.

	Experimental (this paper unless otherwise stated)	Theoretical (this paper)	Discrepancy
Interface plane normal, **n**	$\begin{pmatrix}0.696\\-0.686\\0.213\end{pmatrix}_{\beta_1}$	$\begin{pmatrix}0.6968\\-0.6810\\0.2250\end{pmatrix}_{\beta_1}$	<1.5°
Shear direction, **s**	$\begin{pmatrix}0.660\\0.729\\0.183\end{pmatrix}_{\beta_1}$	$\begin{pmatrix}0.6510\\0.7322\\0.2001\end{pmatrix}_{\beta_1}$	<1.5°
Angle of shear, θ	2.94°	3.28°	0.36°
Twin plane normal, **t**	$\begin{pmatrix}0.020\\0.704\\-0.710\end{pmatrix}_{\beta_1}$	$\begin{pmatrix}-0.01666\\0.7124\\-0.7015\end{pmatrix}_{\beta_1}$	<2.5°
Orientation relationship	$(001)_{\beta_1}$ parallel to $(001)_{\beta'}$	$(001)_{\beta_1}$ 2°40′ from $(001)_{\beta'^1}$ $(010)_{\beta_1}$ 2°27′ from $(010)_{\beta'^2}$	2.5°
	$[111]_{\beta_1}$ parallel to $[011]_{\beta'}$ (Chang and Read[5])	$[111]_{\beta_1}$ 18′ from $[011]_{\beta'^1}$ $[\bar{1}11]_{\beta_1}$ 18′ from $[011]_{\beta'^2}$	0.3°

[14] The precision of measurements with the optical goniometer is (~1′).

error. Both the theoretical and experimental values of the crystallographic features of the transformation are irrational, as they are in the other alloy systems studied. In the two cubic-tetragonal transformations treated by this theory, the agreement with experimental results was equally good. For example, the calculated and observed habit planes differ by $<2°$ in the iron-base systems[3] and by $<1°$ in the In-Tl alloy as reported by Burkart and Read.[4]

CONCLUSIONS

A theory of the cubic to twinned orthorhombic diffusionless phase transformation is presented together with experimental measurements on a gold-cadmium alloy of the interface plane direction, magnitude and direction of shear, twin plane direction, and the orientation relationships. The important elements of the theoretical calculation of these crystallographic features of the transformation are the inhomogeneity of the distortion leading to a twinned product phase and the fact that the interface plane is one of zero average distortion. These calculations are carried out from a knowledge only of the lattice parameters of the initial and final phases and they contain no adjustable parameters. In the AuCd alloy, as in other systems treated by this theory, the irrationality of the interface plane and orientation relationships is inherent in the analysis. The agreement found between calculated results and experimental observations in the AuCd, In-Tl, and iron-base alloys constitutes powerful evidence in favor of the theory of diffusionless phase transformations proposed.

ACKNOWLEDGMENTS

The work was sponsored in part by contract with the U. S. Atomic Energy Commission. The authors wish to thank Dr. L. C. Chang for helpful discussion and Mr. Richard H. Dudley for his assistance in the preparation of the manuscript.

JOURNAL OF APPLIED PHYSICS VOLUME 26, NUMBER 4 APRIL, 1955

On a Nonlinear Transfer System*

I. FLÜGGE-LOTZ AND W. S. WUNCH
Stanford University, Stanford, California
(Received April 23, 1954)

It is shown that a system with discontinuously varying damping and spring coefficients transfers arbitrary inputs well, if the change of the coefficients from one constant value to another is controlled by the deviation between input and output.

1. INTRODUCTION

A TRANSFER system is a mechanical or electrical device which receives at one place an input $y_i(t)$ and is expected to produce at another place an output $y_0(t)$ which is as close as possible to $y_i(t)$.

A simple transfer system may mathematically be described by the equation

$$\bar{a}y_0''+\bar{b}y_0'+\bar{c}y_0=c_iy_i(t). \tag{1}$$

Since c_i is constant and different from zero, the system has only three essential coefficients and may be written

$$ay_0''+by_0'+cy_0=y_i(t). \tag{2}$$

An input with a limited frequency range can be transferred satisfactorily after the transient has died out, if the constants a, b, and c are well chosen. An improved transfer with fewer limitations is possible if the damping coefficient b and the spring coefficient c are not constant, but depend on the deviation $E=y_0-y_i$ (closed loop system).[1–3] With b and c depending on E the differential equation is nonlinear and a mathematical study of the problem becomes difficult. However, if b and c vary discontinuously with E, the differential equation stays linear in intervals; the only trouble is that the length of these intervals is not known in advance and that a step by step integration is tedious and should be avoided when studying the dependency of b and c on E.

2. THE REPRESENTATION OF INPUT AND OUTPUT IN THE PHASE PLANE FOR A SYSTEM WHICH SENSES THE DEVIATION E

With $dy_0/dt=y_0'=\xi_0$ the differential equation of motion becomes

$$\frac{dy_0}{d\xi_0}=\frac{-a\xi_0}{b\xi_0+cy_0-y_i}. \tag{3}$$

* Supported by the Air Research and Development Command and Office of Naval Research under contract.

[1] I. Flügge-Lotz and W. S. Wunch, "Mechanical reproduction of an arbitrary function of time," Stanford University Technical Report No. 19 (Part I), prepared under Contract N6-ONR-251 Task Order 2 for Air Research and Development Command and Office of Naval Research, March 1952.

[2] I. Flügge-Lotz and W. S. Wunch, "The reproduction of an arbitrary function of time (Reducing transfer function dynamic errors by nonlinear components)," Stanford University Technical Report No. 19 (Part II), prepared under Contract N6-ONR-251 Task Order 2 for Air Research and Development Command and Office of Naval Research, September 1952.

[3] W. S. Wunch, "The reproduction of an arbitrary function of time by discontinuous control," Ph.D. thesis, Stanford University, May 1953.

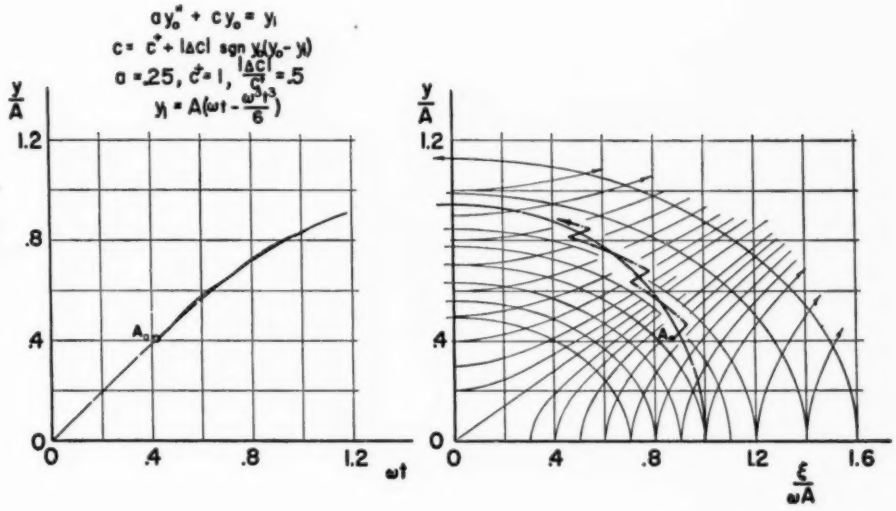

FIG. 1. Transfer with spring control (no damping); displacement *vs* time and velocity.

For a good transfer $y_0 - y_i = E$ should be very small, or if $b\xi_0 \neq 0$, $c \neq 1$, and $|y_0| > 0$ the equation

$$\frac{dy_0}{d\xi_0} = \frac{-a\xi_0}{b\xi_0 + (c-1)y_0} \tag{4}$$

is a good approximation to Eq. (3). The solution of Eq. (4) is given by

$$(y_0\lambda_1 - \xi_0)^{\lambda_1} = L_1(y_0\lambda_2 - \xi_0)^{\lambda_2} \tag{5}$$

with $\lambda_{1,2} = (1/2a)\{-b \pm [b^2 - 4a(c-1)]^{\frac{1}{2}}\}$ and $L_1 = \text{constant}$. Because λ_1 and λ_2 may be real or complex conjugate, the character of the curves represented by Eq. (4) is rather involved. However, there is one simple case:

$$b \equiv 0; \quad \lambda_1 = -\lambda_2 = \left(\frac{1-c}{a}\right)^{\frac{1}{2}}. \tag{6}$$

For this case, Eq. (5) is reduced to

$$\xi_0^2 - (\lambda_1 y_0)^2 = L_2. \tag{7}$$

It is apparent that for $(c-1) > 1$, the approximating curves are ellipses, and for $(c-1) < 1$, hyperbolas. If $c = c^+ + |\Delta c|\ \mathrm{sgn}(y_0 E)$[4] is chosen with $c^+ + |\Delta c| > 1$ and $c^+ - |\Delta c| < 1$, the approximating phase curve consists of portions of ellipses and hyperbolas patched at the points $E = 0$ and $y_0 = 0$. Figure 1 shows a transfer of an input by a system with $b \equiv 0$ and discontinuously varying c. It is necessary to take $(y_0 \cdot E)$ as control function and not E alone in order to guarantee the same way of reproduction for two functions which differ only in sign (see Fig. 2). This means that at $y_0 = 0$ also a switching from hyperbola to ellipse or vice versa takes place.

A system with $b \equiv 0$ yields $dy_0/d\xi_0 \to \infty$ for $y_0 \approx y_i = 0$ and finite ξ_0. A good transfer of an input with finite $dy_i/d\xi_i$ for $y_i = 0$ cannot be expected. Finite, but constant b changes $dy_0/d\xi_0$ from infinite to a finite value $(-a/b)$ for all values $\xi \neq 0$. This, too, cannot be considered a good transfer quality. Detailed investigations show that

$$b = b^+ + |\Delta b|\ \mathrm{sgn}(y_0' E)$$

improves the transfer and that $|\Delta b|/|b^+| > 1$ is desirable. This means that in some intervals energy is dissipated. In others, energy is added to the system.

The approximating curves [the solutions of Eq. (5)] are now more complicated. The ellipses are replaced by curves which spiral around the origin of the phase plane. The hyperbolas of the primitive system with $b \equiv 0$ undergo a kind of deformation. If a network of approximating curves for chosen c^+, Δc, b^+, Δb is designed, the construction of y_0 for any $y_i(\xi_i)$ with the help of an additional diagram $y_i(t)$ is extremely easy. The design of the network is simple because the affine transformation $\bar{y}_0 = ky_0$ and $\bar{\xi}_0 = k\xi_0$ (with $k^2 > 0$) does not change the analytic form of Eq. (5).

The transfer system just described must contain a device to sense the sign of the deviation $E = y_0 - y_i$ at all times. A device sensing the sign of $(y_0 E)$ sets the relay which chooses c and another one sensing $(y_0' E)$

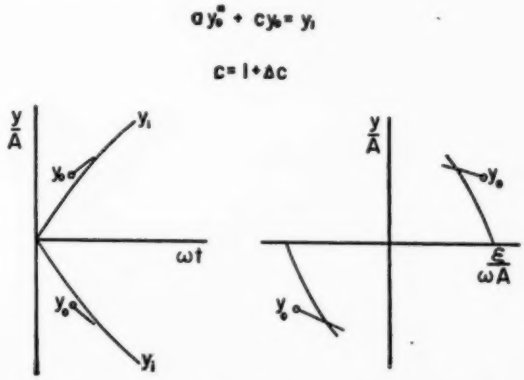

FIG. 2. Transfer with spring control (no damping); displacement *vs* time and velocity.

[4] $\mathrm{sgn} x = x/|x|$; $\mathrm{sgn} x = +1$ for $x > 0$; $\mathrm{sgn} x = -1$ for $x < 0$.

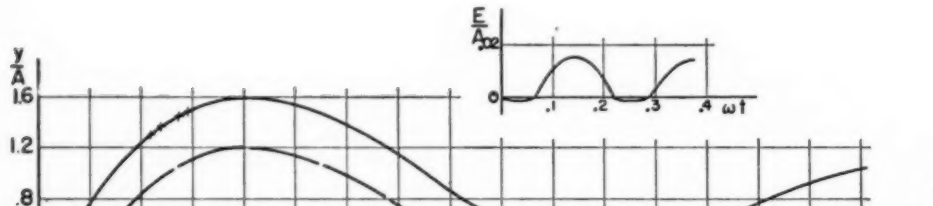

FIG. 3. Arbitrary continuous input functions (displacement plane representation of Fig. 4); displacement *vs* time.

choses b. Switching of the relays occurs at $E=0$; $y_0=0$; $y_0'=0$.

3. QUALITIES OF A TRANSFER SYSTEM BASED UPON SENSING THE SIGN OF THE ERROR E (SYSTEM I)

Two functions are shown in Fig. 3, and their phase diagrams are given in Fig. 4. Several portions of the curves in Fig. 4 are investigated to determine whether a good transfer can be achieved. One finds the lower curve of Figs. 3 and 4 is as easily transferred as the upper until the vicinity of the phase plane origin is reached. Here the deviation of the lower output curve from the input curve becomes too large. By following the output function (dashed line), it is noted that crossing the asymptote in the second quadrant forces the output to cross the ξ axis next, not the y axis as does the input function. Thus the output function must pass through the third and fourth quadrants of the phase plane, thereby generating undesirable deviations. Under similar circumstances, the asymptote crossings in other quadrants by the output function have the same consequences.

A fact akin to this one is the following: once a member of the output function network has been utilized, it may not be used again until the output has at least passed through the next quadrant. But the input function phase curve may cross this particular output network curve several times! The deviations caused by this fact will, in general, not be so large as those produced by the inability of the output function to recross the asymptote in the same quadrant.

Returning to the consideration of the lower curve of Fig. 4, it should be noted that the approximate analysis is no longer valid near the origin of the phase plane where y_0 and y_i have the same order of magnitude as the error. Exact numerical analysis has been used here to show the transfer.

The upper and lower input curves differ only by a constant. Thus the restoring forces in a chosen transfer system are on the average higher for the upper curve and secure a better result. This fact is well known from the simple transfer system with constant coefficients.

Often it is desired to have the output starting with the same value and velocity as the input. A good means for judging the qualities of such a transfer is to look at the phase plane, Fig. 4. Here, by letting the initial velocity of the output approach that of the input, it becomes obvious that identical reproduction may be achieved. However, this would not be the case if the tangent of the spiral type curves of the network would form a steeper angle with the ξ axis than the input curve; in this case finite E values will occur.

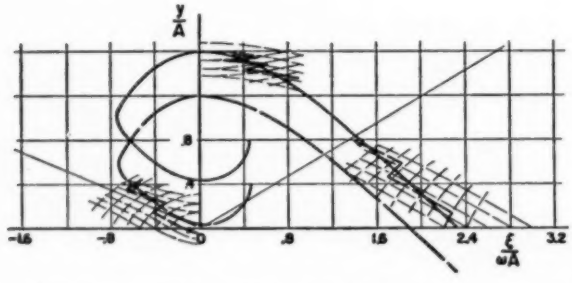

FIG. 4. Arbitrary continuous input functions (phase plane representation of Fig. 3); displacement *vs* velocity.

4. QUALITIES OF A TRANSFER SYSTEM BASED UPON SENSING THE DEVIATION AND ITS RATE OF CHANGE (SYSTEM II)

A. Design Concepts

Although for well-chosen a, b^+, Δb, c^+, and Δc System I can give a good transfer of an arbitrary input, it may still be desirable to diminish deviations between the

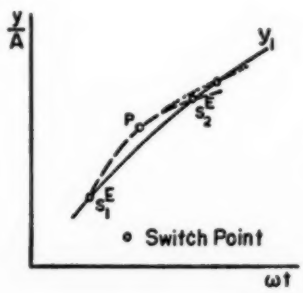

FIG. 5. Methods of deviation reduction, typical displacement functions; displacement *vs* time.

output and input further. Let us again consider the reproduction as performed by System I (see Fig. 5). At switch point S_1^E the deviation $E \equiv y_0 - y_i = 0$ while $y_0' > y_i'$. At point P two other relations exist: $E > 0$ and $y_0' = y_i'$. Subsequent to point P the approach of y_0 to y_i diminishes the error E, the velocity of the output decreases, and y_0 overshoots y_i at S_2^E, where again $E = 0$. A smaller change of the velocity after point P has been passed would be very favorable; the error rate of change $y_0' - y_i'$ should be sensed and used for improving the transfer. The dotted line in Fig. 5 may indicate such an improvement. The switch point indicated by the crossing of the input function and this dotted line will occur later than S_2^E occurred, but on the whole, the transfer will be better. The next problem is to determine how the coefficients b and c must change under the influence of the deviation rate E' in order to give a better transfer than that by System I (which senses the deviation E only).

Detailed studies show the new laws for the coefficients b and c to be:

$$b = b^+ + |\Delta b_1| \operatorname{sgn}[y_0' E] + |\Delta b_2| \operatorname{sgn}[y_0' E'] \qquad (8)$$
$$c = c^+ + |\Delta c_1| \operatorname{sgn}[y_0 E] + |\Delta c_2| \operatorname{sgn}[y_0 E'].$$

TABLE I. Coefficient combinations of System II.

Quadrant 1 ($y_0>0$, $\xi_0>0$):					Quadrant 2 ($y_0>0$, $\xi_0<0$):				
E	E'	a	b	c	E	E'	a	b	c
>0	>0	0.25	0.375	1.5	>0	>0	0.25	−0.125	1.5
>0	<0		0.250	1.4	>0	<0		0.000	1.4
<0	<0		−0.125	0.5	<0	<0		0.375	0.5
<0	>0		0.000	0.6	<0	>0		0.250	0.6

System II contains more relays than System I and senses E' in addition to E.

B. Examples Showing Transfer Improvements

The principal question now is to choose the magnitudes of Δb_2 and Δc_2. It would be desirable to compare results of System II with those of System I as an example. For this reason, the following relations between the different Δb and Δc were assumed:

$$|\Delta b_1|_{II} + |\Delta b_2|_{II} = |\Delta b|_I; \quad |\Delta c_1|_{II} + |\Delta c_2|_{II} = |\Delta c|_I. \qquad (9)$$

The basic values already used for System I were taken:

$$a = 0.25 \quad b^+ = 0.125 \quad c^+ = 1.00. \qquad (10)$$

Additionally, the following four ratios to determine System II were taken:

$$\frac{|\Delta b_1|}{b^+} = 1.5; \quad \frac{|\Delta b_2|}{b^+} = 0.5; \quad \frac{|\Delta c_1|}{c^+} = 0.45; \quad \frac{|\Delta c_2|}{c^+} = 0.05. \qquad (11)$$

The four possible combinations of coefficients available in the first and in the second quadrant of the phase plane are given in Table I. It can be shown that the coefficient combination used in the first quadrant of the phase plane is also used in the third; similarly that in the second, in the fourth.

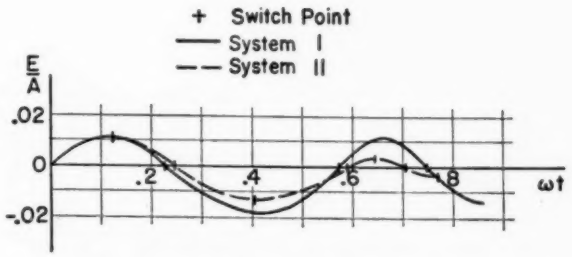

FIG. 6. System I *vs* System II, deviation for $y_i = A\omega t$; displacement *vs* time; $y_0(0) = 0$; $y_0'(0) = 1.2\omega A$.

For the input function $y_i = A\omega t$ the reproduction by System I and System II is compared in Fig. 6. In this diagram only the deviation $E = y_0 - y_i$ is plotted as a function of time. The diagrams in the phase plane and the y,t plane are not given here because a very large scale would be necessary to show the details. It is apparent from this diagram that System II provides a better reproduction than System I.

In Fig. 7 an interesting problem is presented. The input is a constant $y_i = A$. If $y_0(0) = A$ and $y_0'(0) = 0.2\omega A$ are assumed, System I and System II give $|y_0 - y_i|_{\max} < 0.01A$ for $0 < t < \infty$. The output produced by System I shows a deviation E, which is an undamped oscillation; the output produced by System II shows a deviation E, which tends towards zero with increasing t. A primitive transfer system with constant damping and spring coefficient would yield

$$y_{opr} = A_1 e^{\lambda_1 t} + A_2 e^{\lambda_2 t} + A/c.$$

Let us choose the coefficients $a = 0.25$, $b = 0.375$, $c = 1.5$ for this primitive system, which are the coefficients that the transfer with varying coefficients has at the start. Then $(y_{opr} - y_i)_{t\to\infty} = -0.333A$. It is apparent that another choice of coefficients for the primitive transfer system could have provided a better result (for instance $c = 1.0$ would have provided $E_{t\to\infty} \to 0$). However, the problem is not to build a transfer which suits one input extremely well, but to build a system which transfers many inputs equally well.

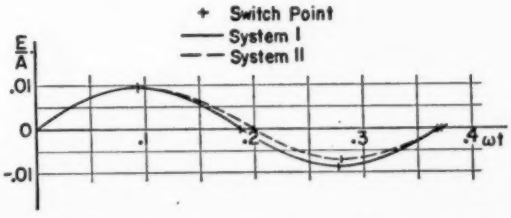

FIG. 7. System I *vs* System II, deviation for $y_i = A$; displacement *vs* time.

TABLE II. System I_1 and System I_2 coefficients.

	Quadrant 1		Quadrant 2	
	$y_0>0$,	$\xi_0>0$	$y_0>0$,	$\xi_0<0$
System I_1	0.375	1.5	−0.125	1.5
	−0.125	0.5	0.375	0.5
System I_2	0.250	1.4	0.000	1.4
	0.000	0.6	0.250	0.6
	b	c	b	c

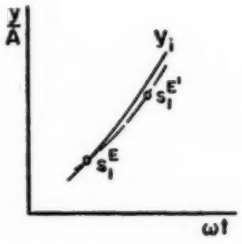

FIG. 8. Marginal reproduction by System II, displacement vs time.

5. THE MARGINAL CASE

System II may be thought to be composed of two Systems I, denoted as Systems I_1 and I_2 (see Table II). This concept of System II allows a closer inspection of its qualities. Because of the greater range of its coefficient values, System I_1 is capable of reproducing functions that System I_2 cannot. Consider now the reproduction of a function that belongs in this category, a "marginal" function, by System II. This function may be described by Fig. 8, which illustrates an exponentially increasing function, $y_i=Ae^{k\omega t}$. Following from the point S_1^E, where the error function and its rate of change become negative, one finds the transfer by System II (System I_1) to be satisfactory until the switch point $S_1^{E'}$ is reached. Whereas the deviation rate would become positive at $S_1^{E'}$ under normal circumstances, thus causing System I_2 coefficients to become effective, one finds these coefficients not capable of producing a positive deviation rate for this marginal function. Thus System II should force the coefficient components of System I_1 to be used. Obviously the mechanism has reached an impasse, for in turn the coefficients of System I_2 are immediately put into action. The true action of System II may be visualized if one considers an infinitesimal time lag to occur between the command and the actual switching. Thus by the continued action of attempting to force System I_2 coefficients to act, the deviation rate is kept zero, and the deviation remains constant. It may be observed that such constant deviations can exist locally without causing undue trouble if they remain within the allowable error limits.

6. DEVIATION ANALYSIS

A good approximation to the maximum deviation in the nth interval is given by the expression

$$E_{\max}=\left|-\frac{1}{2}\frac{(y_{on}'-y_{in}')^2}{y_{on}''-y_{in}''}\right|. \tag{12}$$

The subscript n denotes the initial values for the nth interval. The deviation decreases inversely as the difference $y_{on}''-y_{in}''$ increases. However, y_{on}'' depends upon the constants describing a given system. If the deviation is small, the following substitution may be used for this term:

$$y_{on}''=-\frac{b}{a}y_{on}'-\frac{c-1}{a}y_{on}. \tag{13}$$

Equation (12) gives an idea how to choose a, b^+, c^+, and the Δb and Δc, if some qualities (e.g., frequencies or amplitudes) of the input are known. There is no doubt that small a and large c^+ will be desirable as in the simple transfer system with constant coefficients. However, the variation of b and c permits an increase in the difference $y_{on}''-y_{in}''$ which still keeps $E_{\max}$ small.

Letters to the Editor

Growth of Anodic Ta_2O_5 Films during Illumination with Ultraviolet Light

D. A. VERMILYEA
General Electric Research Laboratory, Schenectady, New York
(Received January 24, 1955)

IT has been reported by Bär[1] and by Young[2] that the optical thickness of an anodic Ta_2O_5 film formed at a given voltage may be increased by a factor of two or three if the film is illuminated during formation with light of wavelength less than 3000 A. The thickness calculated from capacitance measurements was also found to be increased but by a smaller amount. It is the purpose of this note to describe recent experiments which indicate that the thick films formed under such conditions are porous in structure.

A tantalum specimen was anodized at 20 volts in 2 percent H_2SO_4 at 50°C while being irradiated on one side with light from a mercury vapor lamp. The photocurrent on the illuminated side was about 0.008 ma/cm². The formation was interrupted periodically, and the thicknesses of the oxide film on the irradiated and dark sides of the specimen were measured by comparison with an optical thickness step gauge. It may be seen from Fig. 1 that the thickness of the oxide film on the dark side increased rapidly to about 400 A and then remained nearly constant. The thickness of the film on the illuminated side was nearly equal to that on the dark side until about 3000 seconds, after which it grew more rapidly. After about 8000 seconds the growth rate of the film on the illuminated side was constant at 0.038 A per second. The thickness of film on the illuminated side calculated from the measured capacitance assuming the same dielectric constant as for the dark side was 940 A while the optical thickness was 2575 A. When this specimen was etched in HF the film on the illuminated side dissolved very much more rapidly initially than that on the dark side, as shown in Fig. 2, but the rate of solution of the illuminated film decreased as it dissolved.

After the formation a nitrocellulose replica was made of the oxide film surface and examined in the electron microscope. It was found that the film contained about 10^7 to 10^8 pits per square centimeter of surface, each pit having a diameter of about 100 A. Films formed without ultraviolet illumination showed almost no surface structure.

It is believed that these results indicate that the oxide film formed during illumination with ultraviolet light consists of a thick porous outer layer over a thin dense inner layer. A similar oxide structure is known to form on aluminum anodized in 15 percent sulfuric acid.[3] The optical thickness of such a film is greater than the thickness calculated from capacitance measurements because the measured capacitance is very approximately that of the thin inner film in series with the resistance of the porous outer film. The irradiated film corrodes initially at a much greater rate because the corroding solution penetrates the pores of the outer film which then dissolves very rapidly. When the porous film has been removed the inner film dissolves at approximately the same rate as does the film on the dark side.

The mechanism by which the ultraviolet light results in the formation of the porous film is not understood. Because of the similarity of the structure produced by this process with that produced by anodic oxidation of aluminum in 15 percent H_2SO_4, it seems likely that the mechanisms may be similar. A further investigation of this effect is in progress.

[1] W. Bär, Z. Physik 115, 658 (1940).
[2] L. Young, Trans. Faraday Soc. 50, 153 (1954).
[3] Keller, Hunter, and Robinson, J. Electrochem. Soc. 100, 411 (1953).

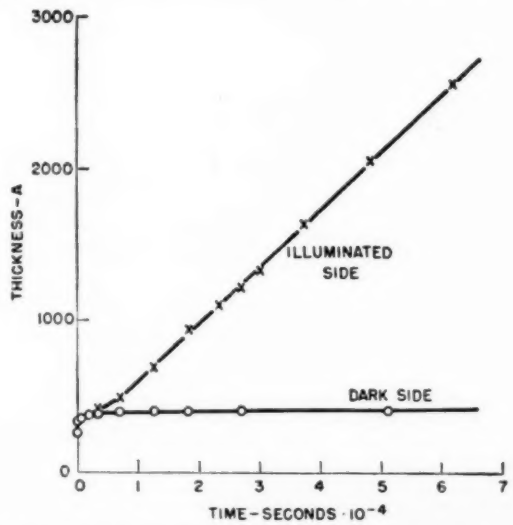

FIG. 1. Thickness of anodic oxide films as a function of time of formation.

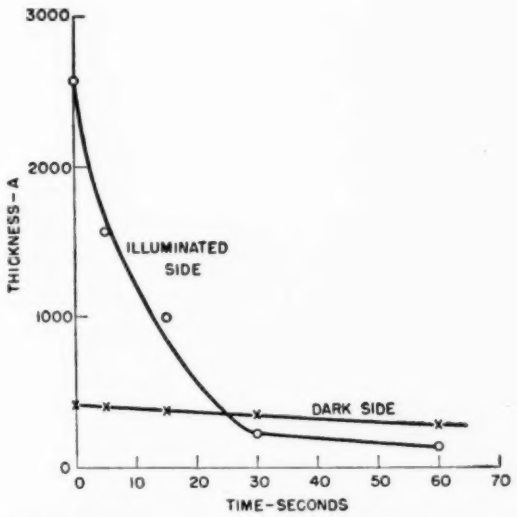

FIG. 2. Thickness of anodic oxide films as a function of time of etching in HF.

Laminar Flow in Channels with Porous Walls at High Suction Reynolds Numbers

JOHN R. SELLARS
Department of Aeronautical Engineering, University of Michigan, Ann Arbor, Michigan
(Received July 31, 1954)

THE problem of laminar flow in channels with porous walls has been considered recently by Berman[1] for the case of low Reynolds numbers. It is the purpose of this paper to extend the problem to very high Reynolds numbers by a method which becomes asymptotically exact as the Reynolds number increases indefinitely.

The problem which Berman treated was that of a laminar incompressible steady flow entering a two-dimensional channel and through whose walls there is a uniform suction velocity.

Berman has shown that the flow may be defined by a stream function of the form

$$\psi = \bar{u}d f(\lambda)[1 - x/L], \qquad (1)$$

where λ is y/d and L is the length from the entrance to the point where all the fluid has entered the walls.

The function f satisfies differential equation

$$f'''=R_s(ff''-f'^2+k_1) \tag{2}$$

with

$$f(0)=f''(0)=f'(1)=0,$$
$$f(1)=0.$$

Here primes denote differentiations with respect to λ, k_1 is a constant to be determined from the boundary conditions, and R_s is the suction Reynolds number.

Thus, it is clear that a complete solution of the problem only involves solving (2) and determining k_1 from the associated boundary conditions. By expanding f in a power series in R_s, Berman obtained a solution valid for R_s of the order of unity. We now consider the case of very high R_s: As a first step we will consider the limiting case of R_s infinite.

In this case (2) becomes

$$ff''-f'^2+k_1=0 \tag{3}$$

with

$$f(0)=f''(0)=0, \quad f(1)=1.$$

The formal procedure of letting $R_s\to\infty$ in (2) does indeed give the perfect fluid solution as may be verified by writing the corresponding perfect fluid problem. The boundary condition which must be dropped since the equation is now of lower order, corresponds to the "no slip" condition on the walls.

The proper solution of (3) is

$$f=\lambda, \quad k_1=1. \tag{4}$$

From this we see that the x-velocity at any point is independent of y. In the case where the Reynolds number is very high, one might expect that this same situation would exist over most of the channel except very near the walls, where there would be a thin boundary layer of slowed up fluid. In this case $f=\lambda$ would be a good approximation to the *magnitude* of the function even near the wall where the actual function's derivative must abruptly approach zero. These considerations form the basis of the following approximation scheme:

First, we integrate (2) to obtain

$$f''=R_s\left(ff'-2\int_0^\lambda f'^2d\lambda+k_1\lambda\right). \tag{5}$$

Here we have put in the boundary condition $f''(0)=0$. In this equation we now replace the term ff' with $\lambda f'$ and $\int_0^\lambda f'^2d\lambda$ with λ, in accordance with the statement that $f=\lambda$ is a good approximation to the magnitude over all the range. Notice that the integral is not very sensitive to the fact that the integrand really departs from unity in the close vicinity of the wall. Now the differential equation (5) becomes

$$f''=R_s[\lambda f'+(k_1-2)\lambda]$$
$$f(0)=f'(1)=0; \quad f(1)=1, \tag{6}$$

and the solution which satisfies the boundary condition is:

$$f=\frac{\lambda-I(\lambda)}{1-I(\lambda)} \tag{7}$$

with

$$k_1=\frac{1-2I(1)}{1-I(1)} \tag{8}$$

where

$$I(\lambda)=\int_0^\lambda \exp\left[\frac{R_s}{2}(\lambda^2-1)\right]d\lambda.$$

For large values of R_s, it may be shown that

$$I(\lambda)\leq I(1)\simeq R_s^{-1}+R_s^{-2}+\cdots. \tag{9}$$

By examining the approximations made in the differential equation it is seen that terms of the order of $(R_s)^{-1}$ have been neglected in comparison with terms of the order of unity. Thus, it is clear that (7) and (8) are good approximations provided that R_s is sufficiently high. One might hope, in fact, that $R_s=50$ is high enough. The above may be thought of as the first step in an iteration process and the steps may now be repeated using the more accurate values. The next step is, of course, quite complicated.

The x-component of velocity is then given by

$$u=\bar{u}\left\{1-\exp\left[\frac{R_s}{2}(\lambda^2-1)\right]\right\}\left\{\frac{1-x/L}{1-I(1)}\right\}. \tag{10}$$

From this we can define an effective boundary layer thickness, δ, which we will define as the distance from the wall to where the velocity reaches 99 percent of the center velocity.

$$\frac{\delta}{d}=1-\lambda_{b.l.}\cong\frac{4.6}{R_s}. \tag{11}$$

So, for $R_s=100$ the "boundary layer" only occupies 4.6 percent of the channel.

The pressure along the axis ($y=0$) is given by

$$p(x)-p(0)=p\bar{u}^2k_1\left(\frac{x}{L}-\frac{1}{2}\frac{x^2}{L^2}\right). \tag{12}$$

Since $k_1\to 1$ as $R_s\to\infty$, it is clear that the pressure gradient is positive as compared to the case of very low Reynolds numbers; in fact, at $x=L$, where $u=v=0$, the pressure approaches the stagnation pressure of the entering (essentially uniform) flow.

[1] Abraham S. Berman, J. Appl. Phys. 124, 1232 (1953).

Variation of Noise with Ambient in Germanium Filaments*

T. G. Maple,† L. Bess,† and H. A. Gebbie†
Lincoln Laboratory, Massachusetts Institute of Technology, Lexington, Massachusetts
(Received December 8, 1954)

THE purpose of this note is to present results of some experiments aimed at a better understanding of $1/f$ noise in semiconductors.[1,2] There is evidence that the noise level is influenced by surface properties, so it was to be expected that changing the medium in contact with the surface might be accompanied by changes in noise.

Table I.

Filament resistivity and type	Current (ma)	Noise factor (db)	$\Delta F/F$
>35Ω−cm p	0.86	21.7	+0.8
35Ω−cm p	0.24	27.4	+0.8
11Ω−cm p	1.53	18.7	−0.5
11Ω−cm n	1.46	11.7	+5.5
11Ω−cm n (filament re-etched)	1.46	12.6	+3.6

F = noise factor
$$=\frac{\text{noise power for a current of 1 ma measured at 40 cps in dry } N_2}{\text{thermal noise power}}$$

$$\Delta F/F=\frac{F(\text{wet } N_2)-F(\text{dry } N_2)}{F(\text{dry } N_2)}$$

The cross section of each filament was approximately 0.05 cm × 0.05 cm.

Table I shows the results of noise power measurements on two terminal filaments when the gas surrounding various filaments was changed from dry nitrogen to wet nitrogen (relative humidity 44 percent). The time between changes, which were repeated cyclically, was about 15 minutes. The values given refer to steady state readings that were reproducible over several cycles, since the first few cycles after etching generally were not reproducible.

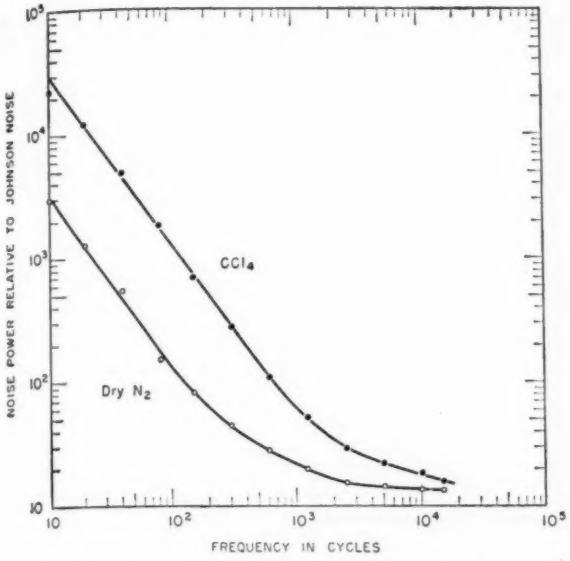

FIG. 1. Noise spectra in dry N_2 and CCl_4; sand-blasted surface.

The noise factor F was calculated with the observed noise power normalized to a current of 1 ma on the assumption that the noise power varies as the square of the current through the filament. In obtaining these results, observations were made over a range of frequencies to verify that $1/f$ noise was dominant at the frequency given (40 cycles/second).

In Fig. 1 is shown the noise spectrum for the same filament successively immersed in dry nitrogen gas and in liquid carbon tetrachloride. The filament was sandblasted to give a low value of minority carrier lifetime and although there was no change of this lifetime with ambient as shown by the decay transient of photo injected carriers in both media, there was a difference in noise power of about 10 db measured at low frequencies where $1/f$ noise is dominant. In these experiments carbon tetrachloride was chosen as an ambient since it was a non-ionic, chemically inert liquid of low conductance in which it was found that the noise level was considerably increased compared with dry nitrogen.

Figure 2 also shows a comparison of noise spectra for a filament in dry nitrogen gas and in liquid carbon tetrachloride. In these cases the filament was etched and as a consequence of the longer lifetime, shot-noise became dominant at lower frequencies than in the previous experiment. The observations for nitrogen gas can be well represented by the addition of $1/f^n (n \cong 1)$ noise and shot-noise. When the filament is in liquid carbon tetrachloride, however, this is not true. Subtraction of a shot-noise component from the observed curve leaves a component which is of the form $1/f^n$ $(n=1.3)$ at low frequencies but which falls off more rapidly at high frequencies and which is always concave downward within our range of observations.

From these observations we draw the following conclusions:

1. That changes in ambient can produce large changes in $1/f$ noise power, thus providing additional evidence of the influence of surface conditions on $1/f$ noise.
2. That changes in $1/f$ noise may be observed even when there is no change of minority carrier lifetime in the filament.
3. In confirmation of the results of reference 2 spectra have been obtained whose shapes can be explained as a simple addition of minority carrier shot-noise and noise with a spectral form of $1/f^n (n \approx 1)$.
4. There are examples (for instance the CCl_4 curve in Fig. 2) of a new type of noise spectrum whose shape cannot be accounted for by a simple addition of shot-noise and $1/f^n$ noise.

* The research in this document was supported jointly by the Army, Navy, and Air Force under contract with the Massachusetts Institute of Technology.

† Staff Member, Lincoln Laboratory, Massachusetts Institute of Technology.

[1] H. C. Montgomery, Bell System Tech. J. **31**, 950–975 (1952).

[2] G. B. Herzog and A. van der Ziel, Phys. Rev. **84**, 1249 (1951); R. H. Mattson and A. van der Ziel, J. Appl. Phys. **24**, 222 (1953).

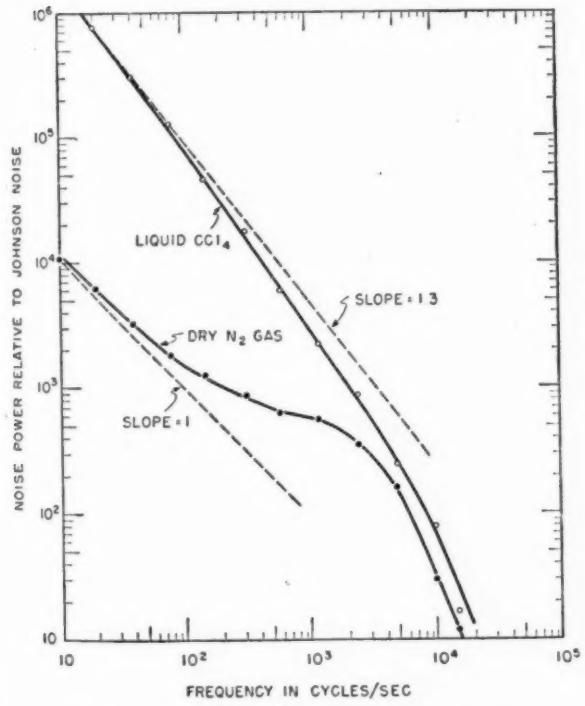

FIG. 2. Noise spectra in dry N_2 and CCl_4; etched surface.

Note on Self-Diffusion of Nickel*

H. BURGESS AND R. SMOLUCHOWSKI
Carnegie Institute of Technology, Pittsburgh, Pennsylvania
(Received January 17, 1955)

IN spite of the recent interest in self-diffusion of metals there seem to be still a few obvious gaps in our knowledge of the pertinent experimental facts. In particular there are no data published on self-diffusion of nickel. Some preliminary measurements of this quantity have been made by the authors a few years ago and the results have been of use to various physicists. It seems perhaps justified to make these incomplete data available before a more systematic study is made.

The technique used was that of plating the isotope Ni^{63} on the surface of a piece of nickel and diffusing it at various temperatures. The measurements were made by measuring the drop of activity of the surface. The particular feature of Ni^{63} is that its activity is a very soft beta radiation which can be measured only by special techniques. In our work a Tracerlab gas flow counter was used with good success. The softness of the beta radiation of nickel has the great advantage that the measured activity corresponds quite closely to the activity of the surface alone: The contribution of the deeper layers plays a small role and thus the well-known difficulty of accounting for it exactly is minimized. The absorption coefficient for the beta activity was estimated from data obtained with thin Formvar layers[1] as μ 1000 cm^{-1}. The diffusion coefficients were measured in the temperature range from 250°C to 1250°C. At 1000°C, the diffusion coefficient is 1.5×10^{-12} cm^2 sec^{-1} and the activation energy lies in the range 61 000 to 65 000 cal/mole. At

about 650°C there occurs a knee in the $\ln D$ *vs* $1/T$ plot and at the lower temperatures the activation energy is between 10 000 and 15 000 cal/mole. This presumably corresponds to grain boundary diffusion.

* Work supported by a U. S. Atomic Energy Commission contract.
[1] The authors are indebted to Raymond N. Nether for performing the Formvar absorption measurements.

Information Required for Missile Guidance

FRED P. ADLER
Hughes Aircraft Company, Culver City, California
(Received December 24, 1954)

THE purpose of this note is to point out that, contrary to statements occasionally found in the literature and the press, the amount of information and the information rates required for missile guidance are actually quite small. Some crude calculations will be presented to illustrate this point.

The two essential functions performed by any missile guidance system are (1) reducing the otherwise existing flight path dispersion, and (2) following any evasive maneuvers of the target (except, of course, in the case of stationary ground targets). In order to avoid unnecessary mathematical complexity, the information requirements for these two functions will be considered separately.

The ensemble dispersion pattern about the target in the absence of any guidance may reasonably be assumed to be represented by identical normal distributions along any two orthogonal miss coordinates measured from the target center. The radial or miss distance, ρ, will then be Rayleigh-distributed and the miss angle, φ, will be uniformly distributed. The combined probability distribution of the miss coordinates ρ and q is thus given by

$$p(\rho,\varphi)=p(\rho)p(\varphi)=\frac{\rho}{\pi\sigma_0^2}\exp\left(-\frac{\rho^2}{\sigma_0^2}\right) \tag{1}$$

where $\sigma_0^2=\langle\rho\rangle_{Av}$. The corresponding information function is

$$H_0=-\int_0^\infty\int_0^{2\pi}p(\rho,\varphi)\log_2[p(\rho,\varphi)]d\rho d\varphi=\log_2(\gamma^{\frac{1}{2}}e\sigma_0/2) \tag{2}$$

where $\ln\gamma=0.577\ldots$ is Euler's constant. The guidance must now reduce the rms miss from σ_0 to some small value σ_1. Assuming that the dispersion pattern in the presence of guidance also has a distribution of the form (1), the corresponding entropy is

$$H_1=\log_2(\gamma^{\frac{1}{2}}e\sigma_1/2). \tag{3}$$

Hence the information which must be supplied by the guidance is given by

$$Q=H_0-H_1=\log_2(\sigma_0/\sigma_1)\text{ bits}. \tag{4}$$

The dispersion σ_0 may be expressed in terms of the average closing speed V_c, the missile flight time t_f and the dispersion angle ϵ which measures the flight path deviation from a collision course (in the absence of guidance) due to initial aiming error, thrust misalignment, etc. Assuming numerical values of 1000 feet per second, 10 seconds, and 10 degrees for V_c, t_f, and ϵ, respectively, yields

$$\sigma_0=V_c t_f\sin\epsilon=1740\text{ feet}. \tag{5}$$

Although selected somewhat arbitrarily, the above values appear reasonable for a relatively short-range missile. The allowable value of σ_1 will depend generally on target size and warhead effectiveness; a value of about 10 feet should be sufficiently small in most cases. Substitution of these values into Eq. (4) yields $Q\approx 7.5$ bits, corresponding to an average information rate, $\langle q\rangle_{Av}=Q/t_f$, of 0.75 bit/second.

The effect of target maneuver will now be considered. If a_m is the maximum acceleration which the target can apply, then $\rho_0=a_m t_f^2/2$ will be the greatest distance it can displace itself from the initial aim point. Assume now that all values of target acceleration between zero and a_m are equally likely, as well as all directions of acceleration. The probability distribution of the target position at time t_f relative to the predicted aim point is therefore

$$p(\rho,\varphi)=1/2\pi\rho_0. \tag{6}$$

In the absence of dispersion this also represents the distribution of the miss. The information function corresponding to this miss distribution is

$$H_0=-\int_0^{\rho_0}\int_0^{2\pi}p(\rho,\varphi)\log_2[p(\rho,\varphi)]d\rho d\varphi=\log_2(2\pi\rho_0). \tag{7}$$

If the final miss distribution is to have again an rms value of σ_1, the information to be supplied by the guidance is the difference between this H_0 and the H_1 of Eq. (3), or

$$Q=H_0-H_1=\log_2(2\pi a_m t_f^2\gamma^{\frac{1}{2}}e\sigma_1)=1.79+\log_2(\rho_0/\sigma_1)\text{ bits} \tag{8}$$

corresponding to a mean rate of

$$\langle q\rangle_{Av}=\frac{1}{t_f}\log_2(2\pi a_m t_f^2/\gamma^{\frac{1}{2}}e\sigma_1)\text{ bits/second}. \tag{9}$$

Now for a bomber target, a value of a_m equal to twice the acceleration of gravity might not be unreasonable. Using the same parameters as before yields $\rho_0=3220$ feet and $Q\approx 10$ bits, $\langle q\rangle_{Av}\approx 1$ bit/second.

The sum of the quantities of information required to reduce dispersion as well as the effect of target maneuver is seen to be about 18 bits, corresponding to an average rate of 1.8 bits/second. Although the actually required rate may exceed this figure because of a number of factors which were neglected in this highly simplified calculation, the result obtained should at least give a valid order-of-magnitude indication.

A feeling for the magnitude of the information rate found above may be obtained by comparing it with that of ordinary speech. Assuming a typical speaking rate of 150 words per minute, an average word length of 5 letters, a twenty-six letter alphabet and a language redundancy of ½ (about typical of English) gives a rate of

$$q=\left(\frac{150}{60}\right)(5)\left(\tfrac{1}{2}\right)\log_2 26\approx 30\text{ bits/second}. \tag{10}$$

It is seen then that in theory it should be possible to guide such a missile by slowly talking to it, provided, of course, one knew the right words (commands) to use.

Books Reviewed

Mathematics in Type. Pp. 58+xiii, William Byrd Press, Richmond, Virginia, 1954. Price $3.00 (50 percent discount to staff of educational institutions).

This book is designed to help authors of journal articles or books who use mathematical expressions. It should thus be of value to the authors of almost all articles in this journal. The hand, line-casting, and monotype methods of composition are described in enough detail so that an author can visualize the problems his notation will cause and can learn how he can make changes which will make the composition less expensive. Marking of a manuscript for the printer, proof corrections, and kinds and sizes of type are discussed also.

Annual Review of Nuclear Science Vol. 4. J. G. BECKERLEY, M. D. KAMEN, AND L. I. SCHIFF (editors). Pp. 483+ix, Annual Reviews, Inc., Stanford, California, 1954. Price $7.00 (foreign $7.50).

Seventeen review articles are presented in this volume of the Annual Review Series. Readers of the *Journal of Applied*

Physics will probably be particularly interested in the following: proton synchrotrons (Blewett); rf and microwave spectroscopy (Pake); use of the stable isotope dilution method in analysis (Inghram); three articles on nuclear particle detection (Bell, Swank, and Marshall); penetration of heavy charged particles in matter (Uehling). The individual reviews present many references and there is an author and a subject index for the volume.

Standard Samples and References. Standards Issued by the National Bureau of Standards. NBS Circular 552, Pp. 23, Government Printing Office, Washington, D. C. Price $0.25 (Foreign: $0.35).

This Circular lists the over 500 standard samples of chemicals, ores, ceramics, and metals which are prepared, certified as to chemical or physical properties, and distributed by the Bureau of Standards. It provides a schedule of fees and instructions for ordering.

Elementary Meteorology. GEORGE F. TAYLOR. Pp. 364+viii, Prentice-Hall, Inc., New York, 1954. Price. $7.95.

This book is an introductory textbook in meteorology. Problems and review questions are included at the end of each chapter. The whole field of meteorology, including instrumentation and climatology, is covered. The mathematics used is only simple algebra, but the geostrophic wind equation is presented and analyzed.

Algebra for College Students. W. M. WHYBURN AND P. H. DAUS. Pp. 290+xi, Prentice-Hall, Inc., New York, 1955. Price $4.25.

It is the stated intention of the authors to present those portions of arithmetic, algebra, and geometry in which the college student's background may be deficient. They have tried to avoid making this text a review of material with which the student is already familiar. The sequence of subjects treated begins with the fundamental direct and inverse operations of algebra. Following this there are chapters on fractions, linear equations, quadratic equations in one unknown, simultaneous quadratic equations, exponents and logarithms, sequences of numbers, and mathematical induction. Numerous problems are included, the answers to which appear at the end of the book.

Mathematics of Engineering Systems. DEREK F. LAWDEN. Pp. 380+viii, John Wiley and Sons, Inc., New York, 1955. Price $5.75.

This work treats a number of mathematical methods which can be used to analyze various physical systems. The book may serve either as a text in applied mathematics for engineering students or as a reference book for the specialist who works in the field of the theory of control systems. Topics treated in the book include linear differential equations with constant coefficients and application to practical systems, Fourier analysis, and nonlinear differential equations. Exercises have been added throughout the text with the solutions given at the back of the book.

The Design and Use of Instruments and Accurate Mechanism—Underlying Principles. T. N. WHITEHEAD. Pp. 283+xiv, Dover Publications, New York, 1954. Price $1.95 (paper) or $3.50 (cloth).

This book is based on the practical experience of a designer and user of instruments and accurate mechanisms. Part I is concerned with a discussion of instrumental errors and is essentially nonmathematical in treatment. Included are sections on systematic, short period, and erratic errors, as well as probability as applied to errors. In Part II the theory of errors is applied to a variety of mechanisms. Entitled *Design*, this part deals with the questions of precision in both kinematic and semikinematic design, accuracy, and the stiffness, isolation, and protection of elements. The planning of an instrument, with various examples, is also discussed at some length. The human factor of judgment in the use of instruments is the subject of the final chapter of the book.

Introduction to Theoretical Mechanics. R. A. BECKER. Pp. 420+xiii, McGraw-Hill Book Company, Inc., New York, 1954. Price $8.00.

This is a text designed for students whose scientific sophistication need be no more extensive than that derived from a thorough groundwork in elementary physics and calculus. In fact, the author does not presuppose prior knowledge of vector analysis and elementary differential equations. Introductions to both are provided. The treatment of the more conventional subjects of statics and dynamics of particles and rigid bodies is supplemented by discussions of topics which have unusual significance in modern physics. Some examples are nonlinear systems in connection with one-dimensional oscillatory motion and general rigid body rotation in space (which reflects the present wide interest in magnetic resonance and microwave spectroscopy). Topics of a more advanced nature are reserved for the end of the book. These include generalized coordinate methods, vibrating systems, and wave motion in strings. The book contains about 400 problems.

The Gyroscope Applied. K. I. T. RICHARDSON. Pp. 384, Philosophical Library, New York, 1954. Price $15.00.

The principal subject of this book is the application of the gyroscope to marine and aircraft instruments and controls. There is a short, nonmathematical introduction to the gyroscope and a short appendix on its elementary mathematics. The book is thoroughly illustrated with photographs and drawings of equipment and block diagrams of control systems.

High-Energy Accelerators. M. STANLEY LIVINGSTON. Pp. 157+viii, Interscience Publishers, Inc., New York, 1954. Price $3.25.

The post-war developments in the field of particle accelerators are described in this book. It presents the physical principles, design considerations, and examples of electron and proton synchrotrons, synchrocyclotrons, and linear accelerators. There is a chapter on alternate gradient ("strong") focusing.

Rocket Exploration of the Upper Atmosphere. R. L. F. BOYD AND M. J. SEATON (editors). Pp. 376+viii, Interscience Publishers Inc., New York, 1954. Price $11.00.

A conference to discuss upper atmosphere research was held at Oxford in August, 1953. The conference was sponsored by the Upper Atmosphere Rocket Research Panel and by the Gassiot Committee of the Royal Society of London. The papers presented at that conference are published in this volume. The editing was performed in consulation with H. S. W. Massey. The book contains five papers on techniques. It contains papers on research concerned with the composition, pressure, and temperature of the upper atmosphere and with ionospheric, solar radiation, and geomagnetic phenomena in the upper atmosphere. There are also papers on cosmic-ray measurements, laboratory studies complementing rocket research, and theoretical investigations.

The Theory of Cohesion. M. A. JASWON. Pp. 245+viii, Interscience Publishers, Inc., New York, 1954. Price $5.75.

The nature of the cohesive forces in atoms, molecules, and solids is the subject of this book, which is Vol. II in the

Metal Physics and *Physical Metallurgy* series. The first third of the book is devoted to an exposition of wave mechanics. Quantum mechanics is then applied to the hydrogen molecule and molecular orbitals. The theory of the cohesive energy in metals, alloys, and covalent solids is then discussed.

Books Received

Strength and Resistance of Metals. JOHN M. LESSELLS. Pp. 450+xvi, numerous Figs., John Wiley and Sons, Inc., New York, 1954. Price $10.00.

Storage Batteries. GEORGE WOOD VINAL. Fourth edition. Pp. 446+xi, Figs. 163, John Wiley and Sons, Inc., New York, 1955. Price $10.00.

Magnetic Amplifiers. H. F. STORM. Pp. 545+xix, numerous Figs., John Wiley and Sons, Inc., New York, 1955. Price $13.50.

Mathematics of Engineering Systems. DEREK F. LAWDEN. Pp. 380+viii, numerous Figs., John Wiley and Sons, Inc., New York, 1955. Price $5.75.

Basic Electricity. VAN VALKENBURGH, NOOGER AND NEVILLE, INC. Pp. 608 in the 5 Volumes, numerous illustrations, John F. Rider Publisher, Inc., New York, 1954. Price $2.00 per Volume (paperbound); $9.00 for the set of 5 Volumes.

Transactions of the American Philosophical Society. Vol. 44, Part 6. The Illumination and Polarization of the Sunlit Sky on Rayleigh Scattering. S. CHANDRASEKHAR AND DONNA D. ELBERT. Pp. 728, Tables 12, American Philosophical Society, Philadelphia, 1954. Price $2.00.

Handbook of Radiology. RUSSELL H. MORGAN. Pp. 518+x, Year Book Publishers, Chicago, 1955. Price $10.00.

Algebra for College Students. WILLIAM M. WHYBURN AND PAUL H. DAUS. Pp. 290+xi, Figs. 42, Prentice-Hall Inc., New York, 1955. Price $4.25.

The Theory of Cohesion. M. A. JASWON. Pp. 245+viii, Interscience Publishers, Inc., New York, 1954, Volume II. Price $5.75.

Annual Review of Nuclear Science. Edited by JAMES G. BECKERLEY. Pp. 483+x, numerous Figs., Annual Reviews, Inc., Stanford, California, 1954, Volume 4. Price $7.00.

The Gyroscope Applied. K. I. T. RICHARDSON. Pp. 384, numerous Figs., Philosophical Library, New York, 1954. Price $15.00.

Introduction to Theoretical Mechanics. ROBERT A. BECKER. Pp. 420+xiii, numerous Figs., McGraw-Hill Book Company, Inc., New York, 1954. Price $8.00.

Announcements

An International Symposium on Electrical Discharges in Gases is being held in Delft, Netherlands from April 25 to 30. It is supported by the International Union of Pure and Applied Physics, by the Technical University of Delft and by the Philips Research Laboratories.

Cover Photograph

This map is the nearest approach yet made to a radio "photograph" of the center of our galaxy. The contours are "isophotes" of equal radio "brightness" as measured at 120 cm wavelength with The Ohio State University radio telescope. The contours suggest the way the sky would appear if our eyes were sensitive to radio waves instead of light. The brightest or highest intensity spot is the center or nucleus of our galaxy at the lower center of the map. This nucleus is obscured by dust from optical observation but stands out as an intense radio source. The plane of our galaxy or Milky Way system is seen to extend toward the upper left. The coordinates are right ascension (α) and declination.

The map and explanation were supplied by Professor John D. Kraus.